Ligand Frameworks for Transition-Metal Complexes That Model Metalloenzyme Active

Denan Wang
Marquette University

LIGAND FRAMEWORKS FOR TRANSITION-METAL COMPLEXES THAT MODEL METALLOENZYME ACTIVE SITES

by
Denan Wang, B. S.

A Dissertation submitted to the Faculty of the Graduate School,
Marquette University,
in Partial Fulfillment of the Requirements for
the Degree of Doctor of Philosophy

Milwaukee, Wisconsin

December 2015

ABSTRACT

LIGAND FRAMEWORKS FOR TRANSITION-METAL COMPLEXES THAT MODEL METALLOENZYME ACTIVE SITES

Denan Wang, B. S.

Marquette University, 2015

Advances in the field of biomimetic inorganic chemistry require the design of sophisticated ligand frameworks that reflect the amazing complexity of metalloenzyme active sites. For instance, most active sites feature extensive hydrogen-bonding interactions between ligands bound to the metal center (the "first" coordination sphere) and nearby units in the outer (or "second") sphere. Since these interactions modify the structural and electronic properties of the active sites, a number of inorganic chemists have sought to design ligands that permit outer-sphere functional groups to interact with first-sphere donors. This dissertation describes our contribution to these broader efforts to model the second coordination sphere. To date, our efforts have centered on the two classes of ligands based on second-sphere amide groups. The first set consists of 2,6-pyridinedicarboxamides with pendant pyridine or pyrimidine groups. Compared to the pincer ligands, the tripodal ligands posed a significantly greater synthetic challenge. We have succeeded in preparing a series of target ligands consisting of one, two, or three second-sphere heterocycles. My work has suggested that the second coordination sphere hydrogen bond interaction can be performed in our synthetic model.

In addition, metalloenzymes with homobinuclear and heterobinuclear active sites play a central role in the chemistry of life. We have generated ligand scaffolds that support homo- and heterobimetallic complexes of relevance to metalloenzyme active sites. Firstly, the synthesis and coordination chemistry of a new asymmetric ligand designed to support nickel based heterobimetallic structures with relevance to bioinorganic chemistry is described. Additionally, we report the synthesis and coordination chemistry of 'non-innocent' pentadentate ligands intended to provide multiple sites for ligand-based oxidation and reduction. This 'non-innocent' ligand series contains a central diarylamido donor that serves as electron donor, in addition to 'hard' donor ligands (oxygen atoms), electron acceptor units, and 'soft' donor ligands. The resulting homobimetallic complexes (M = Co, Cu, and Zn) were characterized with X-ray crystallography and electrochemical methods. In addition, our studies found that the dicobalt(II) complex is a stable and efficient electrocatalyst for both H_2 generation and H_2O oxidation processes (i.e., water splitting).

ACKNOWLEDGMENTS

Denan Wang, B. S.

First of all I would like to thank my advisor, Professor Adam Fiedler for all his guidance and support. I feel so lucky to join to this clean, organized and wonderful working environment. Professor Fiedler was very patient, supportive and encouraging in guiding me towards the right direction, which gave me a tremendous amount of confidence to pursue lab work with much more efficiency. Moreover, he is not only an excellent scientist but also a great friend. He is a very understanding advisor and helps his students in their difficult times.

I would like to thank my committee members, Dr. Ryan, Dr. Dockendorff and Dr. Huang, for their time, patience and suggestions. I would like to thank Dr. Sergey Lindeman for solving the crystal structures of my metal complexes. I would like to thank Dr. Sheng Cai, who was always willing to share his expertise in NMR with me. Moreover, I would thank to Chemistry Department of Marquette University for financial support. I would like to thank the Graduate School and all of the Marquette University administration.

I would like to thank my lab mates Dr. Heaweon Park, Jake Baus, Mike Bittner, Xixi Hong, Amanda Baum, Ann Fisher and Tim Schluechtermann for their thoughtful discussions and assistance during my time at Marquette.

I would like to thank my parents, Jianxing Wang and Bishuang Wu, for always supporting my endeavors. Without their support and patience none of this would have been possible. My sister and brother in law, Lifeng Wang and Chaoqun Lai, have also been very supportive of all my decisions. I would like to specially thank to Yilin for her support and understanding. I would like to thank my relatives who were always there to cheer me up throughout my academic career. I would also like to thank all my friends who accompanied me during my time at Marquette.

TABLE OF CONTENTS

LIST OF TABLES

LIST OF FIGURES

LIST OF SCHEMES

Chapter 1

Introduction: Bioinspired Ligand Design for the Development of New Models of Metalloenzyme Active Sites

Crystallographic structure of human SOD1 (PDB 2VR6).[1]

Abstract: Metalloenzymes perform demanding chemical transformations at ambient temperature and pressure, and play a critical role nearly all metabolic processes. However, numerous questions regarding the function of metalloenzymes remain unanswered. In this chapter, we first discuss the role of the second coordination sphere in tuning the catalytic properties of metalloenzymes, and describe attempts by chemists to generate synthetic complexes with bio-inspired hydrogen-bond networks. Secondly, we will examine several metalloenzyme systems with bimetallic active sites, and describe attempts by synthetic chemists to prepare suitable model complexes.

1.1 Bioinorganic Chemistry

The field of bioinorganic chemistry is concerned with the role of metal ions in biological systems.[2,3] Prominent research topic in this field are the transport and storage of metal ions, the structure and function of metalloenzymes, as well as the design and mechanism of metal-containing medicines.[4] Metalloenzymes have also attracted the attention of synthetic chemists due to their ability to perform demanding chemical transformations at ambient temperature and pressure, often with impressive selectivity.

The relationship between structure and function in metalloenzyme active sites has been the subject of countless studies over the past century. Biochemists have examined metalloenzymes using a combination of structural, spectroscopic, and kinetic methods, and these efforts have helped to elucidate the catalytic mechanism at work. The biochemical studies have often benefited from the insights of inorganic chemists who have extensive knowledge of coordination chemistry, spectroscopic methods, and transition-metal reactivity. At the same time, the existence of metal-containing enzymes has inspired inorganic chemists to design synthetic complexes that mimic key structural, spectroscopic, and/or functional aspects of the biological systems. Thus, a fruitful interplay between enzymologists and inorganic chemists has emerged over the past few decades which has contributed to our present understanding of metalloenzyme function.

Advances in the field of biomimetic inorganic chemistry require the design of sophisticated ligand frameworks that reflect the amazing complexity of metalloenzyme active sites. For instance, most active sites feature extensive hydrogen-bonding interactions between ligands bound to the metal center (the "first" coordination sphere) and nearby units in the outer (or "second") sphere. Since these interactions modify the structural and electronic properties of the active sites, a number of inorganic chemists have sought to design ligands that permit outer-sphere functional groups to interact with first-sphere donors. This dissertation describes our contribution to these broader efforts to model the second coordination sphere. In addition, we present ligand scaffolds that support homo- and heterobimetallic complexes of relevance to metalloenzyme active sites. The structural and functional properties of these bimetallic complexes are described in detail.

1.2. Second Coordination Sphere Interactions in Metalloenzymes and Biomimetic Complexes

1.2.1 Roles of First and Second Coordination Spheres

Since its inception in the late 1800's, the field of coordination chemistry has focused almost exclusively on interactions of metal ions with first-sphere ligands (i.e., those directly coordinated to the metal ion). The first coordination sphere is dominated by covalent bonding between metal ion(s) and the donor atoms of ligands. Both

experimental and theoretical studies have revealed that this primary shell is the dominant factor determining molecular structures, electronic properties, and chemical reactivities for transition metal complexes.[5] More specifically,

First-sphere ligands influence key structural properties, such as coordination number and molecular geometry.

The first coordination sphere impacts the electronic structure of metal ion(s), including spin state, ligand field splitting, redox potentials, and spectroscopic features. For instance, strong-field ligands like CO and CN^- generally result in low-spin metal ions, whereas weak-field ligands like halide anions yield high-spin complexes. The ability of first sphere ligands to tune the electronic structures of metal complexes is often assessed through analysis of d-d transitions in UV-vis absorption spectra.

The first coordination sphere controls the reactivity of metal complexes. The well-known *trans* effect, for example, demonstrates that ligands can modify the labilization of other first shell donors, thereby altering rates of ligand exchange.[6] Structure-function relationships developed by inorganic chemists have led to several coordination complexes that are employed as pharmaceuticals (the best known example is the anti-tumor agent, cisplatin).[7] In addition, transition metal compounds serve as catalysts in numerous industrial processes (e.g. the Monsanto acetic acid process).[8]

While the first coordination sphere determines the structure and reactivity of metal complexes to a large extent, the study of metalloproteins has highlighted the

significance of functional groups that are located nearby, but not directly bonded to, metal center(s). These groups are said to occupy the *second coordination sphere*. 'Metalloproteins' have been examined since the 1950s, when the first X-ray crystal structure of sperm whale myoglobin indicated the presence of an Fe atom.[9] The majority of the 'metalloproteins' are enzymes that require a transition metal cofactor for proper catalytic function.[10-12] Through extensive structural, spectroscopic, and mechanistic studies, the scientific community currently possesses a detailed understanding of the functional role of the metal ion(s) in metalloenzymes. Moreover, synthetic models of metalloenzyme active sites have been developed that mimic the structure and/or reactivity of the biological systems. Even though such complexes have provided valuable insights into metalloenzyme catalysis, many fail to duplicate the biological reactivity.[13] One reason for this failure is the inability of the synthetic complexes to replicate the second coordination spheres of enzyme active sites.

Whereas the first coordination sphere involves direct bonds between metal ions and ligands, the second coordination sphere exerts its influence via noncovalent interactions with first sphere ligands. Often, the entire range of non-covalent interactions is involved: hydrogen bonding, polar and dipolar attractions, dispersion forces, and charge-transfer interactions.[14] Yet hydrogen bonding is undoubtedly the most important type of interaction in metalloenzyme active sites. This phenomenon is illustrated in

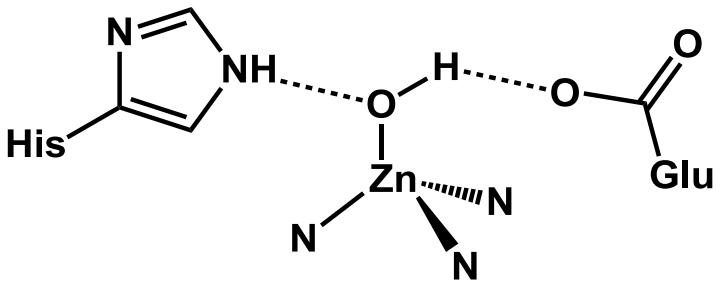

Figure 1.1 Example of H-bond interaction between first and second sphere ligands in the active site of carbonic anhydrase.[15]

The second coordination sphere exerts control over metalloenzyme catalysis in several ways, as described below:

1. ***Steric shell effect***: The protein environment acts as protective shell that encircles the metal-binding region, thereby preventing harmful side reactions with molecules in the cytosol.

2. ***Stabilization of reactive species***: Residues in the second coordination sphere often stabilize high energy intermediates in the catalytic cycle. For example, the iron-dioxygen adduct in myoglobin is a highly polar species that is selectively stabilized by hydrogen bonding to the conserved HisE7 group (**Figure 1.2**).[16] Numerous enzymes lower the energetic barriers to charged or polar catalytic intermediates via H-bonding interactions that mitigate the build-up of charge in the active site. In the urease catalytic cycle, for instance, the anionic tetrahedral intermediate formed after nucleophilic attack of hydroxide on urea is stabilized by H-bonds to three conserved resiudes.[17]

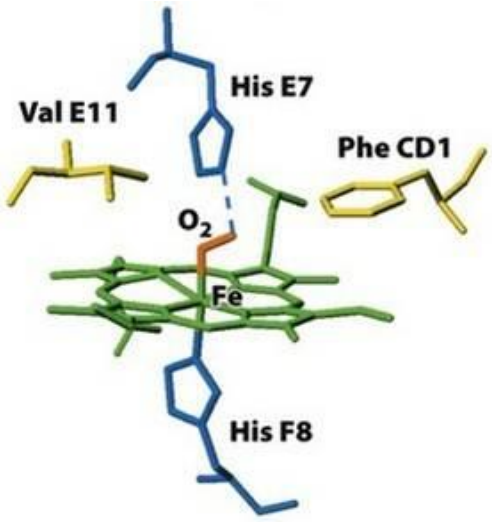

Figure 1.2 Active site structure of oxy-myoglobin.[16]

3. ***Substrate binding***: Substrates in metalloenzymes generally do not ligate the metal centers directly; instead, they coordinate to a proximal region within the active site. Functional groups in the second coordination sphere are crucial in creating a high-affinity pocket that binds substrates via noncovalent interactions. Modifications in second sphere residues allow enzymes with similar active site structures to display remarkable substrate specificity. For example, all members of the cytochrome P450 superfamily of enzymes feature a cysteinate-ligated heme cofactor, yet these enzymes selectively oxidize a wide variety of substrates.[18]

4. ***Acid-base catalysis***: In metalloenzymes, second sphere residues often play the role of acid-base catalysts, alternately accepting and donating protons to the substrate. This strategy is commonplace in zinc enzymes that perform the hydrolysis of biomolecules. An example is provided in **Figure 1.3**, which shows the mechanism of

carboxypeptidase A.[19] The resting state of the enzyme features a Zn(II) center bound to one Glu and two His ligands, in addition to one water molecule. A carboxylate group derived from the second sphere Glu270 residue initially acts as a base, facilitating the deprotonation of the H_2O ligand. This generates a nucleophilic hydroxide ligand that attacks the substrate carbonyl. Formation of the amino product following breakdown of the tetrahedral intermediate requires proton transfer from the second-sphere Glu270 (now acting as an acid). Nearly all hydrolytic enzymes employ a variant of this mechanism.

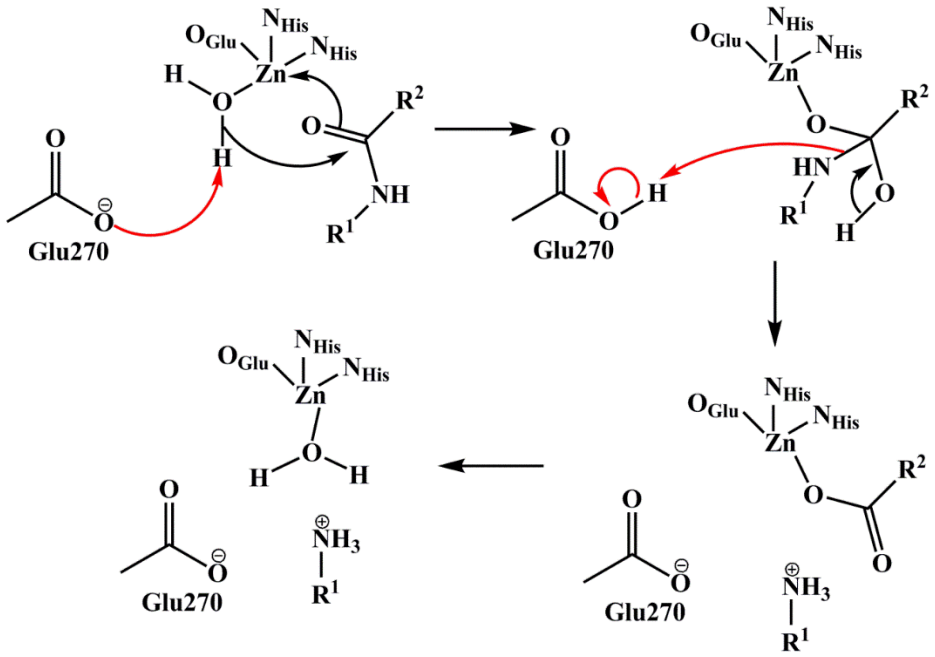

Figure 1.3 Catalytic mechanism of carboxypeptidase A.[19]

5. ***Redox tuning***: Hydrogen bonding between first and second sphere ligands can modulate the redox potentials of metal centers to a significant degree. The classic case of the Fe and Mn superoxide dismutases (SODs)[20] has been well studied. Experiments by Miller and coworkers have demonstrated that the metal specificity of Fe/MnSODs arises from subtle differences in redox tuning between the two enzymes.[21,22] Here, we also mention the heme-containing enzyme, horseradish peroxidase (HRP).[3] The active-site structure of HRP is nearly identical to myoglobin; however, HRP does not bind O_2 and the Fe center is generally in the ferric state. The lower potential of the heme cofactor in HRP is attributed to a conserved Asp residue that serves as an H-bond acceptor to the axial His ligand (**Figure 1.4**). This interaction imparts anionic character to the His ligand, stabilizing the Fe(III) state. Thus, redox tuning by the second coordination sphere often has functional significance.

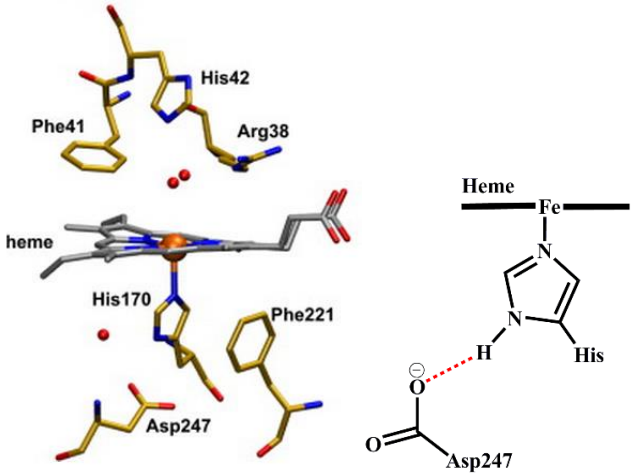

Figure 1.4 Active site structure of HRP displaying the H-bonding interaction between the distal His170 ligand and Asp 247.[3]

1.2.2 Incorporation of Second Coordination Sphere Effects in Synthetic Complexes

Insights gained from metalloenzymes have encouraged inorganic chemists to design ligand frameworks with functionalized second coordination spheres. These ligands generally contain outer-sphere groups capable of forming hydrogen bonds with the first-sphere donors. Yet this task has proven challenging for a number of reasons. Firstly, the designed ligand must be rigid enough to the place the H-bond donor (or acceptor) in the proper orientation with respect to the first sphere ligands. Another common problem is that polydentate ligands that include both first- and second-sphere ligands often coordinate to metal centers in unexpected fashions. For example, an amide moiety that was intended to serve as an outer-sphere H-bond donor (via its N-H group) may coordinate directly to the metal center via its carbonyl group. Ligands with "excess" functional groups also have a greater tendency to form multinuclear complexes and polymeric arrays, since the outer-sphere groups can easily form linkages between metal ions. Finally, ligands that strive to model the first and second coordination spheres are generally more complex than conventional ligands, making them difficult and time-consuming to synthesize. Despite these difficulties, there are many impressive examples of heme and nonheme complexes that incorporate intramolecular H-bonding networks between first and second sphere ligands.

1.2.2.1 Synthetic Heme Complexes with Second Sphere Hydrogen Bond Donors

There are several heme complexes that contain H-bond donors in the second coordination sphere. The earliest example was the "picket-fence" Fe porphyrin generated by Collman in the 1970s (**Figure 1.5**).[23,24] This ligand system was intended to mimic the reversible O_2-binding of enzymes like hemoglobin and myoglobin. The *meso*-carbons of the porphyrin ring are functionalized with four amide groups that (i) provide steric bulk, preventing dimerization and side reactions that often plague heme/O_2 chemistry, and (ii) serve as H-bond donors to the bound O_2 ligand. Interestingly, although the presence of the amide appendages substantially increases dioxygen affinity, the distance between the distal oxygen atom and the nearest N-H donor is too long to be considered a proper H-bond. Thus, it appears that dipole-dipole attractions account for the enhanced O_2 binding in the picket fence complex.

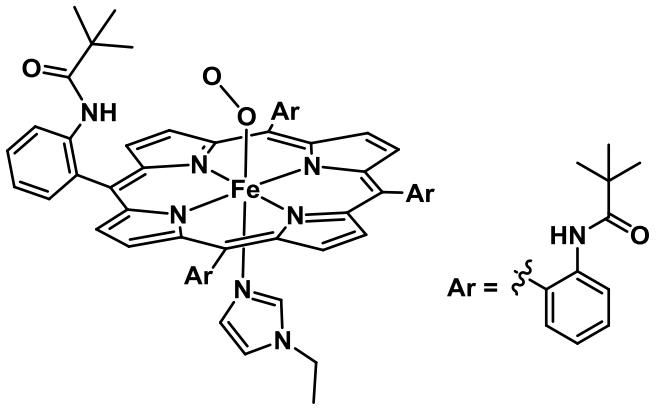

Figure 1.5 Structure of Collman's picket-fence iron porphyrin.[23]

Other chemists have improved upon the "picket fence" approach by reducing the distance between the H-bond donor(s) and the O_2-binding pocket. For instance, Reed has developed a mixed urea/amide porphyrin (**Figure 1.6**) in which one side chain possesses a phenylurea group that forms a strong H-bond with coordinated O_2.[25] This simple modification results in a 9-fold increase in dioxygen affinity relative to the first-generation picket-fence porphyrin.

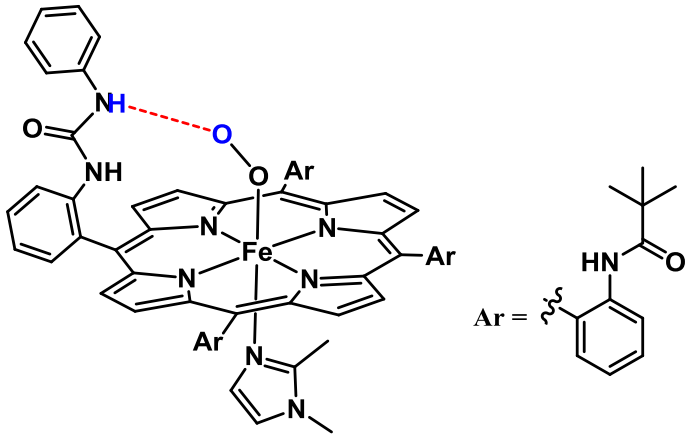

Figure 1.6 Reed's urea/amide-appended porphyrin with bound O_2.[25]

Chemists have also employed H-bond donors not related to the amide/urea motif.[26] For instance, Chang and Nocera prepared porphyrins with a carboxylate donor (derived from Kemp's acid) positioned above the Fe center (**Figure 1.7**). In a similar manner, Nocera's group has generated "hangman" porphyrins featuring carboxylate H-bond donors supported by xanthene units.[27] The flexible hangman construct permits control over the nature of the H-bonding and its distance from the metalloporphyrin.

Significantly, a hangman platform yielded the first example of a porphyrin iron(III)-hydroxide unit surrounded by a well-defined proton transfer network containing a H_2O molecule, as shown in **Figure 1.8**.

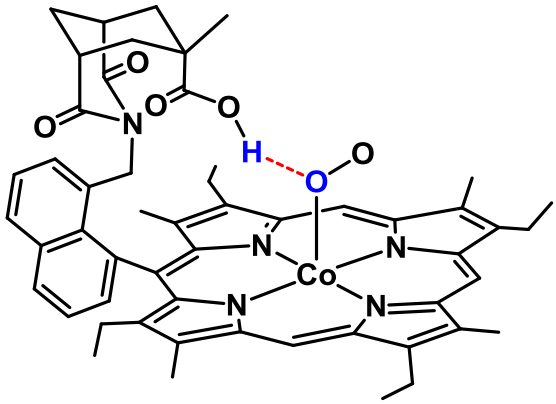

Figure 1.7 Chang's acid-appended porphyrin model.[26]

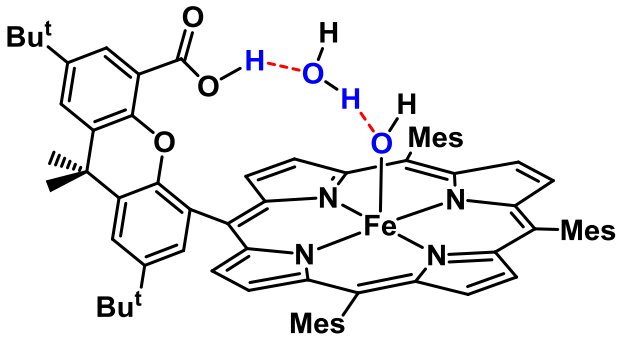

Figure 1.8 Nocera's hangman porphyrin with H- bonding network around Fe^{III}-OH unit.[27]

1.2.2.2 Synthetic Nonheme Complexes with Second Sphere Hydrogen Bond Donors

Nonheme complexes with intramolecular H-bonding interactions have also been designed and characterized in detail. An early example was the manganese(III)-peroxo

complex shown in **Figure 1.9**, originally isolated by Kitajima and coworkers.[28] The complex is supported by a tridentate tris(pyrazolyl)borate ligand substituted at the 3- and 5-positions with isopropyl groups. The X-ray crystal structure revealed that the η^2-peroxo ligand is stabilized by an intramolecular bond with a "free" pyrazole ligand.

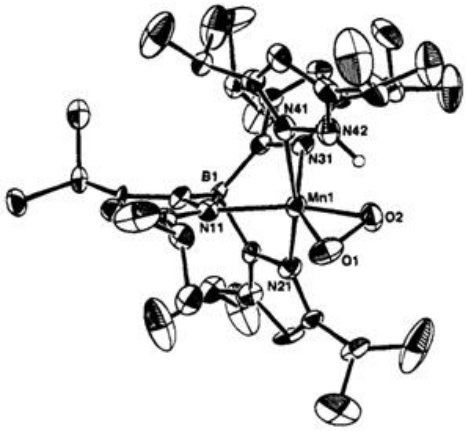

Figure **1.9** X-ray structure of Kitajima's manganese(III)-peroxo complex.[28]

The most common type of nonheme systems with H-bonding networks are based on tripodal ligand frameworks. Masuda's group has been a pioneer in this area,[29-34] generating numerous carboxyamidopyridyl-based ligands with hindered amide groups as H-bond donors (see **Figure 1.10** for an example). The number of H-bond donors in these ligands can be easily adjusted from one to three.

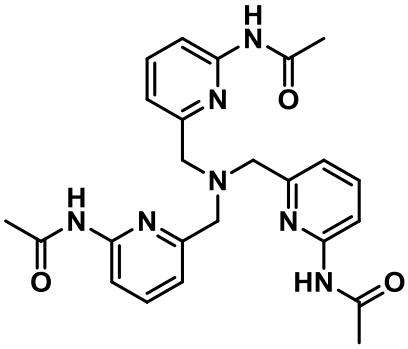

Figure 1.10 One of Masuda's tripodal ligands with appended carboxyamidopyridyl groups.

The presence of the carboxyamido substituents has allowed Masuda to stabilize and isolate elusive intermediates. For instance, he was the first to crystallographically characterize a copper(II)-hydroperoxo species (**Figure 1.11**) of relevance to the catalytic mechanism of copper oxidases.[32] The crystal structure showed that two intramolecular H bonds are formed between the ligand and proximal O-atom of the hydroperoxide.

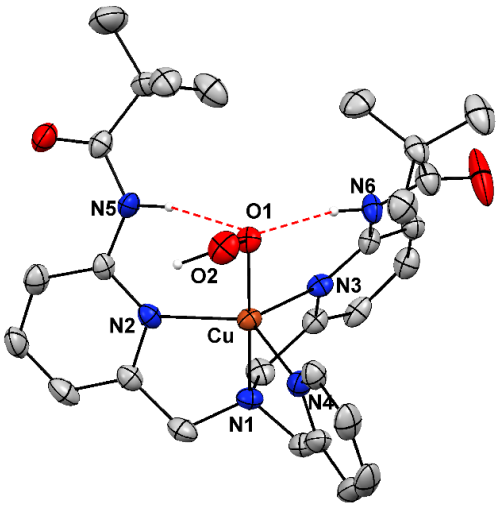

Figure 1.11 X-ray structure of Masuda's Cu(II)-OOH complex stabilized by intramolecular H-bonding interactions.[32]

Another impressive accomplishment of the Masuda group is the iron(III)-hydroxo complex shown in **Figure 1.12** that models the active site of lipoxygenase.[31] Here, the hydroxide ligand is stabilized via H-bonding interactions with the pendant N-H donors; in addition, the hydro group serves as an H-bond donor to coordinated carboxylate, thus forming a stable six-membered ring.

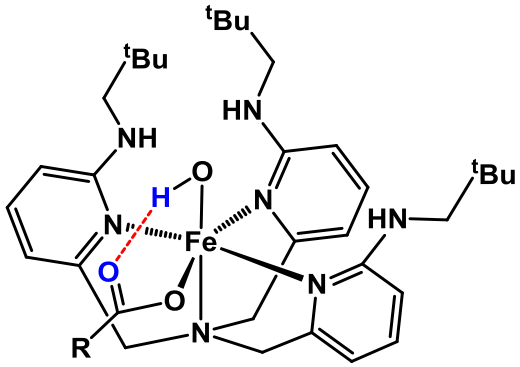

Figure 1.12 Structure of the lipoxygenase model $[Fe^{III}(tnpa)(OH)(RCO_2)]$.[31]

Studies by Berreau and co-workers have shown that hydrogen-bonding groups can enhance the hydrolytic stability of zinc-alkoxide species (**Figure 1.13**). This is relevant to the zinc-catalyzed oxidation of alcohols to aldehydes (or ketones) by the enzyme liver alcohol dehydrogenase (LADH).[35] In the LADH mechanism, the zinc-alkoxide intermediate is generated by displacement of the resting-state H_2O ligand by the alcohol substrate. A serine residue (Ser48) initially acts as an H-bond acceptor to the zinc-bound alcohol, then as an H-bond donor following its deprotonation. While the

functional significance of this interaction is not clear, Berreau and coworkers have succeeded in generating a Zn(II) complex that shares the N_3S donor set of the enzyme and features second sphere N-H groups to stabilize the bound alkoxide.

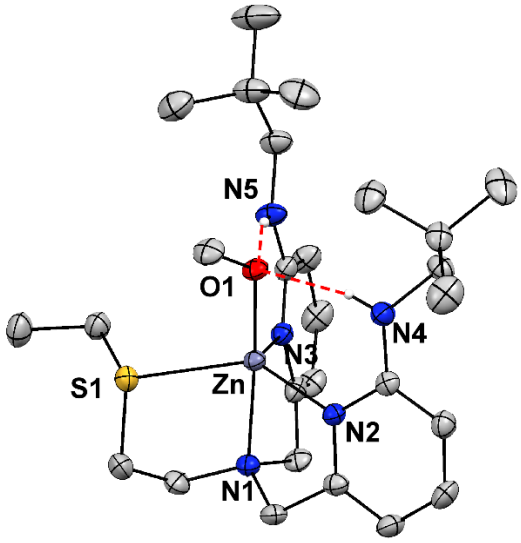

Figure 1.13 X-ray crystal structure of Berreau's zinc-alkoxide species.[35]

Mareque-Rivas and coworkers have shown that intramolecular N–H···O(H)–Zn H-bonds stabilize and facilitate the generation of Zn–OH units in $[(L)ZnOH]^+$ complexes (where L is a TPA derivative with –NHR groups at the 6-positions; R = H or neopentyl).[36,37] The presence of the second sphere –NHR groups was found to lower the pK_a of the zinc-bound H_2O ligand by 1–2 pKa units.[38] In a related complex, a dianionic catecholate ligand forms intramolecular H-bonds with multiple $–NH_2$ groups bound to the pyridyl donors. This interaction results in a 270-mV increase in the catecholate redox potential, suggesting that H-bond networks can modulate the potentials of redox-active

ligands as well as metal centers. The H-bonds also enhance binding of the neutral catechol to the Zn(II) center by a factor of 10^4.[39]

Over the past two decades, Borovik and coworkers have performed extensive work in this field, focusing primarily on the role of the second coordination sphere in promoting O_2 activation by Fe and Mn complexes.[40] The ligand tris(*N*'-*tert*-butylureayl-N-ethylene)amine (H_6buea; **Figure 1.14**) is prototypical of their approach involving tripodal urea-based scaffolds. Each deprotonated urea group in $[H_3buea]^{3-}$ provides an anionic N ligand (α) *and* N-H hydrogen bond donor (α'). The N-H donors form a well-defined cavity around the axial coordination site, allowing a maximum of three intramolecular H-bonds with the axial X-ligand (X = O, S, Se, OH, O_2).[41] Using this ligand scaffold, Borovik crystallographically characterized the first examples of mononuclear Fe(III) and Mn(III) complexes with terminal oxo ligands.[40] In the past, these types of complexes were challenging to isolate because oxo ligands have a strong tendency to form M-(μ-O)-M species; however, in Borovik's system, the second sphere prevents dimerization through a combination steric bulk and H-bonding interactions.

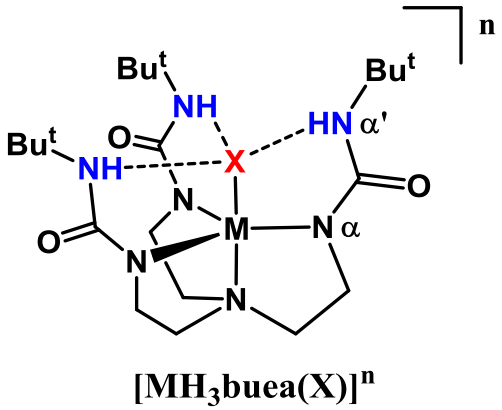

Figure 1.14 Generalized structure of Borovik's complexes featuring the $[H_3buea]^{3-}$ ligand.[40]

Subsequent efforts by Borovik and coworkers have resulted in tripodal ligands that combine both urea and (carboxyamido)pyridyl groups (i.e., Masuda/Borovik hybrids), resulting in a series of ligands with varying charges and H-bond donor properties. For example, the H_5bupa ligand coordinates to Mn(II) as the dianion (H_3bupa^{2-}) to yield $[Mn^{2+}(H_3bupa)]$.[42] The X-ray structure revealed a five-coordinate Mn(II) center ligated by four N-donors (as expected) and the O atom of the appended carbonyl group. This complex reacts directly with O_2 to yield a novel Mn(III)-peroxo complex (**Figure 1.15**). The peroxo ligand binds in a side-on fashion stabilized by three intramolecular H-bond interactions. The related ligand possessing one urea and two (carboxyamido)pyridyl groups (H_3bpaa) was also prepared.[43] The X-ray structure of the corresponding Mn(II) complex $[Mn^{2+}(Hbppa)]$ revealed a six-coordinate center in which two carboxyl O-atoms are bound. Unlike $[Mn^{2+}(H_3bupa)]$, this complex is largely unreactive towards O_2 because of its coordinative saturation.

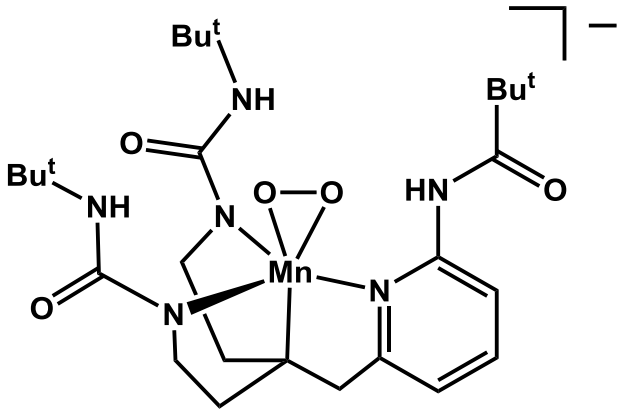

Figure 1.15 Structure of $[Mn^{3+}(H_3bupa)(O_2)]^-$.[42]

The key advantage of Borovik's tripodal design is the relative ease of ligand synthesis and its modular nature; that is, the number of second sphere H-bond donors can be adjusted in a straightforward manner. This flexibility has permitted Borovik to systematically examine the role of H-bond interactions in tuning the reactivity, molecular structure, and spectroscopic and electrochemical properties of transition-metal complexes. For instance, four tris(anionic) ligands were prepared with a variable number of H-bond donors (between 0 and 3; see **Figure 1.16**).[44] Complex $[Co^{2+}(H_3buea)]$, with the full complement of second sphere NH groups, reacts rapidly with O_2 to yield a stable Co(III)-OH product. Similar reactivity was observed for $[Co^{2+}(H_2\mathbf{2}^{iPr})]$, although the resulting Co(III)-OH species decays slowly. The complex possessing only one H-bond donor, $[Co^{2+}(H\mathbf{1}^{iPr})]$, reacts with O_2 only under forcing conditions and the product has diminished stability. Finally, the Co(II) complex lacking H-bond donors is completely unreactive towards dioxygen. This series nicely illustrates the control that second sphere

groups are capable of exerting over transition-metal chemistry in both synthetic and biological systems.

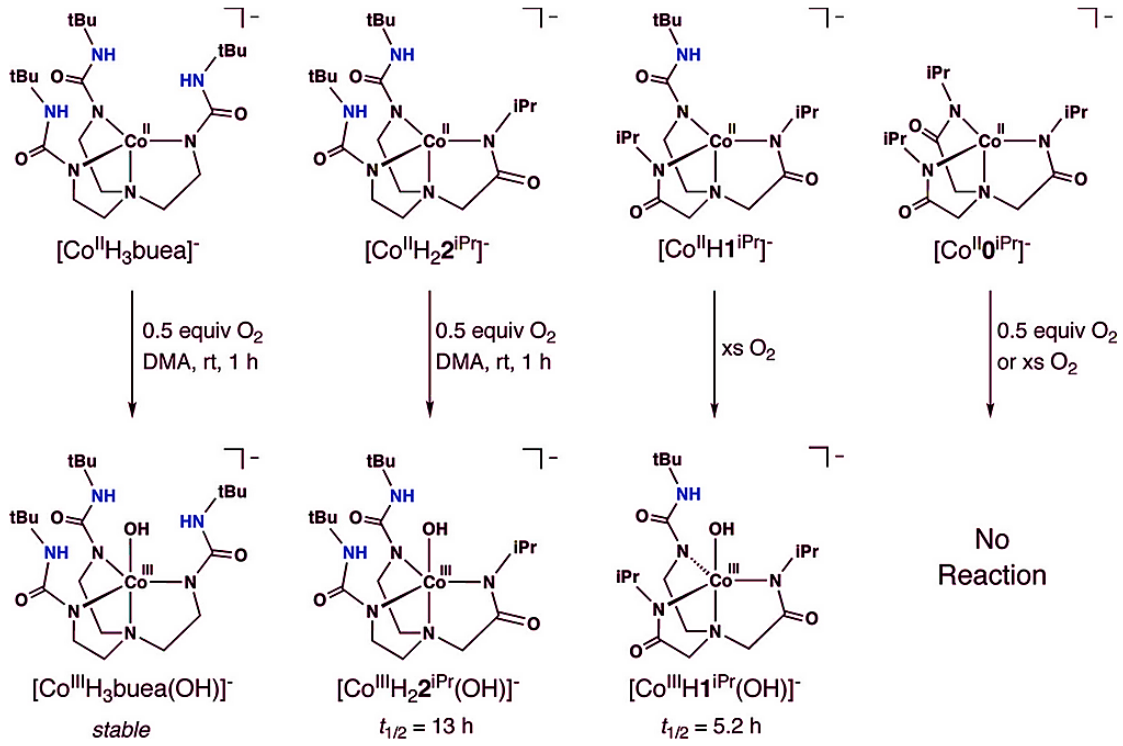

Figure 1.16 O_2 reactivity of Co(II) complexes with 0–3 H-bond donors.[44]

1.3 Bimetallic Active Site in Metalloenzymes and Biomimetic Complexes

1.3.1 Bimetallic Active Sites Involved in Water-Splitting Chemistry

Metalloenzymes with homobinuclear and heterobinuclear active sites play a critical role in the chemistry of life. Of particular relevance to this dissertation are metalloenzymes that perform reactions related to water-splitting, namely, the reduction of

protons to H_2 and the oxidation of H_2O to O_2. These enzymes are described in detail below.

Hydrogenases (H_2ases) catalyze the reversible oxidation of molecular hydrogen.[45] Of the three known classes of hydrogenases, the most abundant are the [NiFe]-hydrogenases ([NiFe]-H_2ases) that contain a heterobimetallic cluster at the site of H_2 activation. The structure of the NiFe cluster has been elucidated by X-ray crystallography. As shown in **Figure 1.17**,[46] the Ni center is coordinated by four cysteine residues, two of which adopt a bridging position between the Ni and Fe centers. The Fe site is ligad by three diatomics: one CO and two CN ligands. While details of the [NiFe]-H_2ase mechanism remain unclear, various studies have determined that the Ni site functions as the redox-active component of the bimetallic cluster, alternating between Ni(I) and Ni(III) oxidation states. In contrast, the Fe atom remains in a low-spin, ferrous state throughout the catalytic cycle, although it likely serves to bind H_2 or hydride ligands.

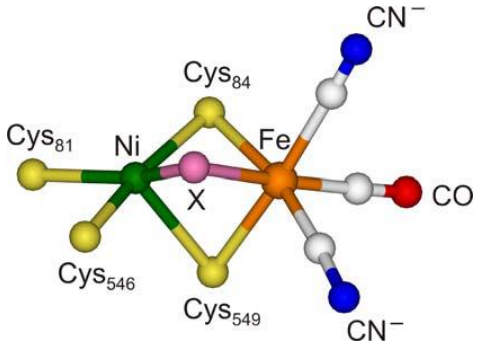

Figure 1.17 The active site structure of [Ni-Fe]-H_2ases.[46]

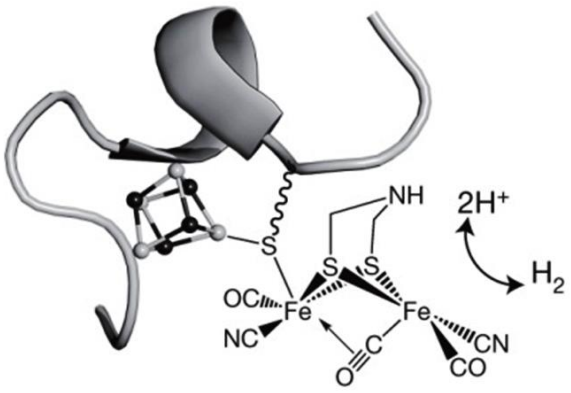

Figure 1.18 The active site structure of [Fe-Fe]-H_2ases.[47]

The less common Fe-only hydrogenases ([FeFe]-H_2ases) are only found in anaerobic bacteria. The active sites of [FeFe]-H_2ases contain a unique 6Fe cluster known as the H-cluster. The H-cluster consists of a $[Fe_4S_4]$ unit linked to a $[2Fe]_H$ subcluster (**Figure 1.18**).[47] Each Fe atom within the $[2Fe]_H$ unit is ligated by one CN and one CO ligand in terminal positions, and the two metal centers are bridged by an dithiolate ligand and an additional CO ligand. The proximal Fe is connected to the Fe/S cubane via a thiolate bridge provided by a nearby Cys residue, while the distal Fe has an open coordination site for substrate (H/H_2) binding during catalysis. The identity of the dithiolate bridge has been a source of controversy, and two possibilities have been proposed: 1,3-propane dithiolate and di(thiomethyl)amine.

Finally, the oxygen-evolving complex (OEC cluster**)** serves as the site of water oxidation (to O_2) within photosystem II – the membrane-bound protein at the center of photosynthesis. Recent X-ray crystallographic results suggest that the OEC is a

$CaMn_4O_4$ cluster in which one of the Mn centers lies outside the main cubane (**Figure 1.19**).[48] The light-driven oxidation of water to dioxygen ($2\ H_2O \rightarrow O_2 + 4\ H^+ + 4\ e^-$) supplies activated electrons for the reduction of CO_2 to carbohydrates. To carry out this complex reaction, photosystem II contains several light-harvesting chlorophyll cofactors that, upon exposure to light, faciliating transfer of an electron from the P_{680} cofactor to quinone (Q_A), thus producing a charge-separated state. The P_{680} cation, in turn, oxidizes a specific tyrosine residue (Tyr_Z) and the resulting phenoxy radical extracts an electron from the nearby OEC. After four consecutive oxidations, the OEC converts bound water molecules to O_2. Although the OEC contains five metal ions, most proposed mechanisms suggest that water binding occurs at the "dangler" Mn center and the adjacent Ca ions. Thus, heterobimetallic complexes are able to serve as relevant OEC models.

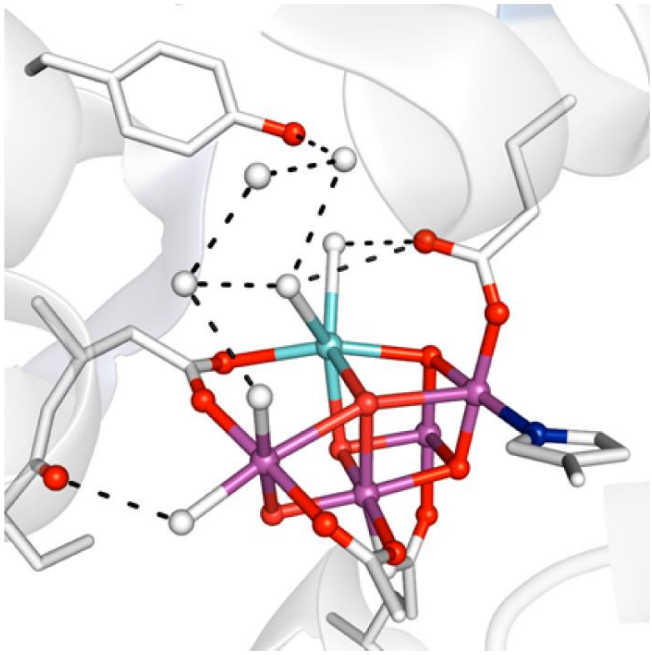

Figure 1.19 The active site structure of OEC.[48] (Red - Oxygen atom; blue-nitrogen atom; light blue – calcium atom; purple – manganese atom; white – hydrogen atom.)

1.3.2 Synthetic Binuclear Complexes as Model of Metalloenzyme Active Site

Synthetic modeling studies of the hydrogenases and OEC have sought to clarify the overall catalytic mechanism and to identify the roles of particular metal ions. However, this task often proves challenging for a number of reasons. The synthesis of faithful models requires ligands that can accommodate two specific metal ions in a homo- or heterobimetallic framework. The designed ligand should result in intermetallic distances similar to the values found in the enzyme active site. Unfortunately, polydentate ligands can coordinate to metal centers in unexpected fashions, leading to

species with the wrong number of metal ions. Regardless of these difficulties, several impressive models of binuclear active sites have been reported during last two decades.

[FeFe]-hydrogenases: The unusual structure of the [2Fe] site within the H-cluster has inspired the preparation of many biomimetic complexes. The laboratories of Rauchfuss, Darensbourg, and Pickett have generated an extensive series of [FeFe]-H_2ases models.[49-59] The first generation of synthetic models replicated the Fe(I)-Fe(I) core of the reduced H-cluster and incorporated key structural elements, such as short a Fe-Fe distance, bridging dithiolates, and mixed CO/CN ligation. These complexes lacked the bridging CO ligand of the [2Fe] component, as well as the mixed-valency of the resting state. However, Rauchfuss and coworkers have recently reported the diiron complex $[Fe_2(adtH)(CO)_3(dppv)(PMe_3)]^+$ (where $adtH^{2-}$ = 2-aza-1,3-propanedithiolate and dppv = cis-1,2-bis(diphenylphosphino)ethene), which consist of a mixed-valent Fe(II)Fe(I) unit with a partially bridging CO ligand.[57] This model reacts slowly with high pressures of H_2 to give a novel $[(\mu\text{-}H)Fe_2(adtH)(CO)_3(dppv)(PMe_3)]^+$ species. Interestingly, the corresponding propanedithiolate complex $[Fe_2(pdt)(CO)_3(dppv)(PMe_3)]^+$ is unreactive toward H_2, highlighting the importance of the basic moiety in the dithiolate ligand for proton transfer steps. Additionally, the reaction of $[Fe_2(adtH)(CO)_3(dppv)(PMe_3)]^+$ with H_2 can be accelerated in the presence of ferrocenium salts, which mimic the role of the attached [4Fe−4S] cubane in the H-cluster. Furthermore, a structural and functional mimic model of the enzyme, the redox-complemented complex $[Fe_2(adtBn)(CO)_3(dppv)$-

(FcP*)]$^{n+}$ (as shown in **Figure 1.20**) has been generated, which can catalyze both proton reduction and hydrogen oxidation.[58]

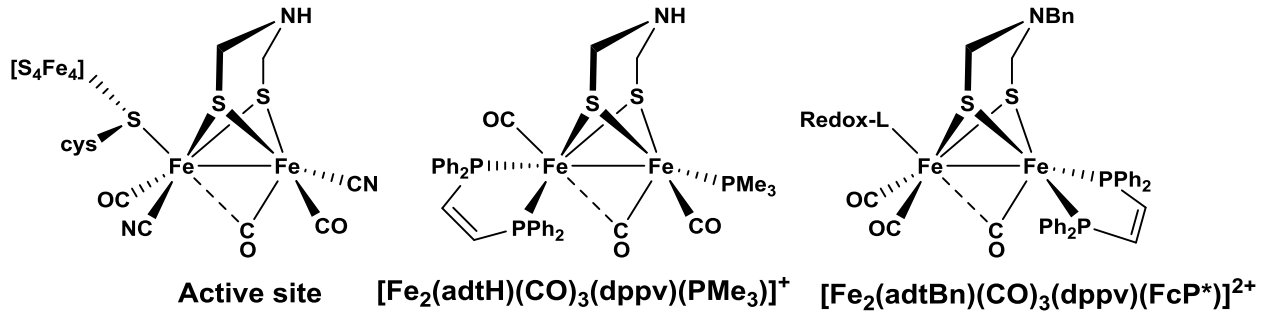

Figure 1.20. Structure of active site and synthetic model of [FeFe]-hydrogenases.[57,58]

OEC cluster: The recent high-resolution crystal structure of OEC revealed a unique structure with $CaMn_3O_4$ cuboidal cluster.[48] The calcium ion is known to be critical for the function of the OEC. In order to examine the contributions of the Ca^{2+} ion, Agapie and coworkers have generated a series of tetranuclear clusters in which the core structure remained unchanged but the identity of the fourth metal ion was varied (**Figure 1.21.**). This allowed Agapie to systematically examine the effect of the fourth (i.e., non-maganese) metal ion on the structural and electrochemical properties of the cluster. [60-64]

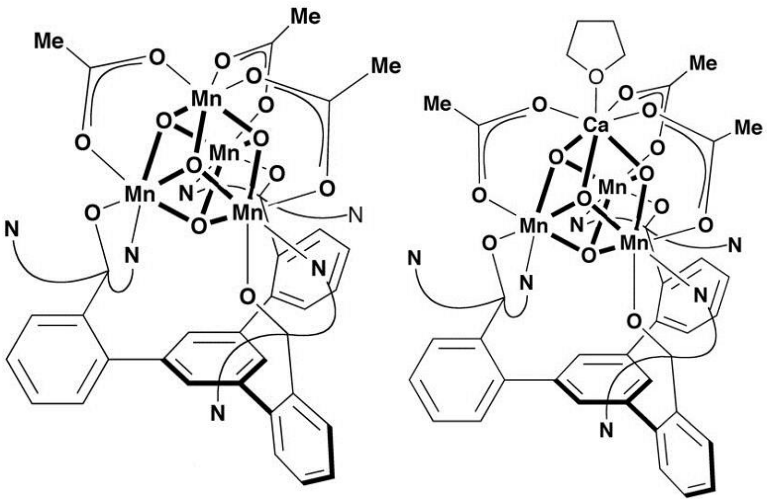

Figure 1.21. Agapie's synthetic model of OEC active site.[60]

Recently, Borovik and coworkers have designed and synthesized a ligand framework to incorporate an auxiliary binding site for a second metal ion. [65,66] These compounds allowed them to isolate a series of heterobimetallic complexes of Mn(III) with a group II metal ion (Ca^{2+} or Sr^{2+}) in close proximity (shown in **Figure 1.22.**). Examination of the influence of the second metal ion on the electron transfer properties of the primary metal center revealed unexpected similarities between Ca(II) and Sr(II) ions, a result with relevance to the OEC.

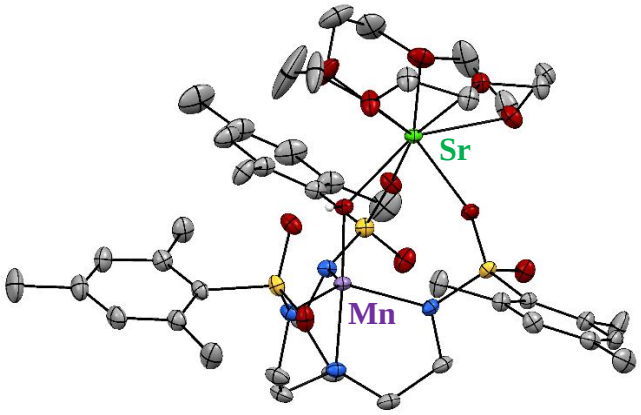

Figure 1.22. Borovik's synthetic model of OEC active site.[66]

1.4 Specific Aims of our Research Efforts

As illustrated in **Figure 1.23**, our approach combines synthetic inorganic chemistry, physical characterization (X-ray crystallography and spectroscopic techniques), computational methodology (density functional theory), and reactivity studies. Using this multifaceted approach, we have pursued the synthesis of new ligand scaffolds designed to support late first row transition metals and incorporate second sphere interactions. We have also sought to incorporate redox-active donors into binucleating frameworks; such moieties could serve as electron reservoirs in multi-electron processes (e.g., proton reduction and water oxidation), similar to the role of iron-sulfur clusters in the catalytic cycles of metalloenzymes like the hydrogenases.

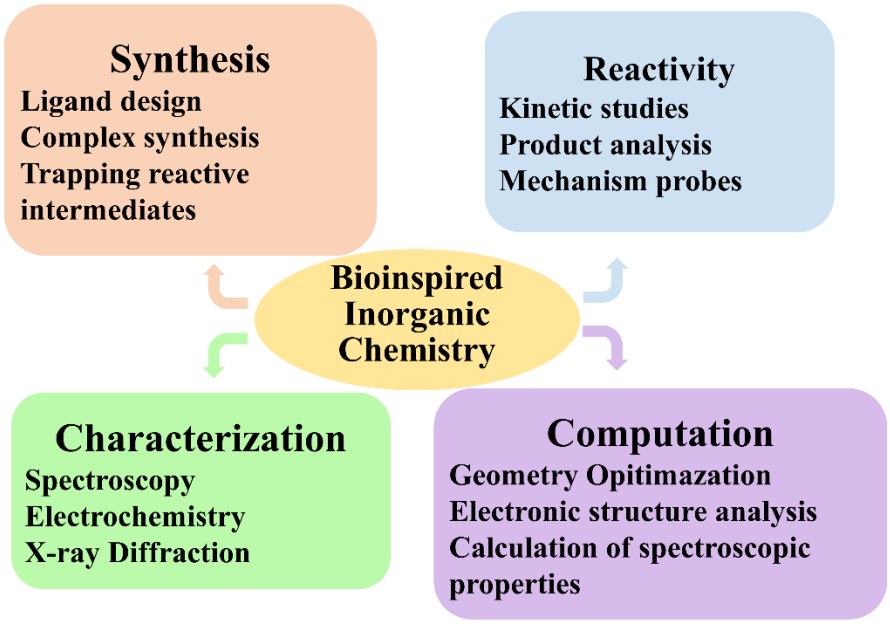

Figure 1.23 Schematic of various methods employed in our bioinspired synthetic approach.

Chapter 2: We have designed ligand frameworks that seek to overcome the drawbacks of systems based on second-sphere amide groups. To date, our efforts have centered on the two classes of ligands. The first set consists of 2,6-pyridinedicarboxamides with pendant pyridine or pyrimidine groups. There are multiple advantages in using these ligands to build second coordination spheres with H-bonding networks. The substituted pyridyl (or pyrimidine) groups are not capable of coordinating to the metal and are therefore free to participate in H-bonding interactions with additional ligands. Moreover, the pyridyl groups can be either neutral or protonated, thus serving as either H-bond acceptors or donors, respectively. Finally, pyridines and pyrimidines have basicities comparable to amino acid side chains.

Chapter 3: Compared to the pincer ligands described in Chapter 2, the tripodal ligands posed a significantly greater synthetic challenge. We have succeeded in preparing a series of target ligands consisting of one, two, or three second-sphere heterocycles. Preliminary results concerning the coordination modes of tripodal ligands with Cu(II) and Fe(II) ions are described.

Chapter 4: The synthesis and coordination chemistry of a new asymmetric ligand designed to support nickel based heterobimetallic structures with relevance to bioinorganic chemistry is described. The resulting $Ni^{II}-M^{II}$ complexes were characterized with X-ray crystallography, spectroscopic and computational methods, and cyclic voltammetry. The metal centers are bridged by two ligands, resulting in short intermetallic distances of 3.0−3.1 Å. Our complexes serve as structural models of the Ni−Fe1 unit in the C-cluster of carbon monoxide dehydrogenase (CODH) – the site of CO_2 reduction to CO and H_2O. Importantly, the redox-active Ni centers in our complexes possess open and labile coordination sites for use in substrate binding and activation.

Chapter 5: The syntheses and characterization of homobimetallic complexes (M = Co, Cu, Zn) supported by a pentadentate ligand ($\mathbf{L^{N3O2}}$) with "fused" NNO pincer-type coordination sites are reported. The $\mathbf{L^{N3O2}}$ chelate consists of a bridging diarylamido group and flanking salicyaldimine donors, and the flexible framework permits the

binding of redox-active auxilary ligands, such as 2,2-bipyridine, and small molecules like O_2.

Chapter 6: The synthesis of ligands based on central diarylamido bis(pincer) framework are described. Specifically, we report the synthesis and coordination chemistry of pentadentate ligands intended to provide multiple sites for ligand-based oxidation and reduction. This 'non-innocent' ligand contains electron acceptor units, in addition to a central diarylamido donor that serves an an as electron donor. A related ligand ($\mathbf{L^{N3P2}}$) ligand incorporates "soft" phosphine donors to encourge the formation of low oxidation state M(I) ions. Preliminary results regarding the binding modes of these redox-active ligands with several transition metal ions will be described.

Chapter 7: Finally, the ability of the dicobalt(II) complex $[Co_2(L^{N3O2})(bpy)_2]ClO_4$ (initially presented in Chapter 5) to serve as an electrocatalyst for proton reduction and water oxidation is examined. Based on bulk electrolysis experiments, this complex is an efficient proton reduction catalyst with a high turnover frequency ($TON \cdot h^{-1}$) of 24.7 and faradaic efficiency of 86%. Moreover, this homobimetallic cobalt complex is also capable of catalyzing water oxidation with a turnover frequency ($TON \cdot h^{-1}$) of 32.2 with a faradaic efficiency of 91%. Proposed mechanisms for these catalytic process are offered at the conclusion of the chapter.

Chapter 2

Synthesis and Characterization of M(II) Complexes with 2,6-Pyridinedicarboxamide Ligands Capable of Forming Intramolecular Hydrogen Bonds

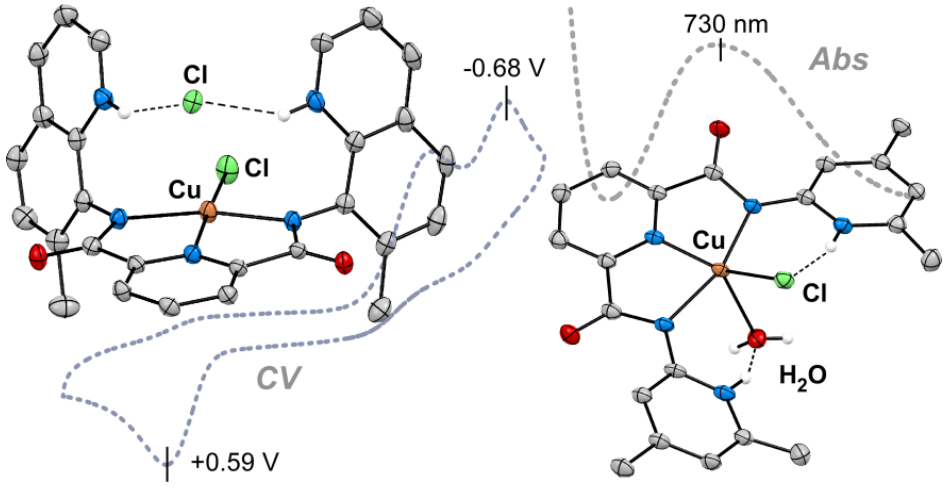

Abstract: A novel series of 2,6-pyridinedicarboxamide ligands have been prepared. The coordination chemistry of these N3 pincer ligands was explored through the preparation of numerous metal complexes with Cu, Fe, or Ni centers. The resulting complexes were characterized with X-ray crystallography, electronic absorption spectroscopy and electrochemistry. In the Cu(II) complexes, intramolecular H-bonds are formed between protonated pyridine (or pyrimidine) groups in the second sphere and first-sphere ligands such as chloride, water, and/or triflate. Unexpected coordination geometries were observed in the Ni(II) and Fe(II) complexes.

Portions of this chapter have appeared in the paper: Wang, D. N.; Lindeman, S. V.; Fiedler, A. T., *Eur J Inorg Chem*, **2013**, 4473-4484.

2.1 Introduction

Multidentate ligands containing 2-pyridinecarboxamide units have proven valuable in coordination chemistry, homogeneous catalysis, and synthetic modeling of metalloenzyme active sites.[67-69] Deprotonation of these ligands generates an *N*-amidato group with impressive σ-donating ability, allowing for the stabilization of metal centers in high oxidation states.[70] Mascharak,[71-75] Tolman,[76,77] Holm[78,79] and others[80] have successfully used the 2,6-pyridinedicarboxamide scaffold to mimic coordination environments found in metallo-biomolecules such as bleomycin, nitrile hydratase, acetyl coenzyme-A synthase, and O_2-activating copper enzymes. Similar ligands have found application in catalysts for asymmetric alkylations,[81,82] epoxide ring-openings,[83] and oxidation reactions.[84-87]

It may be possible to enhance the reactivity and biological relevance of pyridinecarboxamide-based complexes through the incorporation of outer-sphere (i.e., second-sphere) groups capable of forming intramolecular hydrogen bonds. Extensive studies of metalloenzymes have highlighted the importance of such interactions in tuning redox potentials,[88-90] stabilizing intemediates,[91,92] and serving as proton donors/acceptors.[93-95 43,96] In 1997, Redmore *et al.* reported the reaction of $RuCl_2(PPh_3)_3$ with the ligand *N,N'*-bis(6-methyl-2-pyridyl)-2,6-pyridinedicarboxamide (H_2L^A in **Scheme 2.1**).[97] As expected, this pincer ligand coordinates to Ru(II) in a tridentate

fashion via the central pyridine and two amidato donors; however, the appended pyridine rings are both protonated, making the overall ligand a neutral di-zwitterion (labeled $L^{A}\{H\}_2$ to indicate the proton shift). Most significantly, the two pyridinium groups form intramolecular H-bonds with a chlorido ligand.[97] In this chapter, we expand upon Redmore's initial observation through the synthesis of various copper(II) complexes featuring intramolecular H-bonds between protonated heterocycles and first-sphere chlorido and/or aqua ligands.

Substituted *N,N'*-bis(2-pyridyl)-2,6-pyridinedicarboxamide ligands are attractive frameworks for the incorporation of second-sphere H-bonding interactions into transition-metal complexes. First, the ligand syntheses are straightforward and the identity of the pendent group is easily modified; as shown in **Scheme 2.1**, we have utilized 2,6-pyridinedicarboxamides ($H_2L^{B\text{-}D}$) with three different pendant moieties that modify the H-bonding capabilities of the ligand. Pyridine, pyrimidine, and quinoline rings are well-suited to serve as acid/base catalysts due to their moderate basicities. The pyrimidinium group has the added advantage that it can function simultaneously as an H-bond donor and acceptor. Finally, the pendant groups in the 2,6-pyridinedicarboxamide scaffold are generally unable to bind to the metal center, since the resulting ring chelate would be highly strained.

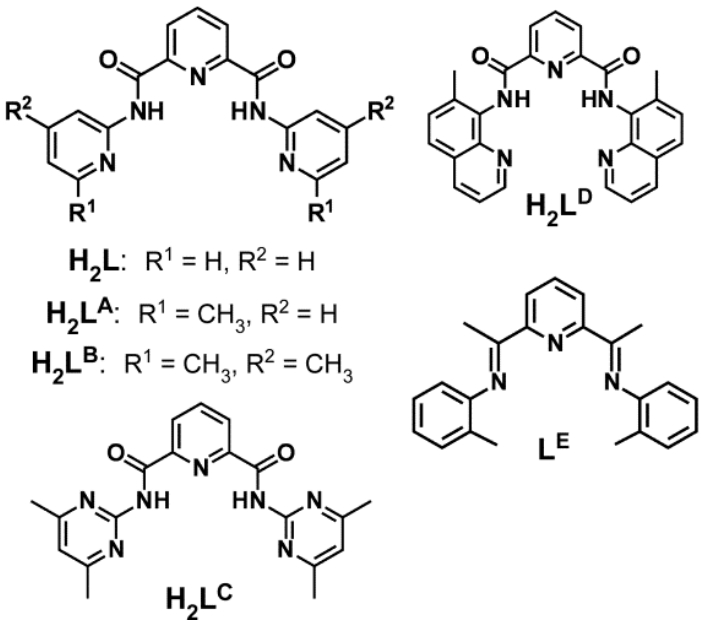

Scheme 2.1 Pincer ligands discussed in this study.

Only one report to date has explored the coordination chemistry of $L^X\{H\}_2$-type ligands with first-row transition metals. Gudasi *et al.* reacted *N,N'*-bis(2-pyridyl)-2,6-pyridinedicarboxamide (H_2L; **Scheme 2.1**) with various divalent first-row cations to generate the putative M(II)/$L^0\{H\}_2$ complexes, although only the copper(II)-dichlorido complex was structurally characterized.[98] The X-ray structure revealed that the pendant pyridinium groups form intramolecular H-bonds with the oxygen atoms of the backbone amides instead of the chlorido ligands, as intended. By contrast, in this chapter, we report the synthesis and X-ray structural characterization of several mononuclear Cu(II) complexes that display the desired H-bonding interactions between first-sphere ligands and protonated outer-sphere groups (see **Scheme 2.2** for an example). The use of methyl-

substituted heterocycles was critical to our success, since it discourages formation of the carbonyl/pyridinium H-bond found in the Gudasi structure. In addition, we find that deprotonation of one (or both) of the pendant groups results in the formation of dicopper(II) complexes. Our results therefore point to the possibilities and limitations of using 2,6-pyridinedicarboxamide-based ligands to construct H-bonding networks in synthetic complexes. Finally, the donor properties of $L^{X}\{H\}_2$-type ligands are examined through the use of spectroscopic, electrochemical, and computational methods. These results are compared to those obtained for a complex that instead contains ligand L^{E} (**Scheme 2.1**) – a member of the well-known class of 2,6-bis(imino)pyridine ligands.

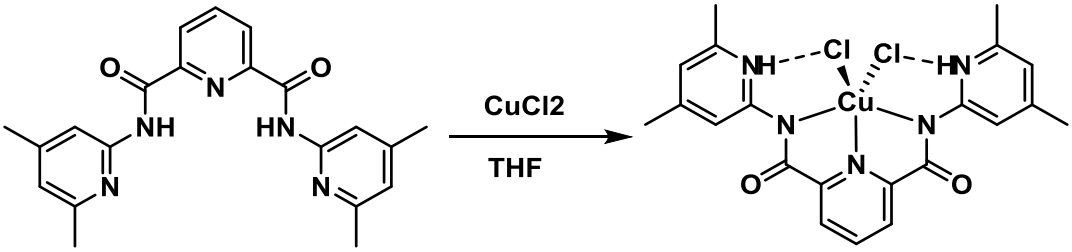

Scheme 2.2 Synthesis of complex $[CuCl_2(L^{C}\{H\}_2)]$ (**1**^{C}).

2.2 Experimental Section

Materials and Physical Methods. All reagents and solvents were purchased from commercial sources and used as received unless otherwise noted. Acetonitrile (MeCN), dichloromethane, and tetrahydrofuran (THF) were purified and dried using a Vacuum Atmospheres solvent purification system. Ligand L^E and complex **7** were prepared using published procedures.[99] Elemental analyses were performed at Midwest Microlab, LLC in Indianapolis, Indiana. Infrared spectra were measured as solid powders using a Thermo Fisher Scientific Nicolet iS5 FT-IR spectrometer with an iD3 ATR accessory. ^{1}H, ^{13}C, and ^{19}F NMR spectra were collected at room temperature with a Varian 400 MHz spectrometer. UV-Vis spectra were collected with an Agilent 8453 diode array spectrometer. Magnetic susceptibility measurements were performed at room temperature with an AUTO balance manufactured by Sherwood Scientific. Electrochemical measurements were conducted in a Vacuum Atmospheres Omni-Lab glovebox using an EC Epsilon potentiostat (iBAS) with 100 mM $(NBu_4)PF_6$ as the supporting electrolyte. A three-electrode cell containing an Ag/AgCl reference electrode, a platinum auxiliary electrode, and glass carbon working electrode was employed for cyclic voltammetric (CV) and square wave (SW) measurements. The ferrocene/ferrocenium ($Fc^{+/0}$) couple was employed as an internal standard. To facilitate comparison to previously-published data, redox potentials are reported versus SCE.

Under these conditions, $Fc^{+/0}$ has an $E_{1/2}$ value of 0.46 V (ΔE = 0.21 V) in CH_2Cl_2 and 0.45 V (ΔE = 0.12 V) in DMF.[100]

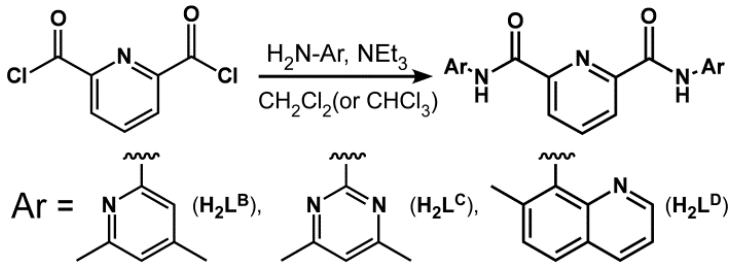

Scheme 2.3 General synthesis of pyridine-2,6-dicarboxamide ligands.

***N,N*-bis(4,6-dimethylpyridin-2-yl)pyridine-2,6-dicarboxamide (H_2L^B).** To a solution of 2-amino-4,6-dimethylpyridine (1.20 g, 9.8 mmol) and triethylamine (2.2 mL, 14.7 mmol) in CH_2Cl_2 (20 mL) was slowly added to pyridine-2,6-dicarbonyl dichloride (1.0 g, 4.9 mmol) in CH_2Cl_2 (**Scheme 2.3**). The mixture was allowed to stir for 2 hours, after which the solvent was removed under reduced pressure. The solid residue was recrystallized from methanol (20 mL), providing the product as a white solid (1.67 g, 91%). ^{1}H NMR ($CDCl_3$): δ = 11.19 (s, 2H, N*H*), 8.48 (d, 2H), 8.17 (s, 2H), 8.14 (t, 1H), 6.80 (s, 2H), 2.50 (s, 6H, C*H*$_3$), 2.39 (s, 6H, C*H*$_3$); ^{13}C NMR ($CDCl_3$): δ = 161.7, 156.2, 150.4, 150.5, 148.7, 139.4, 125.5, 120.7, 112.0, 23.8, 21.4. $C_{21}H_{21}N_5O_2$•H_2O (393.44): calcd. C 64.11, H 5.89, N 17.80; found C 64.46, H 5.90, N 17.80.

***N,N*-bis(4,6-dimethylpyrimidin-2-yl)pyridine-2,6-dicarboxamide (H_2L^C).** To a solution of 2-amino-4,6-dimethylpyrimidine (1.21 g, 9.8 mmol), triethylamine (2.2 mL,

14.7 mmol) in CH_2Cl_2 (20 mL), was slowly added a solution of pyridine-2,6-dicarbonyl dichloride (1.0 g, 4.9 mmol) in CH_2Cl_2 (15 mL). The mixture was allowed to stir for 2 hours, after which the solvent was removed under reduced pressure. The solid residue was recrystallized from methanol (20 ml), providing the product as a white solid (0.76 g, 40%). ^{1}H NMR ($CDCl_3$): δ = 10.69 (s, 2H, N*H*), 8.54 (d, 2H), 8.13 (t, 1H), 6.83 (s, 2H), 2.51 (s, 12H, C*H*$_3$). ^{13}C NMR ($CDCl_3$): δ = 168.4, 161.0, 157.1, 148.6, 139.6, 126.4, 116.2, 24.1. $C_{19}H_{19}N_7O_2$•H_2O (395.42): calcd. C 57.71, H 5.35, N 24.80; found C 57.91, H 5.08, N 24.63.

***N*,*N*-bis(7-methylquinolin-8-yl)pyridine-2,6-dicarboxamide (H_2L^D).** To a solution of 2-amino-7-methylquinoline (450 mg, 2.85 mmol) and triethylamine (0.6 mL, 4.27 mmol) in $CHCl_3$ (20 mL) was slowly added to pyridine-2,6-dicarbonyl dichloride (290 mg, 1.42 mmol) in $CHCl_3$ (15 mL). The mixture was allowed to stir overnight under reflux. After cooling to room temperature and washing with water, the organic phase was dried with $MgSO_4$. The solvent was removed under reduced pressure to provide a brown solid. Purification by column chromatography on silica (10:1 EtOAc:MeOH) provided the final product as a white powder. (427 mg, 65%). ^{1}H NMR ($CDCl_3$): δ = 11.23 (s, 2H, N*H*), 8.57 (dd, 2H), 8.37 (d, 2H), 8.00 (t, 1H), 7.86 (dd, 2H), 7.49 (d, 2H), 7.38 (d, 2H), 7.04 (q, 2H), 2.51 (s, 6H, C*H*$_3$). ^{13}C NMR ($CDCl_3$): δ = 161.7, 149.3, 149.3, 143.3, 138.9, 135.6, 135.1, 131.2, 130.3, 126.6, 125.2, 125.0, 120.3, 20.2. $C_{27}H_{21}N_5O_2$ (447.49): calcd. C 72.47, H 4.73, N 15.65; found C 68.45, H 4.70, N 14.36. The H_2L^X-

type ligands are known to be hygroscopic[80,97,101] thus, the disagreement in the elemental analysis indicates that ~1.5 equivalents of H_2O are present in the sample: $C_{27}H_{21}N_5O_2 \cdot 1.5H_2O$ (474.51): calcd. C 68.34, H 5.10, N 14.75.

$[CuCl_2(L^B\{H\}_2)]$ (1^B): $CuCl_2$ (74.4 mg, 0.55 mmol) and H_2L^B (200 mg, 0.55 mmol) were dissolved in CH_2Cl_2 (10 mL), providing a green-colored solution that was stirred overnight. The solvent was removed under vacuum, and the resulting green solid was washed with Et_2O to yield 198 mg of product. X-ray quality crystals were obtained by slow evaporation of a concentrated CH_2Cl_2 solution (198 mg, 72%). UV/Vis (CH_2Cl_2): λ_{max} (ε) = 880 (sh), 735 nm (180 M^{-1} cm^{-1}). IR (solid): $\tilde{\nu}$ = 1650, 1631, 1606, 1595 cm^{-1}. Elemental analysis indicates that a small amount of CH_2Cl_2 (0.2 equiv) remains in the sample after drying. $C_{21}H_{21}Cl_2CuN_5O_2 \cdot 0.2CH_2Cl_2$ (526.86): calcd. C 48.33, H 4.09, N 13.29; found C 48.38, H 4.17, N 13.43.

$[CuCl_2(L^C\{H\}_2)]$ (1^C): A mixture of $CuCl_2$ (89 mg, 0.66 mmol) and H_2L^C (250 mg, 0.66 mmol) was dissolved in THF (10 mL) and stirred for overnight, affording a light green solution. After removal of the solvent under vacuum, the green solid was washed with Et_2O to give 304 mg of product. Green crystals suitable for crystallographic studies were obtained by vapor diffusion of Et_2O into a concentrated CH_2Cl_2 solution (304 mg, 90%). UV/Vis (CH_2Cl_2): λ_{max} (ε) = 870 (sh), 720 nm (220 M^{-1} cm^{-1}). FTIR (cm^{-1}, solid): 1673, 1622, 1582, 1498. Elemental analysis indicates that a small amount of

CH_2Cl_2 (0.2 equiv) remains in the sample after drying. $C_{19}H_{19}CuCl_2N_7O_2 \cdot 0.2CH_2Cl_2$ (528.84): calcd. C 43.61, H 3.70, N 18.54; found C 43.78, H 4.00, N 18.24.

[$CuCl_2(L^D\{H\}_2)$] (1^D): $CuCl_2$ (64.1 mg, 0.48 mmol) and H_2L^D (200 mg, 0.48 mmol) were dissolved in $CHCl_3$ (10 mL) to stirred overnight in air. The solvent was removed under vacuum to give a dark-green solid that was washed with Et_2O. X-ray quality crystals were grown by layering a concentrated CH_2Cl_2 solution with pentane (212 mg, 80%). UV/Vis (CH_2Cl_2): λ_{max} (ε) = 660 nm (130 M^{-1} cm^{-1}). FTIR (cm^{-1}, solid): 1621, 1584, 1545, 1499. $C_{27}H_{21}Cl_2CuN_5O_2$ (581.94): calcd. C 55.73, H 3.64, N 12.03; found C 55.62, H 3.70, N 12.48.

[$Cu(L^B\{H\}_2)(H_2O)(OTf)$]OTf ($2^B$): $Cu(OTf)_2$ (100 mg, 0.276 mmol) and H_2L^B (108 mg, 0.277 mmol) were mixed in 10 ml of MeCN and stirred overnight, providing a light green solution. After removing the solvent under vacuum, the resulting green solid was washed with Et_2O. X-ray quality crystals were grown by vapor diffusion of Et_2O into a MeCN solution (157 mg, 79%). UV/Vis (MeOH): λ_{max} (ε) = 610 nm (110 M^{-1} cm^{-1}). FTIR (cm^{-1}, solid): 1656, 1626, 1604, 1592. ^{19}F NMR (MeCN): δ = –79.2 ppm. $C_{23}H_{23}CuF_6N_5O_9S_2$ (755.13): calcd. C 36.58, H 3.07, N 9.27; found C 36.69, H 2.99, N 9.37.

[$Cu(L^C\{H\}_2)(H_2O)(OTf)_2$] ($2^C$): $Cu(OTf)_2$ (240 mg, 0.662 mmol) and H_2L^C (250 mg, 0.662 mmol) were dissolved in THF (10 mL) and stirred for overnight in the glovebox, providing a light blue solution. After removing the solvent under vacuum, the

blue solid was washed with Et_2O. X-ray quality crystals were prepared by vapor diffusion of Et_2O into a concentrated MeCN solution (422 mg, 86%). UV/Vis (MeOH): λ_{max} (ε) = 695 nm (105 M^{-1} cm^{-1}). FTIR (cm^{-1}, solid): 3434, 1765, 1623, 1582, 1501. ^{19}F NMR (MeCN): δ = –79.4 ppm. $C_{21}H_{21}CuF_6N_7O_9S_2$ (757.10): calcd. C 33.31, H 2.80, N 12.95; found C 33.53, H 2.88, N 12.68.

[CuCl(L^B{H}$_2$)(H_2O)]OTf (3^B): A mixture of $CuCl_2$ (53.4 mg, 0.40 mmol) and H_2L^B (150 mg, 0.40 mmol) were dissolved in THF (10 mL) and stirred for one hour in the glovebox, affording a green-colored solution. AgOTf (102.8 mg, 0.40 mmol) was then added, resulting in formation of a white precipitate. The solution was stirred for one hour, filtered, and the solvent removed under vacuum. The resulting green solid was washed with Et_2O. Green crystals were obtained by layering a CH_2Cl_2 solution with pentane (125 mg, 50%). UV/Vis (MeOH): λ_{max} (ε) = 703 nm (155 M^{-1} cm^{-1}). FTIR (cm^{-1}, solid): 1641, 1624, 1600, 1578. ^{19}F NMR (MeCN): δ = –79.3 ppm. Elemental analysis indicates that the H_2O ligand was removed under vacuum drying. $C_{22}H_{21}ClCuF_3N_5O_5S$ (623.50): calcd. C 42.38, H 3.39, N 11.23; found C 42.57, H 3.30, N 11.22.

[Cu_2(L^B{H})$_2$($OTf)_2$] (4^B): $Cu(OTf)_2$ (100 mg, 0.277 mmol) and H_2L^B (100 mg, 0.277 mmol) were mixed in MeCN (10 mL) and stirred overnight, providing a deep green solution. After removing the solvent under vacuum, the resulting green solid was washed with Et_2O. Vapor diffusion of Et_2O into a MeOH solution provided dark violet crystals

suitable for XRD analysis (110 mg, 66%). UV/Vis (CH_2Cl_2): λ_{max} (ε) = 601 nm (620 M^{-1} cm^{-1}). FTIR (cm^{-1}, solid): 1671, 1614, 1590, 1579. ^{19}F NMR (MeCN): $\delta = -79.3$ ppm. $C_{44}H_{40}Cu_2F_6N_{10}O_{10}S_2$ (1174.07): calcd. C 45.01, H 3.43, N 11.93; found C 44.99, H 3.31, N 12.02.

$[Cu_2(L^B)_2]$ (5^B): $CuCl_2$ (55.8 mg, 0.415 mmol), NaOMe (56 mg, 1.04 mmol) and H_2L^B (150 mg, 0.415 mmol) were stirred for overnight in 10 ml of MeOH to afford a deep blue solution. Removal of solvent under vacuum gave a deep blue solid that was redissolved in CH_2Cl_2, filtered to remove salt byproducts, and dried under vacuum. X-ray quality crystals were obtained by vapor diffusion of Et_2O into MeOH (106 mg, 58%). UV-vis (CH_2Cl_2): λ_{max} (ε) = 597 nm (570 $M^{-1}cm^{-1}$). FTIR (cm^{-1}, solid): 1630, 1614, 1596, 1551. $C_{42}H_{38}Cu_2N_{10}O_4$ (873.91): calcd. C 57.72, H 4.38, N 16.03; found C 57.42, H 4.78, N 14.47. The discrepancy in the N value is likely due to residual MeOH from the recrystallization.

$[Cu_2(L^C)_2]$ (5^C): $CuCl_2$ (107 mg,0.79 mmol), NaOMe (86 mg, 1.59 mmol) and H_2L^C (300 mg, 0.79 mmol) were stirred for 30 minutes in MeOH (10 mL) to afford a dark red solution. Removal of solvent under vacuum provided a purple solid that was redissolved in CH_2Cl_2, filtered to remove salt byproducts, and dried under vacuum. X-ray quality crystals were obtained by layering a CH_2Cl_2 solution with pentane. The insolublity of $\mathbf{5^C}$ in nearly all solvents (except MeOH) made it difficult to eliminate the

NaCl by-product, thus preventing the isolation of analytically pure solid. UV/Vis (MeOH): λ_{max} = 601 nm. FTIR (cm^{-1}, solid): 1678, 1637, 1585, 1532.

[Cu(L^D)] (6^D): $CuCl_2$ (64 mg, 0.48 mmol), NaOMe (0.96 mmol) and ligand H_2L^D (200 mg, 0.48 mmol) were dissolved in MeOH (10 mL) and allowed to stirred for 30 minutes. Removal of MeOH under vacuum provided solid material that was redissolved with CH_2Cl_2. The solution was filtered to remove insoluble material and the solvent evaporated to give a dark green solid. X-ray quality crystals were grown by vapor diffusion of Et_2O into a solution of 1,2-dichloroethane (198 mg, 79%). UV/Vis (MeCN): λ_{max} = 655 (210 $M^{-1}cm^{-1}$), 830 nm (sh). FTIR (cm^{-1}, solid): 1607, 1581, 1567, 1498. Complex $\mathbf{6^D}$ co-crystallizes with H_2O and elemental analysis indicates that a certain amount of H_2O (~1.5 equiv) remains in the sample after drying. $C_{27}H_{19}CuN_5O_2 \cdot 1.5H_2O$ (536.04): calcd. C 60.49, H 4.14, N 13.07; found C 60.19, H 3.94, N 12.78.

[Fe(L^C{H}$_2$)$_2$][$FeCl_4$]$_2$ (8^C): $FeCl_2$ (83.3 mg, 0.66 mmol), and H_2L^C (250 mg, 0.66 mmol) were dissolved in 10 ml of THF and stirred overnight in the glove box. The solvent was removed to yield a dark purple solid, which was washed with Et_2O. X-ray quality crystals were grown by layering a CH_2Cl_2 solution with pentane. Yield: 265 mg, 78.3%.

[Ni(L^C{H}$_2$)$_2$][$NiCl_4$] (9^C): $NiCl_2$ (83.3 mg, 0.66 mmol), and H_2L^C (250 mg, 0.66 mmol) were dissolved in 10 ml of MeCN and stirred overnight in the glovebox. The

solvent was removed to yield a green solid, which was washed with Et_2O. X-ray quality crystals were grown by layering a CH_2Cl_2 solution with pentane. Yield: 346.5 mg, 71.8%.

Structure Determination. Each complex was characterized with X-ray crystallography; details concerning the data collection and analysis are summarized in **Table 2.7**. The X-ray diffraction data were collected at 100 K with an Oxford Diffraction SuperNova kappa-diffractometer equipped with dual microfocus Cu/Mo X-ray sources, X-ray mirror optics, Atlas CCD detector and a low-temperature Cryojet device. The data were processed with CrysAlisPro program package (Oxford Diffraction Ltd., 2010) typically using a numerical Gaussian absorption correction (based on the real shape of the crystal) followed by an empirical multi-scan correction using SCALE3 ABSPACK routine. The structures were solved using the SHELXS program and refined with the SHELXL program[102] within the Olex2 crystallographic package.[103] All computations were performed on an Intel PC computer with Windows 7 OS. Some structures contain disorder that was detected in difference Fourier syntheses of electron density and accounted for using capabilities of the SHELX package. In most cases, hydrogen atoms were localized in difference syntheses of electron density but were refined using appropriate geometric restrictions on the corresponding bond lengths and bond angles within a riding/rotating model (torsion angles of methyl hydrogens were optimized to better fit the residual electron density).

Density Functional Theory (DFT) Calculations. DFT computations were performed using the ORCA 2.7 software package developed by Dr. F. Neese.[104] In each case, the corresponding X-ray structure provided the starting point for geometry optimizations and the computational model included the entire complex (excluding uncoordinated solvent molecules). The calculations employed the Becke-Perdew (BP86) functional.[105,106] Ahlrichs' valence triple-ζ basis set (TZV) was used for all atoms, in conjunction with the TZV/J auxiliary basis set.[107,108] Extra polarization functions were included on non-hydrogen atoms.

2.3 Results and Discussion.

2.3.1 Synthesis and Structures of Mononuclear Cu(II) Complexes.

While ligands H_2L^A and L^E are known compounds,[97,99] the pincer ligands $H_2L^{B\text{-}D}$ in **Scheme 2.1** were first prepared in our laboratory. Each was generated via the reaction of pyridine-2,6-dicarbonyl dichloride with the appropriate amino-substituted heterocycle under basic conditions. Mononuclear Cu(II) complexes with the general formula, $[CuCl_2(L^X\{H\}_2)]$ (**1^X**), were then prepared by mixing equimolar amounts of $CuCl_2$ and the desired pincer ligand (**Scheme 2.2**). X-ray quality crystals of the **1^X** series were obtained by slow evaporation of CH_2Cl_2 or layering a concentrated solution with pentane. Details concerning the X-ray diffraction (XRD) experiments included in this study are provided in **Table 2.7** and the Experimental Section.

Selected bond distances and angles for complexes in the $\mathbf{1^X}$ series are shown in **Table 2.1**. As displayed in **Figure 2.1**, complexes with pendant pyridyl ($\mathbf{1^B}$) or pyrimidyl ($\mathbf{1^C}$) groups each contain a five-coordinate (5C) Cu(II) center ligated to two chlorido ligands and one neutral $L^X\{H\}_2$ bound in a meridional fashion. These complexes exhibit idealized C_2 symmetry along the Cu–N(1) axis, resulting in nearly equivalent sets of chlorido and amidato donors. The coordination geometries of $\mathbf{1^B}$ and $\mathbf{1^C}$ are best described as distorted trigonal-bipyramidal with the two amidato nitrogens (N(2) and N(3)) occupying the axial positions, although the N(2)–Cu–N(3) axis is bent towards the pyridyl ring with an angle of ~159°. In the equatorial plane, the N(1)–Cu–Cl angles range between 126 and 138° and the Cl(1)–Cu–Cl(2) bonds form approximate right angles. Typical for pyridinedicarboxamide ligands,[71-75,109-111] the shortest metal-ligand bond involves the central pyridine group, with a distance of 1.94 ± 0.01 Å in the $\mathbf{1^X}$ series. The average copper(II)–amidato bond length of 2.05(1) Å is slightly longer than the usual distance of ~2.0 Å found in 5C Cu(II) complexes with *dianonic* 2,6-pyridinedicarboxamide ligands.[71-75,109-111] On the other hand, these bonds are significantly shorter than the corresponding Cu–N bonds in dichloro Cu(II) complexes with neutral 2,6-bis(imino)pyridine ligands (i.e., Schiff bases), which display distances of 2.10 ± 0.02 Å.[99,112,113] This result suggests that the amidato donors of $\mathbf{1^B}$ and $\mathbf{1^C}$ still possess anionic character and strong σ-donating ability, despite the overall neutrality of the $L^X\{H\}_2$ ligands.

Table 2.1 Selected Bond Distances (Å) and Bond Angles (deg) for Complexes $\mathbf{1^X}$.

	$\mathbf{1^B}$	$\mathbf{1^C}$ [a]	$\mathbf{1^D}$
Cu1-Cl1	2.4569(7)	2.4393(5)	2.196(1)
Cu1-Cl2	2.3909(6)	2.3361(5)	3.029(1)
Cu1-N1	1.946(2)	1.939(2)	1.933(3)
Cu1-N2	2.053(2)	2.050(1)	2.028(3)
Cu1-N3	2.050(2)	2.046(2)	2.018(3)
H-bond parameters			
N4···Cl2 (Å)	3.061(2)	3.109(2)	3.066(3) [c]
N5···Cl1 (Å)	3.119(2)	3.138(2)	3.088(3) [c]
N4-H···Cl2 (°)	152.3	161.2	151.3
N5-H···Cl1 (°)	163.9	164.8	152.3
Dihedral "tilt" angle of pendant			
C6-N2-C8-C10/N6	35.0(4)	22.0(3)	64.3(5)
C7-N3-C9-C11/N7	23.0(4)	24.9(3)	70.5(5)
Bond angles			
Cl2-Cu1-Cl1	95.97(2)	97.95(2)	100.11(4)
N1-Cu1-Cl1	126.22(6)	127.44(4)	175.93(9)
N1-Cu1-Cl2	137.81(6)	134.58(5)	83.94(9)
N1-Cu1-N2	79.07(8)	79.69(6)	79.86(1)
N1-Cu1-N3	79.38(8)	79.66(6)	80.56(1)
N2-Cu1-Cl1	94.47(6)	94.66(4)	99.69(8)
N2-Cu1-Cl2	99.95(6)	97.03(5)	89.64(8)
N3-Cu1-Cl1	99.45(6)	97.81(4)	99.79(9)
N3-Cu1-Cl2	94.97(6)	97.46(5)	89.09(9)
N3-Cu1-N2	158.39(8)	159.35(6)	160.40(1)

[a] Complex $\mathbf{1^C}$ features four symmetrically independent units that are chemically equivalent. Metric parameters are only provided for one complex.

[b] Measures the absolute angle between the pyridinedicarboxamide plane and the plane of the pendant heterocycle.

[c] In the $\mathbf{1^D}$ structure, one chloride (Cl2) participates in H-bonding interactions with both N-H groups; see **Figure 2.1**.

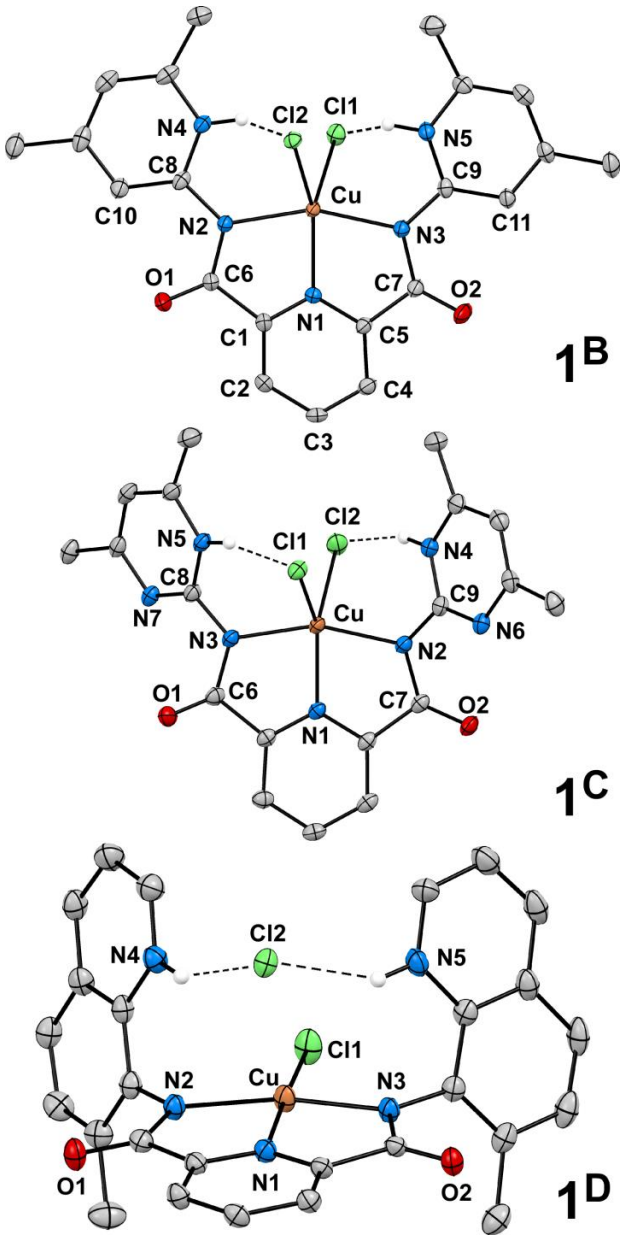

Figure 2.1 Thermal ellipsoid plots (50% probability) derived from the X-ray crystal structures of complexes $\mathbf{1^B}$, $\mathbf{1^C}$, and $\mathbf{1^D}$. Noncoordinating solvent molecules and most hydrogen atoms have been omitted for clarity.

As intended, the $L^X\{H\}_2$ framework in **1^B** and **1^C** gives rise to intramolecular H-bonds between first- and second-sphere groups (**Figure 2.1**). Each chlorido ligand participates in a single H-bond interaction with a pendant pyridinium (or pyrimidinium) ring. The average N···Cl distance of 3.11 Å and N–H···Cl angle of ~160^o provide solid confirmation of this H-bonding assignment. In addition, the protonated heterocycles tilt out of the pyridinedicarboxamide plane unit by 22^o–36^o to accommodate these interactions. Thus, our complexes deviate from the structure reported for the related complex $[CuCl_2(L^0\{H\}_2)]$, in which the pyridinium groups H-bond with the carbonyl groups instead.[98] The presence of methyl substituents on the pendant rings in our systems likely discourages this conformation, since the methyl groups would sterically clash with the chlorido ligands. The Cu-Cl bonds in **1^{B,C}** range from 2.34 to 2.46 Å with an average length of 2.40 Å. Overall, these values lie on the high end of the 2.2-2.4 Å range normally observed in copper(II)-chlorido complexes,[98,114-116,117] suggesting that the H-bonding interactions cause a modest lengthening of the Cu-Cl bond.

The structure of **1^D**, shown in **Figure 2.1**, is unique in the **1^X** series in that the appended quinoline rings adopt a *syn* conformation and form H-bonds with the same chloride anion, Cl2. Compared to the pyridyl and pyrimidyl systems, the N-H donors of the protonated quinoline groups are further removed from the amidato donors, which requires Cl2 to shift away from the Cu center in order to accommodate the H-bonding interactions. Indeed, the Cu···Cl2distance of 3.029(1) Å indicates that the Cu(II)

geometry is effectively square-planar. The reduction in coordination number causes the first-sphere Cu–N/Cl distances to decrease relative to their values in $\mathbf{1^B}$ and $\mathbf{1^C}$, and the N1-Cu-Cl1 angle approaches 180° (the actual value is 175.9(1)°). Thus, changes in the positions of H-bond donating groups can dramatically alter the coordination environment of metal ions.

Copper(II)–triflate complexes with the general formula, $[Cu(L^X\{H\}_2)(OTf)_2(H_2O)]$ ($\mathbf{2^X}$), were synthesized using the H_2L^B and H_2L^C ligands. These complexes were prepared by two separate methods: (i) direct mixing of the 2,6-pyridinedicarboxamide ligand with $Cu(OTf)_2$, or (ii) treatment of the $\mathbf{1^X}$ complex with two equivalents of AgOTf in MeCN (**Scheme 2.4**). X-ray quality crystals of the triflate-containing complexes were obtained by vapor diffusion of diethyl ether into MeCN solutions. The aqua ligand in the $\mathbf{2^X}$ structures (*vide infra*) presumably arises from trace amounts of water in the solvent. The reaction of only one equivalent of AgOTf with complex $\mathbf{1^B}$ gave rise to the mixed chlorido/triflate complex $[CuCl(L^X\{H\}_2)(OTf)(H_2O)]$ ($\mathbf{3^B}$). Since these complexes contain easily-displaceable triflate anions, they are well-suited to serve as scaffolds that permit various ligands to coordinate to the $[Cu(L^X\{H\}_2)]^{2+}$ unit.

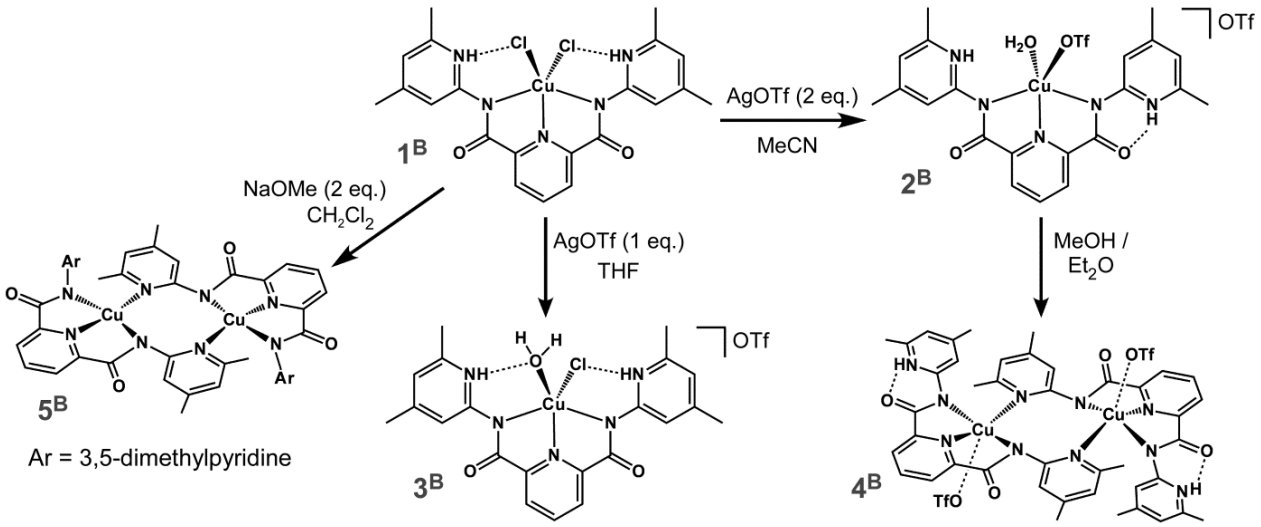

Scheme 2.4 Route of synthesis of mono-bimetallic Cu(II) complexes

The triflate-containing complexes $\mathbf{2^B}$, $\mathbf{2^C}$, and $\mathbf{3^B}$ exhibit considerable structural diversity. The six-coordinate Cu(II) center in $\mathbf{2^C}$ is bound to $L^C\{H\}_2$, an aqua ligand, and two triflates in a *trans* orientation (**Figure 2.2**). The H_2O ligand is tightly bound with a Cu-O1 distance of 1.930(2) Å, while the Cu–N distances are comparable to those observed in the $\mathbf{1^X}$ series (**Table 2.2**). The Cu-O(triflate) distances of 2.415(2) and 2.545(2) Å are indicative of weak dative bonds. Significantly, each protonated pyrimidine group participates in two H-bonding interactions, acting an acceptor to the aqua ligand and a donor to the carbonyl of $L^C\{H\}_2$. This behavior is reminiscent of the ability of His imidazoles to form H-bond networks in biological systems. In contrast, the 4,6-dimethylpyridinium groups in $\mathbf{2^B}$ lack this bifunctional nature, resulting in a very different structure (**Figure 2.2**). One triflate group moves to the outer sphere, resulting in a 5C Cu(II) center with square-pyramidal geometry. In the solid-state, the H_2O ligand of

2^{B} forms intermolecular H-bonds with both bound and unbound triflate anions, and one pyridinium group is co-planar with the $L^{B}\{H\}_2$ ligand due an intramolecular bond with a carbonyl moiety. The other pyridinium group, however, tilts out of the plane to form an intermolecular H-bond with the coordinated triflate of a nearby complex. The case of **2^{B}** is a reminder that the presence of multiple H-bond donors and acceptors in the first and second coordination spheres often leads to complex (and unpredictable) geometries.

Table 2.2 Selected Bond Distances (Å) and Bond Angles (deg) for Complexes **2^{B}**, **2^{C}**, and **3^{B}**.

	2^{B}	**2^{C}**	**3^{B}**
Cu1-N1	1.929(8)	1.915(2)	1.928(2)
Cu1-N2	2.098(8)	2.058(2)	2.067(2)
Cu1-N3	2.054(8)	2.069(2)	2.078(2)
Cu1-O3	1.973(7)	1.930(2)	2.249(2)
Cu1-O4	2.360(7)	2.415(2)	—
Cu1-O7	—	2.545(2)	—
Cu1-Cl1	—	—	2.2900(6)
Dihedral "tilt" angle of pendant ring			
C6-N2-C8-C10/N6	176(1)	176.2(2)	24.8(3)
C7-N3-C9-C11/N7	131.6(9)	173.5(2)	14.6(3)

[a] Measures the absolute angle between the pyridinedicarboxamide plane and the plane of the pendant heterocycle.

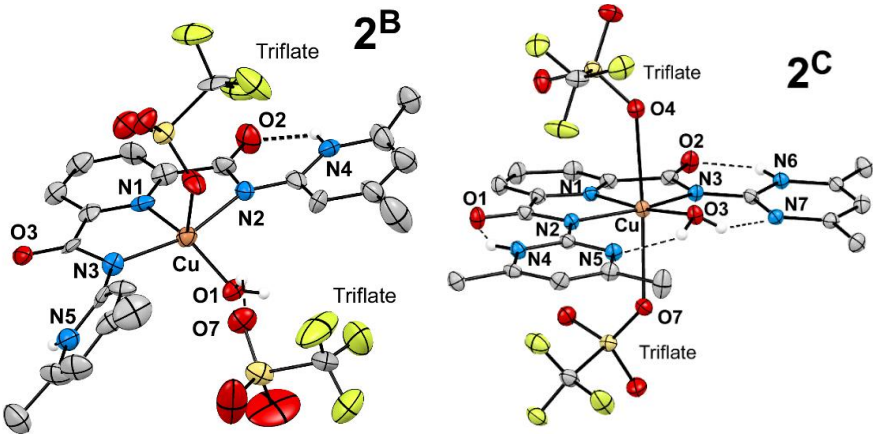

Figure 2.2 Thermal ellipsoid plots (50% probability) derived from the X-ray crystal structures of complexes $\mathbf{2^C}$ (right) and $\mathbf{2^B}$ (left). Noncoordinating solvent molecules and most hydrogen atoms have been omitted for clarity.

The $\mathbf{3^B}$ structure, shown in **Figure 2.3**, resembles the $\mathbf{1^B}$ structure described above, except that one chlorido ligand is replaced by H_2O. The 5C Cu(II) geometry is distorted square-pyramidal (structural parameter, τ,[118] of 0.16) with the aqua ligand in the axial position. Both Cl and H_2O ligands participate in hydrogen-bond interactions with the appended pyridinium groups, displaying rather typical N···Cl and N···O distances of 3.11 and 2.87 Å, respectively. In the solid state, the aqua ligand forms H-bonds with two triflate counteranions, accounting for the lengthy Cu–O(3) distance of 2.249(2) Å (**Table 2.2**).

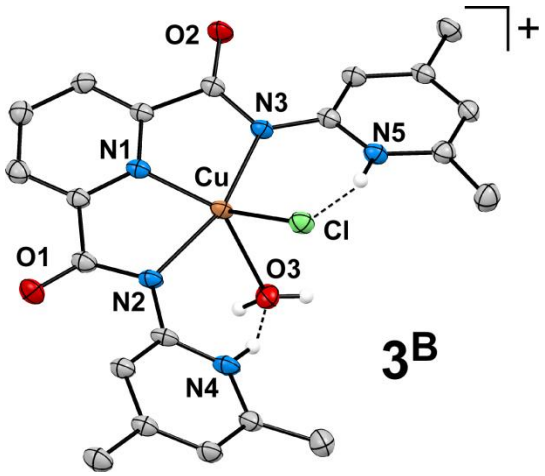

Figure 2.3 Thermal ellipsoid plot (50% probability) derived from the X-ray crystal structure of **3^{B}**. The triflate counteranion, noncoordinating solvent molecules, and most hydrogen atoms have been omitted for clarity. Each aqua ligand forms hydrogen bonds with two outer-sphere triflate anions.

2.3.2 Synthesis, Structures, and Magnetism of Dinuclear Cu(II) Complexes.

While the previous section demonstrated that the $L^{X}\{H\}_2$ framework yields mononuclear Cu(II) complexes with intramolecular H-bond interactions, we found that certain conditions gave rise to dimeric structures instead. For instance, vapor diffusion of diethyl ether into a solution of **2^{B}** in MeOH provides dark violet crystals that are clearly distinct from the light-green crystals obtained from MeCN/Et_2O. XRD analysis revealed that the violet crystals consist of the dicopper complex $[Cu_2(L^{B}\{H\})_2(OTf)_2]$ (**4^{B}**). As shown in **Figure 2.4**, the dimeric structure of **4^{B}** arises from the fact that the monoanionic $L^{B}\{H\}$ ligands now possess an unprotonated pyridyl ring capable of coordinating to a second $[Cu(L^{B}\{H\})]^{+}$ unit (i.e., a "ligand sharing" structure[119]). Each

5C Cu(II) center in **4^{B}** exhibits a square-pyramidal geometry ($\tau = 0.17$) with a weakly-bound triflate anion in the axial position. The two protonated pyridyl rings form intramolecular H-bonds with C=O groups on the opposite $L^{B}\{H\}^{-}$ ligands, enhancing the stability of the dimeric structure. The Cu···Cu distance was found to be 3.858(3) Å. A similar dicopper structure was previously reported by Woolins and coworkers;[80] however, this complex lacks the H-bonding interactions of **4^{B}**, and the axial positions are occupied by aqua ligands instead of triflates.

Dicopper species were also obtained during attempts to deprotonate the $L^{X}\{H\}_2$ ligands of **1^{B}** and **1^{C}**. Reaction of these complexes with two equivalents of base (e.g., NaOMe or NEt_3) in CH_2Cl_2 produced reddish-purple precipitates (**5^{B}** and **5^{C}**; **Scheme 2.4**) that were crystallized by vapor diffusion of pentane into dilute CH_2Cl_2 solutions. X-ray crystallography found that the purple material corresponds to the dimeric $[Cu_2(L^{X})_2]$ complexes, **5^{B}** and **5^{C}**, that contain the fully-deprotonated, dianionic L^{X} ligands. As in the case of **4^{B}**, one pyridyl (or pyrimidyl) donor from each L^{X} ligand forms a link to the second Cu center, although the lack of triflate counteranions in **5^{B}** and **5^{C}** results in 4C centers (**Figure 2.4**). The complexes are C_2-symmetric with Cu···Cu distances of ~3.2 Å. The equivalent Cu(II) ions exhibit distorted square-planar geometries with short Cu–N distances clustered between 1.93 and 2.00 Å (**Table 2.3**).

UV-visible absorption experiments in CH_2Cl_2 confirmed that the dimerization process is reversible, such that sequential additions of acid and base result in

interconversion of the $\mathbf{1}^{\mathbf{B,C}}$ and $\mathbf{5}^{\mathbf{B,C}}$ (see **Figure 2.8**). Complexes $\mathbf{5}^{\mathbf{B}}$ and $\mathbf{5}^{\mathbf{C}}$ were also prepared directly by the reaction of $CuCl_2$, H_2L^X, and two equivalents of NaOMe in MeOH.

Table 2.3 Selected Bond Distances (Å) and Bond Angles (deg) for the Dicopper Complexes $\mathbf{4}^{\mathbf{B}}$, $\mathbf{5}^{\mathbf{B}}$, and $\mathbf{5}^{\mathbf{C}}$.

	$\mathbf{4}^{\mathbf{B}}$		$\mathbf{5}^{\mathbf{B}}$ [a]	$\mathbf{5}^{\mathbf{C}}$ [a]
	Cu1	Cu2		
Cu-N1	1.923(3)	1.930(3)	1.921(2)	1.926(5)
Cu-N2	2.016(3)	2.008(3)	2.000(2)	2.004(5)
Cu-N3	2.035(3)	2.026(3)	1.956(2)	1.974(5)
Cu-N4[a]	2.005(3)	2.008(3)	1.968(2)	1.977(5)
Cu-O5	2.550(3)	2.453(3)	—	—
Cu···Cu	3.858(3)		3.109(2)	3.217(5)
Bond angles				
N1-Cu-N2	79.6(1)	79.6(1)	80.10(6)	80.5(2)
N1-Cu-N3	80.4(1)	80.6(1)	80.74(6)	80.6(2)
N1-Cu-N4	169.5(1)	168.8(1)	169.93(6)	167.4(2)
N2-Cu-N3	159.5(1)	159.8(1)	160.19(6)	160.0(2)
N2-Cu-N4	94.7(1)	94.8(1)	97.08(6)	95.7(2)
N3-Cu-N4	104.3(1)	103.9(1)	102.65(6)	104.2(2)
O5-Cu-N1	87.3(1)	88.7(1)	—	—
O5-Cu-N2	83.4(1)	84.7(1)	—	—
O5-Cu-N3	100.1(1)	99.0(1)	—	—
O5-Cu-N4	100.8(1)	100.6(1)	—	—

[a] The copper centers in $\mathbf{5}^{\mathbf{B}}$ and $\mathbf{5}^{\mathbf{C}}$ are equivalent by symmetry.

A solid-state sample of $\mathbf{5}^{\mathbf{B}}$ provided an effective magnetic moment (μ_{eff}) of 2.4(1) μB at room temperature, somewhat less than the spin-only value of 2.56 μB expected for a dinuclear species with two uncoupled $S = 1/2$ spins. This result indicates the presence of modest antiferromagnetic coupling between the Cu(II) centers. Indeed, broken-

symmetry calculations[120] using density functional theory (DFT) computed an exchange coupling parameter (J) of –41 cm^{-1} for **5^{B}**. Interactions of this magntitude would yield a μ_{eff} of 2.3 μB, which is reasonably close to the value measured experimentally.

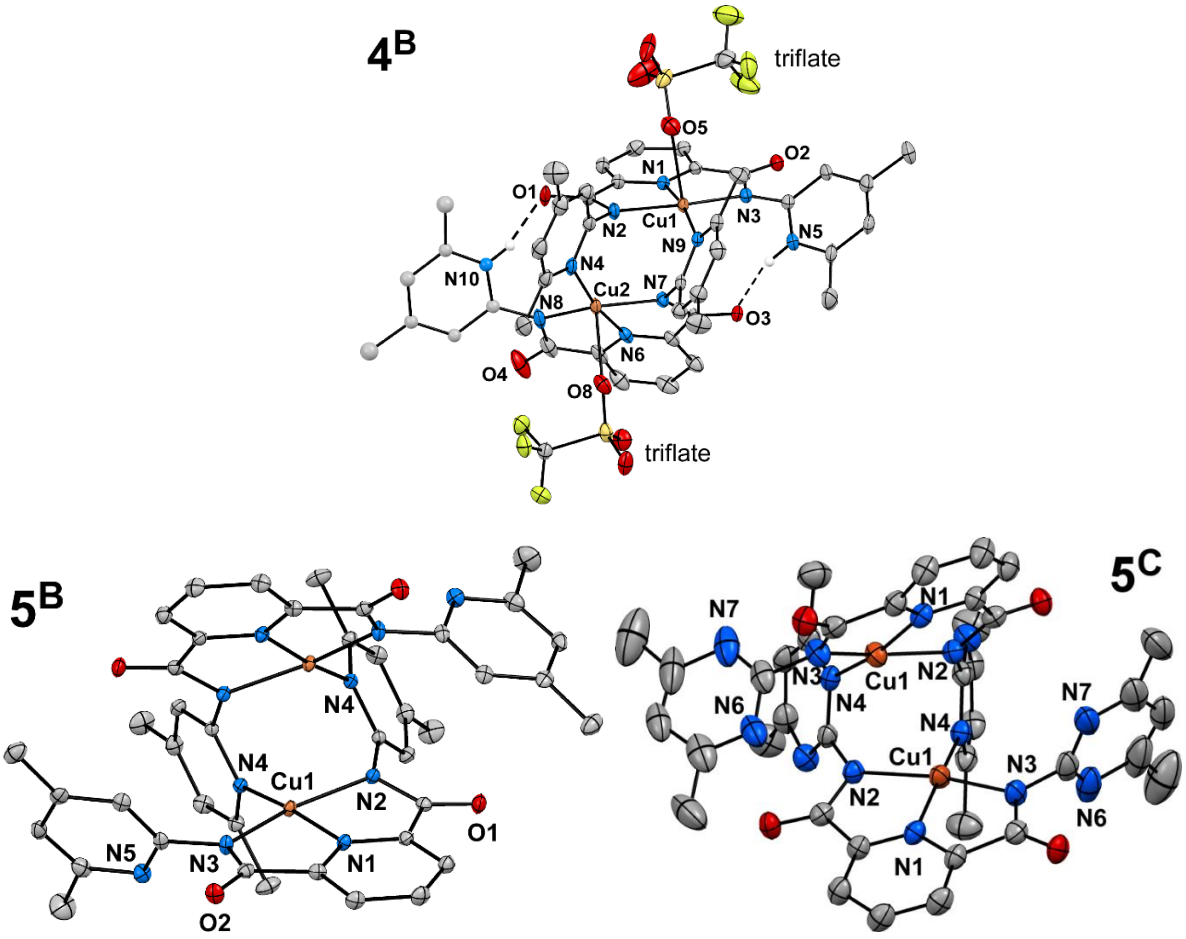

Figure 2.4 Thermal ellipsoid plots (50% probability) derived from the X-ray crystal structures of complexes **4^{B}**, **5^{B}** and **5^{C}**. Noncoordinating solvent molecules and all hydrogen atoms have been omitted for clarity. *Note:* Complex **5^{B}** and **5^{C}** have C_2 symmetry, thus the [Cu(L^{B})] and [Cu(L^{C})] units have identical structures.

Interestingly, deprotonation of the quinoline-appended H_2L^{D} ligand in the presence of $CuCl_2$ does not yield a dicopper species. Instead, a mononuclear 5C complex

[Cu(L^D)] (**6^D**) is formed in which dianionic L^D serves as a pentadentate ligand coordinating via pyridyl, amidato, and quinoline donors. In the X-ray structure of **6^D** (**Figure 2.5**; **Table 2.4**), the Cu(II) ion exhibits a trigonal-bipyramidal geometry with amidato groups in the axial positions. Thus, the L^D(2-) ligand is capable of forming ring chelates involving the pairs of quinoline and amidato donors, whereas this is not feasible in the corresponding L^B- and L^C-based systems.

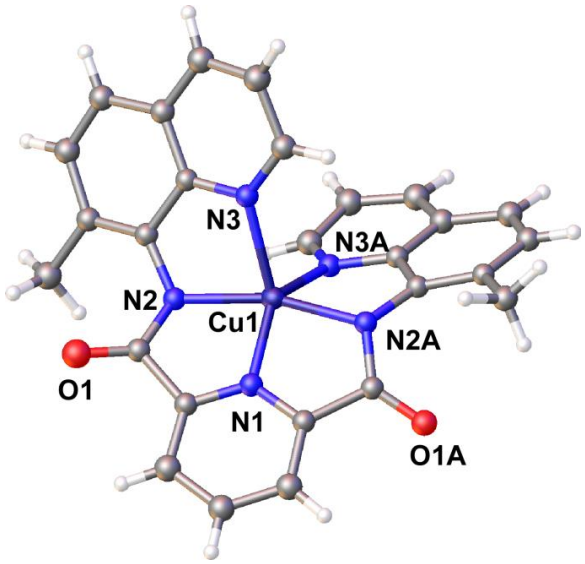

Figure 2.5 X-ray crystal structure of complex **6^D**. Noncoordinating solvent molecules have been omitted for clarity.

Table 2.4 Selected Bond Distances (Å) and Bond Angles (deg) for Complex $\mathbf{6^D}$.

Bond distances		*Bond angles*	
Cu1-N1	1.915(3)	N1-Cu1-N2	81.9(2)
Cu1-N2	1.984(6)	N1-Cu1-N3	134.9(3)
Cu1-N3	2.083(6)	N1-Cu1-N2A	81.5(2)
Cu1-N2A	1.963(6)	N1-Cu1-N3A	132.7(3)
Cu1-N3A	2.129(6)	N2-Cu1-N3	79.9(2)
		N2-Cu1-N2A	163.4(2)
		N2-Cu1-N3A	111.7(3)
		N3-Cu1-N2A	112.4(3)
		N3-Cu1-N3A	92.4(1)
		N2A-Cu1-N3A	79.8(2)

2.3.3 Electronic Absorption Spectroscopy

Electronic absorption spectra of the $\mathbf{1^X}$ series in CH_2Cl_2 are shown in **Figure 2.6** (top). The green color of complexes $\mathbf{1^B}$ and $\mathbf{1^C}$ arises from a broad, asymmetric absorption manifold between 600 and 1100 nm that is comprised of (at least) two bands. These features exhibit molar absorptivities (ε-values) of ~250 $M^{-1}cm^{-1}$, characteristic of d-d transitions. The more intense features in the near-UV region are due to Cl→Cu(II) charge transfer excitations. The $\mathbf{1^{B,C}}$ absorption spectra are typical of five-coordinate Cu(II) complexes with distorted geometries between the square-pyramidal and trigonal-bipyramidal limits.[121 122,123] The absorption maxima (λ_{max}) at 700 nm and the shoulder near 900 nm are assigned to the d_{xy}→ d_{x2-y2} and d_{xz}→d_{x2-y2} transitions, respectively (where the *z*-axis is perpendicular to the CuN_3 plane and the *x*-axis points along the Cu–N(1) bond).

Given that the $\mathbf{1^D}$ structure deviates from those of $\mathbf{1^{B,C}}$ (*vide supra*), it is not surprising that its absorption spectrum is also distinct, having less overall intensity and a single band at shorter wavelength (660 nm); indeed, the $\mathbf{1^D}$ spectrum closely resembles those published for square-planar Cu(II) complexes.[121,124] Likewise, spectra of $\mathbf{2^B}$ and $\mathbf{2^C}$ in MeCN (**Figure 2.6**, bottom) are characteristic of Cu(II) ions in tetragonal environments with strong equatorial donors and weakly-bound axial ligands (likely derived from solvent in this case). The spectrum of $\mathbf{3^B}$, however, closely resembles those reported for 5C complexes $\mathbf{1^B}$ and $\mathbf{1^C}$, suggesting that the former complex maintains a $[CuCl(L^B\{H\}_2)(Y)]^+$ structure in solution, where Y = H_2O or MeCN.

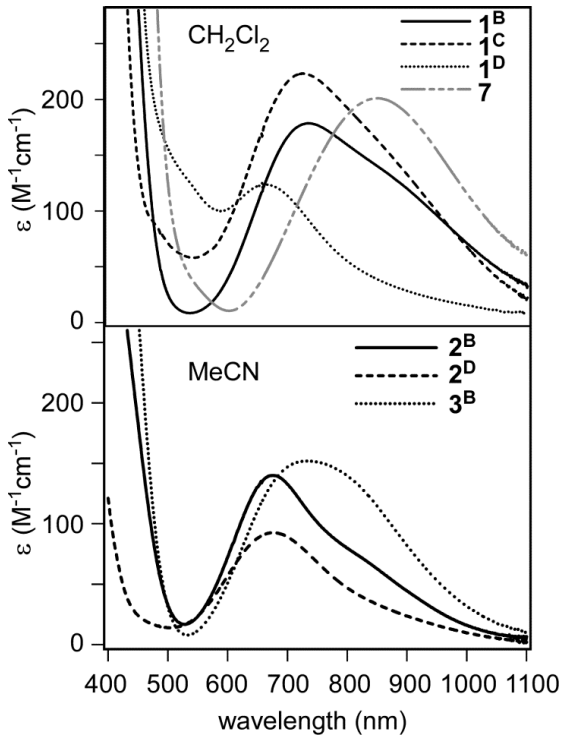

Figure 2.6 Electronic absorption spectra of complexes $\mathbf{1^{B-D}}$ and **7** in CH_2Cl_2 (top) and triflate-containing complexes ($\mathbf{2^B}$, $\mathbf{2^D}$, and $\mathbf{3^B}$) in MeCN (bottom).

In order to compare the electronic properties of the $L^X\{H\}_2$ ligands with the well-established 2,6-bis(imino)pyridine framework, we generated the previously-reported complex $[(L^E)CuCl_2]$ (**7**), where L^E = 2,6-bis(*N*-2-methylphenylacetimino)pyridine (**Scheme 2.1**). The crystallographic structure of **7**, as elucidated by Fan *et al.*,[99] reveals a $CuCl_2N_3$ coordination geometry very similar to those observed for complexes $\mathbf{1^B}$ and $\mathbf{1^C}$, making **7** an excellent reference complex. The absorption spectrum of **7** reveals a peak with λ_{max} = 850 nm (ε = 200 $M^{-1}cm^{-1}$) that arises from a d-d transition (**Figure 2.6**). This feature is red-shifted by ~2100 cm^{-1} relative to the corresponding bands in the $\mathbf{1^B}$ and $\mathbf{1^C}$ spectra, indicating that the 2,6-bis(imino)pyridine framework exerts a considerably weaker ligand field than $L^{B,C}\{H\}_2$. This conclusion is supported by electrochemical experiments, which are described in the following section.

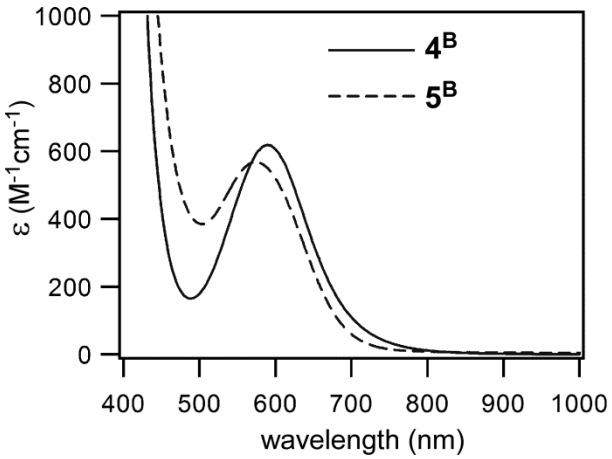

Figure 2.7 Electronic absorption spectra of complexes $\mathbf{4^B}$ and $\mathbf{5^B}$ in CH_2Cl_2.

The absorption spectra of $\mathbf{4^B}$ and $\mathbf{5^B}$ in CH_2Cl_2, shown in **Figure 2.7**, are typical of Cu(II) centers in square-planar geometries. However, in strongly-donating solvents such as DMF and MeOH, our spectroscopic data suggest that these complex exist, at least partially, as monomers. This is apparent when the dark violet crystals of the dicopper species dissolve in MeOH to give blue solutions with absorption features similar to those observed for $\mathbf{2^B}$ and $\mathbf{2^C}$.

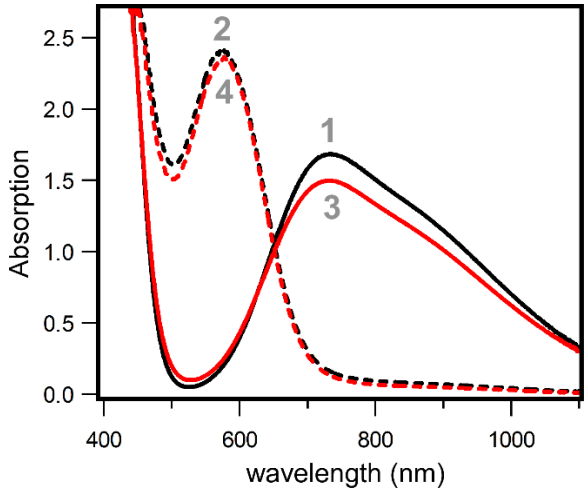

Figure 2.8 UV-vis absorption spectra revealing the reversibility of the dimerization of $\mathbf{1^B}$ to $\mathbf{5^B}$ in CH_2Cl_2. Spectra 1–-4 were obtained sequentially by alternately reacting the initial $\mathbf{1^B}$ solution with base and acid. 1 = initial spectrum of $\mathbf{1^B}$ (conc. = 7 mM); 2 = treatment with 2.0 equiv. of NEt_3; 3 = treatment with 2.0 equiv. of HBF_4; 4 = treatment with an additional 2.0 equiv of NEt_3.

2.3.4 Electrochemistry

The redox properties of mononuclear $Cu/L^X\{H\}_2$ complexes were examined using cyclic voltammetry (CV) in CH_2Cl_2 and DMF solutions with 0.1 M $[NBu_4]PF_6$ as the

supporting electrolyte. The results are summarized in **Table 2.5**. As shown in **Figure 2.9**, complex $\mathbf{1^B}$ displays an irreversible cathodic wave at –0.43 V (versus SCE) in CH_2Cl_2 that corresponds to reduction of the five-coordinate Cu(II) center to Cu(I). Previous studies of similar $[L_{N3}Cu^{2+}Cl_2]$ complexes have demonstrated that reduction often triggers dissociation of one (or both) of the chlorido ligands,[112,113] likely accounting for the irreversible nature of this event. The partially reversible couple observed at higher potential ($E_{1/2}$ = +0.59 V; ΔE = 220 mV) is then assigned to the low-coordinate $Cu^{2+/+}$ species derived from $\mathbf{1^B}$ reduction. The voltammograms collected for $\mathbf{1^B}$ in CH_2Cl_2 and DMF share the same general form, although the potentials are somewhat shifted. In contrast, complexes $\mathbf{1^C}$ and $\mathbf{1^D}$ exhibit markedly different electrochemical behavior in the two solvents. Like $\mathbf{1^B}$, both complexes display irreversible reduction waves at low potentials ($E_{p,c}$ < –0.3 V) in CH_2Cl_2; however, these features disappear in DMF, while the higher-potential event near +0.4 V becomes quasi-reversible (**Table 2.5** and **Figure 2.9**).

The electrochemical data are rationalized in the following manner: one-electron reduction of the $\mathbf{1^X}$ series in CH_2Cl_2 causes dissociation of *both* chlorido ligands, yielding three-coordinate $[Cu^+(L^X\{H\}_2)]^+$ species that are oxidized at potentials between 0.6 and 0.8 V. This conclusion is consistent with the voltammogram measured for $\mathbf{3^B}$ – a complex with only one chlorido ligand. While $\mathbf{3^B}$ is considerably easier to reduce than complexes in the $\mathbf{1^X}$ series (as expected), the corresponding high-potential events all appear at roughly the same potential (+0.63 ± 0.05 V) in CH_2Cl_2 (**Table 2.5**). This result

indicates that reductions of **1^{X}** and **3^{B}** give rise to the same $[Cu^{+}(L^{X}\{H\}_2)]^{+}$-type species, regardless of the number of chlorido ligands in the precursor complex. Using similar reasoning, the two cathodic waves observed for **1^{D}** (**Figure 2.9**) point to a *pre-reduction* equilibrium with the form $[CuCl_2(L^{D}\{H\}_2)] \leftrightarrows [CuCl(L^{D}\{H\}_2)]^{+} + Cl^{-}$ in CH_2Cl_2, such that loss of the weakly-bound, axial chlorido ligand shifts the $Cu^{2+/+}$ potential of **1^{D}** from –0.68 to –0.40 V (**Table 2.5**). Yet **1^{D}** exhibits only one anodic feature at $E_{p,a}$ = +0.59 V, indicating that reduction generates a single species, $[Cu^{+}(L^{D}\{H\}_2)]^{+}$.

Table 2.5 Electrochemical Data for Mononuclear Cu(II)/$L^{X}\{H\}_2$ Complexes.[a]

complex	solvent	$E_{p,c}$ (V) [b]	$E_{1/2}$ (V)	ΔE (mV) [c]	$i_{p,c}$ / $i_{p,a}$ ratio [d]
1^{B}	CH_2Cl_2	–0.43	+0.59	220	0.34
	DMF	–0.27	+0.39	170	0.35
1^{C}	CH_2Cl_2	–0.34	+0.61	180	0.27
	DMF	n.a [a]	+0.40	160	0.79
1^{D}	CH_2Cl_2	–0.40, –0.68	$E_{p,a}$ = +0.59 [b]	—	—
	DMF	n.a	+0.40	150	0.83
2^{C}	DMF	n.a	+0.41	110	1.00
3^{B}	CH_2Cl_2	–0.09	+0.68	210	0.23
4^{B}	CH_2Cl_2	–0.28, –0.68	$E_{p,a}$ = +0.42	—	—
5^{B}	CH_2Cl_2	–0.93, –1.55	$E_{p,a}$ = +0.07	—	—
7	CH_2Cl_2	+0.02	$E_{p,a}$ = +0.56 [b]		

[a] All potentials reported versus SCE; n.a = not observed.
[b] $E_{p,c}$ and $E_{p,a}$ values are given for irreversible reduction and oxidation events, respectively.
[c] $\Delta E = E_{p,a} - E_{p,c}$
[d] Ratio of cathodic current ($i_{p,c}$) and anionic current ($i_{p,a}$).

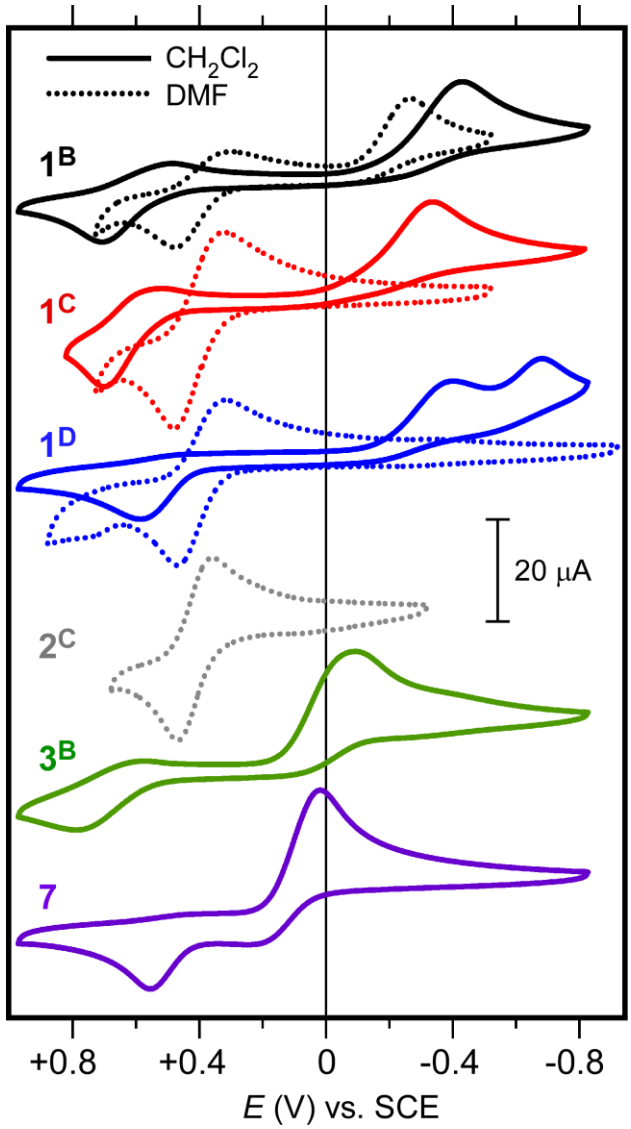

Figure 2.9 Cyclic voltammograms of $\mathbf{1^B}$ (black), $\mathbf{1^D}$ (red), $\mathbf{1^E}$ (blue), $\mathbf{2^D}$ (grey), $\mathbf{3^B}$ (green), and **7** (violet) in CH_2Cl_2 (solid lines) and DMF (dotted lines) containing 0.1 M $[NBu_4]PF_6$ as the supporting electrolyte ([Cu] = ~2.0 mM). Data was collected with a scan rate of 100 mV and each voltammogram was initiated by the cathodic sweep.

While the similarity of the cyclic voltammograms suggests that $\mathbf{1^B}$ maintains the same overall structure in CH_2Cl_2 and DMF, solvation of complexes $\mathbf{1^C}$ and $\mathbf{1^D}$ in DMF facilitates ionization to the $[Cu^{2+}(L^X\{H\}_2)]^{2+}$ state – a well-established process for copper-halide complexes in strongly-donating solvents.[125] As shown in **Figure 2.10**, the

absorption spectra of **1**$^{\mathbf{C}}$ and **1**$^{\mathbf{D}}$ in DMF are dramatically different than those measured in CH_2Cl_2, providing further evidence that solvation in DMF facilitates loss of the chlorido ligands (by contrast, spectra measured for **1**$^{\mathbf{B}}$ are nearly identical in the two solvents). Therefore, only one redox couple is observed for **1**$^{\mathbf{C}}$ and **1**$^{\mathbf{D}}$ in DMF (**Scheme 2.5**). In support of this scenario, the CV of $[Cu^{2+}(L^{C}\{H\}_2)](OTf)_2$ (**2**$^{\mathbf{C}}$), which lacks chlorido ligation, displays a single reversible couple at approximately the same potential in DMF. Therefore, we conclude that the $[Cu(L^{X}\{H\}_2)]^{2+/+}$ units possess $E_{1/2}$ values of ~0.6 V in CH_2Cl_2 and ~0.4 V in DMF.

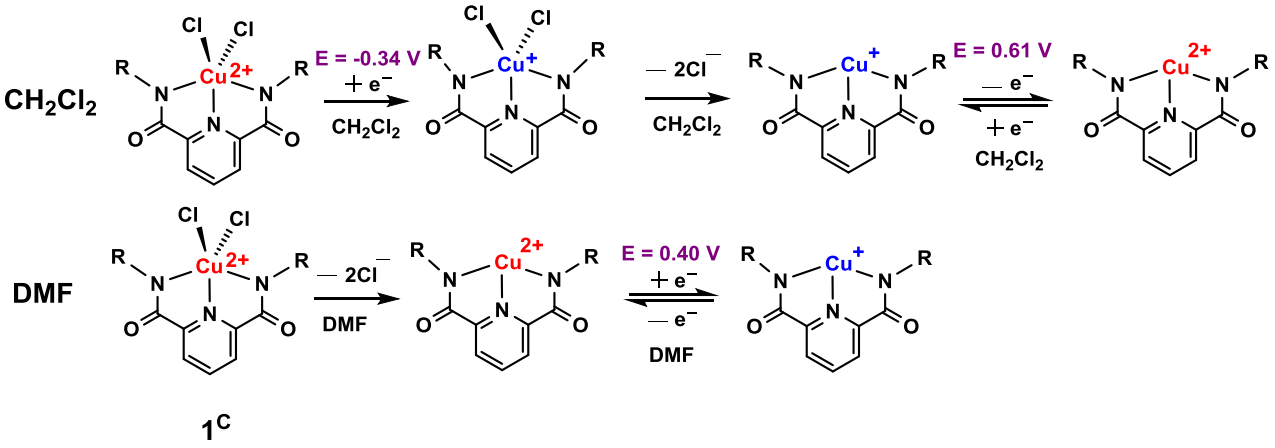

Scheme 2.5 Illustration of electrochemical behaviors of **1**$^{\mathbf{C}}$ in different solvent.

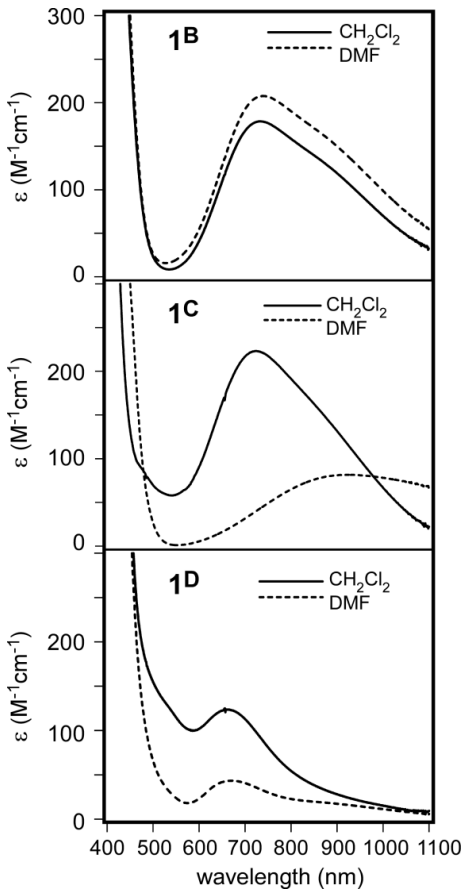

Figure 2.10 Electronic absorption spectra of $[CuCl_2(L^X\{H\}_2)]$ (**1^X**) complexes in CH_2Cl_2 (solid lines) and DMF (dashed lines).

CV data measured for dicopper complexes **4^B** and **5^B** in CH_2Cl_2 are shown in **Figure 2.11**. Both species exhibit two irreversible peaks separated by 0.4 V (**4^B**) or 0.6 V (**5^B**), corresponding to step-wise reduction of the two Cu(II) centers (**Table 2.5**). Given the different protonation states of the L^B ligands in **4^B** and **5^B**, it is not surprising that the former complex is easier to reduce (by 0.65 V) than the latter. The irreversibility of the

cathodic waves suggests that reduction forces the dimeric structures to split apart, and the resulting Cu(I) monomers are then oxidized at higher potentials (**Table 2.5**).

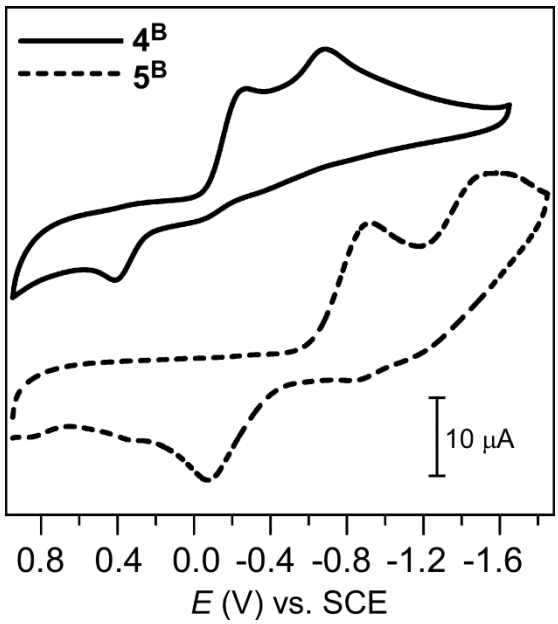

Figure 2.11 Cyclic voltammograms of $\mathbf{4^B}$ (solid line) and $\mathbf{5^B}$ (dashed line) in CH_2Cl_2 containing 0.1 M $[NBu_4]PF_6$ as the supporting electrolyte ([Cu] = 4.0 mM). Data was collected with a scan rate of 100 mV and each voltammogram was initiated by the cathodic sweep.

The redox properties of the reference complex, **7**, were also measured in CH_2Cl_2. The CV displays an irreversible reduction wave at +0.02 V followed by an irreversible anodic event at +0.56 V. The electrochemical behavior of **7** therefore follows the pattern described above for $\mathbf{1^{B\text{-}D}}$, in which reduction initiates chloride dissociation to give a low-coordinate Cu(I) species. However, complex **7** is easier to reduce than $\mathbf{1^B}$ or $\mathbf{1^C}$ by more than 0.35 V, even though the three complexes share nearly identical $CuCl_2N_3$

coordination geometries. DFT calculations indicate that, for all the complexes in this study, the redox-active orbital is the Cu d_{x2-y2} orbital that lies the N_3 plane. This orbital is destablized by ~1800 cm^{-1} upon substitution of L^E with $L^C\{H\}_2$ (*i.e.*, conversion of **7** to $\mathbf{1^C}$), consistent with the cathodic shift in redox potential. Collectively, the spectoscopic and electrochemical data highlight the stronger σ-donating ability of the amidato groups of $L^{B,C}\{H\}_2$ relative to the imines moieties of L^E. Indeed, a survery of the literature reveals that the $\mathbf{1^X}$ potentials lie on the low end of the range normally observed for 5C copper complexes.[126]

2.3.5 Synthesis and Structural Characterization of Fe(II) and Ni(II) Complexes

We sought to generate analogous Fe(II) and Ni(II) complexes using the pyrimidine-appended ligand (H_2L^C). However, the target $[MCl_2(L^C\{H\}_2)]$ complexes appear to undergo ligand disproportionation to yield the complexes $[Fe(L^C\{H\}_2)_2][FeCl_4]_2$ ($\mathbf{8^C}$) and $[Ni(L^C\{H\}_2)_2][NiCl_4]$ ($\mathbf{9^C}$) instead. Metric parameters for both complexes are compared in **Table 2.6**. As shown in **Figure 2.12**, the Fe(II) center in the $[Fe(L^C\{H\}_2)_2]^{2+}$ unit exhibits a distorted octahedral geometry with idealized D_{2d} symmetry. The average Fe-N(pyridine) and Fe-N(amidate) bond lengths were found to be 2.10 and 2.23 Å, respectively (note: the $\mathbf{8^C}$ structure contains two independent formula units with nearly identical geometries). Such Fe-N distances are indicative of high-spin ferrous centers. The tetrahedral $[FeCl_4]^-$ counteranions feature average Fe(III)-Cl

distances of 2.19 Å. The pyrimidine rings in **8**^{C} are each protonated, resulting in the formation of intramolecular H-bonds between the N-H groups and amidate carbonyls. Although a number of bis(2,6-pyridinedicarboxamidate) complexes with Fe(III) centers have been reported,[127-130] **8**^{C} is the first example containing a Fe(II) center, to the best of our knowledge.

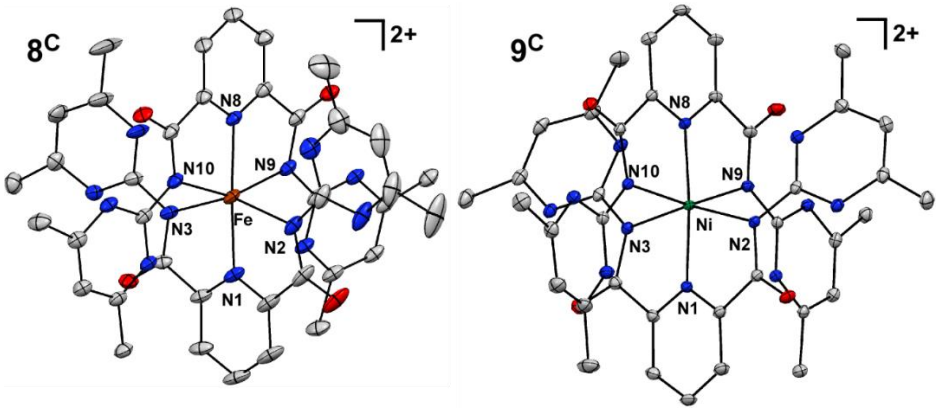

Figure 2.12 Thermal ellipsoid plots (30% probability) derived from the X-ray crystal structures of complexes **8**^{C} and **9**^{C}. Only the $[M(L^{C}\{H\}_{2})_{2}]^{2+}$ complexes in the asymmetric unit are displayed. Noncoordinating solvent molecules, counteranions, and hydrogen atoms have been omitted for clarity.

The primary difference between the **8**^{C} and **9**^{C} structures is the presence of dianionic $[MCl_4]$ counterions in the latter (the Ni(III) state is not as accessible as the Fe(III) state). The average Ni-N(pyridine) and Ni-N(amidate) bond lengths of 1.99 and 2.19 Å, respectively, are slightly shorter than their counterparts in **8**^{C}. These metric parameters are characteristic of high spin Ni(II) centers (S = 1) in six-coordinate geometries. X-ray structures have been previous reported for two bis(2,6-

pyridinedicarboxamidate) complexes with Ni(II) ions;[70,78] in these cases, the amidate nitrogens are attached to phenyl or naphthalene groups, and thus the overall charge of the complexes is –2. As shown in **Table 2.6**, the Ni-N(amidate) bond distances measured for these literature complexes (2.13 and 2.17 Å, on average) are significantly shorter than those observed for **8^{C}** (2.19 Å). This discrepancy is likely due to delocalization of the amidate charge onto the protonated pyrimidine rings in **8^{C}** – a mechanism that is not available for the *N,N'*-bis(aryl)-2,6-pyridinedicarboxamidate(2-) ligands. Further evidence for charge delocalization is found in the shortening of the N(amidate)-C(ring) bonds in **8^{C}** relative to the distances observed the literature complexes, suggesting some imine character. Thus, the crystallographic data suggest that bonding description of the $L^{D}\{H\}_2$ has a significant contribution from the "neutral" resonance structure, even though the "di-zwitterionic" resonance structure is dominant. Our $L^{X}\{H\}_2$ ligands are therefore slightly weaker donors than conventional pyridinedicarboxamidate(2-) ligands.

Table 2.6 Selected Metal-Nitrogen Bond Distances (Å) for Complexes **8^{C}**, **9^{C}**, and Related Literature Complexes.

	$[Fe(L^{C}\{H\}_2)_2][FeCl_4]_2$ (**8^{C}**)	$[Ni(L^{C}\{H\}_2)_2][NiCl_4]$ (**9^{C}**)	**Ref[70]**	**Ref[78]**
M-N1	2.095(3)	1.993(2)	1.994	1.983
M-N2	2.248(4)	2.243(2)	2.135	2.175
M-N3	2.212(3)	2.146(2)	2.126	2.163
M-N8	2.093(3)	1.992(2)	1.994	1.98
M-N9	2.246(3)	2.170(2)	2.135	2.155
M-N10	2.217(3)	2.182(2)	2.126	2.197
Ave	2.185	2.121	2.085	2.109

2.4 Conclusions

In this chapter, we have described the synthesis and coordination chemistry of tridentate pincer ligands, based on the 2,6-pyridinedicarboxamide motif, that feature pendant pyridine, pyrimidine, or quinoline rings. These ligands coordinate to Cu(II) centers as the neutral, di-zwitterions, $L^{X}\{H\}_2$, thus providing two protonated heterocycles capable of serving as H-bond donors and/or acceptors. The [Cu($L^{X}\{H\}_2$)] complexes were characterized with X-ray crystallography and the resulting structures revealed intramolecular H-bonds between first-sphere and the outer-sphere N-H groups. The H-bonding interactions lengthen the Cu-Cl bond distances, and in the case of $\mathbf{1^{D}}$, facilitate dissociation of a chlorido ligand. However, the 2,6-pyridinedicarboxamide framework suffers from a major limitation: deprotonation of the pendant groups promotes formation of dimeric complexes in which appended pyridine (or pyrimidine) groups bind to a second copper ion (**Scheme 2.4**). On the other hand, the 2,6-pyridinedicarboxamide framework prefers to bind to Fe(II) and Ni(II) with octahedral geometry bisligand complexes instead of forming mixing ligand complexes. Thus, we are currently developing modified versions of these ligands that will permit proton transfer reactions without concomitant dimerization.

The electronic properties of the $L^{X}\{H\}_2$ ligand were evaluated with absorption spectroscopy, cyclic voltammetry, and DFT calculations. Anionic pyridine-amidato

ligands are renowned as strong σ-donors that are capable of stabilizing metal centers in high oxidation states.[67-70] Our results indicate that the neutral $L^X\{H\}_2$ ligands retain the electronic features of amidato ligands, despite the presence of the protonated heterocycles that might diminish donor ability due to π-conjugation effects (as illustrated in **Scheme 2.6**). The elevated d-d transition energies and low potentials of the $\mathbf{1^X}$ complexes, relative to the corresponding 2,6-bis(imino)pyridine-based complex (**7**), suggest that the $L^X\{H\}_2$ framework exerts an unusually strong ligand-field for a neutral compound. The $L^X\{H\}_2$ ligands are therefore reminiscent of *N*-heterocyclic carbenes, which also combine impressive σ-donating ability with neutral overall charge. In addition, both types of ligands involve π-conjugation with sp^2-hybridized nitrogen atoms that carry a partial positive charge (**Scheme 2.6**). Thus, the electronic properties of the $L^X\{H\}_2$ framework, in conjunction with their ability to participate in H-bonding interactions, suggests that these ligands may have promising applications in catalyst development. We also anticipate that the presence of outer-sphere hydrogen-bond donors will help stabilize Cu-O_2 and Cu-O_2R (R = H, ^{t}Bu) intermediates that are relevant to O_2-activating copper enzymes.

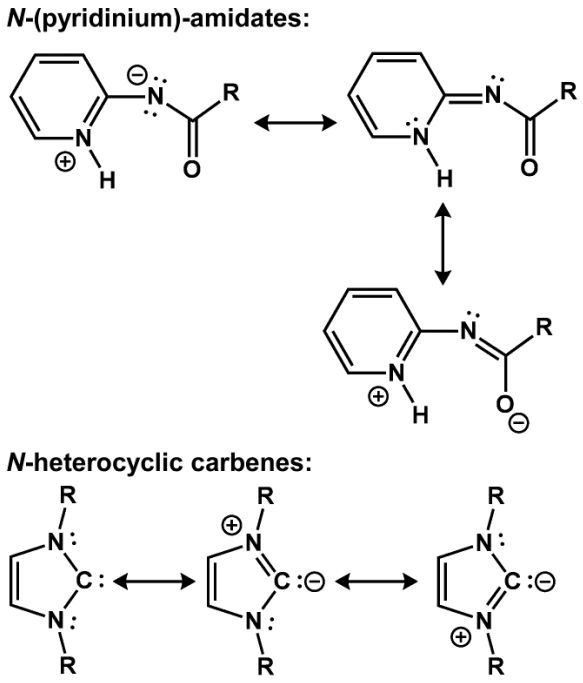

Scheme 2.6 Resonance structures of $L^X\{H\}_2$-type ligands and *N*-heterocyclic carbenes.

Table 2.7 Summary of X-ray Crystallographic Data Collection and Structure Refinement.

	1^{B}	**1**^{C}•0.5 CH_2Cl_2	**1**^{D}•CH_2Cl_2	**2**^{B}	**2**^{C}
Empirical formula	$C_{21}H_{21}Cl_2CuN_5O_2$	$C_{19.5}H_{20}Cl_3CuN_7O_2$	$C_{28}H_{23}Cl_4CuN_5O_2$	$C_{23}H_{23}CuF_6N_5O_9S_2$	$C_{21}H_{21}CuF_6N_7O_9S_2$
Formula weight	509.88	554.32	666.85	755.12	757.11
Crystal system	triclinic	triclinic	triclinic	orthorhombic	triclinic
Space group	*P*-1	*P*-1	*P*-1	$Pna2_1$	*P*-1
a [Å]	7.1019(3)	12.7826(3)	9.4544(7)	28.0304(9)	8.3766(3)
b [Å]	9.8288(4)	15.0326(3)	10.3822(8)	13.2373(5)	9.8949(4)
c [Å]	15.9843(6)	25.2949(4)	15.901(1)	7.9327(2)	19.0738(8)
α [°]	72.240(4)	89.226(1)	106.402(7)	90	98.076(3)
β [°]	82.180(3)	86.712(2)	102.062(7)	90	95.700(3)
γ [°]	87.994(3)	77.779(2)	99.764(6)	90	113.151(4)
Volume [Å^3]	1052.66(7)	4742.6(2)	1420.1(2)	2943.40(16)	1418.3(1)
Z	2	8	2	4	2
ρ_{calc} [g/cm^3]	1.609	1.553	1.56	1.704	1.773
μ [mm^{-1}]	4.052	4.685	4.85	3.273	3.419
Θ range [°]	9.4 to 147.7°	7.0 to 147.8°	9.2 to 148.1°	7.4 to 147.4°	9.5 to 147.6
Reflections collected	15887	95897	13911	15571	21838
Independent reflections	4178 [*R*(int) = 0.0298]	18936 [*R*(int) = 0.0330]	5595 [*R*(int) = 0.0630]	5651 [*R*(int) = 0.0422]	5646 [R(int) = 0.0326]
Data/restraints/parameters	4178 / 0 / 284	18936 / 3 / 1209	5595 / 15 / 418	5651 / 1 / 421	5646 / 0 / 435
Goodness-of-fit on F^2	1.032	1.016	1.013	1.112	1.022
*R*1 / *wR*2 indexes [I >2σ (I)][a]	0.0353 / 0.0919	0.0325 / 0.0871	0.0467 / 0.1044	0.1007 / 0.2383	0.0333 / 0.0831
*R*1 / *wR*2 indexes [all data] [a]	0.0412 / 0.0965	0.0372 / 0.0913	0.0769 / 0.1207	0.1026 / 0.2395	0.0408 / 0.0891

[a] $R1 = \Sigma \, ||F_o| - |F_c|| \, / \, \Sigma |F_o|$; $wR2 = [\Sigma w(F_o^2 - F_c^2)^2 \, / \, \Sigma w(F_o^2)^2]^{1/2}$

Table 2.7 (continued). Summary of X-ray Crystallographic Data Collection and Structure Refinement.

	3^{B}	**4**^{B}•MeOH	**5**^{B}	**5**^{C}	**6**^{D}•H_2O
Empirical formula	$C_{22}H_{23}ClCuF_3N_5O_6S$	$C_{45}H_{44}Cu_2F_6N_{10}O_{11}S_2$	$C_{42}H_{38}Cu_2N_{10}O_4$	$C_{38}H_{34}Cu_2N_{14}O_4$	$C_{27}H_{21}CuN_5O_3$
Formula weight	641.5	1206.11	873.9	877.87	527.04
Crystal system	triclinic	triclinic	monoclinic	monoclinic	monoclinic
Space group	P-1	P-1	C2/c	C2/c	C2/c
a [Å]	10.3358(6)	11.1489(3)	20.1899(4)	19.7551(9)	20.3092(13)
b [Å]	11.0707(6)	15.5689(5)	10.1779(1)	9.8198(4)	10.0074(4)
c [Å]	13.0014(8)	15.6873(6)	19.1402(4)	19.7188(9)	12.8234(9)
α [°]	67.749(5)	98.963(3)	90	90	90
β [°]	69.068(5)	93.322(3)	102.390(2)	103.908(5)	118.907(9)
γ [°]	76.349(5)	105.789(3)	90	90	90
Volume [Å^3]	1277.3(1)	2573.8(2)	3841.5(1)	3713.1(3)	2281.5(2)
Z	2	2	4	4	4
ρ_{calc} [g/cm^3]	1.668	1.554	1.511	1.57	1.521
μ [mm^{-1}]	3.579	2.564	1.165	1.941	1.69
Θ range [°]	7.7 to 147.26°	7.52 to 147.52°	5.96 to 58.22°	9.22 to 147.66°	10 to 148°
Reflections collected	11783	16501	21840	14296	11433
Independent reflections	4998 [R(int) = 0.0217]	16501 [R(int) = 0.0000]	4672 [R(int) = 0.0337]	3688 [R(int) = 0.0380]	2274 [R(int) = 0.0364]
Data/restraints/parameters	4998 / 0 / 364	16501 / 18 / 704	4672 / 0 / 266	3688 / 0 / 266	2274 / 36 / 151
Goodness-of-fit on F^2	1.04	1.076	1.049	1.166	1.041
*R*1 / *wR*2 indexes [I >2σ (I)][a]	0.0374 / 0.0972	0.0917 / 0.2407	0.0316 / 0.0717	0.0944 / 0.2205	0.0467 / 0.1217
*R*1 / *wR*2 indexes [all data] [a]	0.0420 / 0.1017	0.0953 / 0.2474	0.0383 / 0.0753	0.0977 / 0.2222	0.0550 / 0.1295

[a] $R1 = \Sigma \, ||F_o| - |F_c|| \, / \, \Sigma |F_o|$; $wR2 = [\Sigma w(F_o^2 - F_c^2)^2 \, / \, \Sigma w(F_o^2)^2]^{1/2}$

Table 2.7 (continued). Summary of X-ray Crystallographic Data Collection and Structure Refinement.

	8[c]	**9**[c]
Empirical formula	$C_{38}H_{38}Cl_8Fe_3N_{14}O_4$	$C_{42}H_{44}Cl_4N_{16}Ni_2O_{4.35}$
Formula weight	1205.97	1101.76
Crystal system	monoclinic	triclinic
Space group	$P2_1/n$	P-1
a/Å	20.1450(5)	10.31813(19)
b/Å	12.1981(4)	15.4955(3)
c/Å	42.5948(10)	30.5947(4)
α/°	90	88.5917(13)
β/°	102.905(3)	82.6904(13)
γ/°	90	84.0965(14)
Volume/Å^3	10202.4(5)	4825.81(14)
Z	8	4
ρ_{calc}mg/mm^3	1.57	1.516
m/mm^{-1}	11.056	3.512
2Θ range for data collection	7.56 to 148.28°	8.12 to 147.9°
Reflections collected	60246	90609
Independent reflections	20180[R(int) = 0.0445]	19212[R(int) = 0.0430]
Data/restraints/parameters	20180/0/1255	19212/0/1287
Goodness-of-fit on F^2	1.085	1.03
Final R indexes [I>=2σ (I)]	R_1 = 0.0531, wR_2 = 0.1225	R1 = 0.0404, wR2 = 0.1031
Final R indexes [all data]	R_1 = 0.0751, wR_2 = 0.1333	R1 = 0.0468, wR2 = 0.1089

[a] $R1 = \Sigma \, ||F_o| - |F_c|| \, / \, \Sigma |F_o|$; $wR2 = [\Sigma w(F_o^2 - F_c^2)^2 \, / \, \Sigma w(F_o^2)^2]^{1/2}$

Chapter 3

A New Class of Tripodal Ligands Based on the 2,2',2''-Nitrilotris(N-(pyridin-2-yl)acetamide Motif: Synthesis and Coordination Chemistry

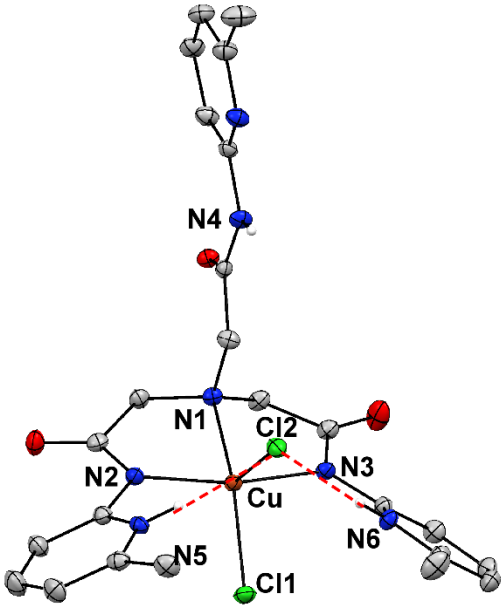

Abstract: The synthesis of ligands based on the 2,2',2''-nitrilotris(*N*-(pyridin-2-yl)acetamide framework are described. These ligand are intended to provide outer-sphere heterocycles (pyridine or pyrimidine) groups capable of participating in H-bonding interactions with first sphere ligands. Preliminary results concerning the coordination modes of these tripodal ligands with Cu(II) and Fe(II) ions are described.

3.1 Introduction

In the previous chapter, we described the synthesis and coordination chemistry of tridentate pincer ligands based on the 2,6-pyridinedicarboxamide motif. These ligands coordinate to metal ions as the neutral, di-zwitterions $L^X\{H\}_2$, thus providing two protonated heterocycles capable of serving as H-bond donors and/or acceptors. Several $[Cu(L^X\{H\}_2)]$ complexes were characterized with X-ray crystallography and the resulting structures revealed intramolecular H-bonds between first-sphere ligands (chloro and aqua ligands) and the outer-sphere N-H groups. However, the 2,6-pyridinedicarboxamide framework suffers from two major limitations: (i) deprotonation of the pendant groups promotes formation of dimeric complexes in which appended pyridine (or pyrimidine) groups bind to a second metal ion, and (ii) the homoleptic bis($L^X\{H\}_2$) complexes appear to be the thermodynamically-favored products when metal ions that favor six-coordinate geometries (such as Fe and Ni) are employed.

As discussed in Chapter 1, several groups have successfully used tripodal ligands to incorporate H-bonding networks into synthetic complexes. The Masuda and Borovik groups in particular have been pioneers in this approach.[29-34,40-44] Their tripodal ligands are generally derived from one of the following frameworks: tris(2-methylpyridyl)amine (tpa),[29-34] *N*,*N*,*N*-tris(2-aminoethyl)amine (tren), or nitrilotriacetamide. Since these ligand coordinate in a tetradentate fashion, it is rare that more than one ligand coordinates to a

first-row transition metal. In addition, the tripodal unit along with its appended H-bond donors possesses considerable steric bulk, which discouraged dimerization and other side-reactions.[40-42]

Given these advantages, we have pursued tripodal analogues of the pincer-type ligands reported in Chapter 2. The simplest example, shown in **Figure 3.1**, is a nitrilotriacetamide-type ligand with *N*,*N*,*N*-tris(6-methylpyridyl) substituents. Similar to the pincer ligands, the amide arms are intended to coordinate in a zwitterionic fashion, i.e., the N-H proton shifts to the pyridine moiety upon metal ion coordination. The synthesis of the tripodal systems is flexible enough to allow formation of mixed ligands featuring both amide and pyridine donors. Thus, we have generated tripodal ligands with one to three amide donors, as illustrated in **Figure 3.1**. In this chapter, we present the synthesis of these ligands and describe preliminary studies of their coordination to Cu and Fe centers.

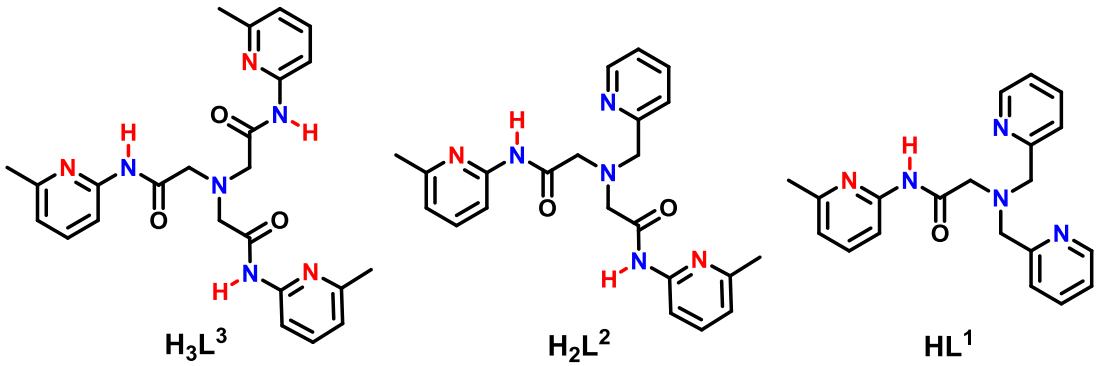

Figure 3.1 General scheme depicting tripodal ligands with varying number of H-bonding groups.

3.2. Experimental Section

Materials and Physical Methods. All reagents and solvents were purchased from commercial sources and used as received unless otherwise noted. Acetonitrile (MeCN), dichloromethane (DCM), and tetrahydrofuran (THF) were purified and dried using a Vacuum Atmospheres solvent purification system. Compounds were characterized and studied using elemental analysis, IR, NMR, UV-Vis and X-ray diffraction. Elemental analyses were performed at Midwest Microlab, LLC in Indianapolis, Indiana. Infrared spectra were measured as a powder on a Thermo Fisher Scientific Nicolet iS5 FT-IR spectrometer with an iD3 ATR accessory, or as KBr pellets using a Nicolet Magna-IR 560 spectrometer. NMR spectra were collected at room temperature with a Varian 400 MHz spectrometer. UV-Vis spectra were collected with an Agilent 8453 diode array spectrometer.

Density Functional Theory (DFT) Calculations. DFT calculations were performed using the ORCA 2.7 software package developed by Dr. F. Neese.[104] In each case, the corresponding X-Ray structure provided the starting point for geometry optimizations and the computational model included the entire complex (excluding counteranions and uncoordinated solvent molecules). Geometry optimizations employed the Becke-Perdew (BP86) functional and Ahlrichs' valence triple-δ basis set (TZV) for all

atoms, in conjunction with the TZV/J auxiliary basis set. Extra polarization functions were used on non-hydrogen atoms.

Crystallographic Studies. The X-ray diffraction data were collected at 100 K with an Oxford Diffraction SuperNova kappa-diffractometer equipped with dual microfocus Cu/Mo X-ray sources, X-ray mirror optics, Atlas CCD detector and a low-temperature Cryojet device. The data were processed with CrysAlisPro program package (Oxford Diffraction Ltd., 2010) typically using a numerical Gaussian absorption correction (based on the real shape of the crystal) followed by an empirical multi-scan correction using SCALE3 ABSPACK routine. The structures were solved using the SHELXS program and refined with the SHELXL program within the Olex2 crystallographic package. All computations were performed on an Intel PC computer with Windows 7 OS. Some structures contain disorder that was detected in difference Fourier syntheses of electron density and accounted for using capabilities of the SHELX package. In most cases, hydrogen atoms were localized in difference syntheses of electron density but were refined using appropriate geometric restrictions on the corresponding bond lengths and bond angles within a riding/rotating model (torsion angles of methyl hydrogens were optimized to better fit the residual electron density).

2-chloro-N-(6-methylpyridin-2-yl)acetamide

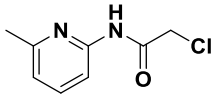

According to the procedure reported by Patil and coworkers,[131] a solution of 2-amino-6-methylpyridine (1,08 g, 10.0 mmol) and triethylamine (1.66 mL, 12.0 mmol) in CH_2Cl_2 (20 mL) was slowly added to 2-chloroacetyl chloride (0.8 mL, 10.0 mmol) in CH_2Cl_2 (20 mL) with ice bath cooling. The mixture was warmed to room temperature and stirred for 40 hours. After the solvent was removed under vacuum, the residue was washed with ice water and the solid was obtained by filtration. The crude product was purifried by crystallization from ethanol to give a white powder (523 mg, 2.84 mmol). Yield: 523 mg, 28.4%; ^{1}H NMR (DMSO) δ: 10.71 (s, 1H), 7.86 (d, 1H), 7.72 (t, 1H), 6.96 (d, 1H), 4.54 (s, 2H), 2.35 (s, 3H). ^{13}C NMR (DMSO) δ: 168.47, 153.44, 147.70, 145.25, 124.34, 115.91, 45.38, 23.73.

Bis(pyridin-2-ylmethyl)amine

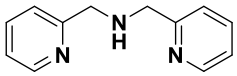

Based on the procedure published by Chomitz and coworkers,[132] a suspension of 2-pyridincarboxaldehyde (0.95 mL, 10.0 mmol) in 30 mL of ethanol was added a solution of 2-(aminomethyl)-pyridine (1.07 mL, 10.2 mmol) in 30 mL of ethanol, and allowed to stir for 4 hours. After cooling the mixture to 0^{o}C, $NaBH_4$ (757 mg, 20 mmol) was added in small portions. The reaction mixture was allowed to stir for 12 hours at RT. HCl (5 M, 24 mL) was then added slowly and stirred for 1 hour. The mixture was treated with 2 M NaOH solution until a pH of 11 was acheived. The mixture was extracted with DCM (6*20 mL), and then organic phase was dried with $MgSO_4$, after that removed solvent

under vacuum, get pure product as brown oil (1.20 g, 6.01 mmol). Yield: 1.20 g, 60.2%; ^{1}H NMR ($CDCl_3$) δ: 8.49 (d, 2H), 7.59 (t, 2H), 7.30 (d, 2H), 7.10 (t, 2H), 3.91 (s, 4H). ^{13}C NMR ($CDCl_3$) δ: 159.41, 149.16, 136.58, 122.37, 122.01, 54.55.

2-(bis(pyridin-2-ylmethyl)amino)- N-(6-methylpyridin-2-yl)acetamide

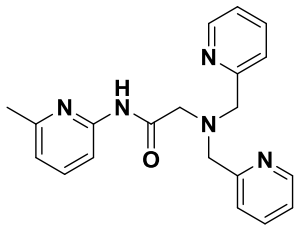

According to a procedure reported by Lee and coworkers,[133] the following compounds were mixed in 30 mL of MeCN: 2-chloro-N-(6-methylpyridine-2-yl)acetamide (2.02 g, 11.0 mmol), 2,2'-dipicolylamine (1.8 mL, 10.0 mmol), N,N-diisopropylethylamine (1.92 mL, 11.0 mmol), and sodium iodide (50 mg). After refluxing for 12 h under argon atmosphere, the mixture was cooled to room temperature and the solvent was removed under reduced pressure to give a brown oil. The oil was purified by silica gel column chromatography using ethyl acetate/methanol (10:1, v/v) as eluent to afford 2.02 g of product. Yield: 2.02 g, 58.2%; ^{1}H NMR (DMSO) δ: 10.43 (s, 1H), 8.52 (d, 2H), 7.90 (d, 1H), 7.83 (t, 1H), 7.75 (t, 2H), 7.47 (d, 2H), 7.25 (t, 2H), 6.91 (s, 1H), 3.97 (s, 4H), 3.59 (s, 2H), 2.34 (s, 3H). ^{13}C NMR (DMSO) δ: 169.41, 159.78, 158.42, 157.44, 149.31, 135.57, 124.43, 122.82, 115.68, 112.8, 112.41, 59.68, 58.01, 23.79.

Diethyl 2,2'-(pyridin-2-ylmethylazanediyl)diacetate

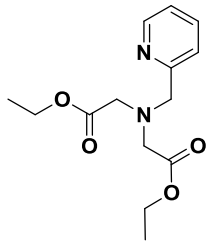

Based on a procedure first reported by Maresca and coworkers,[134] 2-(Aminomethyl)pyridine (1.04 mL, 10.0 mmol) and triethylamine (2.79 mL, 20.0 mmol) were combined in a 100 mL flask with dry THF (20 mL). The solution was cooled with ice bath, and ethyl bromoacetate (2.22 mL, 20.0 mmol) was added dropwise. The reaction was allowed to stir at 0 ^{o}C for 2 hours, then overnightat room temperature. Removal of solvent provided a residue that was dissolved in ethyl acetate and washed with water. The organic phase was dried with $MgSO_4$, and the solvent was removed under vacuum to give a dark red oil. Yield: 2.39g, 85.3%; ^{1}H NMR ($CDCl_3$) δ: 8.46 (d, 2H), 7.61 (t, 1H), 7.54 (d, 1H), 7.10 (t, 1H), 4.10 (q, 4H), 4.0 (s, 2H)， 3.55 (s, 4H), 1.19 (t, 6H). ^{13}C NMR ($CDCl_3$) δ:171.08, 158.86, 148.99, 136.61, 123.06, 122.14, 60.46, 59.82, 54.79, 14.17.

2,2'-(pyridin-2-ylmethylazanediyl)bis(N-(6-methylpyridin-2-yl)acetamide)

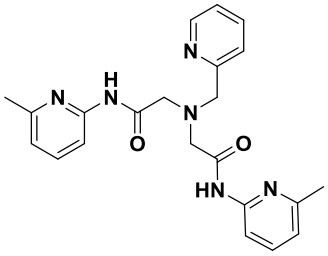

According to the procedure reported by Lu and coworkers,[135] a mixture of NaH (920 mg, 23.0 mmol) and 2-amino-6-methylpyridine (2.38 g, 22.0 mmol) was stirred in

30 mL of petroleum ether for 30 min, then decanted ether and added 30 mL of THF. The reaction system was allowed to stir for 2 hours under reflux. A solution of diethyl 2,2'-(pyridine-2-ylmethyazanediyl)diacetate (2.80 g, 10.0 mmol) in 5 mL of THF was slowly added to the mixture, which was stirred overnight under reflux. The mixture was cooled to room temperature, after the solvent was removed under vacuum. The residue was dissolved in 30 mL of $CHCl_3$ and then washed with water. The aqueous layer was extracted with $CHCl_3$, and the combined organic layers were dried with $MgSO_4$. Removal of solvent under vacuum provided a dark red oil (3.10 g, 7.66 mmol). Yield: 3.10 g, 76.6%. ^{1}H NMR ($CDCl_3$) δ: 10.26 (s, 2H), 8.84 (d, 1H), 7.96 (d, 2H), 7.65 (t, 1H), 7.53 (t, 2H), 7.32 (t, 1H), 6.85 (d, 2H), 4.09 (s, 2H), 3.59 (s, 4H), 2.44 (s, 6H); ^{13}C NMR ($CDCl_3$) δ: 169.36, 163.17, 156.79, 150.63, 149.76, 138.37, 137.11, 123.01, 122.82, 119.10, 110.84, 60.87, 60.02, 24.14.

Triethyl 2,2',2''-nitrilotriacetate

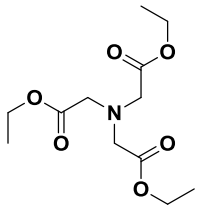

To a mixture of nitrilotriacetic acid in ethanol was added thionyl chloride with stirring and ice cooling. After addition, the mixture was refluxed for 10 hours. The ethanol was evaporated and the residue neutralized with Na_2CO_3 solution. CH_2Cl_2 was used to extract the product from the aqueous layer. The organic layer was dried with

$MgSO_4$ and the solvent was removed under vacuum. Purification by vacuum distillation afforded a colorless oil (4.81 g, 17.47 mmol). Yield: 4.81 g, 87.4%; ^1H NMR ($CDCl_3$) δ: 4.12 (q, 6H), 3.61(q, 6H), 1.22 (t, 9H). ^{13}C NMR ($CDCl_3$) δ: 170.76, 60.62, 55.06, 14.15.

2,2',2''-nitrilotris(N-(6-methylpyridin-2-yl)acetamide)

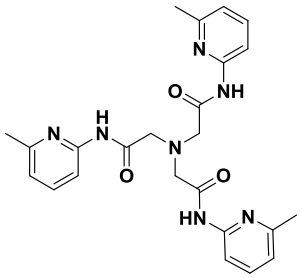

Based on the procedure of Lu and coworkers,[135] a mixture of NaH (1.79 g, 44.7 mmol) and 2-amino-6-methylpyridine (4.65 g, 44.7 mmol) was stirred in 30 mL of petroleum ether for 30 mins, then decanted ether and added 30 mL of THF. The reaction system was allowed to stir for 2 hours under reflux. The solution of diethyl nitrilotriacetate (3.91 g, 14.2 mmol) in 10 mL of THF was slowly added to the mixture, which was stirred overnight under reflux. The mixture was cooled to room temperature and the solvent removed under vacuum. The residue was dissolved in 30 mL of $CHCl_3$ and washed with water. The aqueous layer was extracted with $CHCl_3$. The combined organic layers were dried with $MgSO_4$ and the solvent removed under vacuum. The compound was obtained as a yellow solid (4.07 g, 8.82 mmol). Yield: 4.07 g, 62.0%; ^1H NMR (DMSO) δ: 10.46 (s, 3H), 7.90 (d, 3H), 7.65 (t, 3H), 6.95 (d, 3H), 3.66 (s, 6H),

2.38 (s, 9H). ^{13}C NMR (DMSO) δ: 170.56, 156.95, 151.37, 138.89, 119.11, 110.77, 58.58, 24.02.

[$CuCl_2$(**H_3L^3**)] (**10**): A mixture of $CuCl_2$ (134.5 mg, 1.0 mmol) and **H_3L^3** (461.5 mg, 1.0 mmol) were dissolved in 10 mL of MeCN and stirred overnight in air. The solution turned dark green and a precipitate formed. After removing the solvent under vacuum, the blue solid was washed with Et_2O. Blue crystals were obtained by layering a CH_2Cl_2 solution with pentane. Yield: 510 mg, 86%.

[$FeCl_2$(**HTL^1**)] (**11**): $FeCl_2$ (74.1 mg, 0.584 mmol) and **TLH^1** (203 mg, 0.584 mmol) were dissolved in 10 mL of MeCN and refluxed for overnight under Ar atmosphere. Upon cooling, the brown colored solution provided crystalline precipitate suitable for XRD analysis. After removing the solvent under vacuum, the brown solid was washed with Et_2O. Yield: 187 mg, 67.5%.

3.3 Results and Discussion

3.3.1 Synthesis of Tripodal Ligands

While several tripodal ligand have been prepared in our laboratory, we will only discuss the synthesis of three representative ligands: **HTL^1**, **H_2TL^2**, and **H_3TL^3**, where the superscript indicates the number of amide functional groups. The synthetic routes used to generate these ligands are shown in **Figure 3.2**. The **HTL^1** ligand synthesis required preparation of 2,2'-dipicolylamine and 2-chloro-N-(6-methylpyridin-2-

yl)acetamide via one-step procedures. These precursors were reacted in MeCN for 12 hours in the presence of Hunig's base (*N*,*N*'-diisopropylethylamine) and NaI catalyst. This mixture provided **HTL^{1}** as a brown oil that was purified by column chromatography (58% yield).

Similar procedures were used to prepare ligands **H_2TL^{2}** and **H_3TL^{3}.** The first step in the **H_2TL^{2}** synthesis involved dialkylation of 2-(methylamino)pyridine by ethylbromoacetate to give diethyl 2,2'-(pyridin-2-ylmethylazanediyl)diacetate. Reaction of this product with 2-amino-6- methylpyridine and NaH gave **H_2TL^{2}** as an oil (yield = 77%). The preparation of **H_3TL^{3}** required esterification of nitrilotriacetic acid, again followed by reaction with 2-amino-6- methylpyridine and NaH. **H_3TL^{3}** was isolated as a white powder in 62% yield.

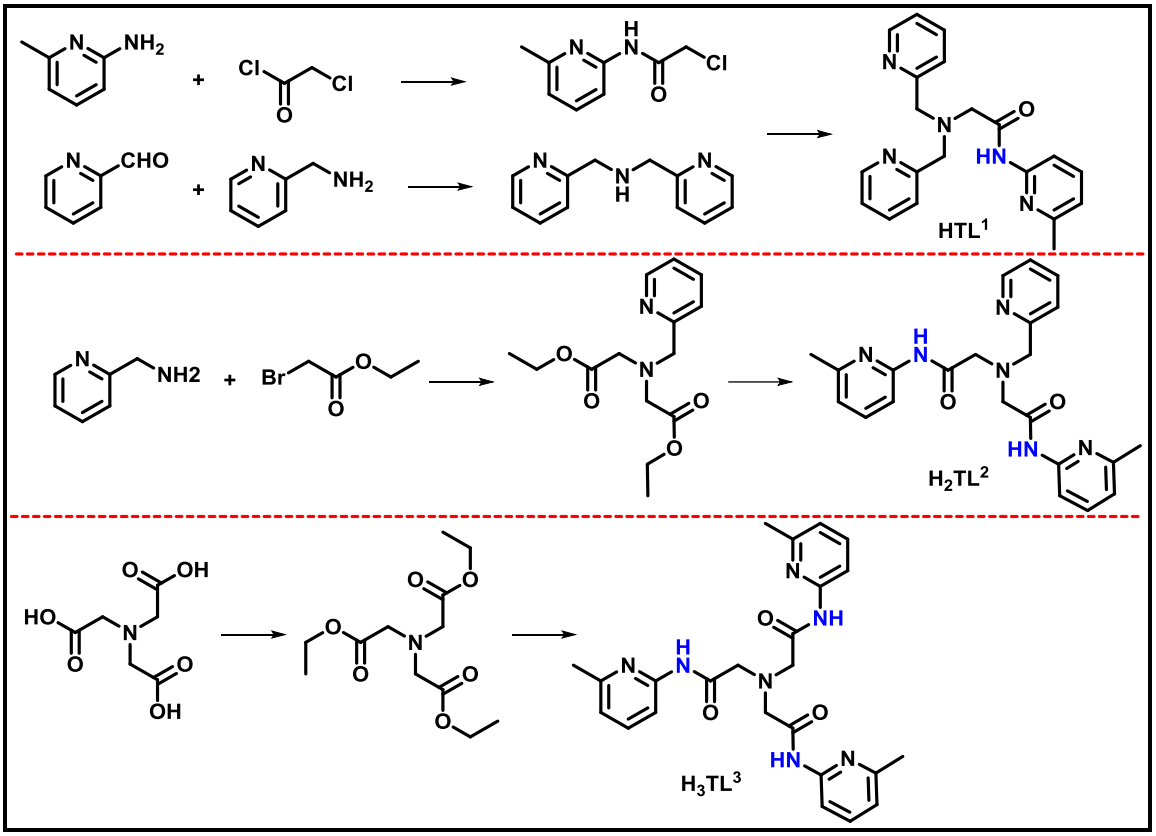

Figure 3.2 Synthetic routes to ligands **HTL[1]**, **H₂TL[2]**, and **H₃TL[3]**.

3.3.2 Synthesis and X-ray Characterization of Metal Complexes.

Reaction of **H₃TL[3]** with $CuCl_2$ in MeCN provided the blue complex [$CuCl_2$(**H₃TL[3]**)] (**10**) in 86 % yield. Crystals suitable for X-ray diffraction (XRD) analysis were obtained by layering a concentrated CH_2Cl_2 solution with pentane; the resulting structure is shown in **Figure 3.3**. The Cu(II) ion has a square-pyramidal coordination with Cl2 occupying the axial position. The **H₃TL[3]** ligand binds to Cu(II) via the central amine and two amidate donors, while the third amide arm remains uncoordinated. This "dangling" arm participates in intermolecular H-bonds with nearby

complexes in the crystal lattice. Interestingly, the axial chloride ligand (Cl2) forms intramolecular H-bonds with two protonated 6-methylpyridyl groups, as indicated by the N···Cl2 distances of 3.1095 and 3.106Å. In a manner reminiscent of complex **1^{D}** in Chapter 2, these H-bonds cause significant lengthening of the Cu-Cl2 bond to 2.7860(7) Å. The remaining copper-ligand bond distances are rather typical: Cu-Cl1 = 2.2640(7) Å, Cu-N(amine) = 2.069(2) Å, and Cu-N(amidate) = 1.988 Å (ave).

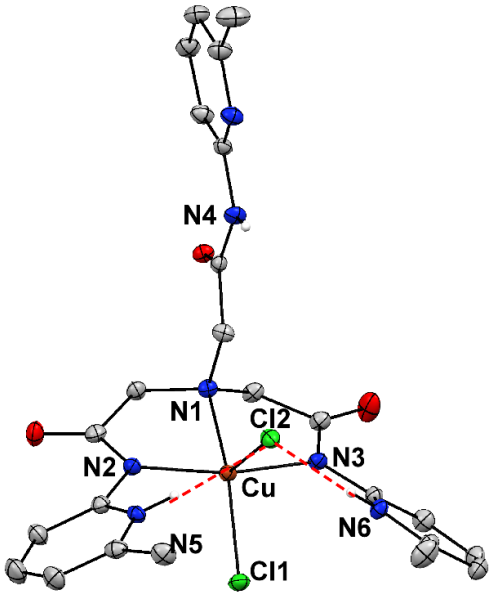

Figure 3.3. Thermal ellipsoid plot (50% probability) derived from X-ray structure of complex **10**.

The crystal structure of **10** verifies that the **H_3TL^3** ligand is capable of creating intramolecular H-bond networks upon complexation to metal centers. Of course, we intended the ligand to coordinate in a tetradenate fashion with each arm ligated to the

same metal center. Efforts are currently underway to generate products with this coordination mode.

The Fe(II) complex [$FeCl_2$(**TLH^1**)] (**11**) was synthesized by combining the tripodal ligand **TLH$_1$** with $FeCl_2$ in dry MeCN under nitrogen atmosphere. The resulting solution was dried under vacuum and washed with diethyl ether to produce a brown solid (yield = 67%). Crystals suitable for X-ray diffraction (XRD) analysis were obtained directly from the reaction mixture; the resulting structure is shown in **Figure 3.4**. The asymmetic unit features a six-coordinate Fe(II) bound to two chlorides, the carbonyl O of the amide group, and three nitrogen atoms (two from pyridyl arms and one from the amine). Unfortunately, the complex does not exhibit intramolecular H-bonding interactions; however, each amide N-H group serves as an intermolecular H-bond donor to a chloride ligand of a nearby unit. The Fe-O(carbonyl) distance is 2.188Å, while the Fe-N bonds have average distances of 2.23 Å. The Fe-Cl bond lenghts of 2.351 and 2.476 Å are common for high-spin Fe(II) centers.

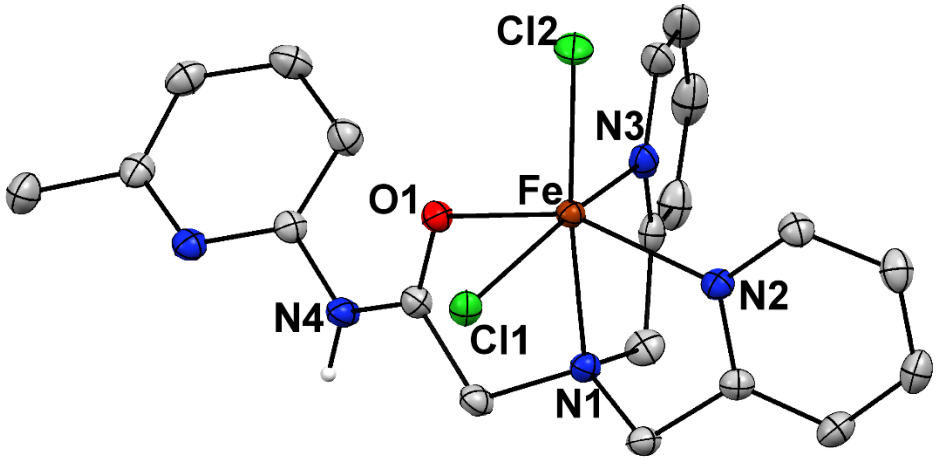

Figure 3.4 Thermal ellipsoid plot (50% probability) derived from X-ray structure of complex **11**.

This structures of complexes **10** and **11** confirm that we have indeed generated the **HTL^1** and **H$_3$TL^3** ligands. In addition, we have an X-ray structure that contains the **H$_2$TL^2** ligand (not shown). This complex structure features a tetranuclear Cu(II) cluster in which the **H$_2$TL^2** ligand serves as a bridging ligand. This result is further proof that ligands with multiple functional groups for second sphere interactions often display unexpected binding modes.

3.3.3. DFT Calculations of Possible Ligand Coordination Modes

In order to examine energetic differences between various **H$_3$TL^3** binding modes, we generated the computational models shown in **Figure 3.5.** Geometry optimizations were performed with ORCA program.

The calculation result showed that the rotated structure is higher in energy than the X-ray structure by 12 kcal/mol. The instability of the rotated structure may arise from steric crowding within the primary coordination sphere, even though there are three H-bond interactions in the rotated structure. The results showed that the distance between N-Cl and the angle of D-H-A are more favorable to the formation of H-bonds than the original structure. The Cu-N4 bond length is quite long in the rotated structure (3.18Å), indicative of steric repulsion. This repulsive force also led to longer Cu-Cl1 and Cu-Cl2 distances in the six-coordiante structure.

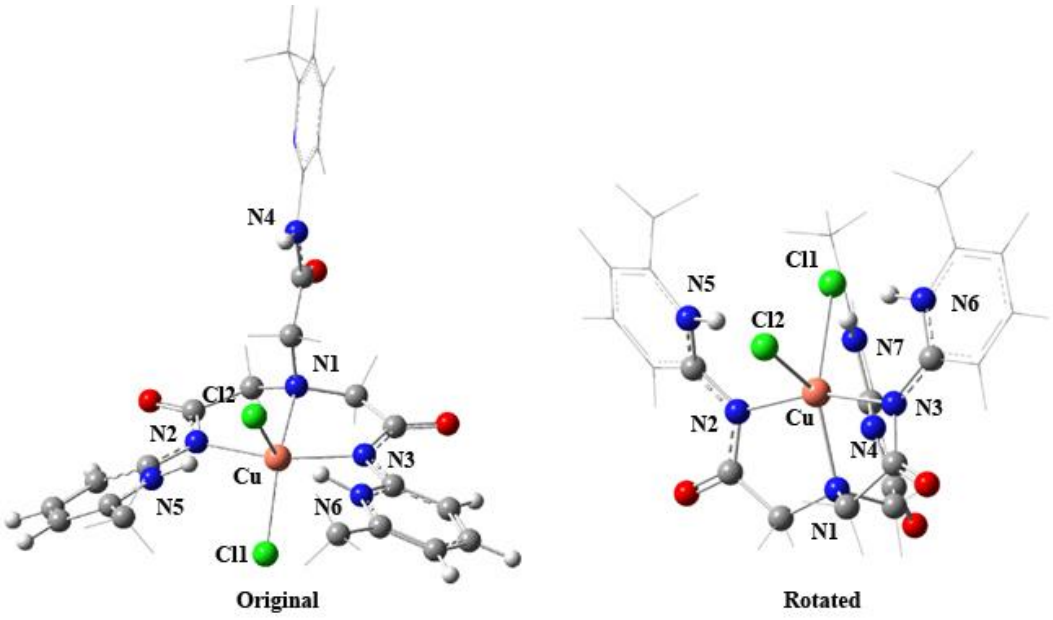

Figure 3.5 DFT-generated models of [$CuCl_2$(**H_3TL^3**)] (**10**).

DFT calculations were also performed with models of [$FeCl_2$(**HTL^1**)] (**11**), as shown in **Figure 3.6**. Both structures feature Fe(II) centers in distorted octahedral

geometries, and the Fe-N and Fe-Cl bond lenghts are similar in the two structures. The rotated model features an intramolecular H-bond interaction that is lacking in the original X-ray structure. Intrestingly, contrary to our experimental results, the calculation found that the rotated model is lower than crystal structure model by 2.3 kcal/mol. This result suggests that synthesis of the desired Fe(II) complex is feasible.

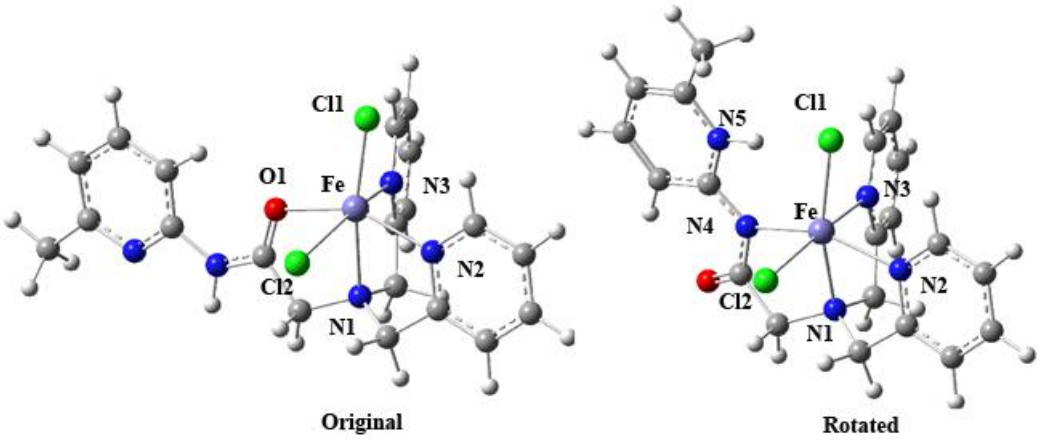

Figure 3.6 DFT geometry-optimized models of [$FeCl_2$(**HTL**^{1})] (**11**).

3.4 Conclusion

In this chapter, we have described the synthesis and coordination chemistry of tripodal ligand frameworks, based on the tripodal scarfold acetamide motif, that feature pendant pyridine or pyrimidine rings. Firstly, we successfully generated all three tripodal ligands with good yield. Based on our synthetic route, the ligand framework can be easily modified with different types of nitrogen containing function group, which make it

possible to study the second sphere H-bond interaction. However, our preliminary metalation study indicated this tripodal ligand frameworks prefers to bind to metal ion with unpredicted fashion.

The solubility of metallated product have caused significant problems, limiting the practical use of this framework for investigating the second sphere H-bond interaction. The efforts to modify the ligand with alkyl substituted pyridine and pyrimidine ring are currently under development in our labs.

Table 3.1 Summary of X-ray crystallographic data collection and structure refinement.

	$[CuCl_2(\mathbf{H_3TL^3})]$ (**10**)	$[FeCl_2(\mathbf{TLH^1})]$ (**11**)
Empirical formula	$C_{26}H_{31}Cl_6CuN_7O_3$	$C_{20}H_{21}N_5OCl_2Fe$
Formula weight	765.82	474.17
Crystal system	monoclinic	monoclinic
Space group	$P2_1/c$	$P2_1/c$
a/Å	11.5977(3)	10.2923(9)
b/Å	30.1556(7)	12.6723(10)
c/Å	9.6680(2)	16.0167(14)
α/°	90	90
β/°	106.930(2)	93.017(8)
γ/°	90	90
Volume/Å^3	3234.70(13)	2086.1(3)
Z	4	4
ρ_{calc}mg/mm^3	1.573	1.51
m/mm^{-1}	5.86	1.001
F(000)	1564	976
2Θ range for data collection	7.96 to 147.9 °	6.92 to 59.04 °
Reflections collected	18060	22199
Independent reflections	6359[R(int) = 0.0382]	5319[R(int) = 0.0558]
Data/restraints/parameters	6359/0/408	5319/0/267
Goodness-of-fit on F^2	1.033	1.058
Final R indexes [I>=2σ (I)]	R_1 = 0.0399, wR_2 = 0.0975	R_1 = 0.0436, wR_2 = 0.1005
Final R indexes [all data]	R_1 = 0.0505, wR_2 = 0.1040	R_1 = 0.0583, wR_2 = 0.1122

Chapter 4

Synthesis of Homo- and Heterobimetallic Ni^{II}–M^{II} ($M = Fe, Co, Ni, Zn$) Complexes Based on an Unsymmetric Ligand Framework: Structures, Spectroscopic Features, and Redox Properties

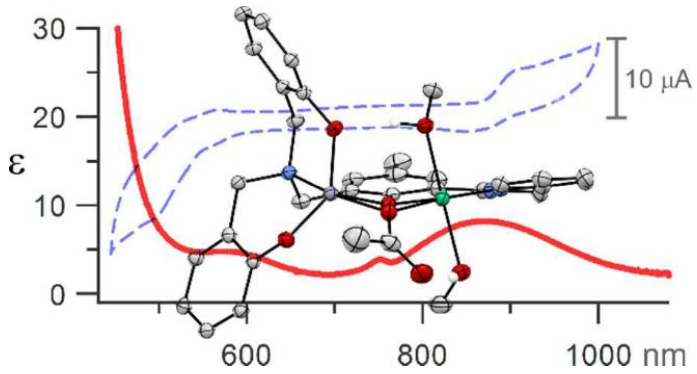

Abstract: The synthesis and coordination chemistry of a new asymmetric ligand designed to support heterobimetallic structures with relevance to bioinorganic chemistry is described. The resulting Ni^{II}–M^{II} complexes were characterized with X-ray crystallography, spectroscopic and computational methods, and voltammetry. The metal centers are bridged by two ligands, resulting in short intermetallic distances of 3.0–3.1 Å. The title complexes serve as structural models of the Ni–Fe1 unit in the C-cluster of carbon monoxide dehydrogenase (CODH) – the site of CO_2 reduction to CO and H_2O. Importantly, the redox-active Ni centers in our complexes possess open and labile coordination sites for use in substrate binding and activation.

Portions of this chapter have appeared in the paper: Wang, D. N.; Lindeman, S. V.; Fiedler, A. T., *Inorganica Chimica Acta*, **2014**, 421 (0), 559-567.

4.1 Introduction

Nickel centers in metalloenzymes are often embedded in polynuclear, heterometallic frameworks that facilitate the activation of small molecules via multiple electron and proton transfers.[136,137] Three examples are shown in **Scheme 4.1**. [NiFe]-hydrogenases feature an unusual heterobimetallic active site with a [NiFe(μ-S_{Cys})$_2$] core; in the available X-ray structures, the Ni···Fe distance ranges from 2.5 to 2.9 Å.[138,139] While only the Ni site is redox-active under catalytic conditions, the Fe^{II} center is believed to play an important role in the binding and heterolytic bond cleavage of H_2.[140,141] The C-cluster of carbon monoxide dehydrogenase (CODH), shown in **Scheme 4.1**, catalyzes the reversible reaction[142,143],

$$CO_2 + 2e^- + 2H^+ \rightarrow CO + H_2O$$

Based on crystallographic data, it appears that substrate binding and activation occurs at the heterobimetallic NiFe1 unit highlighted in **Scheme 4.1**, while the [Fe_3S_4] component is only involved in shuttling electrons.[144-147] The Fe1 center likely serves as a Lewis acid, stabilizing the critical $NiCO_2Fe$ intermediate and facilitating cleavage of the CO bond. Finally, the A-cluster of acetyl-coenzyme A synthase (ACS) consists of a dinickel unit linked to a [Fe_4S_4] cubane via a bridging cysteine residue. In each case, the presence of a metal center adjacent to the redox-active Ni site is critical for efficient catalysis.

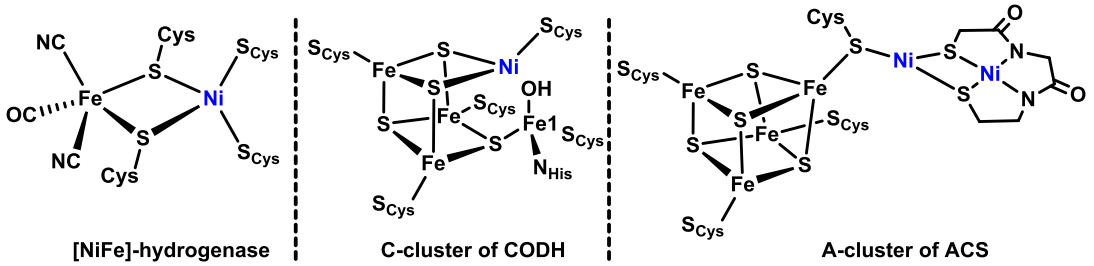

Scheme 4.1 Three Nickel ion involved active site structures of metalloenzymes

These biological precedents suggest that multinuclear Ni-containing complexes may have applications as synthetic catalysts for H_2 generation and CO_2 activation. In an effort to model the NiFe1 unit of the C-cluster, Holm and coworkers generated a series of bio-inspired complexes in which a Ni^{II} center is bound to a 2,6-pyridinedicarboxamidate pincer and a second M^{II} ion is coordinated to a pendant chelate (M = Mn, Fe, and Cu).[148,149] The two metal centers are bridged by a single hydroxo, cyano, or formato ligand; for the hydroxo-bridged complexes, X-ray analysis revealed Ni···M distances near 3.7 Å and NiOM angles of ~140 °. More recently, Uyeda and Peters used a dimine-dioxime ligand to generate a heterobimetallic NiZn complex.[150] The square-planar Ni^{II}center is linked to a [Zn^{2+}(Me_3-TACN)] unit via two oxime bridges (Me_3-TACN = 1,4,7-trimethyl-1,4,7-triazacyclononane). The addition of acetate or nitrite anions yielded triply-bridged structures exhibiting Ni···Zn distances of ~3.45 Å. While numerous heterobimetallic NiM complexes (where M is a biologically-relevant transition metal) exist in the literature, their potential relevance to CODH and CO_2 reduction has not been explored.[151-158]

In this chapter, I will describe the initial efforts from our lab to generate homo- and heterobimetallic complexes containing a coordinatively unsaturated Ni^{II} center in close proximity to a second M^{II} site (M = Fe, Co, Ni, and Zn). Our studies have employed the unsymmetric ligand (L_1^{3-}) shown in **Scheme 4.2**, which contains a central phenolate group capable of bridging the metal ions. Related ligands have been used to model the homo- and heterodinuclear active sites of various metalloenzymes.[159-161] The L_1^{3-} ligand provides two distinct coordination environments: one bearing a Schiff-base moiety linked to a 2-pyridinylmethyl group (site A), and the other consisting of a tertiary amine with two additional phenolate donors (site B). Site A is well-suited for Ni^{II} coordination, while the trisphenolate site binds the second divalent metal ion. The phenolate-rich chelate is intended to depress the redox potentials of the metal centers, thereby enhancing the potential reactivity of the complexes towards electrophilic substrates, such as CO_2. X-ray crystal structures of the bimetallic complexes, described below, revealed that a second bridging ligand is also present: μ-1,1-acetate, hydroxide, or methoxide. As shown in **Scheme 4.2**, the series of complexes are labeled $M_AM_B^X$, where M_A and M_B identify the divalent ions located in the A and B sites, respectively, and X represents the second bridging ligand. The presence of two monoatomic bridging groups leads to short M_A^{II}–M_B^{II} distances of 3.0–3.1 Å. Both metal centers possess open or labile coordination sites for potential use in substrate binding and activation.

In addition to X-ray structural characterization, we have employed electrochemical and spectroscopic methods to analyze the electronic properties of the dinuclear complexes. Specifically, insights into the ligand-field environment were obtained using electronic absorption spectroscopy, and the redox potentials of the metal centers were probed with cyclic and square-wave voltammetry. Collectively, these results provide a foundation for future studies that will examine the reactivity of this new class of heterobimetallic complexes.

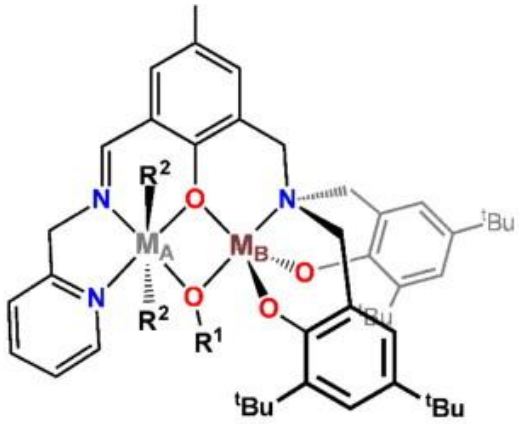

	M_A	M_B	R^1	R^2
NiFe^{OAc}	Ni^{2+}	Fe^{2+}	$C(O)CH_3$	H_2O
NiCo^{OAc}	Ni^{2+}	Co^{2+}	$C(O)CH_3$	MeOH
NiNi^{OAc}	Ni^{2+}	Ni^{2+}	$C(O)CH_3$	MeOH
NiZn^{OAc}	Ni^{2+}	Zn^{2+}	$C(O)CH_3$	MeOH
CoCo^{OAc}	Co^{2+}	Co^{2+}	$C(O)CH_3$	MeOH
NiZn^{OH}	Ni^{2+}	Zn^{2+}	H	vacant
NiNi^{OMe}	Ni^{2+}	Ni^{2+}	CH_3	MeOH

Scheme 4.2 Illustrate of bimetallic complexes with M_A^{II}-M_B^{II} sites

4.2 Experimental

Materials and physical methods. Reagents and solvents were purchased from commercial sources and used as received, unless otherwise noted. The air-sensitive complex **NiFe**^{OAc} was synthesized and handled under inert atmosphere using a Vacuum Atmospheres Omni-Lab glovebox. Elemental analyses were performed at Midwest Microlab, LLC in Indianapolis, IN. Two instruments were used to measure electronic absorption spectra: an Agilent 8453 diode array spectrophotometer and an Agilent Cary 5000 UV−Vis–NIR spectrophotometer. Fourier-transform infrared (FTIR) spectra of solid samples were obtained with a Thermo Scientific Nicolet iS5 FTIR spectrometer equipped with the iD3 attenuated total reflectance accessory. ^{1}H and ^{13}C NMR spectra were recorded at room temperature with a Varian 400 MHz spectrometer. Voltammetric measurements employed an epsilon EC potentiostat (iBAS) at a scan rate of 100 mV/s with 100 mM $(NBu_4)PF_6$ as the supporting electrolyte. The three-electrode cell contained an Ag/AgCl reference electrode, a platinum auxiliary electrode, and a glassy carbon working electrode. Potentials were referenced to the ferrocene/ferrocenium ($Fc^{+/0}$) couple, which has an $E_{1/2}$ value of +0.45 V *versus* the standard calomel electrode (SCE) in DMF.[162] Solid-state magnetic susceptibility measurements were performed at room temperature using an AUTO balance manufactured by Sherwood Scientific. Solution-state magnetic moments were measured in chloroform using the Evans NMR method.

3-(Bromomethyl)-2-hydroxy-5-methylbenzaldehyde (I)

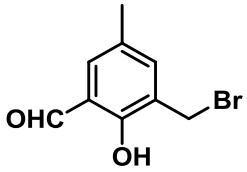

Modifying a published procedure hydrobromic acid (30 mL, 47% in H_2O) was added to a mixture of 5-methylsalicylaldehyde (3.0 g, 22 mmol), paraformaldehyde (0.99 g, 33 mmol) and 10 drops of fuming sulfuric acid.[163] The resulting solution was stirred at 70 ℃ for 6 h, resulting in formation of a white precipitate. After cooling to room temperature, the solid was isolated by filtration and washed with cold water (20 mL). The white product was dried under vacuum and used without further purification. Yield = 4.6 g, 91%. ^{1}H NMR ($CDCl_3$) δ: 2.34 (s, 3H), 4.55 (s, 2H), 7.33 (d, J = 1.4 Hz, 1H), 7.42 (d, J = 1.4 Hz, 1H), 9.85 (s, 1H), 11.30 (s, 1H). ^{13}C NMR ($CDCl_3$) δ: 20.4, 26.9, 120.7, 126.2, 129.5, 134.4, 139.1, 157.7, 196.7.

Bis(3,5-di-tert-butyl-2-hydroxybenzyl)amine (II)

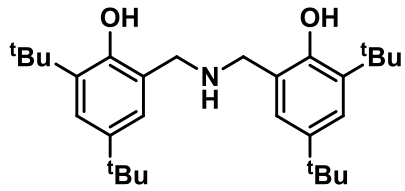

According to a previous report,[164] a mixture of 2,4-di-tert-butylphenol (2.0 g, 10 mmol) and hexamethylenetetramine (2.80 g, 20 mmol) was refluxed for 2 h in formic acid (100 mL, 85%). The reaction yielded crystals of the benzoxazine intermediate (1.85 g) that were subsequently isolated by filtration. This material was dissolved in

ethylene glycol (100 mL) and hydrochloric acid (37%; 40 mL) and heated overnight at 130 ℃. After cooling to room temperature, the hydrochloride salt of the desired product (i.e., II–HCl) was collected by filtration, washed with water, and dried under vacuum. The resulting solid was slowly added to a stirred mixture of aqueous KOH (1.8 M; 30 mL) and diethyl ether (50 mL). The organic layer was separated, dried over $MgSO_4$, and the solvent removed under vacuum to give II as a pure white powder. Yield = 1.27 g, 56% overall. ^{1}H NMR ($CDCl_3$) δ: 1.30 (s, 18H), 1.46 (s, 18H), 3.93 (s, 4H), 6.97 (s, 2H), 7.26 (s, 2H). ^{13}C NMR ($CDCl_3$) δ: 29.8, 31.6, 34.2, 34.8, 51.4, 122.8, 123.5, 124.4, 135.9, 141.6, 152.6.

Compound III

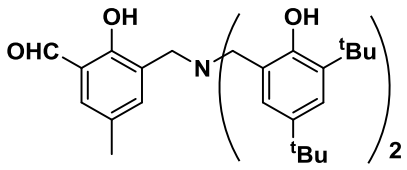

3-(Bromomethyl)-2-hydroxy-5-methylbenzaldehyde (I, 2.14 g, 9.4 mmol) was added dropwise to a solution of bis(3,5-di-tert-butyl-2-hydroxybenzyl)amine (II; 4.24 g, 9.4 mmol) and triethylamine (2.6 mL, 19 mmol) in THF (50 mL). The mixture was refluxed overnight and then filtered to remove the salt byproduct. After evaporation of solvent under vacuum, the crude product was isolated as pale yellow solid. Purification by flash column chromatography (10:1 mixture of hexanes:EtOAc) provided III as a pure solid. Yield = 3.0 g, 53%. ^{1}H NMR ($CDCl_3$) δ: 1.28 (s, 18H), 1.35 (s, 18H), 2.23 (s, 3H),

3.70 (s, 2H), 3.74 (s, 4H), 6.95 (d, J = 2.3 Hz, 2H), 7.08 (s, 1H), 7.19 (d, J = 2.3 Hz, 2H), 7.24 (s, 1H), 9.83 (s, 1H). ^{13}C NMR ($CDCl_3$) δ: 20.1, 29.6, 31.7, 34.1, 34.9, 52.8, 58.2, 120.2, 121.8, 123.5, 125.0, 125.9, 129.2, 133.3, 135.9, 140.1, 141.3, 152.3, 158.1, 196.7.

Ligand L_1H_3

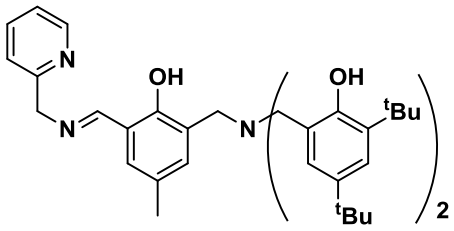

Modifying a published procedure,[165] 2-picolylamine (0.21 mL, 2.0 mmol) was added to a solution of compound III (1.2 g, 2.0 mmol) in methanol (20 mL). The mixture was refluxed overnight under argon, causing the color to change to yellow. Removal of solvent under vacuum provided L_1H_3 as yellow powder, which was used without further purification. Yield = 1.33 g, 96%. ^{1}H NMR ($CDCl_3$) δ: 1.27 (s, 18H), 1.34 (s, 18H), 2.19 (s, 3H), 3.73 (s, 2H), 3.77 (s, 4H), 5.00 (s, 2H), 6.87 (s, 1H), 6.94 (d, J = 2.3 Hz, 2H), 7.00 (s, 1H), 7.18 (d, J = 2.3 Hz, 2H), 7.29 (dd, J = 7.6, 5.0 Hz, 1H), 7.48 (d, J = 7.6 Hz, 1H), 7.80 (t, J = 7.6 Hz, 1H), 8.24 (br s, 3H, OH), 8.40(s, 1H), 8.61 (d, J = 5.0 Hz, 1H). ^{13}C NMR ($CDCl_3$) δ: 20.2, 29.6, 31.7, 34.1, 34.9, 54.0, 58.3, 63.9, 118.2, 122.0, 122.1, 122.7, 123.4, 124.9, 125.0, 127.8, 131.6, 135.5, 136.0, 138.0, 141.2, 148.4, 142.5, 157.6, 157.8, 167.3. FTIR (cm^{-1}, solid): 2951 (s), 2904 (m), 2866 (m), 1632 (m), 1590 (m).

General procedure for synthesis of [NiM(L_1)(μ-OAc)] complexes (NiM_B^{OAc}).

The L_1H_3 ligand (300 mg, 0.434 mmol) and three equivalents of NaOMe (70 mg, 1.3 mmol) were stirred in MeOH (10 mL) for 10 min, followed by addition of $Ni(OAc)_2 \cdot 4H_2O$ (108 mg, 0.434 mmol) and one equivalent of the appropriate $M_B(OAc)_2$ salt. The mixture was stirred overnight and the solvent removed under vacuum. The resulting solid was taken up in THF and filtered through Celite to remove sodium salts. Evaporation of solvent provided the crude solid. The methods used to grow crystals of the complexes are described below.

[NiFe(L_1)(μ-OAc)] ($NiFe^{OAc}$)

X-ray quality crystals were obtained from a 1:1 mixture of acetone:MeCN. Yield: 40%. Material for elemental analysis was purified by recrystallization in a 1:1 mixture of MeCN and MeOH. Anal. Calc. for $C_{49}H_{69}FeN_3NiO_7$ (M_w = 926.63 g mol^{-1}): C, 63.51; H, 7.51; N, 4.53. Found: C, 63.48; H, 7.36; N, 4.80%. UV–Vis [λ_{max}, nm (ε, M^{-1} cm^{-1}) in DMF]: 890 (18), 530 (1000). FTIR (cm^{-1}, solid): 2951 (s), 2902 (m), 2864 (m), 1621 (m), 1603 (m), 1573 (s, ν[CO_{OAc}]). μ_{eff} = 5.02 μ_B (Evans method, $CHCl_3$).

[NiCo(L_1)(μ-OAc)] ($NiCo^{OAc}$)

The crude solid was dissolved in a 1:1 mixture of MeCN and MeOH, which yielded orange crystals after several days. Yield: 60%. Anal. Calc. for $C_{49}H_{69}CoN_3NiO_7$ (M_W = 929.71 g mol^{-1}): C, 63.30; H, 7.48; N, 4.52. Found: C, 63.66; H, 7.43; N, 4.81. UV–Vis–NIR [λ_{max}, nm (ε, M^{-1} cm^{-1}) in DMF]: 1630 (6), 1050 (sh), 830 (7), 640 (sh),

580 (sh). FTIR (cm^{-1}, solid): 2951 (s), 2902 (m), 2864 (m), 1627 (w), 1605 (m), 1565 (s, $\nu[CO_{OAc}]$).μ_{eff} = 4.51 (solid state), 4.72 μ_B (Evans method, $CHCl_3$).

[$Ni_2(L_1)(\mu\text{-}OAc)$] ($NiNi^{OAc}$)

Yellow crystals were grown from a concentrated solution in 1:1 MeCN:MeOH. Yield: 36%. Anal. Calc. for $C_{49}H_{69}N_3Ni_2O_7$ (M_W = 929.47 g mol^{-1}): C, 63.32; H, 7.48; N, 4.52. Found: C, 62.52; H, 7.28; N, 4.84%. UV–Vis [λ_{max}, nm (ε, M^{-1} cm^{-1}) in DMF]: 866 (17), 740 (19), 500 (sh). FTIR (cm^{-1}, solid): 2951 (s), 2903 (m), 2864 (m), 1625 (m), 1605 (s), 1585 (s, $\nu[CO_{OAc}]$). μ_{eff} = 3.66 (solid state), 3.82 μ_B (Evans method, $CHCl_3$).

[$NiZn(L_1)(\mu\text{-}OAc)$] ($NiZn^{OAc}$)

The yellow solid was washed with cold MeOH, dissolved in CH_2Cl_2, and layered with MeOH to provide X-ray quality crystals. Yield: 45%. Anal. Calc. for $C_{49}H_{69}N_3NiO_7Zn$ (M_W = 936.16 g mol^{-1}): C, 62.87; H, 7.43; N, 4.49. Found: C, 62.67; H, 6.97; N, 4.62%. UV–vis [λ_{max}, nm (ε, M^{-1} cm^{-1}) in DMF]: 869 (8), 575 (4). FTIR (cm^{-1}, solid): 2951 (s), 2902 (m), 2863 (m), 1643 (m), 1604 (s), 1586 (s, $\nu[CO_{OAc}]$). μ_{eff} = 2.69 (solid state), 2.67 μ_B (Evans method, $CHCl_3$).

[$Co_2(L_1)(\mu\text{-}OAc)$] ($CoCo^{OAc}$)

Three equivalents of NaOMe (47 mg, 0.87 mmol) were added to a stirred solution of L_1H_3(200 mg, 0.29 mmol) in MeOH (10 mL). After 10 min, two equivalents of $Co(OAc)_2 \cdot 4H_2O$ (144 mg, 0.58 mmol) were added and the resulting mixture was stirred overnight. The solvent was evaporated under vacuum and the crude material dissolved in

THF (10 mL). After filtering through Celite to remove sodium salts, the THF solvent was evaporated to give a yellow solid that was taken up in a 1:1 mixture of MeCN:MeOH. X-ray-quality crystals appeared after a few days. Yield = 111 mg, 41%. Anal. Calc. for $C_{49}H_{69}Co_2N_3O_7$(M_W = 929.95 g mol^{-1}): C, 63.29; H, 7.48; N, 4.52. Found: C, 63.33; H, 7.40; N, 4.90%. UV–Vis–NIR [λ_{max}, nm (ε, M^{-1} cm^{-1}) in DMF]: 1585 (5), 920 (3), 660 (sh), 580 (sh), 530 (sh). FTIR (cm^{-1}, solid): 2952 (s), 2902 (m), 2865 (m), 1626 (w), 1602 (m), 1568 (s, $\nu[CO_{OAc}]$). μ_{eff} = 5.31 μ_B (Evans method, $CHCl_3$).

[NiZn(L_1)(μ-OH)] ($NiZn^{OH}$)

The L_1H_3 ligand (300 mg, 0.434 mmol) and three equivalents of NEt_3 (0.18 mL, 1.3 mmol) were dissolved in MeOH (10 mL), followed by addition of equimolar amounts of $Ni(ClO_4)_2$ $6H_2O$ (159 mg, 0.434 mmol) and $Zn(ClO_4)_2$ $6H_2O$ (162 mg, 0.434 mmol). After stirring for one hour, one equivalent of $(NEt_4)OH$ (0.434 mL, 1.0 M solution in MeOH) was injected, resulting in formation of a light brown precipitate. The solid was collected and washed with cold methanol to provide the crude product as a yellow powder. X-ray-quality crystals were grown by vapor diffusion of pentane into a concentrated 1,2-dichloroethane (DCE) solution. Yield = 162 mg, 40%. Anal. Calc. for $C_{45}H_{59}N_3NiO_4Zn$ ·DCE (M_W = 929.00 g mol^{-1}): C, 60.76; H, 6.84; N, 4.52. Found: C, 60.50; H, 7.02; N, 4.92%. UV–Vis [λ_{max}, nm (ε, M^{-1} cm^{-1}) in DMF]: 848 (18), 510 (sh). FTIR (cm^{-1}, solid): 2949 (s), 2903 (m), 2864 (m), 1626 (m), 1601 (m), 1553 (w).μ_{eff} = 1.43 (solid state), 2.53 μ_B (Evans method, $CHCl_3$).

$[Ni_2(L_1)(\mu\text{-}OCH_3)]$ ($NiNi^{OMe}$)

$Ni(ClO_4)_2$ $6H_2O$ (211 mg, 0.578 mmol) and triethylamine (121 mL, 0.867 mmol) were added to a solution of L_1H_3 (200 mg, 0.29 mmol) in 10 mL of MeOH. After one hour, a single equivalent of $(NEt_4)OH$ (0.29 mmol) was added. The mixture was stirred overnight, eventually giving rise to a dark yellow precipitate. The solvent was removed under vacuum, and the resulting solid was dissolved in THF. Insoluble salts were eliminated by filtration and the THF solvent was removed to yield the crude brown product. X-ray-quality crystals were grown from a concentrated 1:1 solution of MeCN:MeOH. Yield = 147 mg, 57%. Anal. Calc. for $C_{48}H_{69}N_3Ni_2O_6$ (M_W = 901.46 g mol^{-1}): C, 63.95; H, 7.72; N, 4.66. Found: C, 64.01; H, 7.68; N, 4.70%. UV–vis [λ_{max}, nm (ε, M^{-1} cm^{-1}) in DMF]: 890 (20), 760 (25). FTIR (cm^{-1}, solid): 2950 (s), 2902 (m), 2865 (m), 1634 (w), 1604 (m), 1573 (w). μ_{eff} = 3.77 μ_B (Evans method, $CHCl_3$).

Crystallographic studies. X-ray diffraction (XRD) data were collected at 100 K with an Oxford Diffraction SuperNova kappa-diffractometer (Agilent Technologies) equipped with dual microfocus Cu/Mo X-ray sources, X-ray mirror optics, Atlas CCD detector, and low-temperature Cryojet device. The data were processed with the CrysAlis Pro package of programs (Agilent Technologies, 2011), followed by an empirical multi-scan correction using the SCALE3 ABSPACK routine. Structures were solved using the SHELXS program and refined with SHELXL in combination with the Olex2

crystallographic package.[166,167] In most cases, hydrogen atoms were localized in difference syntheses of electron density but were refined using appropriate geometric restrictions of the corresponding bond lengths and bond angles within a riding/rotating model. X-ray crystallographic parameters are provided in **Table 4.1** and experimental details are available in the corresponding CIFs.

4.3. Results and discussion

4.3.1. Ligand and complex syntheses

The novel **L_1H_3** ligand was prepared in four steps via the route shown in **Scheme 4.3**. As demonstrated by Belostotskaya et al,[164] the Duff-like reaction of 2,4-di-tert-butylphenol with hexamethylenetetramine in HCO_2H generates a benzoxazine intermediate that is converted to bis(3,5-di-tert-butyl-2-hydroxybenzyl)amine (**II**) in ethylene glycol and HCl. Bromomethylation of 5-methylsalicylaldehyde provided compound **I**, which participated in a substitution reaction with compound **II** under basic conditions to generate compound **III** in 53% yield. In the final step, the Schiff base and pyridyl donors of L_1H_3 were incorporated by condensation of 2-picolylamine with the aldehyde moiety of compound **III**.

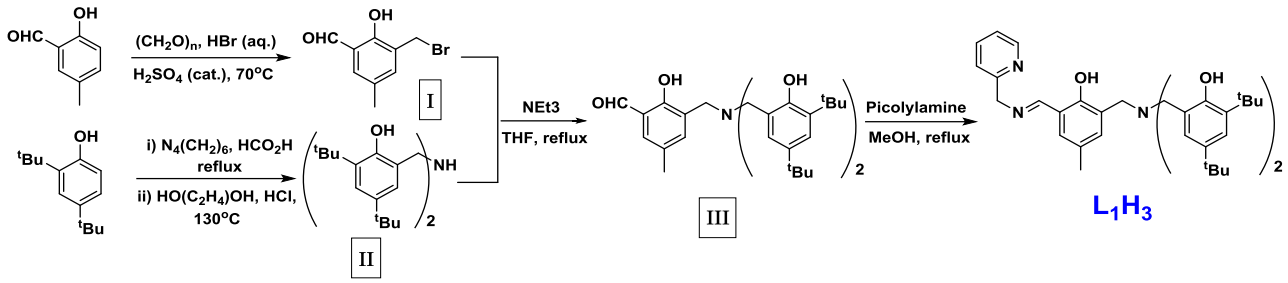

Scheme 4.3 Route of synthesis of ligand $\mathbf{L_1H_3}$

The homo- and heterobimetallic complexes NiM_B^{OAc} (**Scheme 4.2**) were prepared by mixing equimolar amounts of $\mathbf{L_1H_3}$, $Ni(OAc)_2 \cdot 4H_2O$, and the appropriate $M(OAc)_2$ salt in MeOH (M^B = Fe, Co, Ni, or Zn). Three equivalents of base (NaOMe) were required to deprotonate the phenolic groups of $\mathbf{L_1H_3}$. The resulting complexes are soluble in CH_2Cl_2 and most polar aprotic solvents, but only sparingly soluble in MeOH. High-quality crystals were generally obtained from solvent mixtures involving MeOH and either CH_2Cl_2 or MeCN; the single exception was complex $NiFe^{OAc}$, which was crystallized from a 1:1 combination of acetone and MeCN.

Similar reaction conditions were used to generate the μ-OH complex, $NiZn^{OH}$, with three crucial differences: (i) the M^{II} ions were added as perchlorate salts, (ii) triethylamine (NEt_3) was used to deprotonate L_1H_3, and (ii) a single equivalent of $(NEt_4)OH$ was added to supply the bridging ligand and induce precipitation. X-ray quality crystals of $NiZn^{OH}$were obtained by vapor diffusion of pentane into a concentrated DCE solution. The same approach was used in our attempts to prepare the corresponding dinickel(II) complex (i.e.,$NiNi^{OH}$), yet we were not able to grow suitable

crystals from mixtures of DCE (or DCM) and pentane. X-ray quality crystals were obtained, however, from a mixture of MeCN and MeOH. The resulting structure (vide infra) revealed that the Ni^{II} centers are bridged by a solvent-derived methoxide ligand instead of the intended hydroxide group, giving rise to complex $NiNi^{OMe}$. This result indicates that the μ-OH ligand of NiM_B^{OH} is readily exchanged with $^{-}OCH_3$ in methanolic solution.

4.3.2. Crystallographic studies

Solid-state structures of the homo- and heterobimetallic complexes were collected using X-ray diffraction. Details concerning the crystallographic experiments and structure refinements are provided in **Table 4.1**. Complexes $NiCo^{OAc}$, $NiNi^{OAc}$, and $NiZn^{OAc}$ yield quasi-isomorphous crystals in the monoclinic $P2_1/n$ space group, whereas complex $NiFe^{OAc}$ crystallizes in the non-centrosymmetric $P2_1$ group. The structure of $NiZn^{OAc}$, shown in **Figure 4.1**, is representative of the entire series. In each case, the trianionic L_1^{3-} ligand supports a bimetallic core in which the metal centers are bridged by two donors: the central phenolate of L_1^{3-} (O1) and a μ-1,1-acetate group (O4). The complexes are neutral overall due to the presence of the acetate ligand. As intended, the Ni^{II} center occupies the "tetragonal" position (site A) defined by the Schiff-base (N2) and pyridyl (N3) donors in addition to the two bridging groups. Two solvent-derived ligands, either MeOH or H_2O, bind to Ni in a *trans* orientation. The M_B^{II} ion is located in the "tripodal"

five-coordinate position (site B) attached to the amino donor (N1) and two terminal phenolates (O2 and O3).

Table 4.1 Summary of X-ray crystallographic data collection and structure refinement.

	NiFeOAc·4 acetone	NiCoOAc	NiNiOAc	NiZnOAc	CoCoOAc
Empirical formula	C59H89FeN3NiO11	C49H69CoN3NiO7	C49H69N3Ni2O7	C49H69N3NiO7Zn	C49H69Co2N3O7
Formula weight	1130.89	929.71	929.49	936.15	929.93
Crystal system	monoclinic	monoclinic	monoclinic	monoclinic	monoclinic
Space group	P21	P21/n	P21/n	P21/n	P21/n
a (Å)	10.3503(2)	10.21448(8)	10.1841(1)	10.2153(1)	10.2249(2)
b (Å)	20.2208(3)	20.4809(2)	20.5261(3)	20.4672(3)	20.6272(3)
c (Å)	15.6385(3)	22.7461(3)	22.8062(4)	22.7709(3)	22.7256(4)
α (°)	90	90	90	90	90
β (°)	107.257(2)	97.7635(9)	98.208(1)	97.818(1)	97.741(2)
γ (°)	90	90	90	90	90
V (Å3)	3125.7(1)	4714.90(8)	4718.6(1)	4716.7(1)	4749.0(1)
Z	2	4	4	4	4
Dcalc (g/cm3)	1.202	1.31	1.308	1.318	1.301
λ (Å)	0.7107	1.5418	0.7107	1.5418	0.7107
μ (mm−1)	0.589	3.67	0.851	1.539	0.751
θ-Range (°)	5.6–59.0	7.8–147.2	5.7–58.9	5.8–147.8	5.6–59.0
Reflections collected	36415	45296	40517	45332	38008
Independent reflections (Rint)	14 441 (0.0338)	9423 (0.0284)	11 527 (0.0312)	9435 (0.0312)	11 671 (0.0289)
Data/restraints/parameters	14441/7/714	9423/0/574	11527/0/574	9435/0/574	11671/0/574
Goodness-of-fit (GOF) on F2	1.042	1.041	1.067	1.023	1.033
R1/wR2 (I > 2σ(I))[a]	0.0359/0.0768	0.0389/0.1097	0.0383/0.0880	0.0339/0.0924	0.0365/0.0878
R1/wR2 (all data)[a]	0.0422/0.0813	0.0430/0.1132	0.0485/0.0936	0.0392/0.0965	0.0475/0.0946

[a] $R1 = \sum||Fo|-|Fc||/\sum|Fo|$; $wR2 = [\sum w(Fo2-Fc2)2/\sum w(Fo2)2]1/2$

Table 4.1 (continued) Summary of X-ray crystallographic data collection and structure refinement.

	NiZnOH·DCE	NiNiOMe·MeOH
Empirical formula	C47H63N3Ni2O4Cl2Zn	C49H73N3Ni2O7
Formula weight	928.98	933.52
Crystal system	monoclinic	monoclinic
Space group	P21/c	P21/c
a (Å)	14.4458(3)	20.8266(6)
b (Å)	19.0800(2)	13.0162(3)
c (Å)	17.1363(2)	18.9697(4)
α (°)	90	90
β (°)	106.356(2)	110.255(3)
γ (°)	90	90
V (Å3)	4532.0(1)	4824.4(2)
Z	4	4
Dcalc (g/cm3)	1.362	1.285
λ (Å)	1.5418	1.5418
μ (mm−1)	2.606	1.378
θ-Range (°)	7.1–147.6	8.2–147.2
Reflections collected	43809	45182
Independent reflections (Rint)	9000 (0.0357)	9558 (0.0416)
Data/restraints/parameters	9000/5/559	9558/0/579
Goodness-of-fit (GOF) on F2	1.031	1.043
R1/wR2 (I > 2σ(I)) a	0.0324/0.0847	0.0413/0.1137
R1/wR2 (all data) a	0.0375/0.0888	0.0482/0.1212

[a] $R1 = \sum||Fo|-|Fc||/\sum|Fo|$; $wR2 = [\sum w(Fo2-Fc2)2/\sum w(Fo2)2]1/2$

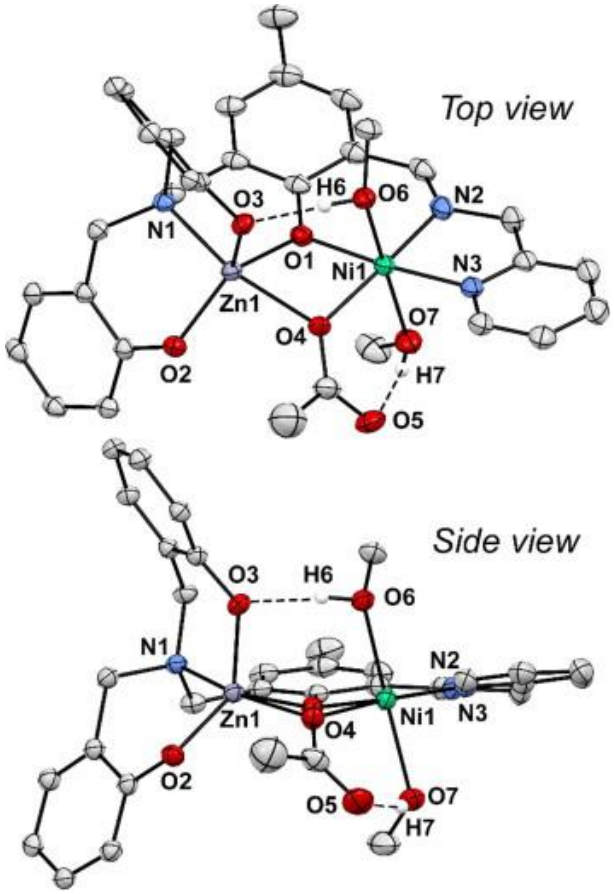

Figure 4.1 Thermal ellipsoid plots (50% probability) derived from the X-ray structure of $NiZn^{OAc}$. Most hydrogen atoms and the tert-butyl substituents of the terminal phenolate donors have been removed for clarity.

Metal ion assignments were established by comparing R-factors and thermal parameters for the four possible configurations (two homobimetallic and two heterobimetallic). For complexes $NiFe^{OAc}$ and $NiZn^{OAc}$, the experimental data strongly support the metal ion identities and positions indicated in **Scheme 4.2**; however, in the case of $NiCo^{OAc}$, replacement of Co for Ni (or vice versa) causes little change in R-factor. We therefore synthesized the analogous dicobalt(II) complex, $CoCo^{OAc}$. **Table 4.2** provides a quantitative comparison of bond distances and angles in

the $NiNi^{OAc}$, $CoCo^{OAc}$, and $NiCo^{OAc}$ structures. The three complexes have identical ligand sets and quasi-isomorphous unit cells; thus, any structural differences must be due to the presence of different metal ions in the A and B sites. The B-site metric parameters in the $CoCo^{OAc}$ structure are nearly identical to those observed for $NiCo^{OAc}$, with root-mean-square (rms) deviations of merely 0.007 Å and 0.36 ° for metal–ligand bond distances and angles, respectively. In contrast, the B-sites in the $NiNi^{OAc}$ and $NiCo^{OAc}$ structures are significantly different (**Table 4.2**); in particular, the Ni2–N1 and Ni2–O4 distances are shorter in $NiNi^{OAc}$ by ∼0.06 Å, and the O1–M_B–O2 and O1–M_B–O3 angles shift by ∼5 °. Thus, it is clear that the B-site in $NiCo^{OAc}$ is occupied by Co^{II}. For site A, the $NiCo^{OAc}$ structure more closely matches $NiNi^{OAc}$ than $CoCo^{OAc}$ with respect to both bond lengths and angles (**Table 4.2**). We are confident, therefore, that the $NiCo^{OAc}$ structure corresponds to a heterobimetallic complex with Ni^{II} in site A and Co^{II} in site B.

Table 4.2 Root-mean-square Deviations in Metal–Ligand Bond Distances (Å) and Angles (deg) for the A- and B-Sites within the **NiCo**^{OAc}, **CoCo**^{OAc}, and **NiNi**^{OAc} Structures.

	rms deviation from **NiCo**^{OAc} structure		
		Site **A**	Site **B**
NiNi^{OAc}	bond distances (Å)	0.014	0.04
	bond angles (°)	1.14	2.54
CoCo^{OAc}	bond distances (Å)	0.0349	0.0066
	bond angles (°)	1.58	0.36

As shown in **Table 4.3**, metric parameters for structures in the NiM_B^{OAc} series exhibit little variation across the series. The presence of two monoatomic bridges results in short $Ni_A\cdots M_B$ distances of 3.12 ± 0.02 Å and average bridge angles ($Ni–O–M^B$) of 97 °. The $Ni\cdots M_B$ distance is also reduced by the "puckering" of the [$Ni–O(1/4)–M_B$] diamond core, which deviates from planarity by nearly 19 °. Each axial solvent ligand serves as an intramolecular hydrogen bond (H-bond) donor: one to the terminal phenolate group (O3), the other to the non-coordinating carbonyl moiety (O5) of acetate (**Figure 4.1**). These interactions are facilitated by the aforementioned puckering of the central core, which tilts the phenolate acceptor (O3) towards the H6–O6 donor of the proximal MeOH (or H_2O).

In the NiM_B^{OAc} series, the Ni_A^{II} center exists in a distorted octahedral environment with trans angles of 174 ± 3 ° and cis angles ranging between 82 ° and 98 °. The average nickel-ligand bond distance is 2.03 Å in the equatorial plane and 2.12 Å in the axial direction, consistent with the presence of a high-spin (S = 1) center. This conclusion is corroborated by the solid-state magnetic moment (μ_{eff}) of 2.69 μ_B measured for $NiZn^{OAc}$. The coordination geometries of the M_B centers are best described as trigonal–bipyramidal, as indicated by τ-values greater than 0.50 (τ = 0 for an ideal square-pyramid and 1 for an ideal trigonal bipyramid; **Table 4.3**).[168] The amino (N1) and acetate (O4) donors occupy the axial positions, while the phenolate donors (O1–O3) constitute the equatorial plane. For each complex, the M_B–L distances display considerable variability,

ranging from 1.96(3) Å for the terminal phenolates to 2.17(4) Å for the axial M_B–O4 bond. The average M_B–L distance of ~2.05 Å, however, suggests that each M_B^{II} ion in the NiM_B^{OAc} series is high-spin. Indeed, the magnetic moment of 4.51 μ_B measured for solid$NiCo^{OAc}$ is close to the spin-only value of 4.80 μ_B expected for a molecule with uncoupled S = 1 and S = 3/2 centers.

Table 4.3 Selected Bond Distances (Å) and Bond Angles (deg) for NiM_B^{OAc} Complexes (M_B = Fe, Co, Ni, Zn) and $NiNi^{OMe}$ Measured with X-ray Diffraction.

Bond distances	$NiFe^{OAc}$	$NiCo^{OAc}$	$NiNi^{OAc}$	$NiZn^{OAc}$	$NiNi^{OMe}$
Ni(1)···MB(1)	3.1165(4)	3.0960(5)	3.1210(3)	3.1329(4)	3.0744(4)
Ni(1)–N(2)	1.976(2)	1.981(2)	1.979(2)	1.976(2)	2.014(2)
Ni(1)–N(3)	2.072(2)	2.058(2)	2.053(2)	2.055(2)	2.085(2)
Ni(1)–O(1)	2.030(2)	2.032(1)	2.007(1)	2.025(1)	2.030(1)
Ni(1)–O(4)	2.042(2)	2.031(2)	2.047(1)	2.037(1)	1.977(1)
Ni(1)–O(6)	2.117(2)	2.116(2)	2.100(1)	2.107(1)	2.124(2)
Ni(1)–O(7)	2.119(2)	2.129(2)	2.134(2)	2.130(1)	2.128(1)
MB(1)–N(1)	2.154(2)	2.094(2)	2.035(2)	2.095(1)	2.072(2)
MB(1)–O(1)	2.116(2)	2.054(2)	2.070(1)	2.108(1)	2.059(1)
MB(1)–O(2)	1.943(2)	1.940(1)	1.945(1)	1.933(1)	2.001(1)
MB(1)–O(3)	1.983(2)	1.950(1)	1.959(1)	1.959(1)	1.999(1)
MB(1)–O(4)	2.196(2)	2.199(1)	2.134(1)	2.174(1)	1.980(1)
Bond-angles					
Ni(1)–O(1)–MB(1)	97.46(6)	98.53(6)	99.90(6)	98.57(5)	97.50(6)
Ni(1)–O(4)–MB(1)	94.62(6)	94.02(6)	96.55(6)	96.07(5)	101.97(6)
O(1)–MB(1)–O(2)	126.06(6)	129.00(6)	134.74(6)	129.11(5)	104.14(6)
O(1)–MB(1)–O(3)	109.43(6)	110.52(6)	105.88(6)	108.73(5)	136.31(6)
O(1)–MB(1)–O(4)	78.36(6)	78.48(5)	77.38(5)	77.02(5)	77.76(6)
O(1)–MB(1)–N(1)	88.03(6)	90.34(6)	90.05(6)	89.06(5)	89.21(6)
O(2)–MB(1)–O(3)	124.44(7)	119.85(6)	118.29(6)	121.23(5)	119.26(6)
O(2)–MB(1)–O(4)	97.42(6)	95.17(5)	95.03(5)	95.33(5)	92.65(6)
O(2)–MB(1)–N(1)	93.72(6)	95.15(6)	96.63(6)	96.83(5)	92.66(6)
O(3)–MB(1)–O(4)	90.50(6)	87.96(6)	86.73(5)	87.31(5)	94.56(6)
O(3)–MB(1)–N(1)	90.38(6)	92.12(6)	93.09(6)	93.22(5)	93.39(6)
O(4)–MB(1)–N(1)	165.84(6)	168.05(6)	166.84(6)	165.43(5)	166.78(6)
τ-value [a]	0.66	0.65	0.54	0.61	0.51

[a] For a definition of the τ-value, five-coordinate complexes with ideal square-pyramidal geometries have τ-values of 0.0, and those with ideal trigonal–bipyramidal geometries have values of 1.0.

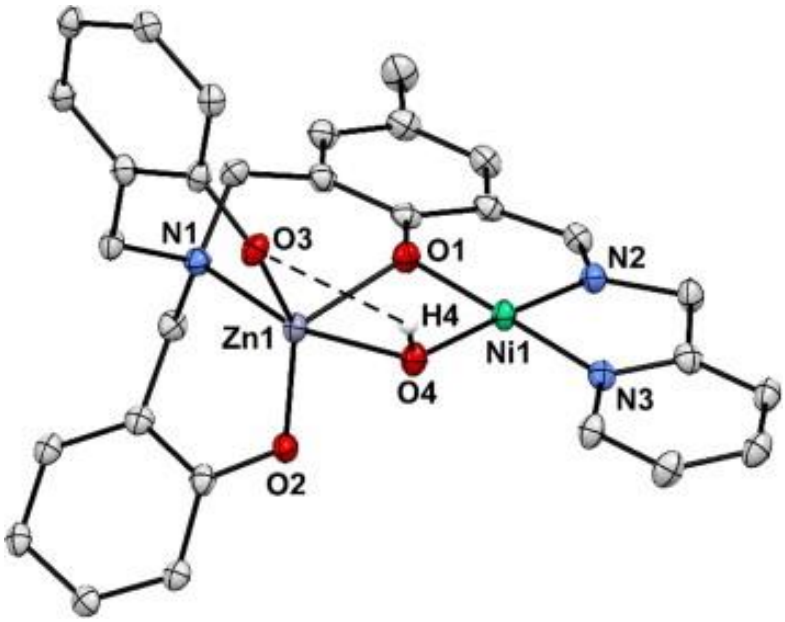

Figure 4.2 Thermal ellipsoid plot (50% probability) derived from the X-ray structure of $NiZn^{OH}$. The non-coordinating DCE molecule, most hydrogen atoms, and the tert-butyl substituents of the terminal phenolate donors have been removed for clarity. Selected bond lengths (Å): Ni1Zn1 2.9967(4), Ni1–O1 1.844(1), Ni–1O4 1.859(1), Ni1–N2 1.841(2), Ni1–N3 1.870(2), Zn1–O1 2.127(1), Zn1–O2 1.950(1), Zn1–O3 1.964(1), Zn1–O4 2.054(1), Zn1–N1 2.138(1).

The X-ray structure of $NiZn^{OH}$, shown in **Figure 4.2**, reveals a heterobimetallic [Ni(μ-OH)Zn] core supported by the L_1^{3-} chelate. The μ-OH ligand forms an intramolecular H-bond with the O3 atom of a terminal phenolate donor. While the $ZnNO_4$ units in $NiZn^{OH}$ and $NiZn^{OAc}$ display similar metric parameters, the geometries of the Ni_A^{II} sites are quite different in the two structures. Since crystals of $NiZn^{OH}$ were obtained from DCE/pentane, this structure lacks the solvent-derived ligands found in the NiM_B^{OAc} series. The Ni_A center of $NiZn^{OH}$ adopts a four-coordinate geometry with Ni_A–O/N bond lengths of 1.85 ± 0.02 Å – approximately 0.17 Å shorter than the

corresponding distances in the $NiZn^{OAc}$ structure. These parameters suggest that the Ni_A^{II} center in $NiZn^{OH}$ is low-spin (S = 0), consistent with its square-planar coordination environment. However, the magnetic moment of $NiZn^{OH}$ powder is 1.43 μ_B at room temperature, nearly half-way between the spin-only limits of 0.0 (S = 0) and 2.83 μ_B (S = 1). Thus, it appears that a mixture of high- and low-spin Ni_A^{II} centers exist in the solid state. Regardless, in the $NiZn^{OH}$ structure, the short Ni_A–O(1/4) distances bring the two metal centers closer together, resulting in a $Ni_A\cdots Zn_B$ distance of slightly less than 3.0 Å.

As noted above, our attempts to isolate the dinickel(II) analog of $NiZn^{OH}$ were unsuccessful; however, X-ray quality crystals of $NiNi^{OMe}$ can be grown by dissolving the putative $NiNi^{OH}$ complex in a mixture of MeOH and MeCN. In the resulting structure, the second bridging position is occupied by methoxide (**Scheme 4.2**), but otherwise the geometry of $NiNi^{OMe}$ is quite similar to that of $NiNi^{OAc}$ (**Figure 4.3**). In both cases, the binding of solvent-derived MeOH ligands gives rise to a six-coordinate, high-spin Ni_A^{II} center. A comparison of metric parameters reveals only minor differences between the two structures, although the Ni–OMe bond distances are noticeably shorter than the Ni–OAc distances (**Table 4.3**). Interestingly, whereas the $NiNi^{OAc}$ structure features two intramolecular H-bonds, the replacement of acetate with methoxide forces one of the MeOH ligands to form an intermolecular H-bond with an outersphere MeOH molecule.

This solvate, in turn, serves as an H-bond donor to the phenolate moiety of a second NiNi^{OMe} complex (**Figure 4.3**).

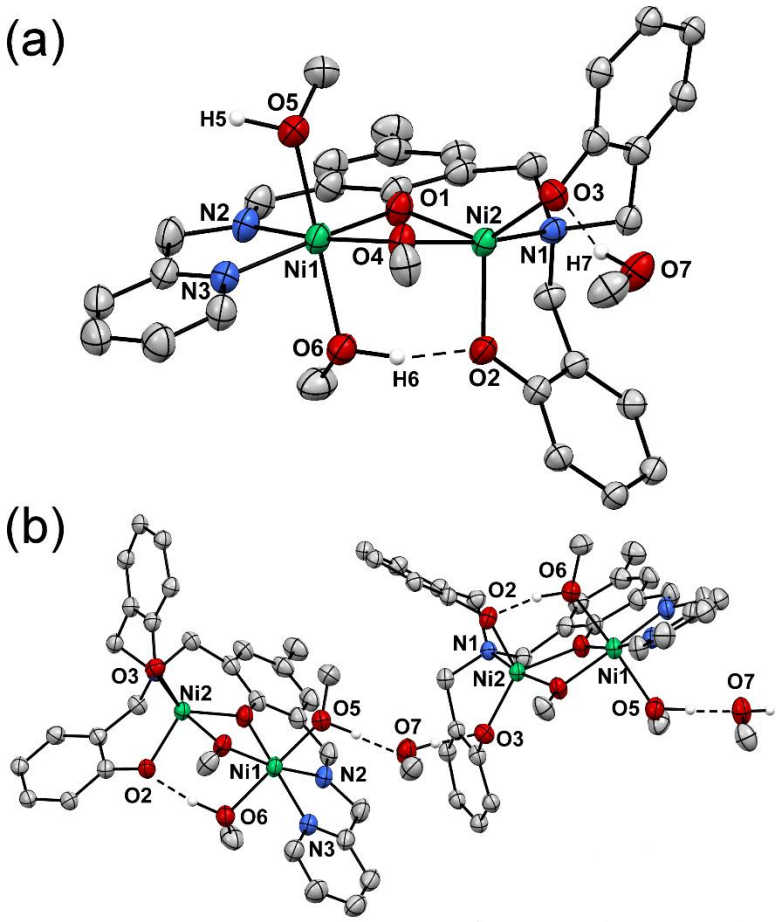

Figure 4.3. Thermal ellipsoid plots (50% probability) derived from the X-ray structure of **NiNi^{OMe}**. Most hydrogen atoms and the *tert*-butyl substituents of the terminal phenolate donors have been removed for clarity. (a) shows only the **NiNi^{OMe}** unit, while (b) displays the two hydrogen-bonds formed by each MeOH solvate: O(5)–H···O(7) and O(7)–H···O(3).

4.3.3. Magnetic, Spectroscopic, and Electrochemical Properties in Solution

The magnetic moments of the NiM_B^X complexes in $CHCl_3$ solutions were determined using the Evans NMR method.[169] The $NiZn^X$ complexes exhibit μ_{eff} values of 2.67 (X = OAc) and 2.53 μ_B (X = OH), characteristic of S = 1 complexes. Thus, in contrast to its solid-state structure, the Ni^{II} center in $NiZn^{OH}$ is unambiguously high-spin in solution, even in a non-coordinating solvent like $CHCl_3$. For complexes with two paramagnetic centers, the following values were measured: μ_{eff} = 3.82 ($NiNi^{OAc}$), 3.77 ($NiNi^{OMe}$), 4.72 ($NiCo^{OAc}$), and 5.02 μ_B ($NiFe^{OAc}$). These experimental magnetic moments are slightly lower than the theoretical spin-only values expected for uncoupled paramagnets, indicating the presence of weak magnetic interactions between the metal centers.

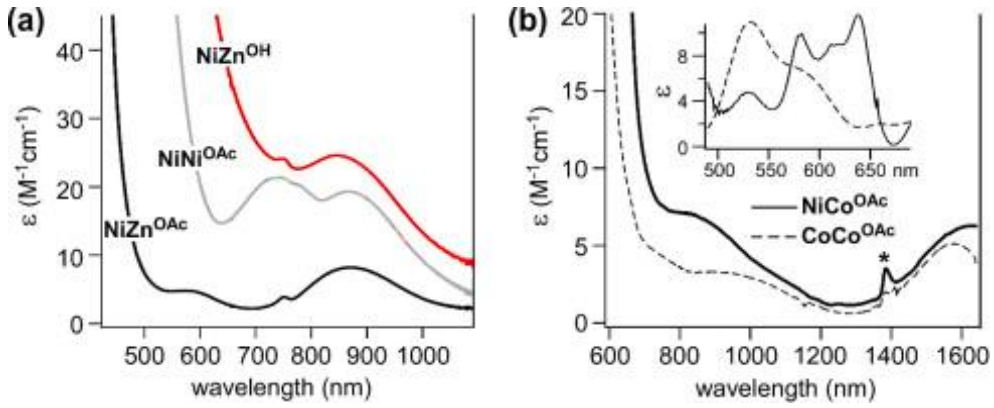

Figure 4.4 Electronic absorption spectra of select $M_AM_B^X$ complexes measured at room temperature in DMF. The baselines of the $NiNi^{OAc}$ and $NiZn^{OH}$ spectra were shifted upward slightly to enhance clarity. The modified spectra shown in the inset of (b) were obtained via electronic subtraction of the broad absorption feature that trails into the visible region

UV–Vis absorption spectra of the reported NiM_B^X complexes were measured in DMF at room temperature; select data are shown in **Figure 4.4**. Typical for complexes with high-spin Ni^{II} centers, the $NiZn^{OAc}$ spectrum displays two bands in the visible region at 870 and 575 nm (ε = 8 M^{-1} cm^{-1}) arising from the $^3A_{2g} \rightarrow {}^3T_{2g}$ and $^3A_{2g} \rightarrow {}^3T_{1g}(F)$ transitions, respectively.[121] In addition, the spin-forbidden $^3A_{2g} \rightarrow {}^1E_g$ transition is evident at 750 nm. Complex $NiZn^{OH}$ exhibits ligand-field transitions at similar energies, although the higher-energy band is obscured by features attributed to μ-OH → Ni^{II} charge transfer (CT) transitions. Analysis of transition energies in the $NiZn^{OAc}$ spectrum yields a ligand-field splitting (Δ_o) of 11500 cm^{-1} and Racah parameters of B = 730 cm^{-1} and C = 3870 cm^{-1} (the free ion B-value is 1030 cm^{-1}). These parameters are characteristic of six-coordinate Ni^{II} ions with partial pyridyl coordination.[170] In the $NiNi^{OAc}$ spectrum, an "extra" ligand-field band arising from the second Ni^{II} center is apparent at 740 nm (**Figure 4.4(a)**).

As shown in **Figure 4.4(b)**, both $NiCo^{OAc}$ and $CoCo^{OAc}$ exhibit two bands in the near infrared (NIR) region with λ_{max} = ~1600 and 1050 nm. As the $NiZn^X$ spectra are featureless in this region, these band must arise from the Co^{II} center in the five-coordinate B-site. In addition, multiple Co^{II}-derived features appear as shoulders in the 500–650 nm region of the $NiCo^{OAc}$ and $CoCo^{OAc}$ spectra. These peaks are clearly evident in the inset of **Figure 4.4(b)**, where the broad absorption manifold that trails into the visible region has been removed (electronically) to provide a level baseline.[171] In order to

assign these features, we have built upon the ligand-field approach developed by Ciampolini et al. in their seminal study of M^{II} ions in trigonal bipyramidal complexes.[172] Assuming approximate D_{3h} geometry, the 3d orbitals split into three levels: E″(d_{xz}, d_{yz}), E'(d_{xy}, $d_{x^2-y^2}$) and $A_1'(d_{z^2})$, listed in order of increasing energy. The conversion from O_h to pseudo-D_{3h} symmetry causes the T_{1g} and T_{2g} states to split into two components, as shown in **Figure 4.5**. The ground state term symbol for high-spin d^7 ions is $^4A_2'$. Using this figure, the band near 1600 nm (6250 cm^{-1}) can be assigned to the $^4A_2' \rightarrow {}^4E''(F)$ transition that, in the strong field limit, corresponds to promotion of an E″(d_{xz}, d_{yz}) electron to the E′(d_{xy}, $d_{x^2-y^2}$) orbitals. The band at 1050 nm then arises from the $^4A_2' \rightarrow {}^4E'(F)$ transition, and the two peaks at 640 and 580 nm spectrum are assigned to $^4A_2' \rightarrow {}^4A_2'(P)$ and $^4A_2' \rightarrow {}^4E''(P)$ transitions, respectively (these features appear in both spectra at roughly the same wavelengths). The weak peak at 610 nm in the $NiCo^{OAc}$ spectrum is tentatively assigned to the spin-forbidden $^4A_2' \rightarrow {}^2A_1'(G)$ transition, which gains intensity from the nearby spin-allowed transitions.

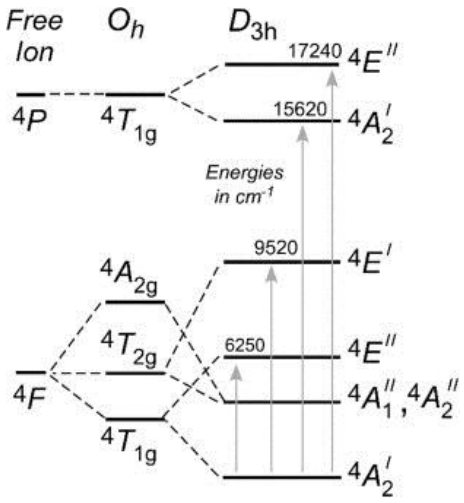

Figure 4.5 Energy level diagram indicating the ligand-field states for a high-spin d7 ion in three coordination environments: free ion, octahedral (O_h), and trigonal– bipyramidal (D_{3h}). The experimentally-determined transition energies for the Co^{II} ion in $NiCo^{OAc}$ are provided in wavenumbers (cm^{1-}). Partially adapted from reference[162].

Analysis of the $CoCo^{OAc}$ spectrum is more complex due to the presence of a second Co^{II} center in the A-site. Based on spectra reported for six-coordinate high-spin Co^{II} complexes,[170] the prominent band at 530 nm (18 870 cm^{-1}) is assigned to the $^4T_{1g}(F) \rightarrow {}^4T_{1g}(P)$ transition, while the corresponding $^4T_{1g}$ (F) $\rightarrow {}^4T_{2g}(F)$ transition (generally quite weak) is likely part of the broad absorption manifold centered at 1000 nm (**Figure 4.4(b)**). Interestingly, the $NiCo^{OAc}$ spectrum also exhibits a band at 530 nm, although its intensity is much lower. This result suggests that our $NiCo^{OAc}$ sample is contaminated with a small amount of $CoCo^{OAc}$ – a possibility previously considered in our analysis of the XRD data (vide supra).

The electrochemical properties of representative $M_AM_B^{OAc}$ complexes were examined by voltammetric methods in DMF solutions with 0.1 M $(NBu_4)PF_6$ as the

supporting electrolyte and scan rates of 100 mV/s. As shown in **Figure 4.6**, the cyclic voltammogram (CV) of $NiZn^{OAc}$ displays a quasi-reversible redox couple at −1.17 V (ΔE = 0.20 V) that corresponds to one-electron reduction of the Ni_A^{II} center (all potentials are relative to SCE). The CV's of $NiNi^{OAc}$ and $NiCo^{OAc}$ also feature a cathodic wave at −1.17 V due to the Ni ion in the A-site, but a second peak from the redox-active M_B^{II} ion is also apparent at more negative potentials (−1.36 V for $NiNi^{OAc}$ and 1.45 V for $NiCo^{OAc}$). These redox event are very evident in the corresponding square-wave voltammograms (SWVs), represented by the dotted lines in **Figure 4.6**. The $NiNi^{OAc}$ data indicate that the $Ni^{2+/+}$potential is ∼0.20 V lower in the B-site than the A-site, on account of the two terminal phenolate donors in the former. Interestingly, the CV and SWV data for $CoCo^{OAc}$ exhibit a single cathodic feature at −1.44 V with approximately twice the amount of those observed for $NiCo^{OAc}$, suggesting that the two Co^{II} ions are reduced at nearly identical potentials.

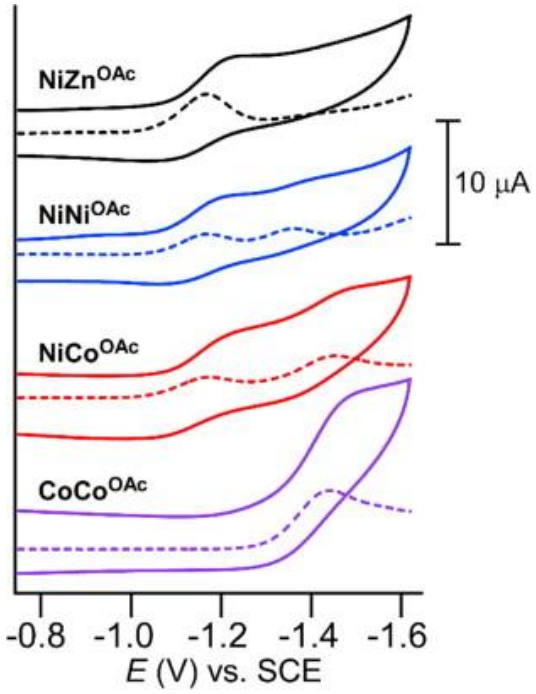

Figure 4.6 Cyclic voltammograms (solid lines) of $NiZn^{OAc}$, $NiNi^{OAc}$, $NiCo^{OAc}$, and $CoCo^{OAc}$ collected in DMF with 0.1 M $(NBu_4)PF_6$ as the supporting electrolyte and scan rates of 100 mV/s. The corresponding square-wave voltammograms are indicated by the dashed lines. In all cases the voltammogram was initiated by the cathodic sweep. The solution concentrations were 2.0 mM.

The $M_AM_B^{OAc}$ complexes are also susceptible to irreversible oxidations, as indicated by the electrochemical data in **Figure 4.7**; however, these anodic features are less well-defined than their cathodic counterparts, especially in the case of $NiZn^{OAc}$. Complexes containing a redox-active M_B ion–$NiNi^{OAc}$, $NiCo^{OAc}$, and $CoCo^{OAc}$ – each display an irreversible peak near 0.30 V that is assigned to one-electron oxidation of the M_B^{II} center. An additional irreversible feature is evident near 0.75 V that, based on literature precedents,[173-175] likely arises from oxidation of one (or more) of the phenolate groups in L_1^{3-} to give a phenoxyl radical species.

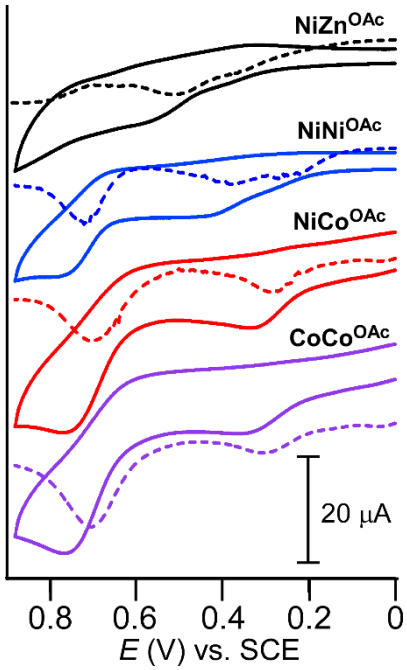

Figure 4.7 Cyclic voltammograms (solid lines) of **NiZn^{OAc}**, **NiNi^{OAc}**, **NiCo^{OAc}**, and **CoCo^{OAc}** collected in DMF with 0.1 M $(NBu_4)PF_6$ as the supporting electrolyte and scan rates of 100 mV/s. The corresponding square-wave voltammograms are indicated by the dashed lines. In all cases the voltammogram was initiated by the anodic sweep. The solution concentrations were 2.0 mM.

4.4 Conclusions

In this chapter, we have described the synthesis and coordination chemistry of a new unsymmetric ligand (L_1H_3) designed to support heterobimetallic structures. The Schiff-base and pyridyl donors of the tetragonal A-site favor Ni^{II} binding, while the phenolate donors of the tripodal B-site are capable of coordinating various M^{II} ions (M = Fe, Co, Ni, Zn). In the X-ray crystal structures of the resulting $M_AM_B^X$ complexes, the two M^{II} centers are bridged by the central phenolate donor of L_1^{3-} and an X anion,

where X = μ-1,1-OAc, –OH, or –OCH_3. With the exception of the Ni_A^{II} center in the solid-state structure of$NiZn^{OH}$, the M^{II} ions in both coordination sites are high-spin, as determined by detailed analyses of structural parameters, UV–Vis–NIR absorption spectra, and magnetic susceptibility measurements. The Ni_A^{II} centers undergo one-electron reduction at −1.17 V (versus SCE), while the Ni_B^{II} and Co_B^{II} ions are reduced at lower potentials.

As stated in the Introduction, our efforts were inspired by the active site of CODH, which utilizes a NiFe1 unit and a nearby [Fe_3S_4] cluster to reversibly reduce CO_2 to CO and H_2O. The bimetallic complexes described here reproduce several key features of the Ni–Fe1 fragment in CODH. Similar to enzymatic active site, the NiM_B^X complexes position a redox-active Ni^{II} center in close proximity to a second transition metal; indeed, the $Ni_A\cdots M_B$ distances of 3.0 - 3.1 Å observed in the NiM_B^X series are close to the average Ni-Fe1 distance of ∼2.8 Å found in CODH.[143] It is our intention that the M^B ion will facilitate CO_2 activation by serving as a Lewis acid and (perhaps) a source of reducing equivalents; thus, the B-site contains three phenolate anions to depress the M_B redox potential. The Ni center in CODH has three "permanent" ligands: the thiolate of Cys526 and two sulfides from the [Fe_3S_4] cluster (**Scheme 4.1**). Likewise, the Ni_A^{II} centers are bound to only three L_1-derived donors, thereby providing three exchangeable coordination sites in a meridional arrangement. The presence of cis-labile sites is expected to be advantageous for CO_2 binding and activation, since studies

of CODH suggest that the energetic barrier to C–O bond cleavage (typically the rate-determining step) is lowered[176] if the resulting hydroxide is able to adopt a bridging position between two metal centers.[144,145] Given these promising structural features, we are currently exploring the ability of the NiM_B^X series to serve as electrocatalysts for CO_2 reduction. We also plan to incorporate redox-active donors into the L_1 framework; such moieties could serve as electron reservoirs in multi-electron processes, similar to the role of the $[Fe_3S_4]$ cluster in the catalytic cycle of CODH.

Chapter 5

Bimetallic Complexes Supported by a Redox-Active Ligand with Fused Pincer-Type Coordination Sites

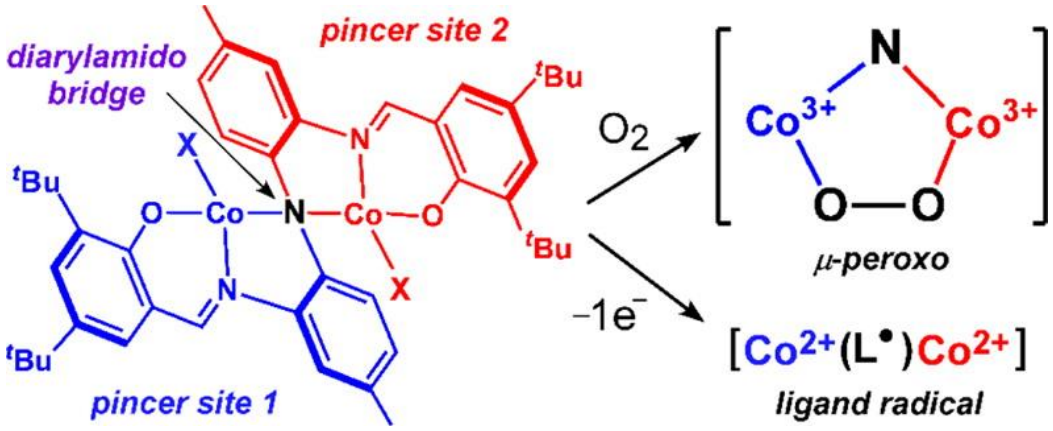

Abstract: The syntheses, X-ray structures, and electrochemical properties of homobimetallic complexes (M = Co, Cu, Zn) supported by a pentadentate ligand ($\mathbf{L}^{\mathbf{N3O2}}$) with "fused" NNO pincer-type coordination sites are reported. The $\mathbf{L}^{\mathbf{N3O2}}$ chelate consists of a bridging diarylamido group and flanking salicyaldimine donors, and the flexible framework permits the binding of redox-active auxilary ligands, such as 2,2'-bipyridine, and small molecules like O_2. The S = 1/2 species arising from oxidation of the $\mathbf{L}^{\mathbf{N3O2}}$ ligand was characterized with EPR spectroscopy.

Portions of this chapter have appeared in the paper: Wang, D. N.; Lindeman, S. V.; Fiedler, A. T., *Inorg Chem*, **2015**, 8744–8754.

5.1 Introduction

Tridentate ligands that coordinate in a meridional fashion are often called pincers due to their rigidity and tightly-binding nature.[177-179] Pincer ligands have found application in nearly all areas of inorganic chemistry, including transition-metal catalysis,[180-183] sensors,[184,185] and materials science.[186,187] While considerable diversity exists within this ever-expanding ligand family, a classic type of pincer features a central diarylamido unit with two flanking phosphine donors (PNP pincers).[188-190] Several diarylamido-based NNN pincers have also been generated, where the *N*-donor arm is an imine, amine, or heterocyclic donor.[191-199] Such ligands have been used in the preparation of low-coordinate, yet highly stable, transition-metal complexes capable of performing diverse chemical transformations.

Given the remarkable utility of mononuclear pincer complexes, there has been interest in developing binuclear complexes that contain two pincer-type compartments. The presence of two metal ions offers several catalytic advantages, most crucially the possibility of cooperative action in substrate binding/activation and the ability to perform multiple electron transfers (assuming the metal centers are redox active). A few "bis(pincer)" complexes have been prepared by the dimerization of mononuclear species[200] in most of these cases, the metal centers are doubly-bridged by either the pincer arms[201] or exogenous ligands not connected to the pincer unit.[202,203] In other

systems, the two metal centers are bridged by pyrazine[204], 1,4-phenylene[205,206], or ferrocene[207] spacers, resulting in metal-metal distances greater than 6 Å. Some groups have connected the pincer compartments by more flexible spacers,[208] thereby allowing the metal centers to approach one another in space. For example, the Ozerov group recently generated a series of ligands in which two PNN pincer units are connected by an alkyl spacer, $(CH_2)_n$ (n = 2 or 4).[209] These ligands were used to prepare hydride-bridged palladium complexes with Pd–Pd distances near 3 Å, as well as a complex featuring a metal-metal bond (Pd–Pd distance of 2.56 Å).

As described in this chapter, short intermetallic distances can also be achieved by removing the spacer between the two pincer sites entirely. In such "fused" ligands, the two pincer coordination pockets share one of the donor arms, which then serves as the single bridge between the metal centers. This approach to bis(pincer) design has not been widely employed, but Meyer and coworkers have reported fused (or "two-in-one") PNN[210] and NNN[211] pincer ligands featuring a bridging pyrazolate that provides one *N*-donor to each ferrous center (**Figure 5.1(a)**). Here, we expand upon the fused approach through the synthesis of the novel bis(pincer) ligand $\mathbf{L^{N3O2}}$, shown in **Figure 5.1(b)**. Like conventional PNP and NNN pincers, the $\mathbf{L^{N3O2}}$ ligand contains a central diarylamido donor; however, the presence of the two salicyaldimine chelates allows $\mathbf{L^{N3O2}}$ to behave as a binucleating ligand with the diarylamido unit in a bridging position. The resulting

framework provides pincer-type coordination to two metal centers in close proximity (3 Å or less).

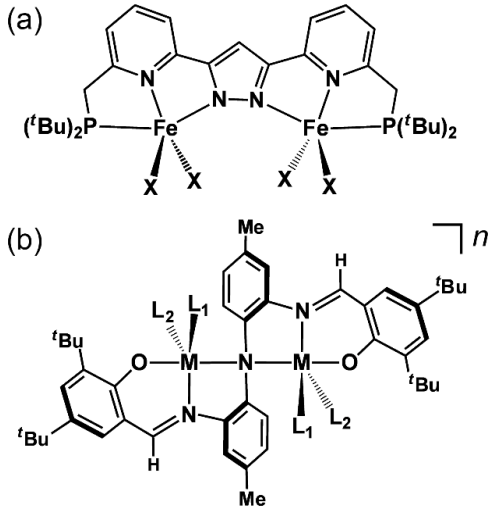

Figure 5.1 Complexes featuring fused (or "two-in-one") pincer ligands: (a) PNN bis(pincer) ligand recently reported by Meyer and coworkers,[15] and (b) the $\mathbf{L^{N3O2}}$ ligand described in this chapter.

While not nearly as common as binucleating frameworks with phenolate or pyrazolate bridges, ligands like $\mathbf{L^{N3O2}}$ that feature a bridging diarylamido unit have yielded complexes with attractive electronic and structural properties. For instance, PNP ligands have been used to generate various bimetallic(I) complexes with $M_2(\mu\text{-}NAr_2)_2$ diamond cores (M = Cu,[212] Ni,[213] and Co[214]). Although these complexes utilize PNP ligands, the resulting four-coordinate M(I) centers exist in pseudo-tetrahedral N_2P_2 environments instead of pincer-like sites. Spectroscopic and computational analysis revealed that the redox chemistry occurs primarily at the bridging N atoms[215,216] – a

finding consistent with previous studies of mononuclear complexes with PNP pincer ligands.[217,218] The "noninnocent" nature of μ-NAr_2 ligands is a potential asset in catalytic processes requiring multiple electron transfers.[219,220] Another advantage of diarylamido ligands is their intrinsic chirality due to the relative orientation of the aromatic rings, which gives rise to atropisomers with C_2 symmetry.[209,221] Thus, diarylamido-based ligands could lead to chiral bimetallic complexes for enantioselective catalysis.

To date, the vast majority of bimetallic complexes with bridging diarylamido ligands have featured $M_2(\mu\text{-}NAr_2)_2$ diamond cores.[212-214,222-225] However, such structures are not ideal for catalysis or small molecule activation, as the steric bulk of the four phenyl rings limits access to the metal centers. In contrast, the $\mathbf{L^{N3O2}}$ ligand provides a more open framework that preserves three vacant coordination sites on each metal center in a meridional arrangement, similar to mononuclear pincer-based complexes. These open coordination sites are available for the binding of substrates and/or auxiliary ligands (L^{aux}) with advantageous structural or electrochemical properties, as described below. Due to the presence of the salicyaldimine chelates, $\mathbf{L^{N3O2}}$ bears a resemblance to binucleating salen and Schiff base ligands that have proven useful in catalysis and materials chemistry.[226-229] The variable dihedral angle between aryl rings of the amido unit imparts rotational flexibility to the pendant salicyaldimine arms.

Table 5.1 Complexes reported in this chapter.

General formula: $[M_2(L^{N3O2})(L^{aux})_2]X$

Complex	M	L^{aux}	X
12	Cu	1MeBI	TfO^-
13	Cu	bpy	TfO^-
14	Zn	bpy	TfO^-
15	Co	bpy	ClO_4^-
16	Co	bpy^{Br2}	ClO_4^-
17	Zn	$S\text{-}^{iPr}OxPy$	TfO^-

$S\text{-}^{iPr}OxPy$ = 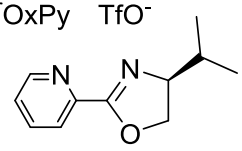

Here the syntheses and X-ray structural characterization of the homobimetallic complexes **12-17** are indicated in **Table 5.1**. These complexes have the general formula $[M_2(\mathbf{L^{N3O2}})(L^{aux})_2]^+$ (M = Co, Cu, Zn), where L^{aux} represents 1-methylbenzimidazole (1MeBI), 2,2'-bipyridine (bpy), or 4,4-dibromo-2,2-bipyridine (bpy^{Br2}). Chiral $[Zn_2(\mathbf{L^{N3O2}})]^+$ frameworks were prepared using the optically-active bidentate ligand (*S*)-2-(4-isopropyl-4,5-dihydro-oxazolyl)pyridine (*S*-^{iPr}OxPy; **Table 5.1**). First-row transition metals were selected because of their earth-abundance, redox-active nature (except for Zn), and proven ability to perform small-molecule activation. The electrochemical properties of **13-16** were thoroughly examined with cyclic and square-wave voltammetries. These bpy-containing complexes exhibit an abundance of electrochemical features arising from both ligand- and metal-based events; indeed,

complexes **13** and **15** exhibit six redox events over a potential range of nearly 3.0 V. The electronic structures of $[Co_2(\mathbf{L^{N3O2}})(bpy)_2](ClO_4)$ (**15**) and its one-electron oxidized derivative ($\mathbf{15^{ox}}$) were examined with spectroscopic and computational methods. These results indicate that $\mathbf{15^{ox}}$ is an $S = 1/2$ species in which the μ-NAr_2 unit of the $\mathbf{L^{N3O2}}$ ligand carries a large amount of unpaired spin density. Finally, we demonstrate that $[Co_2(\mathbf{L^{N3O2}})(bpy^{Br2})_2](ClO_4)$ (**16**) reacts with O_2 to yield a dicobalt(III) complex with a bridging peroxo ligand, suggesting that these bimetallic complexes are capable of small molecule activation.

5.2 Experimental Section

Materials and Physical Methods. Unless otherwise noted, all reagents and solvents were purchased from commercial sources and used as received. Dichloromethane and acetonitrile were purified and dried using a Vacuum Atmospheres solvent purification system. Due to their air-sensitive nature, the dicobalt(II) complexes (**15** and **16**) were handled under inert atmosphere using a Vacuum Atmospheres Omni-Lab glovebox. Elemental analyses were performed at Midwest Microlab, LLC in Indianapolis, IN.

UV-vis absorption spectra were obtained with an Agilent 8453 diode array spectrometer, and CD spectra were recorded using a Jasco J-715 spectropolarimeter. Infrared (IR) spectra of solid samples were measured with a Thermo Scientific Nicolet

iS5 FTIR spectrometer equipped with the iD3 attenuated total reflectance accessory. ^{1}H NMR spectra were collected at room temperature with a Varian 400 MHz spectrometer. EPR experiments were performed using a Bruker ELEXSYS E600 equipped with an ER4415DM cavity, an Oxford Instruments ITC503 temperature controller, and an ESR-900 He flow cryostat. The program EasySpin4 was used to simulate the experimental spectra.[230] Electrochemical measurements were performed with an epsilon EC potentiostat (iBAS) under nitrogen atmosphere at a scan rate of 100 mV/s with 0.1 M $(NBu_4)PF_6$ as the electrolyte. A three-electrode cell containing an Ag/AgCl reference electrode, a platinum auxiliary electrode, and a glassy carbon working electrode was employed for voltammetric measurements. Under these conditions, the ferrocene/ferrocenium ($Fc^{+/0}$) couple has an $E_{1/2}$ value of +0.47 V in MeCN.

Bis(4-methyl-2-nitrophenyl)amine.

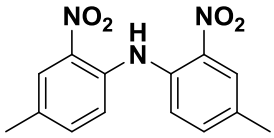

This procedure was adapted from previously published reports.[231,232] A round-bottom flask equipped with a stir bar was charged with a mixture of concentrated nitric acid (70%; 10 mL) and glacial acetic acid (45 mL). The mixture was cooled to 0 ^{o}C and bis(4-methylphenyl)amine (5.00 g, 25.4 mmol, 1.0 eq.) was added. The yellow mixture was stirred for 10 min in an ice/water bath before the dropwise addition of isoamyl nitrite (8.75 g, 75 mmol, 3.0 eq.) over the course of 5 min. The solution turned to dark green;

after stirring for an additional 10 minutes, the solution changed to an orange color and a precipitate started to form. The orange precipitate was collected via filtration, washed with diethyl ether, and dried under vacuum (6.45 g, 22.5 mmol, 89 % yield). ^{1}H NMR (400 MHz, $CDCl_3$) δ: 2.37 (s, 6H, C*H*$_3$) , 7.32 (d, *J* = 8.5 Hz, 2H, Ar*H*), 7.42 (d, *J* = 8.5 Hz, 2H, Ar*H*), 7.99 (s, 2H, Ar*H*), 10.80 (s, 1H, N*H*). ^{13}C NMR (101 MHz, $CDCl_3$) δ: 20.43, 119.73, 125.25, 126.33, 131.73, 135.19, 135.85.

Bis(4-methyl-2-aminophenyl)amine.

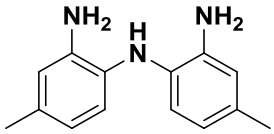

A 250 mL pressure vessel equipped with a stir bar was filled with solid bis(4-methyl-2-nitrophenyl)amine (3.00 g, 10.45 mmol, 1.0 eq.), MeOH (100 mL), and 10% Pd/C (500 mg, 0.47 mmol, 0.0045 eq.). The flask was pressurized with H_2 gas (46 psi), and the mixture was stirred at 65 ^{o}C for 4 hours, during which the bright orange solution became colorless. The mixture filtered through Celite, washed with cold MeOH, and the solvent removed under vacuum to yield a light purple oil. The oil residue was triturated with Et_2O (20 mL) to give a pale brown powder, which was collected by filtration and dried under vacuum (2.25 g, 9.93 mmol, 95% yield). ^{1}H NMR (300 MHz, $CDCl_3$) δ: 2.25 (s, 6H, C*H*$_3$), 3.56 (s, 4H, N*H*$_2$), 4.80 (s, 1H, N*H*), 6.54 (d, *J* = 7.9 Hz, 2H, Ar*H*), 6.63 – 6.58 (m, 4H, Ar*H*). ^{13}C NMR (75 MHz, $CDCl_3$) δ: 21.14, 109.99, 117.27, 120.49, 129.10, 133.11, 138.61.

Pro-Ligand H_3L^{N3O2}.

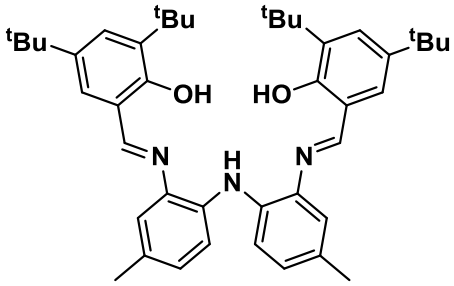

To a solution of bis(4-methyl-2-aminophenyl)amine (454 mg, 2.0 mmol, 1.0 eq.) in MeOH (30 mL) was added 3,5-di-tert-butyl-2-hydroxybenzaldehyde (937.3 mg, 4.0 mmol, 2.0 eq.) and 5 drops of formic acid. The mixture was heated overnight at 60 ^{o}C under an inert atmosphere, giving rise to a bright yellow precipitate. The yellow solid was collected by filtration and dried under vacuum to yield pure $H_3\mathbf{L}^{\mathbf{N3O2}}$ as a yellow powder (1.20 g, 1.82 mmol, 91% yield). X-ray quality crystals were obtained by slow evaporation of a $H_3\mathbf{L}^{\mathbf{N3O2}}$ solution in a mixture of CH_2Cl_2:CH_3OH (9:1). Anal. Calcd for $C_{44}H_{57}N_3O_2$ (M_W = 659.96 g mol^{-1}): C, 80.08; H, 8.71; N, 6.37. Found: C, 80.32; H, 8.89; N, 6.27. ^{1}H NMR (400 MHz, $CDCl_3$) δ: 1.17 (s, 18H, C(C*H*$_3$)$_3$), 1.30 (s, 18H, C(C*H*$_3$)$_3$), 2.35 (s, 6H, C*H*$_3$), 6.55 (s, 1H, N*H*), 6.99 (s, 2H, Ar*H*), 7.02 (d, *J* = 8.2 Hz, 2H, Ar*H*), 7.17 (s, 2H, Ar*H*), 7.36 – 7.30 (m, 4H, Ar*H*), 8.64 (s, 2H, Ar*H*), 13.26 (s, 2H, N=C-*H*). ^{13}C NMR (101 MHz, $CDCl_3$) δ: 20.79, 29.13, 31.46, 34.11, 34.81, 116.46, 118.56, 119.27, 126.75, 127.78, 127.89, 130.44, 134.26, 136.82, 138.47, 140.22, 158.15, 163.94.

$[Cu_2(L^{N3O2})(1MeBI)_2](OTf)$ (12).

The pro-ligand $H_3\mathbf{L}^{\mathbf{N3O2}}$ (66.0 mg, 0.100 mmol), 1MeBI (26.4 mg, 2.0 eq.), and $Cu(OTf)_2$ (72.3 mg, 2.0 eq.) were added to a 25 mL flask containing MeCN (5 mL). After stirring for 5 minutes, NEt_3 (42 μL, 3.0 eq.) was added, causing the solution to turn from brown to reddish brown. The mixture was stirred for two hours and then filtered through Celite. A small amount of MeOH (1 mL) was slowly added to the filtrate, and the resulting solution was allowed to slowly evaporate over the course of two days. This process yielded orange-brown crystals that were collected, washed with Et_2O (3 mL), and dried under vacuum. Yield = 65 mg (54%). X-ray-quality crystals were grown from a concentrated 1:1 solution of CH_2Cl_2:MeOH. The resulting structure revealed uncoordinated MeOH molecules in the asymmetric unit, and elemental analysis suggest that a small amount (~1.0 equiv) remains after drying. Anal. Calcd for $C_{61}H_{70}Cu_2F_3N_7O_5S{\bullet}CH_3OH$ (M_W = 1229.4 g mol^{-1}): C, 60.56; H, 6.07; N, 7.97. Found: C, 60.35; H, 5.69; N, 7.82. UV-vis [λ_{max}, nm (ε, $M^{-1}cm^{-1}$) in MeCN]: 310 (19,000), 424 (13,100). FTIR (cm^{-1}; solid): 2953 (m), 2903 (w), 2864 (w), 1593 (m), 1523 (m), 1493 (m), 1456 (m), 1420 (m), 1358 (s), 1151 (s). ^{19}F NMR (δ, CD_3CN): -79.3 (OTf). ^{1}H NMR (δ, CD_3CN): -30.6 (2H), 1.4 (18H), 2.2 (18H), 4.0 (6H), 6.2 (2H), 7.5 (2H), 8.8 (2H), 16.2 (2H), 22.7 (2H), 30.5 (2H), 40.2 (2H), 41.8 (6H), 51.7 (2H). μ_{eff} = 2.41 μ_B (Evans method).

[$Cu_2(L^{N3O2})(bpy)_2$](OTf) (13).

The procedure was nearly identical to the one used to prepare complex **12**; the only difference was the replacement of 1MeBI with bpy (31.2 mg, 2.0 eq.). Yield = 104 mg (84%). Anal. Calcd for $C_{65}H_{70}Cu_2F_3N_7O_5S$ (M_W = 1245.4 g mol^{-1}): C, 62.68; H, 5.67; N, 7.87. Found: C, 62.46; H, 5.73; N, 7.85. UV-vis [λ_{max}, nm (ε, $M^{-1}cm^{-1}$) in MeCN]: 298 (40,200), 430 (15,100), 495 (sh). FTIR (cm^{-1}; solid): 2948 (m), 2904 (w), 2863 (w), 1593 (m), 1521 (m), 1489 (m), 1352 (s), 1152 (s). ^{19}F NMR (δ, CD_3CN): -79.3 (OTf). ^1H NMR (δ, CD_3CN): -29.5 (2H), 1.4 (18H), 2.8 (18H), 8.9 (2H), 9.6 (2H), 10.1 (2H), 12.9 (4H), 13.3 (2H), 18.1 (2H), 25.9 (2H), 33.6 (2H), 36.0 (2H), 39.9 (6H), 45.1 (2H), 116.0 (2H). μ_{eff} = 2.36 μ_B (Evans method).

[$Zn_2(L^{N3O2})(bpy)_2$](OTf) (14).

To a 25 mL flask were added the pro-ligand H_3**L^{N3O2}** (66.0 mg, 0.100 mmol), 2,2'-bipyridine (31.2 mg, 2.0 eq.), and $Zn(OTf)_2$ (72.7 mg, 2.0 eq.). The components were dissolved in a 1:1 mixture of MeCN:CH_2Cl_2 (5 mL) and stirred for 5 minutes. The addition of NEt_3 (42 μL, 3.0 eq.) caused the solution to turn to an orange color. The mixture was stirred overnight, filtered through Celite, and the solvent removed under vacuum. The resulting powder was washed with Et_2O (5 mL), dried under vacuum, and dissolved in a 1:1 mixture of MeCN:MeOH (4 mL). Slow evaporation over the course of two days provided orange crystals that were collected via filtration, washed with Et_2O, and dried under vacuum. Yield = 96 mg (77%). Orange crystals, suitable for X-ray

diffraction, were grown from a concentrated 1:1 solution of CH_2Cl_2:MeOH. Anal. Calcd for $C_{65}H_{70}F_3N_7O_5SZn_2$ (M_W = 1249.1 g mol^{-1}): C, 62.50; H, 5.65; N, 7.85. Found: C, 62.16; H, 5.60; N 7.76. UV-vis [λ_{max}, nm (ε, $M^{-1}cm^{-1}$) in MeCN]: 425 (24,300), 460 (19,600). FTIR (cm^{-1}; solid): 2949 (m), 2904 (w), 2865 (w), 1598 (m), 1523 (m), 1487 (m), 1379 (s), 1159 (s). ^{19}F NMR (δ, CD_3CN) δ: -79.4 (OTf). ^1H NMR (δ, CD_3CN): 1.11 (s, 18H, C(C*H*$_3$)$_3$), 1.37 (s, 18H, C(C*H*$_3$)$_3$), 2.13 (s, 6H, C*H*$_3$), 5.54 (d, *J* = 8.3 Hz, 2H, $\mathbf{L^{N3O2}}$-Ar*H*), 6.17 (d, *J* = 8.3 Hz, 2H, $\mathbf{L^{N3O2}}$-Ar*H*), 7.03 (s, 2H, $\mathbf{L^{N3O2}}$-Ar*H*), 7.21 (dd, *J* = 8.1, 5.5 Hz, 2H, bpy-Ar*H*), 7.26 (d, *J* = 2.7 Hz, 2H, $\mathbf{L^{N3O2}}$-Ar*H*), 7.39 (d, *J* = 2.7 Hz, 2H, $\mathbf{L^{N3O2}}$-Ar*H*), 7.45–7.51 (m, 2H, bpy-*H*), 7.96 (d, *J* = 8.1 Hz, 2H, bpy-*H*), 7.99 – 8.07 (m, 8H, bpy-*H*), 8.48 (s, 2H, N=C-*H*), 8.75 (d, *J* = 6.3 Hz, 2H, bpy-*H*).

$[Co_2(L^{N3O2})(bpy)_2](ClO_4)$ (15).

The procedure was identical to the one used to prepare complex **14**, except for the substitution of $Co(ClO_4)_2$•6 H_2O (73.2 mg, 2.0 eq.) for $Zn(OTf)_2$. Yield = 85 mg (71%). Brown crystals, suitable for X-ray diffraction, were grown from a concentrated 1:1 solution of acetone:MeOH. Anal. Calcd for $C_{64}H_{70}ClCo_2N_7O_6$ (M_W = 1186.6 g mol^{-1}): C, 64.78; H, 5.95; N, 8.26. Found: C, 62.37; H, 5.86; N, 7.91 (the discrepancies are due to small amounts of $[HNEt_3]ClO_4$ salt, which persists even after multiple recrystallizations). UV-vis [λ_{max}, nm (ε, $M^{-1}cm^{-1}$) in MeCN]: 440 (13,800), 590 (sh). FTIR (cm^{-1}; solid): 2956 (m), 2904 (w), 2867 (w), 1587 (m), 1511 (m), 1441 (m), 1360 (s), 1162 (m). ^1H NMR (δ, CD_3CN): 0.74 (s, 18H, C(C*H*$_3$)$_3$), 1.30 (s, 18H, C(C*H*$_3$)$_3$), 2.09 (s, 6H, C*H*$_3$),

5.48 (d, *J* = 8.4 Hz, 2H, $\mathbf{L^{N3O2}}$-Ar*H*), 6.13 (d, *J* = 8.4 Hz, 2H, $\mathbf{L^{N3O2}}$-Ar*H*), 7.01 (s, 2H, $\mathbf{L^{N3O2}}$-Ar*H*), 7.15 (d, *J* = 2.4 Hz, 2H, $\mathbf{L^{N3O2}}$-Ar*H*), 7.23 (d, *J* = 2.4 Hz, 2H, $\mathbf{L^{N3O2}}$-Ar*H*), 7.34 (t, *J* = 6.0 Hz, 2H, bpy-*H*), 7.68 (t, *J* = 6.0 Hz, 2H, bpy-*H*), 7.73 (s, 2H, N=C-*H*), 7.84 (d, *J* = 6.0 Hz, 2H, bpy-*H*), 7.96 – 8.12 (m, 6H, bpy-*H*), 8.18 (d, *J* = 7.9 Hz, 2H, bpy-*H*), 10.23 (d, *J* = 6.0 Hz, 2H, bpy-*H*).

$[Co_2(L^{N3O2})(bpy^{Br2})_2](ClO_4)$ (16).

This complex was prepared in the same manner as complexes **14** and **15**, with the exception that bpy^{Br2} (62.8 mg, 2.0 eq.) was used as the auxiliary ligand. Yield = 86 mg (57%). The X-ray structure revealed two uncoordinated MeOH molecules in the asymmetric unit. Anal. Calcd for $C_{64}H_{66}Br_4ClCo_2N_7O_6 \bullet 2CH_3OH$ (M_W = 1566.3 g mol^{-1}): C, 50.61; H, 4.76; N, 6.26. Found: C, 48.98; H, 4.48; N, 6.31 (the discrepancies are due to small amounts of $[HNEt_3]ClO_4$ salt). UV-vis [λ_{max}, nm (ε, $M^{-1}cm^{-1}$) in MeCN]: 260 (30,000), 340 (14,900), 420 (8,900), 580 (sh). FTIR (cm^{-1}; solid): 3070 (w), 2948 (m), 2900 (w), 2863 (w), 1589 (m), 1543 (w), 1520 (m), 1492 (w), 1462 (m), 1397 (m), 1251 (m), 1170 (m). ^{1}H NMR (δ, CD_3CN): 0.77 (s, 18H, C(C*H*$_3$)$_3$), 1.31 (s, 18H, C(C*H*$_3$)$_3$), 2.17 (s, 6H, C*H*$_3$), 5.62 (d, *J* = 8.2 Hz, 2H, $\mathbf{L^{N3O2}}$-Ar*H*), 6.23 (d, *J* = 8.2 Hz, 2H, $\mathbf{L^{N3O2}}$-Ar*H*), 7.10 (s, 2H, $\mathbf{L^{N3O2}}$-Ar*H*), 7.17 (d, *J* = 2.5 Hz, 2H, $\mathbf{L^{N3O2}}$-Ar*H*), 7.30 (d, *J* = 2.5 Hz, 2H, $\mathbf{L^{N3O2}}$-Ar*H*), 7.57 (dd, *J* = 6.0, 1.9 Hz, 2H, bpy-*H*), 7.65 (d, *J* = 6.0 Hz, 2H, bpy-*H*), 7.80 (s, 2H, N=C-*H*), 7.92 (dd, *J* = 6.3, 1.9 Hz, 2H, bpy-*H*), 8.27 (d, *J* = 1.9 Hz, 2H, bpy-*H*), 8.46 (d, 2H, *J* = 1.9 Hz, bpy-*H*), 9.95 (d, *J* = 6.3 Hz, 2H, bpy-*H*).

[$Co_2(O_2)(L^{N3O2})(bpy^{Br2})_2$](ClO$_4$) (16-O$_2$).

Complex **16** was dissolved in a 1:1 mixture of CH_2Cl_2:MeOH and exposed to air. Slow evaporation over the course of several days provided dark brown crystals of both **16** and **16-O$_2$** that were collected via filtration, washed with Et_2O, and dried under vacuum. Attempts to separate the two complexes were unsuccessful. Regardless, the spectroscopic features of **16-O$_2$** were distinguished by comparison to data collected with pure samples of 16. FTIR (cm^{-1}; solid): 2948 (m), 2899 (w), 2863 (w), 1588 (m), 1543 (w), 1518 (m), 1493 (m), 1462 (m), 1398 (m), 1252 (m), 1170 (m), 1080 (s). 1H NMR (δ, CD_3CN): 0.77 (s, 18H, $C(CH_3)_3$), 1.36 (s, 18H, $C(CH_3)_3$), 2.32 (s, 6H, CH_3), 5.63 (d, J = 8.4 Hz, 2H, **L^{N3O2}**-Ar*H*), 6.55 (d, J = 8.4 Hz, 2H, **L^{N3O2}**-Ar*H*), 7.17 (d, J = 6.4 Hz, 2H, bpy-*H*), 7.35 (d, J = 2.4 Hz, 2H, **L^{N3O2}**-Ar*H*), 7.37 (dd, J = 6.4, 2.0 Hz, 2H, bpy-*H*), 7.63 (d, J = 2.4 Hz, 2H, **L^{N3O2}**-Ar*H*), 7.70 (d, J = 2.0 Hz, 2H, bpy-*H*), 8.34 (dd, J = 6.1, 1.9 Hz, 2H, bpy-*H*), 8.37 (d, J = 1.9 Hz, 2H, bpy-*H*), 8.45 (s, 2H, **L^{N3O2}**-Ar*H*), 8.61 (s, 2H, N=C-*H*), 9.00 (d, J = 6.1 Hz 2H, bpy-*H*).

[$Zn_2(L^{N3O2})$(*S*-^{iPr}OxPy)$_2$](OTf) (17).

To a 25 mL flask were added the pro-ligand H_3**L^{N3O2}** (66.0 mg, 0.100 mmol), $Zn(OTf)_2$ (72.7 mg, 2.0 eq.), and *S*-^{iPr}OxPy (38 mg, 2.0 eq.). The components were dissolved in a 3:1 mixture of MeCN:CH_2Cl_2 (8 mL) and stirred for 5 minutes. The addition of NEt_3 (42 μL, 3.0 eq.) caused the yellow solution to turn to a red-orange color. The mixture was stirred for one hour, filtered through Celite, and the solvent removed

under vacuum. The resulting powder was washed with pentane (5 mL) and dried under vacuum to give analytically pure material. Yield = 73.2 mg (56%). Anal. Calcd for $C_{67}H_{82}F_3N_7O_7SZn_2$ (M_W = 1317.2 g mol^{-1}): C, 61.09; H, 6.27; N, 7.44. Found: C, 60.79; H, 5.81; N, 7.97 (the slight discrepancies are due to small amounts of NEt_3). UV-vis [λ_{max}, nm (ε, M^{-1}cm^{-1}) in MeCN]: 420 (21,000), 460 (18,300). FTIR (cm^{-1}; solid): 3055 (w), 2953 (m), 2906 (w), 2867 (w), 1653 (w), 1606 (m), 1591 (m), 1523 (m), 1487 (m), 1402 (m), 1236 (s), 1153 (s). ^{19}F NMR (δ, CD_3CN): -79.4. ^{1}H NMR (δ, CD_3CN): 0.52 (d, *J* = 6.8 Hz, 6H, CH(C*H*$_3$)$_2$), 0.59 (d, *J* = 6.8 Hz, 6H, CH(C*H*$_3$)$_2$), 1.11 (s, 18H, C(C*H*$_3$)$_3$), 1.36 (s, 18H, C(C*H*$_3$)$_3$), 1.56–1.62 (m, 2H, C*H*(CH$_3$)$_2$), 2.22 (s, 6H, C*H*$_3$), 3.92–3.82 (m, 2H, oxazol-*H*), 4.48 (dd, *J* = 9.4, 6.9 Hz, 2H, oxazol-*H*), 4.65 (t, *J* = 9.4 Hz, 2H, oxazol-*H*), 6.80 (d, *J* = 8.2 Hz, 2H, **L^{N3O2}**-Ar*H*), 6.89 (d, *J* = 8.2 Hz, 2H, **L^{N3O2}**-Ar*H*), 6.93 (s, 2H, **L^{N3O2}**-Ar*H*), 7.12 (d, *J* = 2.7 Hz, 2H, **L^{N3O2}**-Ar*H*), 7.16 (dd, *J* = 7.9, 5.0 Hz, 2H, py-*H*), 7.40 (d, *J* = 2.7 Hz, 2H, **L^{N3O2}**-Ar*H*), 7.57 (d, *J* = 7.9 Hz, 2H, py-*H*), 7.98 (t, *J* = 7.9 Hz, 2H, py-*H*), 8.10 (s, 2H, N=C-*H*), 8.58 (d, *J* = 5.0 Hz, 2H, py-*H*).

Crystallographic Studies. X-ray diffraction data were collected at 100 K with an Oxford Diffraction SuperNova diffractometer equipped with a 135 mm Atlas CCD detector and Cu(Kα) radiation source. The resulting data were processed with the CrysAlis Pro program package (Agilent Technologies, 2011). An absorption correction was performed on the real crystal shape followed by an empirical multi-scan correction using SCALE3 ABSPACK routine. Structures were solved using the SHELXS program

and refined with the SHELXL program[102] within the Olex2 crystallographic package.[103] All non-hydrogen atoms were refined with anisotropic displacement parameters. Hydrogen atoms were generally positioned geometrically and refined using appropriate geometric restrictions on bond lengths and bond angles within a riding/rotating model, and the torsion angles of $-CH_3$ hydrogens were optimized to better fit residual electron density. For complexes **12**, **14**, and **16-O$_2$**, the unit cells contained large void spaces filled with heavily disordered solvent and exact localization of these molecules was not feasible. The solvent-mask procedure implemented in Olex2 was therefore applied to account for the contribution of these solvent molecules to diffraction intensities. X-ray crystallographic parameters are provided in **Table 5.5**.

DFT Computations: DFT calculations were carried out using the ORCA 2.7 software package developed by Dr. F. Neese (MPI for Chemical Energy Conversion).[104] When X-ray structures were not available (**15^{ox}** and **17**), computational models were generated via geometry optimizations that employed the Becke-Perdew (BP86) functional.[105,106] The computational models of **15** and **15^{ox}** omitted the *tert*-butyl substituents of the phenolate donors. Calculations of the four possible isomers of **17**, however, involved the entire complex without modification of the **L^{N3O2}** or *S*-^{iPr}OxPy ligands. Once the optimized models were obtained, molecular energies and electronic structure parameters were calculated using Becke's three-parameter hybrid functional for exchange along with the Lee-Yang-Parr correlation functional (B3LYP).[233,234] All

calculations utilized Ahlrichs' valence triple-ζ basis set (TZV) and TZV/J auxiliary basis set, in conjunction with polarization functions on all atoms.[107,108,235] Solvent effects were calculated using the conductor-like screening model (COSMO)[236] with a dielectric constant (ε) of 36.6 for MeCN. Exchange coupling constants (*J*) were obtained using Noodleman's broken symmetry approach ($H = -2JS_A \bullet S_B$).[120,237] Isosurface plots of molecular orbitals were prepared with Laaksonen's gOpenMol program.[238]

5.3 Results and Discussion

5.3.1 Synthesis of H_3L^{N3O2} and Bimetallic Complexes.

The pro-ligand $H_3\mathbf{L}^{\mathbf{N3O2}}$ is prepared by the route shown in **Figure 5.2**. The final step in the synthesis is the condensation of bis(2-amino-4-methylphenyl)amine with two equivalents of 3,5-di-*tert*-butylsalicylaldehyde. Formation of the two salicyaldimine units required the presence of *tert*-butyl groups on the phenol ring. Salicylaldehydes with less bulky substituents reacted instead with the central diarylamine moiety to give a cyclized 2-(benzimidazol-2-yl)phenol product (**Figure 5.3**). The identity of $H_3\mathbf{L}^{\mathbf{N3O2}}$ was confirmed by ^{1}H NMR and X-ray crystallography. In the solid state, $H_3\mathbf{L}^{\mathbf{N3O2}}$ adopts a twisted conformation featuring hydrogen-bonds between phenol donors and imine acceptors (**Figure 5.2**).

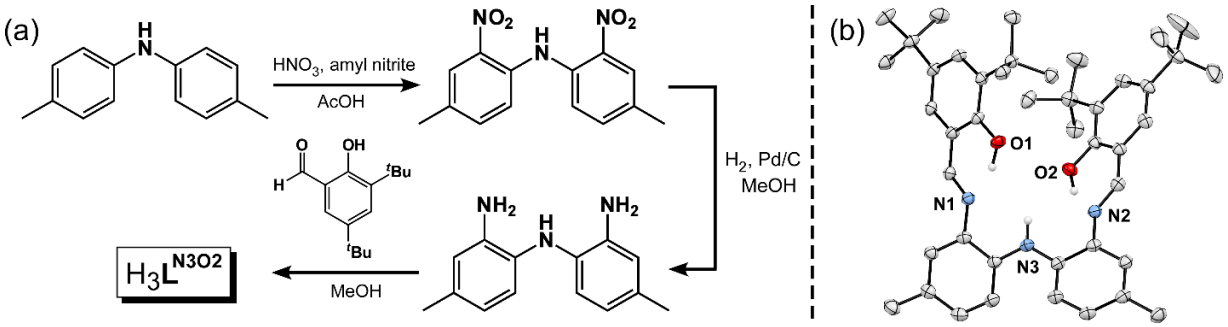

Figure 5.2 (a) Synthetic route for the pro-ligand H_3L^{N3O2}. (b) Molecular structure of H_3L^{N3O2} determined by X-ray crystallography (50% probability thermal ellipsoids).

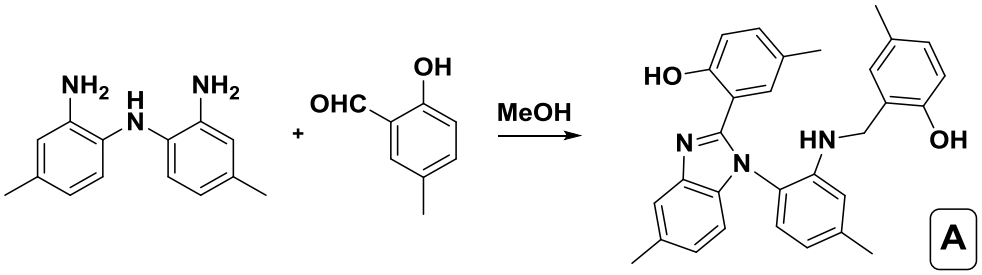

Figure 5.3 Product (**A**) arising from the reaction of bis(4-methyl-2-aminophenyl)amine with 5-methylsalicylaldehyde.

The bimetallic complexes **12-17** were prepared by the reaction of $H_3\mathbf{L}^{\mathbf{N3O2}}$ with two equivalents of the appropriate MX_2 salt (M = Co, Cu, Zn; X = OTf, ClO_4) in the presence of NEt_3, along with addition of two equivalents of the desired auxiliary ligand (1MeBI, bpy^{R2}, or *S*-^{iPr}OxPy). The resulting complexes are soluble in CH_2Cl_2 and polar aprotic solvents, but insoluble in MeOH. All of the complexes possess a dark orange-brown color due to an absorption manifold with λ_{max} near 420 nm ($\varepsilon \sim 10^4\ M^{-1}cm^{-1}$). This feature is attributed to π–π^* transitions of the $\mathbf{L}^{\mathbf{N3O2}}$ ligand based on its intensity and consistent presence irrespective of metal ion or auxiliary ligand. As expected, dicopper

complexes **12** and **13** give rise to ^{1}H NMR spectra with broad, paramagnetically shifted peaks (**Figure 5.4**). Using the Evans method, effective magnetic moments (μ_{eff}) of 2.38 $\pm$0.03 μ_B were measured for **12** and **13** at room temperature; these values are slightly less than the spin-only value of 2.56 μ_B expected for a binuclear species with two uncoupled *S* = 1/2 spins. In contrast, ^{1}H NMR spectra of the dizinc and dicobalt complexes (**14**-**16**) display sharp peaks with chemical shifts indicative of diamagnetic ground states (**Figure 5.5**). The lack of paramagnetism in the dicobalt complexes **15** and **16** is somewhat surprising, and it suggests the presence of strong antiferromagnetic coupling between the Co^{2+} centers – a matter that will be examined below.

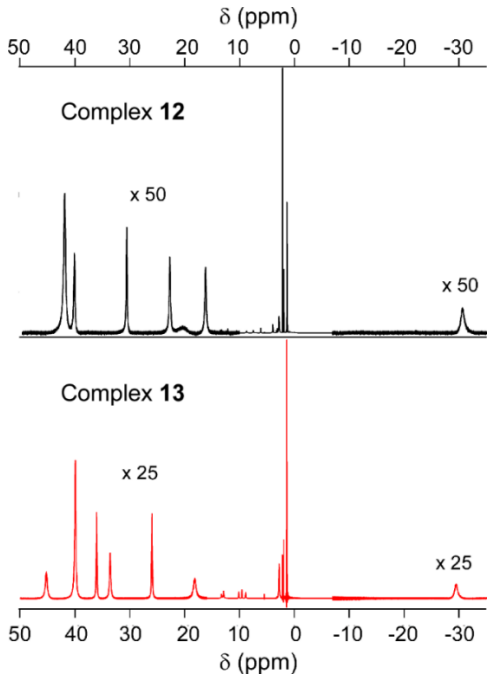

Figure 5.4 ^{1}H NMR spectra of complexes **12** and **13** in MeCN-d_3. Paramagnetically-shifted peaks in the high- and low-field regions were enlarged for the sake of clarity.

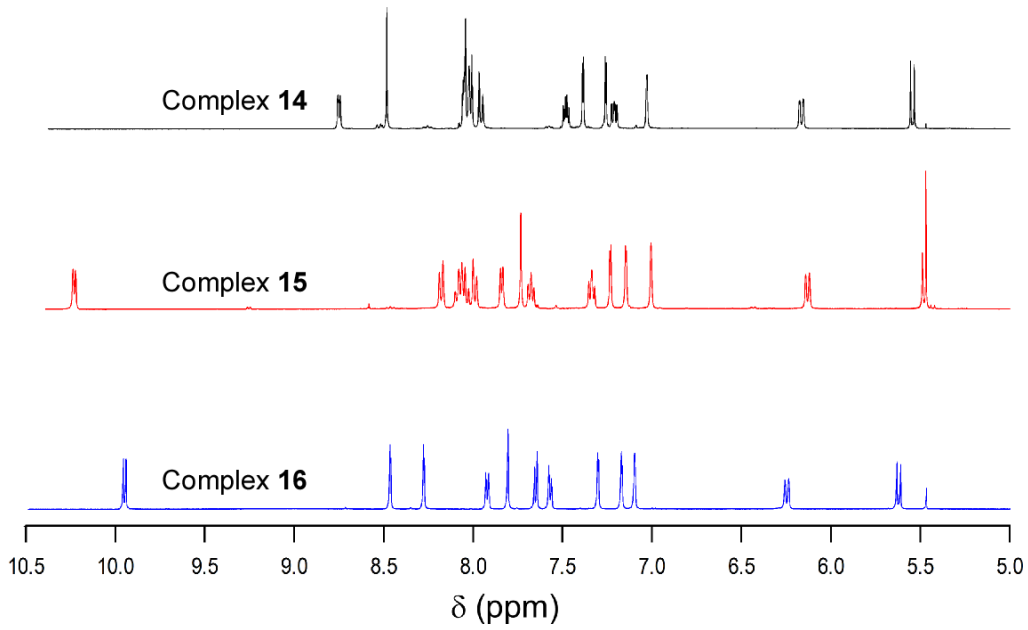

Figure 5.5 ^{1}H NMR spectra of complexes **14-16** in MeCN-d_3. Only the aromatic regions are shown for the sake of clarity.

5.3.2 Solid State Structures of Complexes 12-16.

Dark orange-brown crystals of the bimetallic complexes **12-16** suitable for X-ray diffraction analysis were grown from concentrated 1:1 solutions of CH_2Cl_2 and MeOH (or 1:1 acetone:MeOH in the case of **15**). Attempts to generate X-ray quality crystals of **17** were unsuccessful. Selected bond lengths and angles are provided in **Table 5.2** and **5.3**, and the representative structures of $[Cu_2(\mathbf{L^{N3O2}})(1MeBI)_2]^+$ ($\mathbf{12}^+$) and $[Cu_2(\mathbf{L^{N3O2}})(bpy)_2]^+$ ($\mathbf{13}^+$) are shown in **Figure 5.6(b)**. In each structure, the $\mathbf{L^{N3O2}}$ ligand supports a bimetallic core in which the metal centers are solely bridged by the central diarylamido group. For example, the unit cell of **12** contains two symmetrically-independent dicopper complexes with Cu1···Cu2 separations ($d_{Cu\text{-}Cu}$) of 3.0069(4) and

3.1202(4) (**Table 5.2**). The central $[Cu_2N]^{3+}$ unit exhibits a Cu1-N3-Cu2 angle near 97°, giving rise to an intermetallic "cleft". As intended, the $\mathbf{L^{N3O2}}$ framework provides meridional $[N,N,O]^{2-}$ coordination to both Cu^{2+} centers. The amido and phenolate donors of the fused pincer-type sites are pulled back slightly with O(1/2)-Cu(1/2)-N3 bond angles of 165 ± 3°. The Cu-O/N bond distances range from approximately 1.90 Å for the phenolate donors (O1, O2) to 2.05 Å for the bridging amido (N3) ligand. The additional coordination of two 1MeBI auxiliary ligands to each Cu^{2+} ion results in distorted square-planar geometries, although Cu1 is also weakly bound to a MeOH solvate (the Cu1-O6 distance is greater than 2.40 Å). The planes of the 1MeBI ligands are oriented nearly perpendicular to the square-planar $[CuN_3O]$ units, and the 1MeBI phenyl rings are positioned parallel to the imine groups on the inside of the cleft (**Figure 5.6(a)**).

Table 5.2. Selected Bond Distances (Å) and Angles (°) for the Two Symmetry-Independent Units (**A** and **B**) in the Crystal Structure of $[Cu_2(\mathbf{L}^{\mathbf{N3O2}})(1MeBI)_2]OTf$ (**12**).

Bond lengths	A	B
Cu1···Cu2	3.0069(4)	3.1202(4)
Cu1–O1	1.908(2)	1.921(2)
Cu1–N1	1.940(2)	1.950(2)
Cu1–N3	2.049(2)	2.061(2)
Cu1–N4 (1MeBI)	1.991(2)	2.006(2)
Cu1–O6 (MeOH)	2.537(2)	2.404(2)
Cu2–O2	1.902(2)	1.898(2)
Cu2–N2	1.920(2)	1.925(2)
Cu2–N3	2.035(2)	2.039(2)
Cu2–N6 (1MeBI)	1.987(2)	1.982(2)
Bond angles	A	B
Cu1–N3–Cu2	94.83(8)	99.10(8)
O1–Cu1–N1	92.55(7)	92.46(7)
O1–Cu1–N3	162.50(7)	162.62(7)
O1–Cu1–N4	88.53(7)	90.19(7)
N1–Cu1–N3	84.05(7)	84.20(7)
N1–Cu1–N4	175.12(8)	175.51(8)
N3–Cu1–N4	96.31(7)	94.32(7)
O2–Cu2–N2	94.05(7)	93.55(7)
O2–Cu2–N3	164.17(7)	167.41(7)
O2–Cu2–N6	89.15(7)	89.46(8)
N2–Cu2–N3	84.13(7)	84.46(7)
N2–Cu2–N6	166.02(8)	168.43(8)
N3–Cu2–N6	96.40(7)	94.96(8)
Twist angle [a]	66.3	73.2

[a] The twist angle refers to the angle between the planes of the aryl rings of the central amido unit.

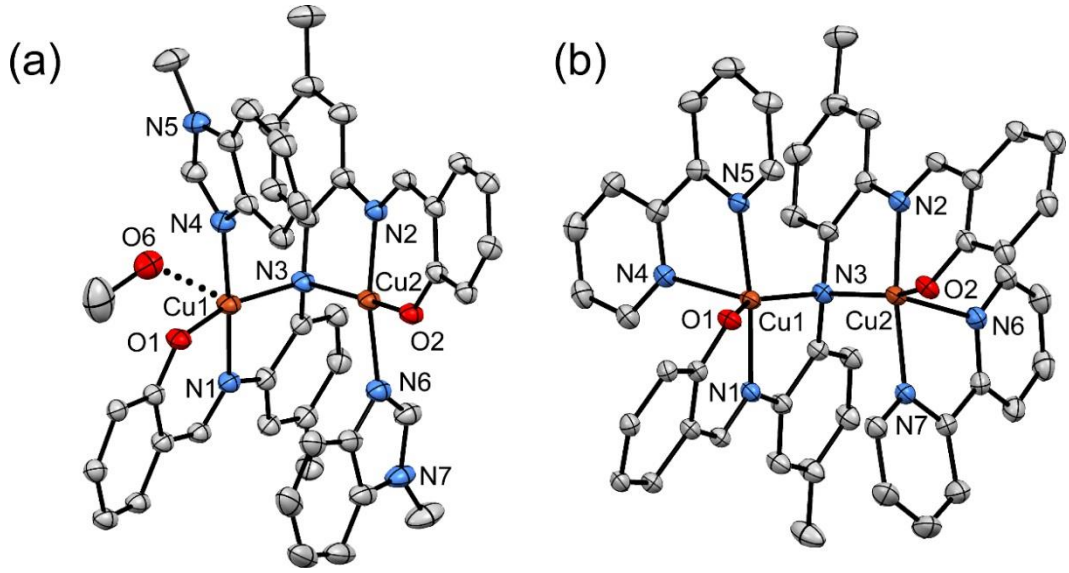

Figure 5.6 Thermal ellipsoid plots (40% probability) derived from the X-ray crystal structures of complexes **12** (a) and **13** (b). Hydrogen atoms, counteranions, and *tert*-butyl substituents of the phenolate donors have been omitted for the sake of clarity.

The meridional binding mode of the $\mathbf{L^{N3O2}}$ framework causes each half of the ligand to adopt an orientation in which the salicyaldimine unit is roughly co-planar with the adjacent arylamido ring. However, these planar halves of the $\mathbf{L^{N3O2}}$ ligand are rotated relative to one another due to the twisting of the diarylamido unit. The solid-state structures of **12-16** revealed "twist angles" between 60 and 73º for the aryl rings bonded to N3 (**Tables 5.2** and **5.3**). Therefore, the bimetallic complexes possess idealized C_2 symmetry and exist as racemic mixtures of (*M*)- and (*P*)-enantiomers, as illustrated in **Figure 5.7** [*Note*: The (*P*)-enantiomers of **12** and **13** are displayed in **Figure 5.6**]. In the next section, It will demonstrated that use of a chiral auxiliary ligand can force the $\mathbf{L^{N3O2}}$ ligand to favor one conformation over the other, resulting in a single diastereomeric product.

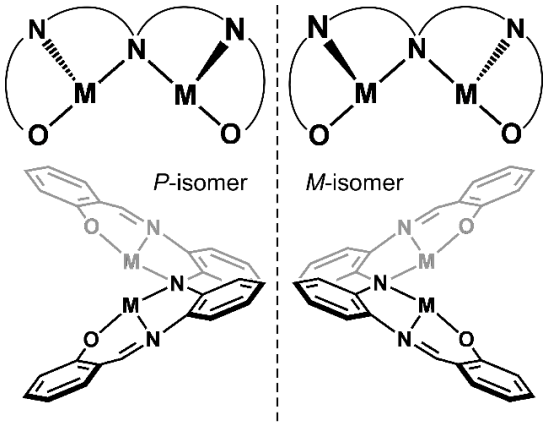

Figure 5.7 Illustration of the two possible orientations of the C_2-symmetric $\mathbf{L^{N3O2}}$ ligand in complexes **12**-**17**. The designations of the atropisomers (*M* and *P*) were based on rules developed for binapthyl systems.

The three bpy-containing complexes **13**-**15** (**Table 5.1**) yield quasi-isomorphous crystals in the monoclinic $P2_1/c$ space group (**Table 5.5**). The structure of $[Cu_2(\mathbf{L^{N3O2}})(bpy)_2]^+$ (**13**$^+$), shown in **Figure 5.6(b)**, is representative of the series. In each complex, the two metal ions occupy equivalent binding sites defined by the pincer-type *N*,*N*,*O*-chelates of the $\mathbf{L^{N3O2}}$ ligand, which adopts the same C_2-symmetric ("twisted") conformation described above. Coordination of the bidentate bpy ligands results in five-coordinate M^{2+} ions with distorted square-pyramidal (**15**) or trigonal-bipyramidal (**14**) geometries, as indicated by τ-values[118] in **Table 5.3**. The presence of the fifth donor causes the M^{2+} ions to move out of the plane defined by the meridional $\mathbf{L^{N3O2}}$ chelate by amounts ranging from 0.36 (**15**) to 0.80 Å (**14**). Each bpy ligand places one pyridyl donor *trans* to the imine N-atom (N1 or N2), while the other is located outside the cleft in a position opposite the intermetallic bond vector. Unlike the 1MeBI ligands in **12**, the bpy

ligands in **13-15** do not block access to the space between the metal ions, thus permitting the binding of small-molecules like O_2 (*vide infra*).

Table 5.3. Selected Bond Distances (Å) and Angles (°) Obtained from the Crystal Structures of Complexes **13-15**.

	complex **13**		complex **14**		complex **15**	
Bond distances	Cu1	Cu2	Zn1	Zn2	Co1	Co2
M1···M2	2.9667(5)		3.2820(5)		2.7010(5)	
M1–O1 / M2–O2	1.924(2)	1.921(2)	1.952(1)	1.956(1)	1.899(2)	1.895(2)
M1–N1 / M2–N2	1.940(2)	1.940(2)	2.054(1)	2.058(1)	1.889(2)	1.888(2)
M1–N3 / M2–N3	2.063(2)	2.052(2)	2.086(1)	2.103(1)	1.966(2)	1.964(2)
M1–N4 / M2–N6	2.201(2)	2.228(2)	2.100(1)	2.100(1)	2.064(2)	2.059(2)
M1–N5 / M2–N7	2.010(2)	2.008(2)	2.116(1)	2.118(1)	1.942(2)	1.943(2)
M–$L_{N/O}$ (ave)	2.028	2.030	2.062	2.067	1.952	1.950
Bond angles	Cu1	Cu2	Zn1	Zn2	Co1	Co2
M1–N3–M2	92.28(8)		103.15(6)		86.85(8)	
O1/O2–M–N1/N2	92.69(8)	92.58(9)	89.07(5)	88.52(5)	93.52(8)	93.92(7)
O1/O2–M–N3	146.38(8)	152.33(8)	140.53(5)	133.17(5)	158.41(7)	156.69(7)
O1/O2–M–N4/N6	114.49(8)	112.33(8)	114.66(5)	118.85(5)	106.01(7)	105.79(7)
O1/O2–M–N5/N7	91.23(8)	88.30(8)	90.43(5)	94.39(5)	84.38(7)	86.33(7)
N1/N2–M–N3	83.05(8)	84.09(9)	81.72(5)	80.43(5)	85.02(8)	84.76(7)
N1/N2–M–N4/N6	93.85(8)	94.33(8)	97.25(5)	97.34(5)	91.98(8)	91.57(8)
N1/N2–M–N5/N7	171.34(9)	171.63(9)	174.87(5)	175.18(5)	171.85(8)	172.13(8)
N3–M–N4/N6	99.09(8)	95.33(8)	104.57(5)	107.69(5)	95.57(8)	97.51(8)
N3–M–N5/N7	97.87(8)	98.93(8)	101.83(5)	100.25(5)	99.83(8)	98.11(7)
N4/N6–M–N5/N7	77.50(8)	77.66(8)	78.33(5)	77.89(5)	81.08(8)	80.81(8)
τ-value [a]	0.42	0.32	0.57	0.70	0.22	0.26
twist angle [b]	64.0		67.6		61.7	

[a]For definition of the τ-value, see reference[168]. [b]The twist angle refers to the angle between the planes of the aryl rings of the central amido unit.

Table 5.3 reveals several trends in metric parameters across the **13-15** series. The M-$L_{N/O}$ bond distances and intermetallic separations are strongly dependent on metal ion

identity, both following the general order of Zn > Cu > Co. Of particular note is the observed Co···Co distance ($d_{Co\text{-}Co}$) of 2.701 Å, which is remarkably short given the presence of only one bridging ligand. A search of the Cambridge Structural Database found that nearly all di- and polycobalt complexes with $d_{Co\text{-}Co} < 2.8$ Å possess multiple bridging groups. While it is not proper to invoke the existence of a Co-Co bond in **15**, since the intermetallic distance exceeds the sum of van der Waals radius of Co (2.486 Å), this feature points to strong electronic interactions between the Co^{2+} centers. In addition, the average Co-$L_{N/O}$ distance of 1.951 Å in **15** is unusually small. High-spin Co^{2+} complexes with N_4O ligand sets typically exhibit average Co-$L_{N/O}$ lengths of 2.07 ± 0.05 Å, while the handful of low-spin [CoN_4O] structures in the literature feature average Co-$L_{N/O}$ bonds of 1.95 ± 0.05 Å.[239-241] Thus, the crystallographic data indicate that **15** consists of two low-spin Co^{2+} centers in square-pyramidal environments. The electronic structure of this complex is described in more detail in the DFT section below.

Not surprisingly, the solid-state structures of complex **15** and its bpy^{Br2}-containing congener (**16**) are quite similar, with one exception: the addition of bromine substituents causes a modest lengthening of the Co···Co distance from 2.701 to 2.837 Å, with a concomitant increase in the Co1-N3-Co2 bond angle (**Table 5.4**). Otherwise, the Co-N/O bond lengths in **15** and **16** differ by less than 0.025 Å, indicating that both complexes feature low-spin Co^{2+} centers.

Table 5.4 Selected Bond Distances (Å) and Angles (°) Obtained from the Crystal Structures of Complexes **16** and **16-O_2**.

	16		**16-O_2**	
Bond distances	Co1	Co2	Co1	Co2
Co1···Co2	2.8366(5)		3.253(1)	
Co1–O1 / Co2–O2	1.900(1)	1.897(1)	1.873(4)	1.904(3)
Co1–N1 / Co2–N2	1.887(2)	1.891(2)	1.888(4)	1.881(4)
Co1–N3 / Co2–N3	1.980(2)	1.986(2)	2.011(4)	2.042(4)
Co1–N4 / Co2–N6 (bpy)	2.048(2)	2.062(2)	1.955(5)	1.971(4)
Co1–N5 / Co2–N7 (bpy)	1.949(2)	1.959(2)	1.990(4)	2.002(4)
Co1–O3 / Co2–O4			1.868(4)	1.846(4)
O3–O4			1.372(6)	
Bond angles	Co1	Co2	Co1	Co2
Co1–N3–Co2	91.33(7)		106.7(2)	
O1/O2–Co–N1/N2	92.90(7)	93.52(7)	95.13(18)	92.80(16)
O1/O2–Co–N3	162.98(7)	154.99(7)	177.54(17)	177.04(16)
O1/O2–Co–N4/N6	99.71(7)	104.81(6)	88.53(18)	88.02(16)
O1/O2–Co–N5/N7	82.84(6)	89.08(6)	83.60(18)	86.73(16)
N1/N2–Co–N3	85.12(7)	84.44(7)	84.72(18)	84.69(17)
N1/N2–Co–N4/N6	96.87(7)	93.28(7)	93.10(18)	94.08(18)
N1/N2–Co–N5/N7	174.67(7)	173.61(7)	175.07(17)	175.62(18)
N3–Co–N4/N6	97.31(7)	100.19(7)	93.93(18)	93.71(16)
N3–Co–N5/N7	99.90(7)	95.65(7)	96.76(18)	95.89(17)
N4/N6–Co–N5/N7	80.76(7)	80.41(7)	82.12(18)	81.55(16)
τ-value[a]	0.19		0.31	

[a]For definition of the τ-value, see reference[168].

5.3.3 Formation of the Chiral Complex [Zn_2(*P*-L^{N3O2})(*S*-^{iPr}OxPy)$_2$]OTf (17).

There has been a long-standing interest in developing chiral bimetallic complexes for use in asymmetric catalysis and supramolecular chemistry.[242-249] As noted above, the bimetallic complexes **12-16** possess helical chirality due to the C_2-symmetry imposed by the $\mathbf{L^{N3O2}}$ framework (**Figure 5.7**). We were curious whether the use of a chiral auxiliary ligand would bias the helical sense of the $\mathbf{L^{N3O2}}$ ligand, thereby yielding a single

diastereomeric product. To this end, the reaction of $Zn(OTf)_2$ and $H_3\mathbf{L}^{\mathbf{N2O3}}$ with the auxiliary ligand *S*-^{iPr}OxPy (**Table 5.1**) was performed in the presence of base. The ^{1}H NMR spectrum of the resulting product (**17**), shown in **Figure 5.8**, displays only one set of well-resolved peaks arising from the $\mathbf{L}^{\mathbf{N3O2}}$ and *S*-^{iPr}OxPy ligands, indicating that the material largely consists of a single diastereomer. However, a number of weak and poorly-resolved features are also apparent (indicated by the asterisks in **Figure 5.8(a)**); if these are assigned to the minor diastereomer, then relative peak heights suggest that at least 85% of **17** exists as the major product. Further evidence of diastereomeric excess is provided by circular dichroism (CD) spectroscopy. As shown in **Figure 5.8(b)**, the CD spectrum of **17** exhibits positive and negative bands at 470 and 380 nm, respectively, corresponding to the two overlapping bands in the absorption spectrum. Since these features arise from $\mathbf{L}^{\mathbf{N3O2}}$-based transitions (*vide supra*), we can conclude that the $\mathbf{L}^{\mathbf{N3O2}}$ ligand largely exists in a single helical conformation. As expected, the CD spectrum of the bpy-containing dizinc(II) analog (**14**) is featureless across the UV-vis region (**Figure 5.8**) because the complex exists as a racemic mixture of *M*- and *P*-enantiomers.

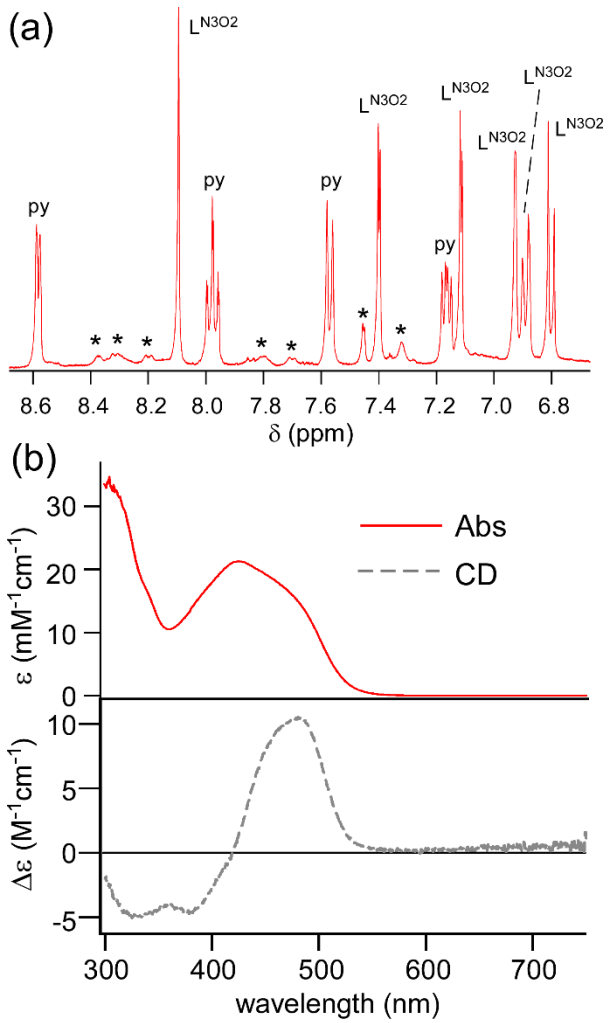

Figure 5.8 *Top*: Aromatic region of the ^{1}H NMR spectrum of complex **17** in MeCN-d_3. The peaks are assigned to either the pyridyl (py) moiety of *S*-^{iPr}OxPy or the $\mathbf{L^{N3O2}}$ ligand based on splitting patterns and comparison to data collected for $H_3\mathbf{L^{N3O2}}$ and **14**. Each of the 10 assigned features integrates to two H-atoms. The ill-defined peaks marked with asterisks arise from the minor diastereomeric product. *Bottom*: Absorption and CD spectra of **17** collected at room temperature in MeCN.

In complex **17**, the oxazoline ring of the asymmetric *S*-^{iPr}OxPy ligand can be positioned either *cis* or *trans* to the imine donors (N1 and N2). The combination of geometric and stereo isomerism gives rise to four possible C_2-symmetric structures: *trans*-(*M*,*S*,*S*), *cis*-(*M*,*S*,*S*), *trans*-(*P*,*S*,*S*), and *cis*-(*P*,*S*,*S*). The energy of each isomer was

computed using DFT and the most stable structure was found to be *cis*-(*P*,*S*,*S*), shown in **Figure 5.9**. This isomer minimizes steric interactions between the isopropyl groups of *S*-^{iPr}OxPy and the $\mathbf{L^{N3O2}}$ ligand. Relative to *cis*-(*P*,*S*,*S*), the *cis*-(*M*,*S*,*S*) diastereomer is higher in energy by 6.4 kcal/mol because the isopropyl groups are directed towards the central aryl rings. The *trans*-(*M*,*S*,*S*) and *trans*-(*P*,*S*,*S*) structures are even more unfavorable energetically (7.0 and 9.9 kcal/mol, respectively), as the isopropyl groups sterically clash with either the phenyl rings of the diarylamido unit (*M*-isomer) or the *tert*-butyl substituents of the phenolate donors (*P*-isomer). These DFT results suggest that the major isomer of **17**, observed spectroscopically in solution, corresponds to the *cis*-(*P*,*S*,*S*) diasteromer. Based on the computed energy differences, we would not expect to detect the minor isomer at room temperature. The fact that the minor *cis*-(*M*,*S*,*S*) diastereomer is observed in the ^{1}H NMR spectrum of **17** (**Figure 5.8**) suggests that the *M*- and *P*-isomers cannot easily interconvert to yield the thermodynamically-favored product, and thus the product ratio is also affected by kinetic factors.

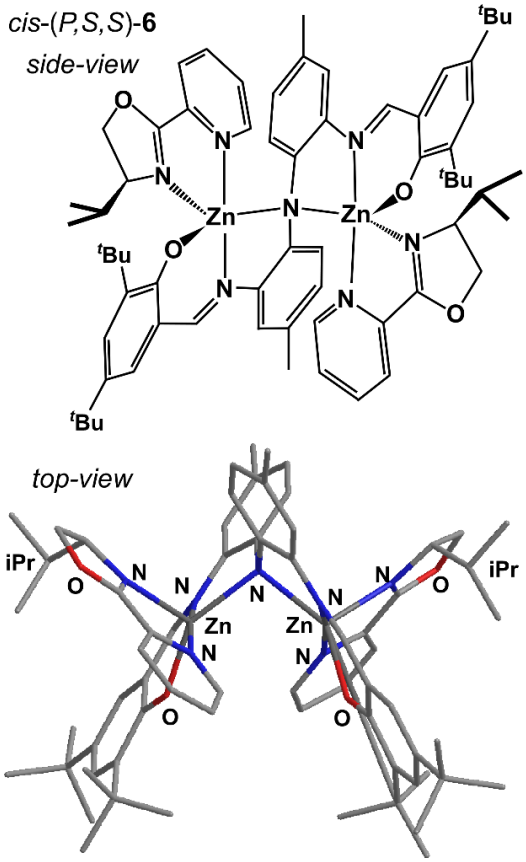

Figure 5.9 Depictions of the *cis*-(*P*,*S*,*S*) diastereomer of complex **17**.

5.3.4 Electrochemical Studies.

Voltammetric methods were used to examine the electrochemical properties of complexes **13-16** in MeCN solutions with 0.1 M $(NBu_4)PF_6$ as the supporting electrolyte and scan rates of 100 mV/s. The reported potentials are relative to the Fc/Fc^+ couple. The cyclic and square-wave voltammograms (CV and SWV) of the dicopper complex **13**, shown in **Figure 5.10**, reveal three redox features at negative potentials of -1.40, -1.83, and -2.06 V. The two lowest-potential events are quasi-reversible whereas the peak at -

1.40 V is irreversible. The SWV of the analogous dicobalt complex (**15**) displays three peaks at very similar potentials of -1.42, -1.81, and -2.04 V. Assignment of these features to either metal- or ligand-based reductions is aided by comparison with data collected for **14**, which contains redox-inactive Zn^{2+} ions. The voltammogram of **14** retains the two lowest-potential features at -1.95 and -2.08 V; however, the first reduction wave is absent (**Figure 5.10**). Therefore, we can confidently assign the two events at E < -1.7 V to reduction of the bpy auxiliary ligands, while the event near -1.4 V is attributed to reduction of the Cu_2^{4+} and Co_2^{4+} units to yield mixed-valent species. Electrochemical data obtained for the bpy^{Br2}-containing dicobalt complex (**16**) provide further confirmation of these assignments. Relative to **15**, the two lowest-potentials peaks of **16** are shifted positively by ~0.23 V, reflecting the electron-withdrawing capacity of the 4-Br substituents. In contrast, the metal-based peak experiences a much smaller shift from -1.42 to -1.33 V. The redox-active nature of bpy ligands has been well-established in numerous studies,[250-252] including recent efforts by the Wieghardt group.[253,254-259] The homoleptic $[Fe(bpy)_3]^{2+}$ complex, for example, exhibits sequential reductions of the three bpy ligands at potentials of -1.66, -1.94, and -2.10 V.[253] The corresponding potentials in **13**-**15** are more negative than those reported for $[Fe(bpy)_3]^n$ by 100-150 mV, likely due to the trianionic nature of the $\mathbf{L^{N3O2}}$ framework.

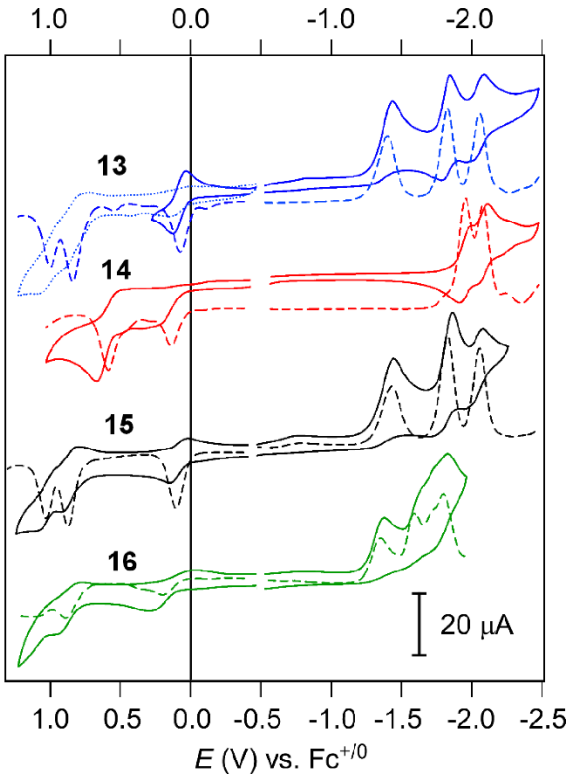

Figure 5.10 Cyclic voltammograms (solid lines) of complexes **13-16** collected in MeCN with 0.1 M $(NBu_4)PF_6$ as the supporting electrolyte. The corresponding square-wave voltammograms are indicated by the dashed lines. All scan rates were 100 mV/s. Data in the high- and low-potential regions were generally collected in separate scans. Two CVs with different sweep widths are provided for complex **13**.

To more positive potentials, all four complexes exhibit a feature between 0.07 and 0.19 V. While this redox event is quasi-reversible for **13** and **15** (ΔE = 83 and 115 mV, respectively), it is irreversible in the cases of **14** and **16**, as evident in the diminished intensity of the corresponding peaks in the SWV (**Figure 5.10**). Given its presence across the **13-16** series, it is logical to attribute this feature to a ligand-based event. Indeed, a survey of the literature revealed that the diarylamido moieties of PNP pincer ligands are oxidized between +0.32 and -0.34 V,[213,218,260,261] and the di(2-pyrazolylaryl)amido pincers

of Gardinier and coworkers undergo oxidation near 0.0 V.[195,262] The common feature near 0.1 V in complexes **13**-**16** is therefore assigned to oxidation of the μ-NAr_2 unit of the $\mathbf{L^{N3O2}}$ ligand. Evidence for formation of a ligand-based radical upon one-electron oxidation of **15** (**Scheme 5.1**) is provided in the EPR and DFT studies described in section 5.3.5.

In addition, complexes **13** and **15** exhibit two closely-spaced waves centered near 0.90 V (**Figure 5.10**). These features correspond to successive oxidations of the divalent metal ions, although the processes likely involve partial oxidation of the phenolate donors as well. Support for the latter conclusion is found in the CV and SWV data of the dizinc(II) analog (**14**), which display an ill-defined event in the same region despite the absence of redox-active metal ions. Previous studies of related mononuclear complexes have detected phenolate oxidations in the range of 0.5 to 1.5 V versus $Fc^{+/0}$,[263-266] although it is often difficult to distinguish between ligand- and metal-based events due to the high covalency of metal-phenolate bonds.

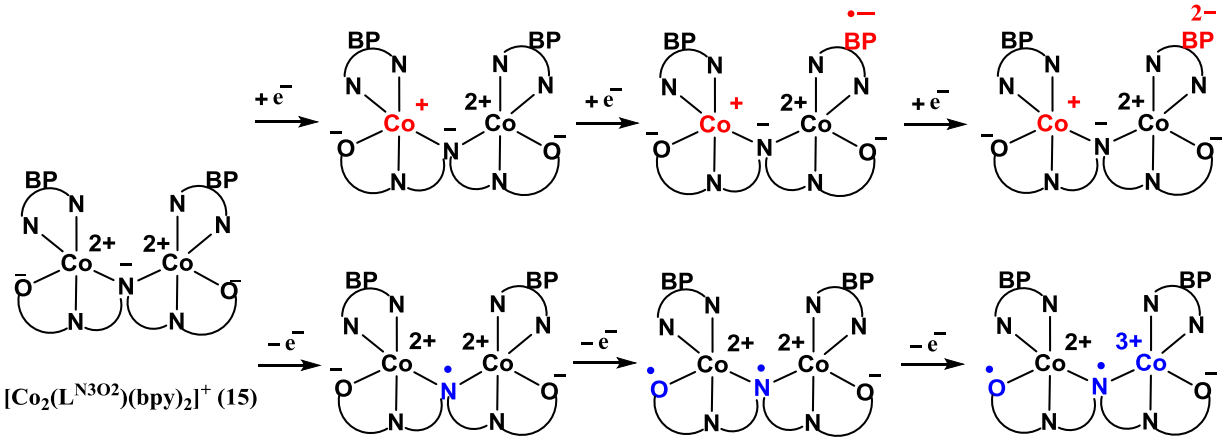

Scheme 5.1 Illustration of redox behaviors of $[Co_2(\mathbf{L}^{N3O2})(bpy)_2]^+$ (**15**) in MeCN.

5.3.5 Spectroscopic and Computational Studies of 15 and 15^{ox}.

Density functional theory (DFT) was employed to examine the unusual electronic properties of $[Co_2(\mathbf{L}^{N3O2})(bpy)_2]^+$ ($\mathbf{15}^+$), namely, its diamagnetism and short Co-Co distance. These calculations employed the hybrid B3LYP functional and crystallographically-determined structure, although the *tert*-butyl substituents of the phenolate rings were replaced with H-atoms. The proper wavefunction for the $S = 0$ ground-state was obtained using the broken-symmetry (BS-DFT) approach pioneered by Noodleman and others.[267,268] The BS-DFT calculations revealed strong antiferromagnetic (AF) coupling between the low-spin Co^{2+} centers, with a computed exchange coupling constant (J) of -1050 cm^{-1} (based on the Yamaguchi definition[269,270] of $H = -2J\, S_A \bullet S_B$). The AF coupling arises from direct overlap of the $3d(z^2)$-based singly-occupied molecular orbitals (SOMOs) localized on each Co^{2+} center (the local z-axes are directed

along the axial Co-N bonds; see **Figure 5.11**). The overlap integral (*S*) for these two magnetic orbitals with opposite spin is 0.29, consistent with the presence of a *partial* Co-Co bond in **15**. The magnitude of the computed *J*-value ensures that the triplet state is not accessible at room-temperature.

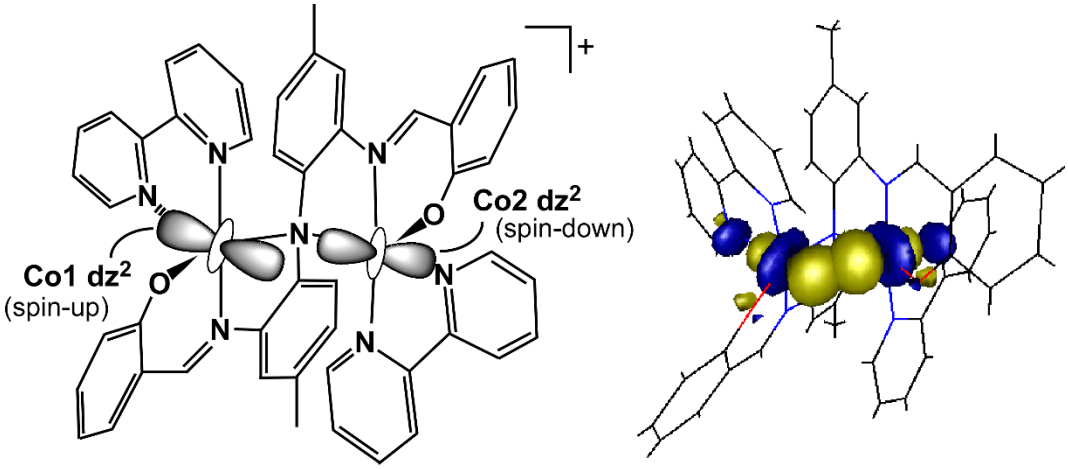

Figure 5.11 *Left*: Schematic illustrating the origin of antiferromagnetic coupling from the direct overlap of the 3d(z^2)-based SOMOs localized on each Co^{2+} center in complex **15**. *Right*: DFT-derived contour plots of the singly-occupied 3d(z^2)-based MOs.

Based on the electrochemical results presented above, we sought to generate the oxidized form of complex **15** via chemical means. Treatment of **15** with one equivalent of 1'-acetylferrocenium (AcFc; E = 0.27 V) in MeCN causes the ligand-based absorption band near 400 nm to red-shift and decrease in intensity (**Figure 5.12**; insert), indicative of a change in the π-system of the $\mathbf{L^{N3O2}}$ ligand. The X-band EPR spectrum of the one-electron oxidized species ($\mathbf{15^{ox}}$), shown in **Figure 5.12**, consists of a broad derivative

feature centered at g = 2.02. The presence of ^{59}Co hyperfine splitting at both high and low fields is particularly evident in the 2nd-harmonic spectrum. The data is nicely simulated (**Figure 5.12**) with the following spin-Hamiltonian parameters: a pseudo-axial **g**-tensor ($g_{x,y,z}$ = 2.059, 2.037, 1.995) and hyperfine coupling constants of $A_{x,y,z}$ = 23, 21, and 7.1 G for both Co ions. Low-spin, five-coordinate Co^{2+} centers typically display A_{max} values between 80 and 120 G, and g_x-values near 2.40.[271] In contrast, the modest *g*-anisotropy and small *A*-values of **15^{ox}** more closely resemble the EPR parameters of mononuclear Co/O_2 adducts ($g_{x,y}$ = 2.08 and A_{max} ~ 20 G), where the unpaired spin largely resides on the superoxo ligand.[271] Therefore, the EPR data provide further evidence that one-electron oxidation of **15** generates a ligand-based radical, although the unpaired spin is partially delocalized over the two Co ions.

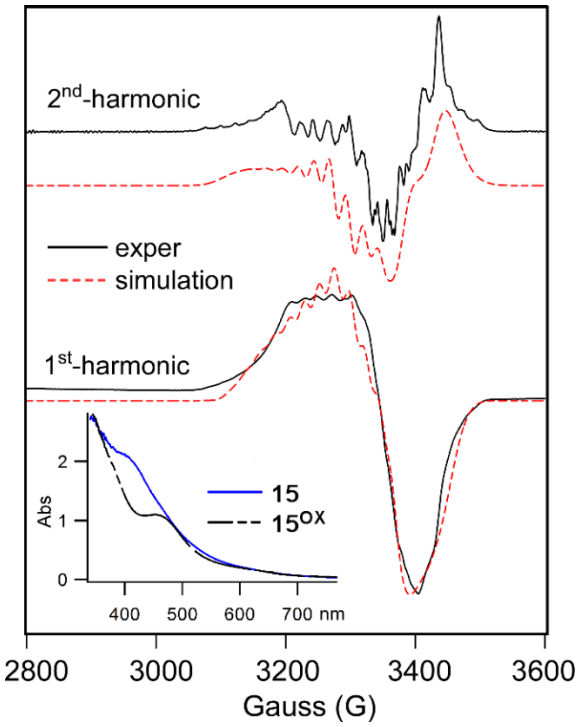

Figure 5.12 X-band EPR spectrum of **15^{ox}** (black, solid) in frozen MeCN at 77 K. The presence of ^{59}Co hyperfine splitting is clearly apparent in the corresponding 2nd-harmonic data (top). The simulated spectra (red, dashed) were obtained with the following parameters: $g_{x,y,z}$ = 2.059, 2.037, 1.995; $A_{x,y,z}$ = 23, 21, and 7.1 G; mwFreq = 9.434 GHz. *Inset*: Absorption spectra of **15** (blue, solid) and **15^{ox}** (black, dashed) in MeCN (conc. = 0.1 mM).

The nature of the **L^{N3O2}**-based radical was probed with BS-DFT calculations. Because a crystal structure of **15^{ox}** is not available, a computational model was obtained via geometry optimization. Comparison of Mulliken spin populations indicate that one-electron oxidation of **15** to **15^{ox}** causes a dramatic increase in the amount of unpaired spin density on the **L^{N3O2}** ligand (from 0.04 to 0.74 spins), while the spin of the Co centers remains nearly constant. The **15^{ox}** model contains three unpaired electrons: two are localized in Co(dz^2)-based MOs, while the third is primarily localized on the central μ-

NAr_2 unit of the $\mathbf{L^{N3O2}}$ ligand. The contour plot of the $\mathbf{L^{N3O2}}$-based SOMO, shown in **Figure 5.13**, reveals overlap between the $2p_z$ orbital of the bridging N-atom (N3) and Co 3d orbitals, accounting for the observable ^{59}Co hyperfine splitting in the EPR spectrum of $\mathbf{15^{ox}}$. The DFT calculations are therefore consistent with the formulation of $\mathbf{15^{ox}}$ as $[Co^{2+}{}_2(\mathbf{L^{N3O2,\bullet}})(bpy)_2]^{2+}$, in agreement with the electrochemical and spectroscopic data already presented.

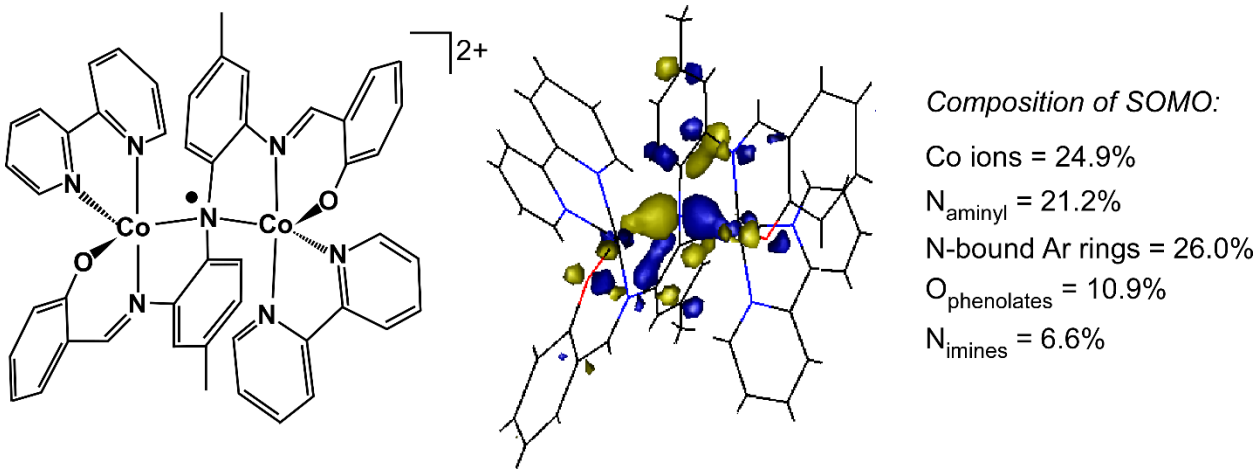

Figure 5.13 Contour plot of the singly-occupied molecular orbital (SOMO) localized on the $\mathbf{L^{N3O2}}$ ligand of $\mathbf{15^{ox}}$. The percent composition of this SOMO is also provided.

5.3.6 Reactivity of Complex 16 with O_2.

If exposed to air, solutions of **16** in 1:1 CH_2Cl_2:MeOH provide dark-brown crystals with unit cell parameters distinct from those determined for anaerobically-grown crystals (**Table 5.5**). X-ray diffraction analysis determined that the aerobic crystals

consist of $[Co_2(O_2)(\mathbf{L^{N3O2}})(bpy)_2]ClO_4$ (**16-O$_2$**), where a diatomic O_2 ligand bridges in a μ-1,2-fashion between the six-coordinate cobalt centers (**Figure 5.14**). The O3-O4 distance of 1.372(6) Å identifies the bridging ligand as a peroxide (O_2^{2-}) moiety. The $[Co_2O_2]$ unit adopts a twisted orientation with a Co-O-O-Co dihedral angle of 56.3° and Co1···Co2 distance of 3.253(1) Å – considerably longer than the $d_{Co\text{-}Co}$ value of 2.70 Å found for **16**. Significantly, the **16-O$_2$** structure proves that small molecules are able to access the open coordination sites within the intermetallic cleft, despite the steric bulk of the nearby *tert*-butyl substituents of the phenolate donors. Moreover, the dramatic 0.55 Å increase in intermetallic separation upon O_2 binding highlights the structural pliability of the $\mathbf{L^{N3O2}}$ scaffold.

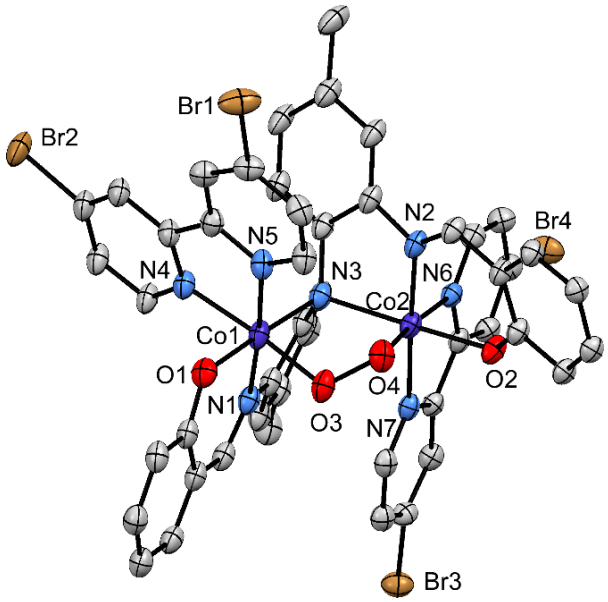

Figure 5.14 Thermal ellipsoid plot (30% probability) derived from the X-ray crystal structure of complex **16-O$_2$**. Hydrogen atoms, counteranions, and *tert*-butyl substituents of the phenolate donors have been omitted for the sake of clarity.

Comparison of metric parameters indicates that the conversion of **16→16-O_2** involves oxidation of the low-spin Co^{2+} centers to Co^{3+}. This conclusion is evident in the shortening of the axial Co1-N4 and Co2-N6 bonds by ~0.09 Å due to the transfer of two Co(d_{z^2})-based electrons to O_2 (**Table 5.4**). In contrast, O_2-binding does not cause significant changes in the O-C, N-C, and C-C bond lengths of the $\mathbf{L^{N3O2}}$ ligand, indicating a lack of radical character. Based on the electrochemical data presented above, one might have assumed that O_2 binding would result in oxidation of the $\mathbf{L^{N3O2}}$ ligand. It appears that the increase in coordination number from 5 to 6, coupled with the dianionic nature of the peroxide ligand, suppresses the redox potentials of the Co centers relative to $\mathbf{L^{N3O2}}$. These factors favor metal-centered oxidation over ligand-based oxidation in formation of the dicobalt-peroxo complex.

5.4 Conclusions

As demonstrated in this chapter, the easily-prepared $\mathbf{L^{N3O2}}$ ligand is capable of supporting homobimetallic frameworks (M = Co, Cu, Zn) with adjacent pincer-type compartments consisting of a bridging diarylamido group and salicyaldimine chelates (**Figure 5.1**). The "fused" nature of the pincer sites results in short intermetallic distances between 2.7 and 3.3 Å, as determined by X-ray crystallography. While several complexes with [$M_2(\mu\text{-}NAr_2)_2$] cores have been reported in the literature, complexes **12-17** are rather unique in containing only a single diarylamido bridge.[272] Because of this,

the unsaturated metal centers are capable of binding auxiliary ligands, such as 1MeBI, bpy^{R2}, and *S*-^{iPr}OxPy. These auxiliary ligands impart additional features to the bimetallic complexes that may prove useful in future applications; for example, the noninnocent bpy^{R2} ligands in **13**-**16** account for two redox events at low potentials, while the optically-active *S*-^{iPr}OxPy ligand compels the C_2-symmetric structures to favor the *P*-configuration. Thus, the $\mathbf{L^{N3O2}}$ ligand provides a versatile platform for the synthesis of bimetallic complexes with tunable electronic and structural properties.

Electrochemical studies of the bpy-containing complexes **13** and **15** found six redox couples over a range of 3.0 V arising from both metal- and ligand-based events. The one-electron oxidation of **15** near 0.1 V triggers formation of a $\mathbf{L^{N3O2}}$-based radical localized on the diarylamido donor, as indicated by EPR and DFT studies of $\mathbf{15^{ox}}$. This finding is consistent with previous studies of $[M_2(\mu\text{-}NAr_2)_2]$ complexes. The ability to perform several electron-transfers is critical for synthetic catalysts involved in small-molecule activation, such as the reduction of O_2 (to H_2O) and H^+ (to H_2). Redox-active ligands, like bpy and $\mathbf{L^{N3O2}}$ in complexes **13**-**16**, can serve as electron reservoirs for multielectron transformations. Most significantly, *the complexes described here feature open and accessible coordination sites between the metal centers for small-molecule binding*. As highlighted by formation of the μ-peroxo complex $\mathbf{16\text{-}O_2}$ (**Figure 5.14**), the $\mathbf{L^{N3O2}}$ scaffold has the structural flexibility to accommodate the changes in coordination number and oxidation state that occur during catalytic cycles. Therefore, we are currently

evaluating the ability of these promising binuclear complexes to serve as electrocatalyts for the reduction of O_2 and H^+.

Table 5.5 Summary of X-ray crystallographic data collection and structure refinement

	$H_3\mathbf{L}^{N3O2}$	**1**•2.5MeOH	**2**•2CH_2Cl_2•MeOH[a]	**3**•CH_2Cl_2	**4**•2MeOH•acetone
Empirical	$C_{44}H_{57}N_3O_2$	$C_{63.5}H_{80}Cu_2F_3N_7O_{7.5}S$	$C_{68}H_{78}Cl_4Cu_2F_3N_7O_6S$	$C_{66}H_{72}Cl_2F_3N_7O_5SZn_2$	$C_{69}H_{84}ClCo_2N_7O_9$
Formula weight	659.93	1277.50	1447.35	1334.01	1308.77
Crystal system	triclinic	triclinic	monoclinic	monoclinic	monoclinic
Space group	*P*-1	*P*-1	$P2_1/c$	$P2_1/c$	$P2_1/c$
a [Å]	9.9973(3)	16.5852(5)	13.69383(18)	13.90318(12)	13.58121(17)
b [Å]	14.7313(5)	19.3538(4)	24.2156(3)	22.51761(16)	24.3465(3)
c [Å]	14.8047(5)	21.8526(6)	21.4722(2)	22.85172(15)	21.1737(2)
α [°]	101.685(3)	83.0414(19)	90	90	90
β [°]	109.567(3)	68.429(3)	99.1436(12)	100.1123(8)	100.4205(12)
γ [°]	95.189(3)	87.206(2)	90	90	90
Volume [$Å^3$]	1982.02(12)	6475.0(3)	7029.79(15)	7042.97(9)	6885.74(15)
Z	2	4	4	4	4
ρ_{calc} [g/cm^3]	1.106	1.314	1.319	1.258	1.284
λ (Å)	1.5418	1.5418	1.5418	1.5418	1.5418
μ [mm^{-1}]	0.517	1.699	2.50	2.29	4.63
Θ range [°]	6.2 to 147.5	5.8 to 147.8	6.5 to 147.6	6.5 to 147.4	6.6 to 147.3
Reflections	15488	119292	66840	68466	66905
Independent	15488	25669 (0.0501)	14010 (0.0437)	14000 (0.0325)	13740 (0.0293)
Data/restraints/p	15488/0/465	25669/19/1614	14010/0/859	14000/0/789	13740/34/935
Goodness-of-fit	1.073	1.054	1.038	1.056	1.054
*R*1/*wR*2 indexes	0.0519 / 0.1504	0.0461 / 0.1304	0.0573 / 0.1640	0.0349 / 0.0978	0.0490 / 0.1292
*R*1/*wR*2 indexes	0.0594 / 0.1563	0.0551 / 0.1375	0.0631 / 0.1716	0.0376 / 0.1000	0.0524 / 0.1317

[a] One of the CH_2Cl_2 solvates is only 40% occupied.

Table 5.5 (continued). Summary of X-ray crystallographic data collection and structure refinement

	16•2MeOH	**16-O$_2$**•2CH_2Cl_2
Empirical formula	$C_{66}H_{74}Br_4ClCo_2N_7O_8$	$C_{66}H_{70}Br_4Cl_5Co_2N_7O_8$
Formula weight	1566.27	1704.04
Crystal system	triclinic	triclinic
Space group	*P*-1	*P*-1
a [Å]	11.7740(3)	13.1787(3)
b [Å]	13.3797(3)	13.8609(3)
c [Å]	21.9485(5)	22.2351(3)
α [°]	103.594(2)	81.946(2)
β [°]	90.977(2)	89.983(2)
γ [°]	93.698(2)	71.562(2)
Volume [Å^3]	3351.89(13)	3810.93(13)
Z	2	2
ρ_{calc} [g/cm^3]	1.552	1.485
λ (Å)	1.5418	1.5418
μ [mm^{-1}]	7.510	7.915
Θ range [°]	6.8 to 148.3	7.1 to 148.4
Reflections collected	37783	71885
Independ. reflections (R_{int})	13369 (0.0296)	15226 (0.0440)
Data/restraints/parameters	13369/0/831	15266/0/843
Goodness-of-fit on F^2	1.025	1.099
*R*1/*wR*2 indexes [I >2σ(I)]	0.0292 / 0.0700	0.0730 / 0.2090
*R*1/*wR*2 indexes [all data]	0.0315 / 0.0716	0.0834 / 0.2197

Chapter 6

Synthesis and Characterization of Metal Complexes Supported by Redox-Active Ligand L^{N3P2} and L^{N5}

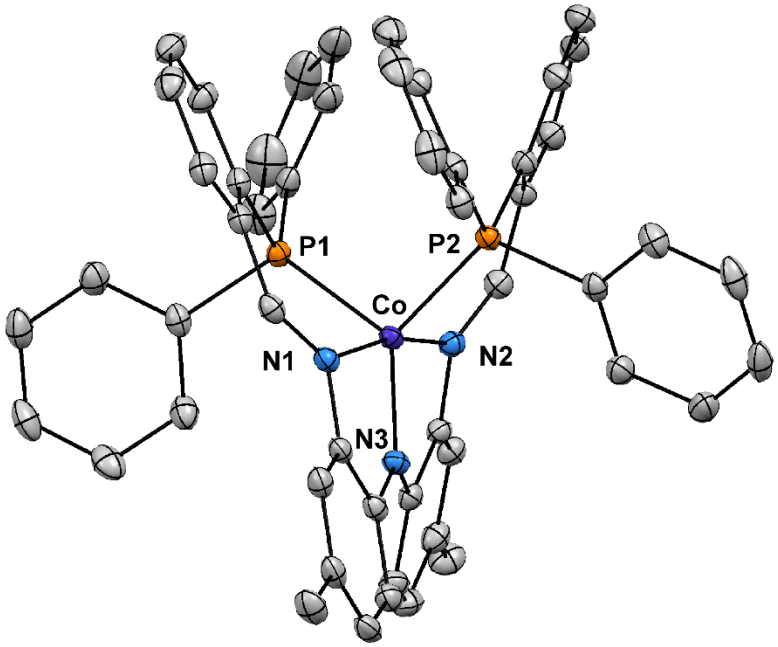

Abstract: Our lab has designed and synthesized ligands $\mathbf{L^{N5}}$ and $\mathbf{L^{N3P2}}$ as analogues of the "fused" pincer-type $\mathbf{L^{N3O2}}$ ligand reported in Chapter 5. The $\mathbf{L^{N5}}$ ligand incorporates neutral quinoline rings into the arms of the pincer units in order to modify the chemical and redox properties of the resulting complexes (relative to the $\mathbf{L^{N3O2}}$-based species). The $\mathbf{L^{N3P2}}$ ligand contains "soft" phosphine donors in an effort to stabilize low metal oxidation states in electrocatalytic processes. The coordination chemistry of the $\mathbf{L^{N5}}$ and $\mathbf{L^{N3P2}}$ scaffolds and the electrochemical properties of the corresponding complexes are described.

6.1 Introduction

It is difficult to overstate the importance of transition metals in both biological[3] and industrial catalysis.[273] While metalloenzymes typically employ first-row transition metal ions (e.g., Fe, Cu, Mn) in the activation of small molecules, synthetic catalysts rely heavily on second- and third-row transition metals (Pd, Ru, Rh, and Pt) that are rare and expensive. As indicated by **equations 1-4**, the activation of small molecules like N_2, O_2, H_2, and CO_2 is often a multielectron process.

$$N_2 + 6H^+ + 6e^- \rightarrow NH_3 \qquad \textbf{equation 1}$$

$$O_2 + 4H^+ + 4e^- \rightarrow 2\ H_2O \qquad \textbf{equation 2}$$

$$H_2 \rightarrow 2H^+ + 2e^- \qquad \textbf{equation 3}$$

$$CO_2 + 2H^+ + 2e^- \rightarrow CO + H_2O \qquad \textbf{equation 4}$$

Since first-row transition metal ions are best suited for one-electron transfers, nature requires large and complex polynuclear metal clusters to carry out these transformations. Examples include the FeMo cofactor (FeMoCo) of nitrogenase, the oxygen-evolving complex (OEC) of photosystem II, the H-cluster of [FeFe]-hydrogenase, and the C-cluster of carbon monoxide dehydrogenase (CODH). The elaborate structures of the bioclusters are difficult to replicate in synthetic models.

One strategy for generating easily-synthesized complexes capable of multielectron catalysis involves the use of redox-active (or “non-innocent”) ligands that

have the ability to store and release electrons over the course of the catalytic cycle. The research groups of Heyduk, Soper, and Chirik have pioneered the utilization of redox-active ligands in the activation of small molecules. Heyduk and coworkers have paired redox-active ligands with d^0 metal ions (e.g., Zr^{4+} and Ti^{4+}) to confer late-transition-metal reactivity upon complexes containing early transition metals.[274-277] Soper and coworkers discovered that redox-active aminophenol-derived ligands can be used to bring about palladium-like organometallic oxidative addition and reductive elimination reactions at square planar later first row metal centers.[278] They also demonstrated how the ability of redox-active ligands to undergo reversible one-electron transfer can be used to bring about bimetallic oxygen homolysis.[279,280] Similarly, Chirik and coworkers have had great success in utilizing the redox-active ligand bis(imino)pyridine to perform N_2 and C–H activation reactions at Fe, Mn, and Co centers.[281,282]

In chapter 5, we described the synthesis and coordination chemistry of a redox-active ligand ($\mathbf{L^{N3O2}}$) containing "fused" pincer-type coordination sites (Shown as **Scheme 6.1**). In such "fused" ligands, the two pincer coordination pockets share one of the donor arms, which then serves as the single bridge between the metal centers. Short intermetallic distances can be achieved through this binding mode.[283] Another advantage of this framework is the flexibility which permits the attachment of redox-active auxiliary ligands, such as 2,2-bipyridine, and small molecules like O_2. However, the bis(pincer) ligand $\mathbf{L^{N3O2}}$ framework suffers from two major limitations: (i) the bis(pincer) ligand

$\mathbf{L^{N3O2}}$ framework can only serve as an electron donor, and (ii) all donor atoms (three N and two phenolate O) are relatively "hard", making it difficult to access to the low oxidation states necessary for electrocatalytic reductions.

On the other hand, the preparation of ligands with 'softer' phosphorous or sulfur donors would likely cause dramatic changes in the redox properties of transition metal ions. Indeed, a classic type of pincer ligand, popularized by Ozerov and coworkers, features a central diarylamido unit with two flanking phosphine arms (PNP pincers).[188,200,209,218,260,272] In addition, Peters and coworkers have recently reported N_2 activation at low-valent diiron complexes that feature tripodal thiolate- and phosphine-based ligands.[284]

With the goal of preparing noninnocent ligands with "softer" donors, we have designed and synthesized pro-ligand H$\mathbf{L^{N5}}$ and H$\mathbf{L^{N3P2}}$ as analogues of the "fused" pincer-type ligand described in Chapter 5.[283] The structures of these ligands are provided in **Scheme 6.1**. This chapter presents the ligand syntheses and describes the nature of their coordination to different metal ions. Interestingly, neither the $\mathbf{L^{N5}}$- or $\mathbf{L^{N3P2}}$-based complexes replicate the unique (bis)pincer geometries of the $\mathbf{L^{N3O2}}$ complexes. Instead, the $\mathbf{L^{N3P2}}$ framework gives rise to only mononuclear complexes, while two $\mathbf{L^{N5}}$ ligands are involved in the formation of bimetallic complexes. Unfortunately, the $\mathbf{L^{N5}}$ ligand is also plagued by side-reactions that limit its overall utility.

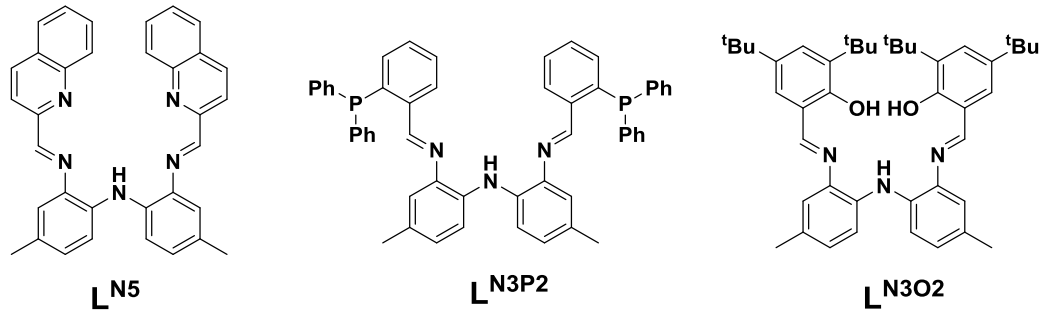

Scheme 6.1 The structures of pro-ligands H$\mathbf{L}^{\mathbf{N5}}$, H$\mathbf{L}^{\mathbf{N3P2}}$ and $H_3\mathbf{L}^{\mathbf{N3O2}}$.

6.2 Experimental

Materials and Physical Methods. All reagents and solvents were purchased from commercial sources and used as received unless otherwise noted. Acetonitrile (MeCN) and dichloromethane (DCM) were purified and dried using a Vacuum Atmospheres solvent purification system. Compounds were characterized and studied using IR, NMR, UV-Vis and X-ray diffraction. Infrared spectra were measured as a powder on a Thermo Fisher Scientific Nicolet iS5 FT-IR spectrometer with an iD3 ATR accessory, or as KBr pellets using a Nicolet Magna-IR 560 spectrometer. NMR spectra were collected at room temperature with a Varian 400 or 300 MHz spectrometer. UV-Vis spectra were collected with an Agilent 8453 diode array spectrometer.

Crystallographic Studies. The X-ray diffraction data were collected at 100 K with an Oxford Diffraction SuperNova kappa-diffractometer equipped with dual microfocus Cu/Mo X-ray sources, X-ray mirror optics, Atlas CCD detector and a low-

temperature Cryojet device. The data were processed with CrysAlisPro program package (Oxford Diffraction Ltd., 2010) typically using a numerical Gaussian absorption correction (based on the real shape of the crystal) followed by an empirical multi-scan correction using SCALE3 ABSPACK routine. The structures were solved using the SHELXS program and refined with the SHELXL program within the Olex2 crystallographic package. All computations were performed on an Intel PC computer with Windows 7 OS. Some structures contain disorder that was detected in difference Fourier syntheses of electron density and accounted for using capabilities of the SHELX package. In most cases, hydrogen atoms were localized in difference syntheses of electron density but were refined using appropriate geometric restrictions on the corresponding bond lengths and bond angles within a riding/rotating model (torsion angles of methyl hydrogens were optimized to better fit the residual electron density).

Pro-Ligand HL^{N5}.

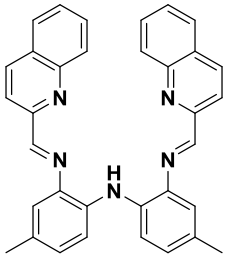

A 100 mL round-bottom flask equipped with a stir bar was charged with bis(2-amino-4-methylphenyl)amine (454 mg, 2 mmol, 1 equiv), 2-quinolinecarboxyladehyde (629 mg, 4 mmol, 2 equiv), 4 Å molecular sieve, and 30 mL of dry toluene. The solution was stirred overnight at 90 ℃ under nitrogen gas atmosphere. The reaction was

monitored with TLC. The solution turned to deep red color as the reaction progressed. Upon completion, the reaction mixture was filtered to remove the molecular sieves, and the toluene was evaporated under vacuum. The deep red residue was redissolved in 5 mL of diethyl ether. Removal of the ether yields a deep red powder (896 mg, 1.77 mmol, 88.6% yield) with 90% purity. This compound was used in metalation reactions without further purification. ^{1}H NMR (300 MHz, $CDCl_3$) δ 2.35 (s, 6H), 6.64 (s, 2H), 7.13 (d, *J* = 8.0 Hz, 2H), 7.21 (s, 2H), 7.56 – 7.48 (m, 4H), 7.63 (m, 4H), 7.75 (m, 2H), 8.16 (d, *J* = 8.2 Hz, 2H), 8.28 (t, *J* = 9.2 Hz, 2H), 8.91 (s, 2H).

2-(2-bromophenyl)-1,3-dioxolane

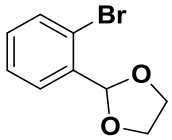

This procedure was adapted from previously published reports.[285] 2-Bromobenzaldehyde (5.84 mL, 50 mmol, 1.0 eq.), ethylene glycol (4.18 mL, 75 mmol, 1.5 eq.) and *p*-toluenesulfonic acid (63 mg) were dissolved in toluene (100 mL) and refluxed while the evolved water was collected in a Dean-Stark trap. After water was no longer evolved (overnight), the solution was cooled and washed with a saturated solution of $NaHCO_3$ (40 mL), followed by a saturated solution of NaCl (20 mL). The solution was dried over $MgSO_4$, filtered, concentrated on a rotary evaporator, and then distilled to give 2-(o-bromophenyl)-1,3-dioxolane as a colorless oil (9.4 g, 41 mmol, 82% yield). ^{1}H NMR (400 MHz, $CDCl_3$) δ 4.01-4.08 (m, 4H), 6.10 (s, 1H), 7.22 (m, 1H), 7.34 (m, 1H),

7.56 (dd, J = 8.0, 1.5 Hz, 1H), 7.60 (dd, J = 8.0, 2.0 Hz, 1H). ^{13}C NMR (100 MHz, $CDCl_3$) δ: 65.6, 102.7, 123.0, 127.5, 127.9, 130.7, 133.1, 136.7.

(2-(1,3-dioxolan-2-yl)phenyl)diphenylphosphane

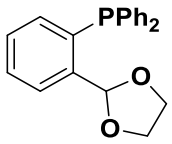

This procedure was adapted from previously published reports.[286] A solution of 2-(o-bromophenyl)-1,3-dioxolane (4.95 g, 21.6 mmol, 1.0 eq.) in dry THF (100 mL) was cooled to -78 ℃ and kept under an inert atmosphere. n-Butyllithium in hexanes (9.2 mL, 23 mmol, 1.1eq.) was slowly added dropwise. After stirring for 2 h at -78 ℃, diphenylphosphine chloride (3.99 mL, 21.6 mmol, 1.0 eq.) was added dropwise. The reaction was allowed to warm up to room temperature overnight, before the addition of H_2O (100 mL). The organic phase was extracted with Et_2O, dried over anhydrous $MgSO_4$, decanted and the solvent removed. The resulting oily liquid was purified by recrystallization from hot EtOH and cooled to -30 ℃ to afford 2-(o-diphenyl-phosphinophenyl)-1,3-dioxolane as a waxy white solid (5.3 g, 15.85 mmol, 73.3% yield). ^{1}H NMR (400 MHz, $CDCl_3$) δ 3.90-4.12 (m, 4H), 6.45 (d, J = 5.0 Hz, 1H), 6.99 (dd, J = 7.5, 5.0 Hz, 1H), 7.23- 7.32 (m, 5H), 7.30-7.35 (m, 6H), 7.4 (m, 1H), 7.7 (m, 1H),; ^{13}C NMR (100MHz, $CDCl_3$) δ 65.5, 101.8, 126.6, 128.6, 128.7,129.4, 133.8, 134.0, 134.2, 136.0, 137.1, 142.1; ^{31}P NMR (162 MHz, $CDCl_3$) δ - 15.86 (s).

2-(diphenylphosphanyl)benzaldehyde

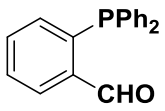

This procedure was adapted from previously published reports.[286] 2-(o-diphenylphosphinophenyl)-1,3-dioxolane (5.3 g, 15.85 mmol, 1.0 eq.) and *p*-toluenesulfonic acid (200 mg) were dissolved in acetone (100 mL) and refluxed at 70 ℃ for 8 h. While still warm, H_2O (30 mL) was added and the volume reduced to ~40 mL by solvent evaporation. The resulting mixture was cooled to -30 °C overnight, and the precipitate filtered and dried in vacuo to afford 2-(diphenylphosphino)benzaldehyde as a bright yellow powder (4.12 g, 14.2 mmol, 90% yield). ^{1}H NMR (400 MHz, $CDCl_3$) δ 6.96-7.00 (m, 1H), 7.28-7.39 (m, 10H), 7.43-7.56 (m, 2H), 7.98-8.03 (m, 1H), 10.55 (d, J = 5.0 Hz, 1H); 13C NMR (100 MHz, $CDCl_3$) δ 128.7, 128.8, 129.1, 130.7, 133.7, 133.9, 134.1, 134.2, 136.1, 141.3, 191.7; ^{31}P NMR (162 MHz, $CDCl_3$) δ -11.03 (s).

Pro-Ligand HL^{N3P2}.

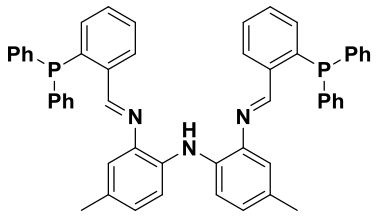

A 100 mL round-bottom flask equipped with a stir bar was charged with bis(2-amino-4-methylphenyl)amine (227 mg, 1.0 mmol, 1 equiv), 2-(diphenylphosphino)benzaldehyde (580 mg, 2.0 mmol, 2 equiv), 4 Å molecular sieve, and 30 mL of dry toluene. The solution was stirred overnight at 90 ℃ under nitrogen gas atmosphere. As the reaction progressed, the solution turned to a deep red color. The

reaction was monitored with TLC. Once the reaction was complete, the mixture was cooled to room temperature, filtered to remove the molecular sieve, and the toluene was evaporated under vacuum. The deep red residue was redissolved in 5 mL ether, filtered, the ether was removed to yield a deep red powder as product (632 mg, 0.83 mmol, 83% yield). This compound was used for metalation reactions without further purification. ^{1}H NMR (400 MHz, $CDCl_3$) δ 2.22 (s, 6H), 6.92 (d, *J* = 6.4 Hz, 4H), 7.21 – 7.07 (m, 8H), 7.38 – 7.30 (m, 22H), 8.74 (d, *J* = 12.0 Hz, 2H), 9.16 (s, 1H). ^{13}C NMR (101 MHz, $CDCl_3$) δ 20.66, 114.60, 118.39, 127.67, 128.69, 128.76, 128.88, 128.92, 129.01, 129.10, 130.61, 133.26, 134.04, 134.24, 135.56, 136.10, 136.20, 139.38, 156.08, 156.33. ^{31}P NMR (162 MHz, $CDCl_3$) δ -13.64.

Complex Synthesis

[Co(L^{N3P2})](ClO_4). To a 25 mL flask were added the ligand **L^{N3P2}** (77.1 mg, 0.1 mmol), and $Co(ClO_4)_2 \cdot 6H_2O$ (73.2 mg, 0.2 mmol, 2.0 eq.). The components were dissolved in a 1:1 mixture of MeCN:CH_2Cl_2 (5 mL) and stirred for 5 minutes. The addition of NEt_3 (14 μL, 0.1 mmol, 1.0 eq.) caused the solution to turn to a deep brown color. The mixture was stirred overnight, filtered through Celite, and the solvent removed under vacuum. The resulting powder was washed with pentane (5 mL) and dried under vacuum. Slow evaporation over the course of a week provided deep red-brown crystals that were collected via filtration. (23 mg, 0.0247 mmol, 24.7% yield). Single

crystals suitable for X-ray diffraction, were grown from a concentrated solution of CH_2Cl_2 and MeCN in a 1 to 1 ratio.

[Ni(L^{N3P2})](ClO4). The procedure was nearly identical to the one used to prepare complex [Co($\mathbf{L}^{N3P2}$)](ClO4); the only difference was the replacement of $Co(ClO_4)_2 \cdot 6H_2O$ with $Ni(ClO_4)_2 \cdot 6H_2O$. Slow evaporation over the course of a week provided deep brown color crystals that were collected via filtration. (17 mg, 0.018 mmol, 18% yield). Single crystals suitable for X-ray diffraction, were grown from a concentrated solution of CH_2Cl_2 and MeCN in a 1 to 1 ratio.

[Fe(L^{N3P2})](OTf). The procedure was nearly identical to the one used to prepare complex [Co($\mathbf{L}^{N3P2}$)](ClO4); the only difference was the replacement of $Co(ClO_4)_2 \cdot 6H_2O$ with $Fe(OTf)_2$ (19% yield).

$[Zn_2(L^{N5})_2][OTf]_2$. To a 25 mL flask were added the ligand $\mathbf{L}^{N5}$ (50.6 mg, 0.1 mmol) and $Zn(OTf)_2$ (72.7 mg, 0.2 mmol, 2.0 eq.). The components were dissolved in MeCN (5 mL) and stirred for 5 minutes. The addition of NEt_3 (14 μL, 0.1 mmol, 1.0 eq.) caused the solution to turn to a deep blueish-brown color. The mixture was stirred overnight, filtered through Celite, and the solvent removed under vacuum. The resulting powder was washed with pentane (5 mL) and dried under vacuum to produce crude product. Pure product and X-ray quality crystals can be obtained by recrystallization from vapor diffusion of Et_2O into a concentrated MeCN solution (19 mg, 25.3% yield).

$[Cu_2(L^{N5'})_2][OTf]_2$. To a 25 mL flask were added the ligand $\mathbf{L^{N5}}$ (50.5 mg, 0.100 mmol, 1.0 eq.), and $Cu(OTf)_2$ (72.3 mg, 0.2 mmol, 2.0 eq.). The components were dissolved in dichloromethane (DCM) (5 mL) and stirred for 5 minutes. The addition of NEt_3 (14 μL, 0.1 mmol, 1.0 eq.) caused the solution to turn to a deep brown color. The mixture was stirred overnight, filtered through Celite, and the solvent removed under vacuum. The resulting powder was washed with pentane (5 mL), dried under vacuum, and dissolved in a 1:1 mixture of CH_2Cl_2:MeOH (4 mL). Slow evaporation over the course of two days provided dark purple crystals that were collected via filtration, washed with pentane, and dried under vacuum (21 mg, 30% yield). Dark purple crystals, suitable for X-ray diffraction, were grown from slow evaporation of concentrated 1:1 solution of CH_2Cl_2:MeOH.

$[Fe_2(L^{N5''})_2Cl_4$. To a 25 mL flask were added the ligand $\mathbf{L^{N5}}$ (50.5 mg, 0.100 mmol, 1.0 eq.), and $FeCl_2$ (25.3 mg, 0.2 mmol, 2.0 eq.). The components were dissolved in dichloromethane (DCM) (5 mL) and stirred for 5 minutes. The addition of NEt_3 (14 μL, 0.1 mmol, 1.0 eq.) caused the solution to turn to a deep brown color. The mixture was stirred overnight, filtered through Celite, and the solvent removed under vacuum. The resulting powder was washed with pentane (5 mL), dried under vacuum. Recrystallization from laying pentane into concentrated DCM solution (20 mg, 15% yield). Dark brown crystals, suitable for X-ray diffraction, was grown from the same method.

6.3 Result and discussion

6.3.1 Ligands synthesis

The H$\mathbf{L}^{\mathbf{N5}}$ and H$\mathbf{L}^{\mathbf{N3P2}}$ pro-ligands are prepared by the route shown in **Scheme 6.2**. The syntheses involve condensation of bis(2-amino-4-methylphenyl)amine with two equivalents of either 2-quinoline-aldehyde (in the case of $\mathbf{L}^{\mathbf{N5}}$) or 2-(diphenylphosphino)benzaldehyde (in the case of $\mathbf{L}^{\mathbf{N3P2}}$). The presence of 4 Å molecule sieves are required to remove the water generated during the reaction. Both ligands have a deep red color. Based on ^{1}H NMR data, the purity of the products is around 90%, and the ligands were used for subsequent metalation reactions without further purification.

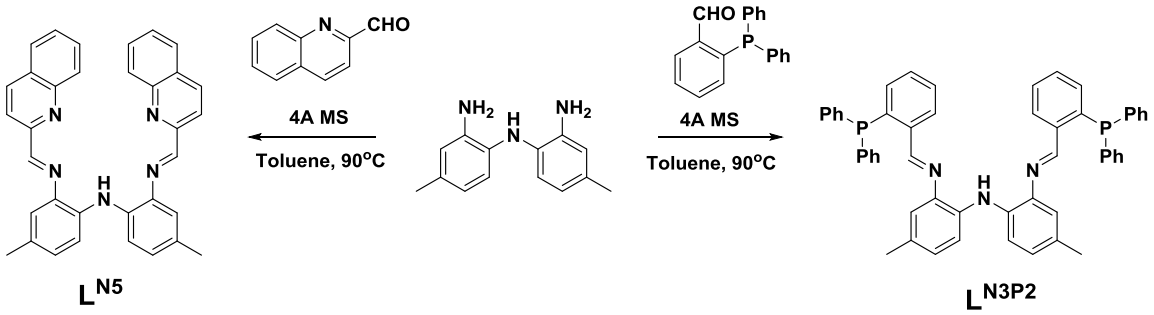

Scheme 6.2 Synthetic routes for ligands $\mathbf{L}^{\mathbf{N5}}$ and $\mathbf{L}^{\mathbf{N3P2}}$**.**

6.3.2 Synthesis and Structure of Complexes $[M(L^{N3P2})]^{+}$ (M = Fe, Co and Ni)

The structural properties of $\mathbf{L}^{\mathbf{N3P2}}$ were initially examined by looking at its coordination to the Co(II) ion. Formation of the desired $[Co_2(\mathbf{L}^{\mathbf{N3P2}})(bpy)_2]^{3+}$ product

was attempted by addition of $Co(ClO_4)_2 \cdot 6H_2O$ and 2,2'-bipyridine (bpy) to a dichloromethane (DCM) solution of H$\mathbf{L}^{\mathbf{N3P2}}$. This combination resulted in the immediate formation of a dark red/brown solution. We were able to isolate a brown solid that was recrystallized by vapor diffusion of diethyl ether into an acetonitrile solution of the complex. X-ray diffraction studies, however, indicated that the compound was not the expected analogue of $[Co_2(\mathbf{L}^{\mathbf{N3O2}})(bpy)_2]ClO_4$. Instead, the structure revealed a mononuclear, five-coordinate cobalt(II) complex bound to a single $\mathbf{L}^{\mathbf{N3P2}}$ ligand (Shown as **Figure 6.1**).

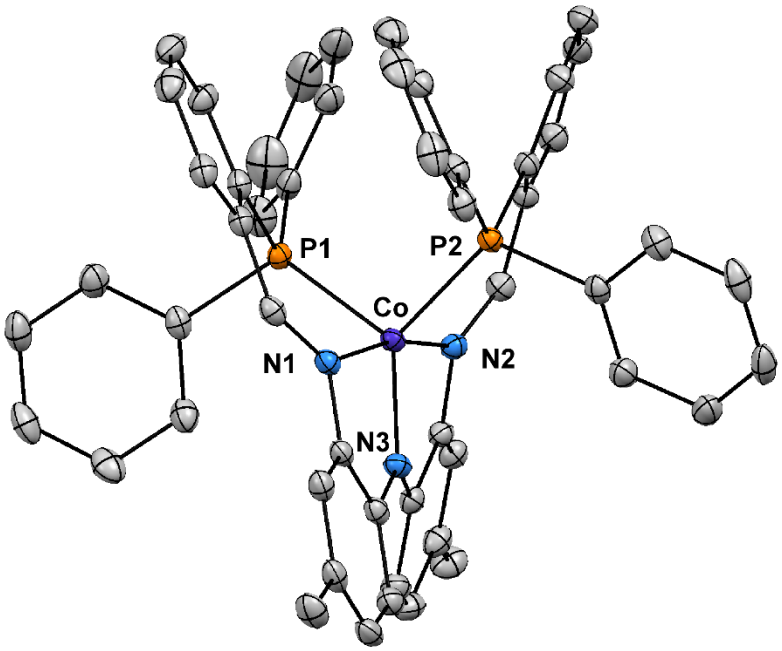

Figure 6.1 Thermal ellipsoid plot (50% probability) derived from X-ray structure of $[Co(\mathbf{L}^{\mathbf{N3P2}})]ClO_4$.

The Co(II) ion has a distorted trigonal bipyramidal geometry with a τ–value of 0.595 (see **Table 6.1**). The central amido nitrogen donor and two phosphorus atoms occupy the trigonal equatorial plane, while the two imine N-donors are found in the axial positions (see **Figure 6.1**). Compared to the structure of $[Co_2(\mathbf{L^{N3O2}})(bpy)_2]ClO_4$ (complex **15**) presented in Chapter 5, the substitution of phosphine for phenolate donors causes a lengthening of the equatorial bonds: the Co-O bond have an average length of 1.90 Å in 15, while the Co-P bonds in $[Co(\mathbf{L^{N3P2}})]^+$ have an average length of 2.22 Å (As shown in **Table 6.1**). Unlike $\mathbf{L^{N3O2}}$, the $\mathbf{L^{N3P2}}$ ligand is able to coordinate in a pentadentate fashion to a single metal center because the C-P and Co-P bonds in $[Co(\mathbf{L^{N3P2}})]^+$ are considerably longer than the corresponding C-O and Co-O bonds in **15**. Thus, the $\mathbf{L^{N3P2}}$ ligand is easily able to "wrap around" a single metal center without introducing excessive strain. The geometry of $[Co(\mathbf{L^{N3P2}})]ClO_4$ is also stabilized by π-stacking interactions between a phosphine phenyl ring and the diarylamido unit.

By following the same procedure and substituting $Ni(ClO_4)_2•6H_2O$ in place of $Co(ClO_4)_2•6H_2O$, we are able to isolate analogous complex $[Ni(\mathbf{L^{N3P2}})](ClO_4)$. X-ray diffraction studies indicated that the compound adopted the same coordination geometry as Co species (shown as **Figure 6.2**).

Table 6.1 compares the bond distances and angles of $[Ni(\mathbf{L^{N3P2}})]ClO_4$ and $[Co(\mathbf{L^{N3P2}})]ClO_4$. The largest difference is bond distances is 0.035 Å, while the largest difference in bond angles is 7 º.

Table 6.1 Selected Bond Distances (Å) and Angles (°) for the Crystal Structures of [Co($\mathbf{L}^{\mathbf{N3P2}}$)$ClO_4$ and [Ni($\mathbf{L}^{\mathbf{N3P2}}$)$ClO_4$.

Bond Distances	[Ni($\mathbf{L}^{\mathbf{N3P2}}$)]($ClO_4$)	[Co($\mathbf{L}^{\mathbf{N3P2}}$)]($ClO_4$)
M-P1	2.2522(5)	2.2121(5)
M-P2	2.2471(5)	2.2169(5)
M-N1	1.8961(16)	1.9258(15)
M-N2	1.9074(16)	1.9169(15)
M-N3	1.9086(16)	1.8652(15)
Bond Angles		
P2-M-P1	110.49(2)	103.224(19)
N1-M-P1	92.43(5)	92.12(5)
N1-M-P2	95.26(5)	95.85(5)
N1-M-N2	167.07(7)	167.24(6)
N1-M-N3	83.50(7)	83.75(6)
N2-M-P1	97.06(5)	98.00(5)
N2-M-P2	89.64(5)	89.42(5)
N2-M-N3	83.81(7)	83.72(6)
N3-M-P1	126.13(5)	131.54(5)
N3-M-P2	123.37(5)	125.24(5)
τ-value	0.683	0.595

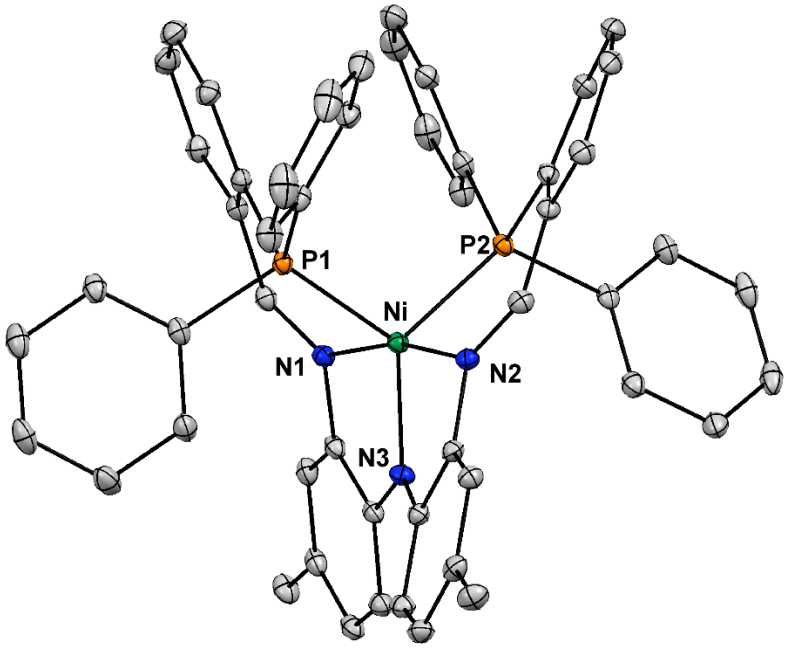

Figure 6.2 Thermal ellipsoid plot (30% probability) derived from X-ray structure of [Ni($\mathbf{L}^{\mathbf{N3P2}}$)]$ClO_4$.

The Fe species [Fe($\mathbf{L^{N3P2}}$)](OTf) analogue has been prepared by using $Fe(OTf)_2$ as the source of ferrous ion. Attempts to grow single crystals suitable for X-ray diffraction have been unsuccessful to date. However, the UV-Vis spectra and electrochemical properties of [Fe($\mathbf{L^{N3P2}}$)](OTf) have been explored, as described in the next section.

6.3.3 Electrochemical Properties and UV- spectra of $[M(L^{N3P2})]^+$ Complexes.

The electrochemical properties of $[Co(\mathbf{L^{N3P2}})]ClO_4$ were examined using voltammetric methods in dichloromethane solutions with 0.1 M $(NBu_4)PF_6$ as the supporting electrolyte and scan rates of 100 mV/s. The reported potentials are relative to the Ag/AgCl couple. The cyclic and square-wave voltammograms (CV and SWV) of the complexes, shown in **Figure 6.3**, reveal three redox features at -0.83 V, 0.20 V, and 1.35 V. Assignment of these features to either metal- or ligand-based events was assisted by comparison to data collected in Chapter 5 for the dicobalt analogue $[Co_2(\mathbf{L^{N3O2}})(bpy)_2]ClO_4$ (**15**). The quasi-reversible redox couple at 0.21 V corresponds to one-electron oxidation of the central diarylamido unit. This redox couple is shifted negatively by 350 mV relative to the corresponding feature in the CV of complex **15**. The quasi-reversible redox couple at -0.83 V is assigned to one-electron reduction of Co(II) to Co(I). This Co(II)-based reduction is shifted positively by 200 mV in $[Co(\mathbf{L^{N3P2}})]ClO_4$ compared to **15**, reflecting the switch from hard, negatively-charged phenolates to soft, neutral phosphines. Finally, the quasi-reversible redox couple at 1.37

V corresponds to one-electron oxidation of Co(II) to Co(III). Based on the electrochemical data, we can conclude that the phosphine-containing $\mathbf{L^{N3P2}}$ ligand makes it easier to access to low oxidation states and stabilize different oxidation states of Co (Co^{2+}, Co^{+} and Co^{3+}).

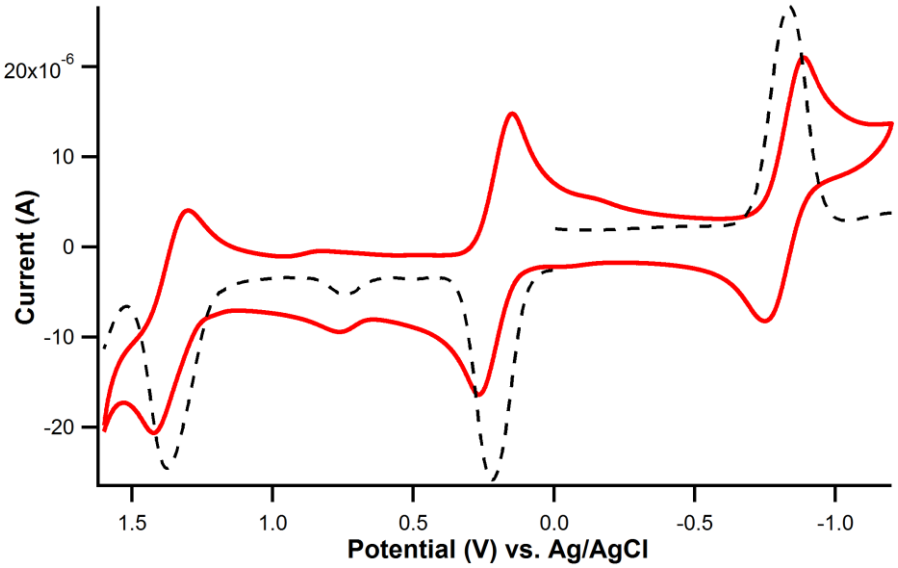

Figure 6.3 Cyclic voltammograms of [Co($\mathbf{L^{N3P2}}$)][ClO_4] collected in dichloromethane with 0.1 M (NBu_4)PF_6 as the supporting electrolyte. The corresponding square-wave voltammograms is indicated by the dashed line. All scan rates were100 mV/s.

Based on the electrochemical results presented above, we sought to generate the one-electron oxidized form of [Co($\mathbf{L^{N3P2}}$)]ClO_4 via chemical means. Treatment of the complex with one equivalent of 1'-acetylferrocenium ($^{Ac}Fc^{+}$; E = 0.73 V vs. Ag/AgCl) in dichloromethane causes the ligand-based absorption band near 500 nm to blue shift and increase in intensity (shown in **Figure 6.4**), indicative of a change in the pi-system of the

$\mathbf{L}^{\mathbf{N3P2}}$ ligand. Unfortunately, we have not been able to grow X-ray quality crystals of this species.

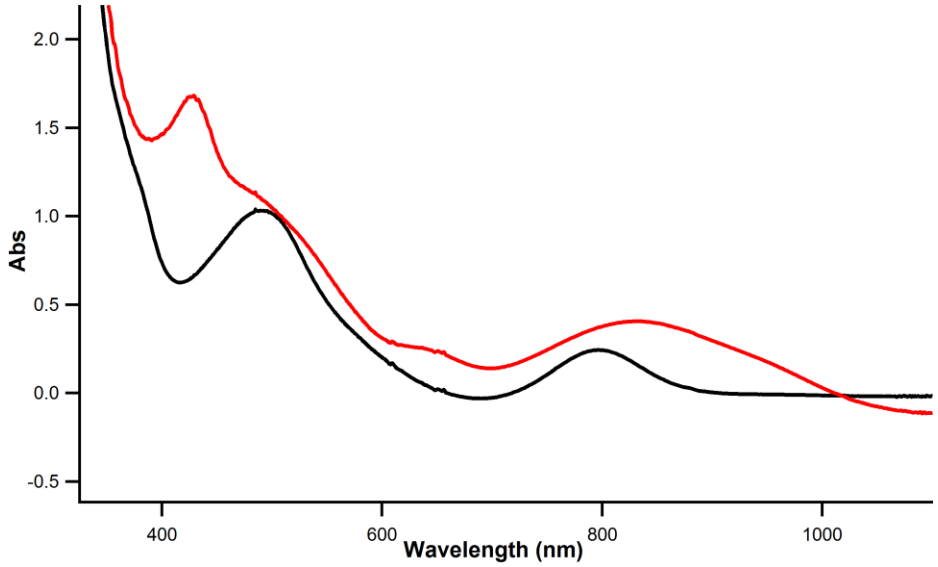

Figure 6.4 Absorption spectra of [Co($\mathbf{L}^{\mathbf{N3P2}}$)]$ClO_4$ (black color) and oxidized form (red color) in dicholomethane (conc. = 0.05 mM).

The electrochemical properties of [Ni($\mathbf{L}^{\mathbf{N3P2}}$)]$ClO_4$ and [Fe($\mathbf{L}^{\mathbf{N3P2}}$)](OTf) were examined using voltammetric methods in dichloromethane solutions with 0.1 M $(NBu_4)PF_6$ as the supporting electrolyte and scan rates of 100 mV/s. The reported potentials are relative to the Ag/AgCl couple. The cyclic and square-wave voltammograms (CV and SWV) of the complexes are shown in **Figure 6.5**. For [Ni($\mathbf{L}^{\mathbf{N3P2}}$)]$ClO_4$, the quasi-reversible redox couple at 0.45 V corresponds to one-electron oxidation of the central diarylamido unit. The redox couples at 1.24 and -0.64 V arise from oxidation and reduction, respectively, of the Ni(II) center. The weaker redox feature

at -0.04 V does not appear in the initial scan; we therefore assigned this feature to a decomposed species that arises after first reduction scan.

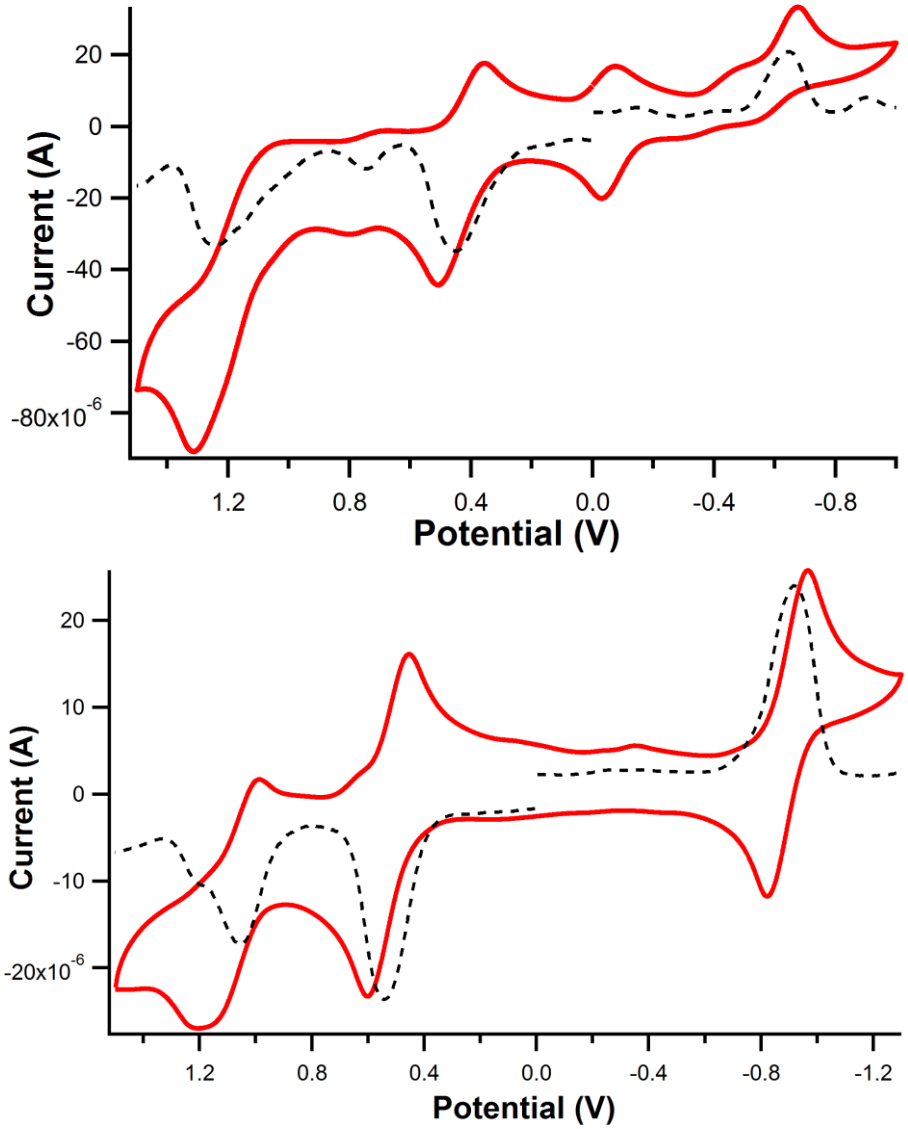

Figure 6.5 Cyclic voltammograms of **(top)** [Ni($\mathbf{L}^{\mathbf{N3P2}}$)][$ClO_4$] and **(bottom)** [Fe($\mathbf{L}^{\mathbf{N3P2}}$)](OTf) collected in DCM with 0.1 M (NBu_4)PF_6 as the supporting electrolyte. The corresponding square-wave voltammograms is indicated by the dashed line. All scan rates were100 mV/s.

For [Fe($\mathbf{L}^{\mathbf{N3P2}}$)](OTf), the quasi-reversible redox couple at 0.54 V corresponds to one-electron oxidation of the central diarylamido unit. The reduction potential on the central diarylamido unit is strongly dependent on metal ion identity, following the order of Co (0.21 V) < Ni (0.45 V) < Fe (0.54 V). The redox couples at 1.05 and -0.91 V are correspond to oxidation and reduction, respectively, of the Fe(II) ion.

Attempts to chemically generate the one-electron oxidized form of [Fe($\mathbf{L}^{\mathbf{N3P2}}$)](OTf) were carried out by treatment of the complex with one equivalent of 1'-acetylferrocenium ($^{Ac}Fc^{+}$; E=0.73 V vs. Ag/AgCl) in DCM. This causes the ligand-based absorption band near 580 nm to blue shift to 550 nm and increase in intensity, while the band near 420 and 800 nm decrease in intensity (shown in **Figure 6.6**), indicative of a change in the pi-system of the $\mathbf{L}^{\mathbf{N3P2}}$ ligand. Unfortunately, we have not been able to grow X-ray quality crystals of this species.

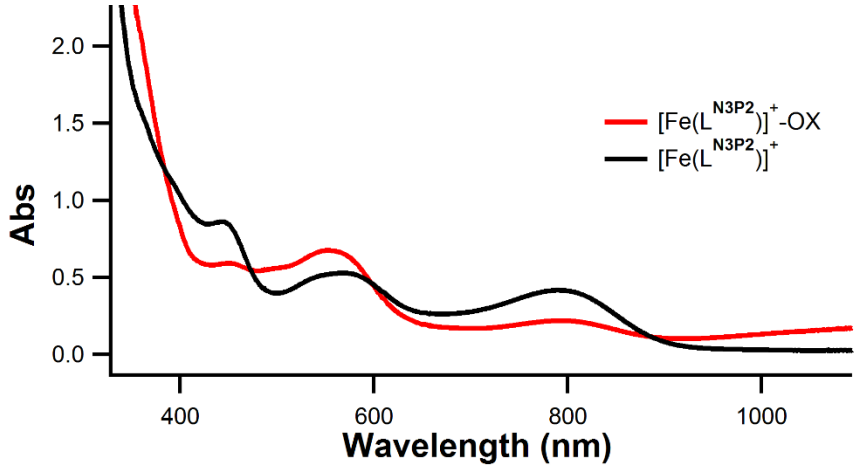

Figure 6.6 Absorption spectra of [Fe($\mathbf{L}^{\mathbf{N3P2}}$)](OTf) (black color) and oxidized form (red color) in dicholomethane (conc. = 0.05 mM).

6.3.4 Complex $[Zn_2(L^{N5})_2][OTf]_2$

For the metalation of $\mathbf{L^{N5}}$, we initially attempted the reaction of two equivalents of $Zn(OTf)_2$ and 2,2'-bipyridine (bpy) with one equivalent of $\mathbf{L^{N5}}$ in CH_2Cl_2. This combination resulted in the immediate formation of a dark red/brown solution. Deep brown crystals were obtained by vapor diffusion of diethyl ether into an acetonitrile solution of the complex. The structurally characterized complex, shown in **Figure 6.7**, features two helically-shaped $\mathbf{L^{N5}}$ ligands chelated to two Zn(II) ions each. The central amido group acts as a bridge between the Zn centers. The six-coordinate Zn(II) ions exist in distorted octahedral geometries. The X-ray structure reveals π-stacking interactions between a diarylamido ring and the quinoline of the opposite ligand.

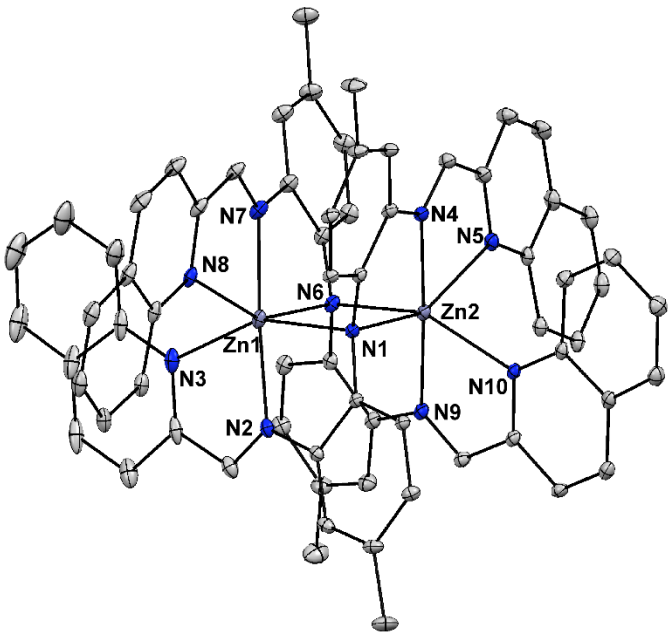

Figure 6.7 Thermal ellipsoid plot (30% probability) derived from X-ray structure of $[Zn_2(\mathbf{L^{N5}})_2](OTf)_2$.

This structure of $[Zn_2(\mathbf{L^{N5}})_2](OTf)_2$ confirmed that we have indeed created the $\mathbf{L^{N5}}$ ligand. In addition, the $\mathbf{L^{N5}}$ ligand can bind in the "fused" bis-pincer fashion first reported for the $\mathbf{L^{N3O2}}$ ligand in Chapter 5. However, the coordinative saturation of the Zn(II) centers makes it impossible to bind redox-active auxiliary ligands or small molecules like O_2 or H^+.

6.3.5 Complex $[Cu(I)_2\mathbf{L^{N5'}}_2][OTf]_2$

Metalation of the $\mathbf{L^{N5}}$ ligand was also attempted via reaction with $Cu(OTf)_2$ and 2,2'-bipyridine in CH_2Cl_2. This reaction was completed in the glovebox and stirred overnight. After workup of the reaction, brown crystal were isolated by vapor diffusion of diethyl ether into an acetonitrile solution of the complex. X-ray crystallographic analysis revealed that a side reaction has occurred during the reaction to yield the dicopper(I) structure shown in **Figure 6.8**. The $\mathbf{L^{N5}}$ ligand has undergone an oxidative cyclization to yield the tetradentate $\mathbf{L^{N5'}}$ ligand, as illustrated in **Scheme 6.3.** The two-electron oxidation of the ligand is coupled to reduction of the Cu(II) centers to Cu(I). Each Cu(I) ion is bound to two $\mathbf{L^{N5'}}$ ligands to give a distorted tetrahedral geometry. The antiparallel and π-stacked benzimidazole groups are separated by 3.4 Å.

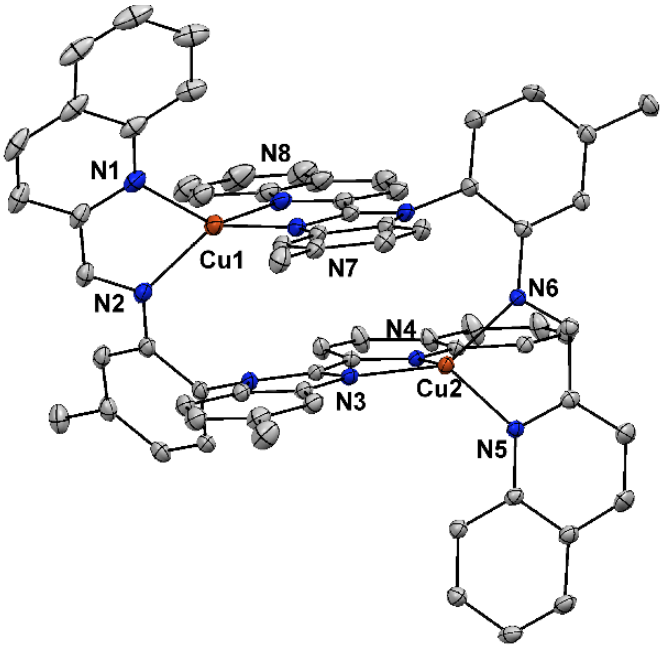

Figure 6.8 Thermal ellipsoid plot (30% probability) derived from X-ray structure of $[Cu(I)\mathbf{L}^{N5'}]_2[OTf]_2$.

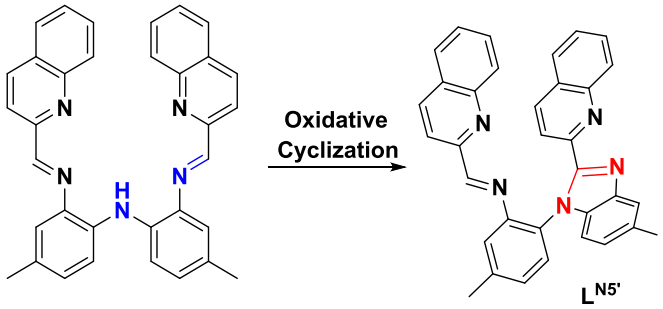

Scheme 6.3 The oxidative cyclization of $\mathbf{L}^{N5}$ to yield $\mathbf{L}^{N5'}$

The electrochemical properties of $[Cu_2(\mathbf{L}^{N5'})_2](OTf)_2$ were studied by voltammetric methods in CH_2Cl_2 solutions with 0.1 M $(NBu_4)PF_6$ as the supporting electrolyte and scan rates of 100 mV/s. The reported potentials are relative to the Ag/AgCl reference. The cyclic and square-wave voltammograms (CV and SWV) of the complexes are shown in **Figure 6.9**. The cyclic voltammogram displays a quasi-

reversible redox couple at 0.9 V that corresponds to oxidation of Cu^{+} to Cu^{2+}. The two quasi-reversible redox couples at -0.88 and -0.98 V, by corresponds to sequential reduction of the two 'non-innocent' imine-quinoline chelates.

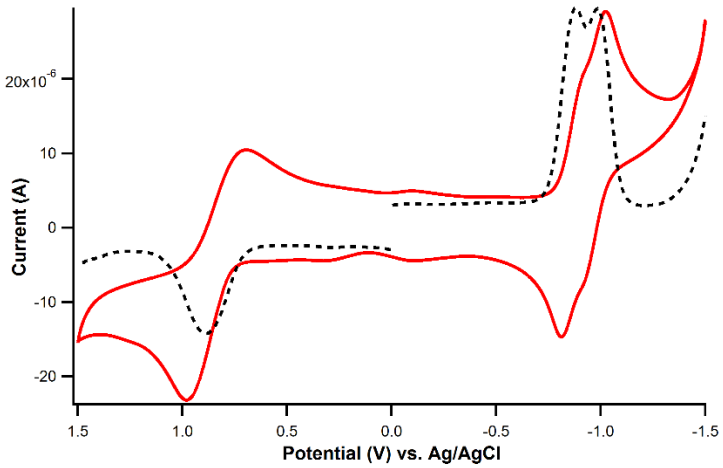

Figure 6.9 Cyclic voltammograms of $[Cu_2(\mathbf{L^{N5'}})_2](OTf)_2$ collected in dichloromethane with 0.1 M $(NBu_4)PF_6$ as the supporting electrolyte. The corresponding square-wave voltammogram is indicated by the dashed line. All scan rates were 100 mV/s.

6.3.6 Complex $Fe_2(L^{N5''})_2Cl_4$

We then explored the reaction of $\mathbf{L^{N5}}$ with $FeCl_2$ in the presence of base (NEt_3) in a solution of CH_2Cl_2. This reaction was performed in a glovebox and stirred overnight, and the crude product was recrystallized by vapor diffusion of diethyl ether into an acetonitrile solution of the complex. The resulting brown crystals were analyzed with X-ray diffraction. The resulting structure revealed another type of $\mathbf{L^{N5}}$ side reaction, as illustrated in **Scheme 6.4**. In this case, a cyclization occurs between the central amido

group and one ligand arm to generate a benzimidazole unit, while the other imine group is reduced due to net transfer of H_2. Thus, the rearrangement of $\mathbf{L}^{N5}$ to $\mathbf{L}^{N5}$" does not involve oxidation (or reduction) of the compound.

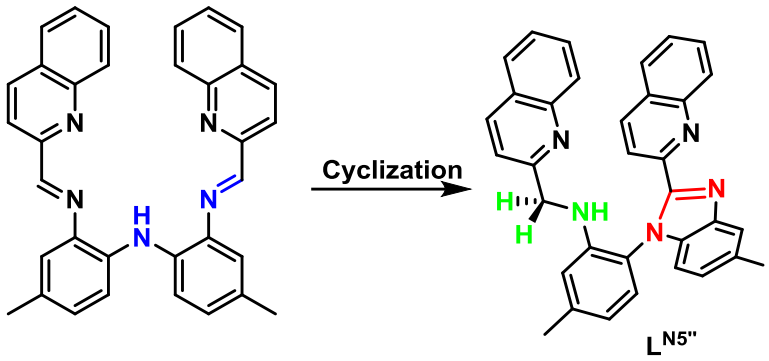

Scheme 6.4 Illustration of second side reaction on ligand $\mathbf{L}^{N5}$

This centrosymmetric complex $[Fe_2(\mathbf{L}^{N5"})_2Cl_4]$ contains two iron(II) centers bridged by two chloride anions to yield a $[Fe_2(\mu\text{-}Cl)_2]$ diamond core. The five-coordinate Fe(II) ions are also bound to a terminal chloride and a bidentate $\mathbf{L}^{N5}$" ligand coordinating via its benzimidazole and quinoline donors. The coordination geometry is distorted trigonal bipyramidal ($\tau = 0.62$). The other "dangling" arm of the $\mathbf{L}^{N5}$" ligand does not bind to iron.

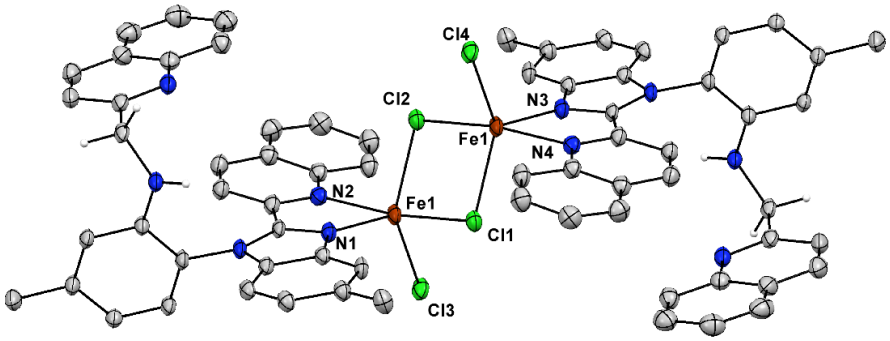

Figure 6.10 Thermal ellipsoid plot (30% probability) derived from X-ray structure of $Fe_2(\mathbf{L}^{\mathbf{N5''}})_2Cl_4$.

6.4 Conclusion

The crystal structures shown in **Figure 6.1** and **Figure 6.7**, provide clear evidence that the $\mathbf{L}^{\mathbf{N3P2}}$ and $\mathbf{L}^{\mathbf{N5}}$ ligands were successfully synthesized. However, ligand $\mathbf{L}^{\mathbf{N3P2}}$ prefers to form mononuclear complexes, and does not adopt the dinucleating mode of ligand $\mathbf{L}^{\mathbf{N3O2}}$. Based on electrochemistry data obtained for $[Co(\mathbf{L}^{\mathbf{N3P2}})]ClO_4$, inclusion of a "softer" phosphine donor aids in the stabilization of different Co oxidation states (Co^+, Co^{2+} and Co^{3+}).

As for the ligand $\mathbf{L}^{\mathbf{N5}}$ framework, it can coordinate two metal ions in the manner of a "fused" (bis)pincer coordination site. However, as it carries less steric bulk than the $\mathbf{L}^{\mathbf{N3O2}}$ ligand, two $\mathbf{L}^{\mathbf{N5}}$ ligands are capable of binding to the same dimetallic unit, thereby giving rise to saturated, six-coordinate M(II) centers that are likely unreactive towards small molecules. In addition, $\mathbf{L}^{\mathbf{N5}}$ has an unfortunate tendency to undergo side-reactions

in the presence of metal ions, yielding the $\mathbf{L^{N5'}}$ and $\mathbf{L^{N5''}}$ derivatives that fail to generate the desired complexes.

Table 6.2 Summary of X-ray crystallographic data collection and structure refinement.

	$Co(\mathbf{L}^{N3P2})ClO_4$	$Ni(\mathbf{L}^{N3P2})ClO_4$	$[Cu(I)_2(\mathbf{L}^{N5'})_2][OTf]_2$
Empirical formula	$C_{52}H_{42}N_3O_4P_2ClCo$	$C_{52}H_{42}N_3O_4P_2ClNi$	$C_{70}H_{50}Cu_2F_6N_{10}O_6S_2$
Formula weight	929.21	928.99	1432.4
Crystal system	monoclinic	monoclinic	triclinic
Space group	$P2_1/n$	$P2_1/n$	P-1
a [Å]	12.07182(18)	12.16598(15)	14.3256(3)
b [Å]	23.8546(4)	23.8161(3)	14.6384(3)
c [Å]	15.0088(2)	14.9330(2)	17.2483(3)
α [°]	90	90	88.3828(17)
β [°]	95.9504(14)	96.4537(13)	84.2646(16)
γ [°]	90	90	70.7256(19)
Volume [$Å^3$]	4298.78(11)	4299.36(10)	3397.16(12)
Z	4	4	2
ρ_{calc} [g/cm^3]	1.436	1.435	1.4
λ (Å)	MoKα (λ = 0.71073)	CuKα (λ = 1.54184)	MoKα (λ = 0.71073)
μ [mm^{-1}]	0.588	2.344	0.763
Θ range [°]	5.7 to 58.9	7.02 to 147.8	5.56 to 59.04
Reflections collected	49015	58992	76507
Independent reflections (R_{int})	10788 [R_{int} = 0.0402, R_{sigma} = 0.0383]	8523 [R_{int} = 0.1032, R_{sigma} = 0.0488]	17234 [R_{int} = 0.0320, R_{sigma} = 0.0291]
Data/restraints/parameters	10788/0/570	8523/0/570	17234/0/869
Goodness-of-fit on F^2	1.045	1.051	1.104
*R*1/*wR*2 indexes [I >2σ(I)]	R_1 = 0.0378, wR_2 = 0.0832	R_1 = 0.0381, wR_2 = 0.0817	R_1 = 0.0486, wR_2 = 0.1426
*R*1/*wR*2 indexes [all data]	R_1 = 0.0547, wR_2 = 0.0919	R_1 = 0.0495, wR_2 = 0.0881	R_1 = 0.0615, wR_2 = 0.1512

Table 6.2 (continued). Summary of X-ray crystallographic data collection and structure refinement.

	$[Zn_2(\mathbf{L}^{N5})_2][OTf]_2$	$Fe_2(\mathbf{L}^{N5''})_2Cl_4$
Empirical formula	$C_{74}H_{62}F_6N_{10}O_7S_2Zn_2$	$C_{70}H_{58}Cl_8Fe_2N_{10}$
Formula weight	1512.2	1434.56
Crystal system	triclinic	triclinic
Space group	P-1	P-1
a [Å]	14.8735(5)	12.2112(6)
b [Å]	16.3143(5)	12.2538(6)
c [Å]	17.0799(6)	12.6667(6)
α [°]	78.283(3)	68.738(4)
β [°]	83.714(3)	74.788(4)
γ [°]	62.890(3)	89.919(4)
Volume [$Å^3$]	3611.6(2)	1695.17(14)
Z	2	1
ρ_{calc} [g/cm^3]	1.391	1.405
λ (Å)	CuKα (λ = 1.54184)	CuKα (λ = 1.54184)
μ [mm^{-1}]	1.997	6.724
Θ range [°]	6.18 to 147.34	7.54 to 148.24
Reflections collected	51503	18375
Independent reflections (R_{int})	13307 [R_{int} = 0.0584, R_{sigma} = 0.0361]	6702 [R_{int} = 0.0356, R_{sigma} = 0.0374]
Data/restraints/parameters	13307/38/983	6702/0/408
Goodness-of-fit on F^2	1.064	1.114
*R*1/*wR*2 indexes [I >2σ(I)]	R_1 = 0.0739, wR_2 = 0.2031	R_1 = 0.0754, wR_2 = 0.2183
*R*1/*wR*2 indexes [all data]	R_1 = 0.0877, wR_2 = 0.2134	R_1 = 0.0871, wR_2 = 0.2316

Chapter 7

Electrocatalytic Activity of the Bimetallic Cobalt Complex $[Co_2(L^{N3O2})(bpy)_2]ClO_4$ Towards Proton Reduction and Water Oxidation

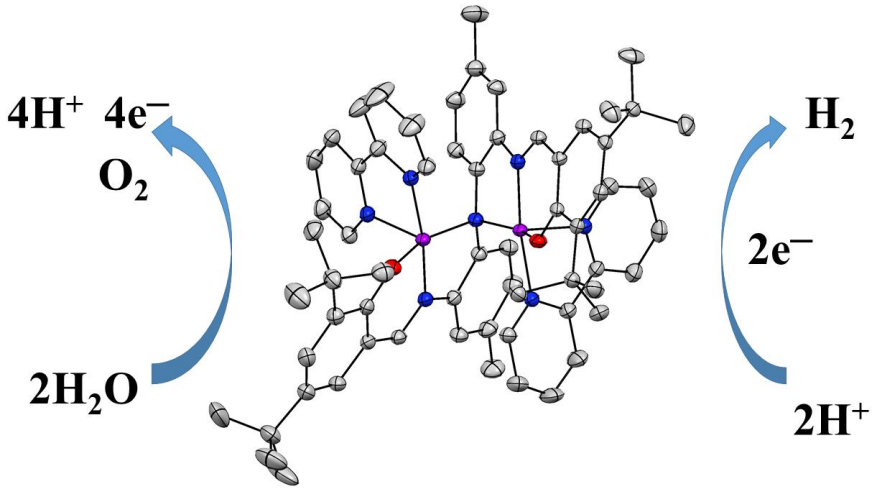

Abstract: In this chapter, the ability of $[Co_2(\mathbf{L}^{N3O2})(bpy)_2]ClO_4$ to serve as an electrocatalyst for proton reduction and water oxidation was investigated. Based on bulk electrolysis experiment, this dicobalt(II) complex is an efficient proton reduction catalyst with high turnover frequency ($TON \bullet h^{-1}$) of 24.7 and faradaic efficiency of 86%. The title complex is also capable of catalyzing water oxidation with a turnover frequency ($TON \bullet h^{-1}$) of 32 and a faradaic efficiency of 91%. Proposed mechanisms to explain catalytic process has been described.

These studies were performed in collaboration with the laboratory of Prof. Claudio Verani at Wayne State University (Detroit, MI).

7.1 Introduction

Projections of global energy needs for sustainable development suggest a nearly 50% increase by 2030.[287] Until now, world energy consumption is mainly supplied by non-renewable fossil fuels, which will be depleted within the next hundred years, and also lead to an increase in atmospheric CO_2 levels resulting in 'greenhouse effects' on global climate. [288-290] Although energy supplied by renewable resources has increased in recent years, a clean and abundant source of energy that can significantly reduce fossil fuel consumption has not yet been realized. Therefore, there is a demand to develop renewable energy sources to overcome the deficiency of fossil fuels.

Hydrogen gas (H_2) is expected to be a suitable energy source to replace fossil fuels.[287-290] The oxidation of hydrogen, by either fuel cell or combustion, yields water as its only product, making it environmentally benign in energy conversion.[291,292] Furthermore, hydrogen gas is a renewable energy carrier when it is generated from renewable sources of electricity, such as solar, wind, or hydroelectric power. Therefore, splitting water into hydrogen and oxygen is one of the most attractive topics for sustainable energy production.[293,294] During the last two decades, there has been significant progress in developing first-row transition metal catalysts in place of rare noble metal catalysts for proton reduction to hydrogen.[295-302]

Another key challenges to water splitting is the development of efficient catalysts for the water oxidation half-reaction that exhibit low overpotentials, good stability, and high turnover rates.[303] Discovering efficient catalysts for the water oxidation reaction has attracted the attention of numerous chemists in recent years.[304-310] The major improvements in the properties of these catalysts include reducing overpotentials, increasing catalyst durability, and using earth-abundant elements.[304]

With the goal of developing suitable electrocatalysts for water splitting processes, we have sought to prepare bimetallic complexes that incorporate "noninnocent" (redox-active) ligands. The ability to perform multiple electron transfers is critical for synthetic catalysts involved in small-molecule activation, such as the reduction of protons and oxidation of water.[311-315] Based on the cyclic and square-wave voltammogram data reported in Chapter 5, bpy-containing complexes like $[Co_2(\mathbf{L^{N3O2}})(bpy)_2]ClO_4$ (**15**) exhibit six redox couples over a range of 3.0 V that arise from both metal- and ligand-based events.[283] Redox-active ligands, like bpy and $\mathbf{L^{N3O2}}$, can therefore serve as electron reservoirs for multielectron transformations.

In this chapter, we describe our efforts to characterize the electrocatalytic activity of $[Co_2(\mathbf{L^{N3O2}})(bpy)_2]ClO_4$ for H_2 generation under weakly acidic conditions. This dicobalt(II) complex proved to be an efficient proton reduction catalyst with a high turnover frequency (TOF) of 24.7 turnovers per hour ($TON \bullet h^{-1}$) and a Faradaic efficiency of 86% (Faradaic efficiency: the ratio of the actual mass of a substance produced from an

electrolyte process by the passage of current to the theoretical mass produced according to Faraday's law). To determine whether the dinuclear structure of complex **15** is critical to the catalytic mechanism, a monocobalt(II) analogue (**18**) was prepared and its performance under identical conditions was examined. In addition, we explored the catalytic activity of complex **15** towards water oxidation; preliminary data measured a TOF of 32.2 TON•h^{-1} and Faradaic efficiency of 91% during the catalytic process. Possible catalytic mechanisms are currently under investigation using computational methods.

7.2 Experimental

Materials and Physical Methods. All reagents and solvents were purchased from commercial sources and used as received unless otherwise noted. Acetonitrile (MeCN), dichloromethane (DCM), and tetrahydrofuran (THF) were purified and dried using a Vacuum Atmospheres solvent purification system. Compounds were characterized and studied using elemental analysis, IR, NMR, UV-Vis and X-ray diffraction. Elemental analyses were performed at Midwest Microlab, LLC in Indianapolis, Indiana. Infrared spectra were measured as a powder on a Thermo Fisher Scientific Nicolet iS5 FT-IR spectrometer with an iD3 ATR accessory, or as KBr pellets using a Nicolet Magna-IR 560 spectrometer. NMR spectra were collected at room temperature with a Varian 400 MHz and 300 MHz spectrometer. UV-Vis spectra were collected with an Agilent 8453 diode array spectrometer.

N-(2,4-dinitrophenyl)-2,4,6-trimethylaniline

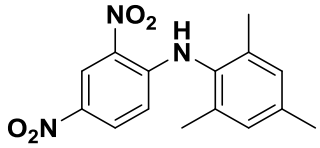

This procedure was adapted from previously published reports.[316] A round-bottom flask equipped with a stir bar was charged with a mixture of 1-chloro-2,4-dinitrobenzene (2.0 g; 10 mmol), 2,4,6-trimethylaniline (3.5 mL, 25 mmol) and potassium carbonate (2.76 g, 20 mmol). The mixture was heated to 140 ^{o}C and stirred overnight, which lead

to a bright yellow mixture. The mixture was cooled to room temperature and washed with hexane to remove excess 2,4,6-trimethylaniline. The residue was dissolved in 30 mL of water, then extracted three times with 50 mL of dichloromethane (DCM). The solvent was removed under vacuum to yield a bright orange powder as pure product (1.26 g, 4.2 mmol, 42 % yield). ^{1}H NMR (300 MHz, CDCl3) δ 2.15 (s, 6H), 2.35 (s, 3H), 6.48 (d, J = 9.5 Hz, 1H, Ar*H*), 7.03 (s, 2H, Ar*H*), 8.11 (d, J = 9.5 Hz, 1H, Ar*H*) 9.20 (s, 1H, Ar*H*), 9.57 (s, 1H, N*H*). ^{13}C NMR (75 MHz, $CDCl_3$) δ: 18.24, 21.27, 115.60, 124.53, 130.08, 130.49, 130.61, 131.29, 135.97, 137.20, 138.88, 148.21.

N-(2-amino-4-nitrophenyl)-2,4,6-trimethylaniline

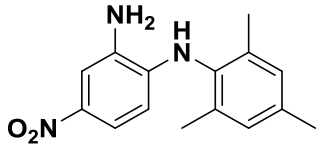

This procedure was adapted from previously published reports.[317] 0.6 g (2.0 mmol) of N-(2,4-dinitrophenyl)-2,4,6-trimethylaniline were introduced into a 100 mL flask fitted with a stir bar and reflux condenser. $NaHCO_3$ (0.42 g, 5.0 mmol) was dissolved into 10 mL of CH_3OH at high temperature and then added to the flask. A 33% solution of Na_2S solution (3.0 mL, 10 mmol of Na_2S) were added dropwise over the course of 10 mins while stirring. The whole mixture was refluxed for 4 hours. At the end of this period the reaction was poured into 100 mL of water. The mixture was cooled and the resulting precipitate was filtered and dried, yielding a deep red powder as pure product (0.369 g, 1.36 mmol, 68% yield). ^{1}H NMR (300 MHz, $CDCl_3$) δ 2.12 (s, 6H),

2.32 (s, 3H), 3.58 (s, 2H, N*H*$_2$), 5.56 (s, 1H, N*H*), 6.11 (d, *J* = 8.6 Hz, 1H, Ar*H*), 6.97 (s, 2H, Ar*H*), 7.66 (d, *J* = 8.6 Hz, 1H, Ar*H*), 7.71 (s, 1H, Ar*H*).

Proligand $H_2\mathbf{L}^{\mathbf{N2O}}$

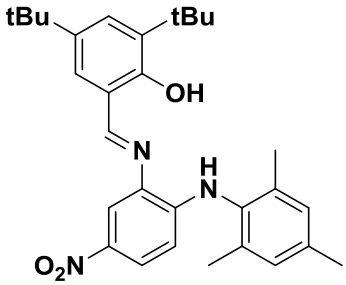

To a solution of *N*-mesityl-4-nitrobenzene-1,2-diamine (271 mg, 1.0 mmol, 1.0 eq.) in MeOH (30 mL) was added 3,5-di-tert-butyl-2-hydroxybenzaldehyde (234 mg, 1.0 mmol, 1.0 eq.) and *p*-toluenesulfonic acid (20 mg, 0.1 mmol, 0.1 eq.). The mixture was heated overnight at 60 ^{o}C under an inert atmosphere, giving rise to a bright yellow precipitate. The yellow solid was collected by filtration and dried under vacuum to yield pure $H_2\mathbf{L}^{\mathbf{N2O}}$ as a yellow powder (0.45 g, 0.93 mmol, 93% yield). ^{1}H NMR (400 MHz, $CDCl_3$) δ: 1.36 (s, 9H), 1.46 (s, 9H), 2.18 (s, 6H), 2.34 (s, 3H), 6.21 (d, *J* = 9.0 Hz, 1H, Ar*H*), 6.42 (s, 1H, Ar*H*), 7.00 (s, 2H, Ar*H*), 7.35 (d, *J* = 2.4 Hz, 1H, Ar*H*), 7.53 (d, *J* = 2.4 Hz, 1H, Ar*H*), 7.96 (d, *J* = 9.0 Hz, 1H, Ar*H*), 8.04 (s, 1H, Ar*H*), 8.85 (s, 1H, N=C-*H*), 12.76 (s, 1H, O-*H*). ^{13}C NMR (101 MHz, $cdcl_3$) δ: 18.13, 21.00, 29.40, 30.96, 31.42, 34.27, 35.14, 104.97, 109.95, 114.37, 118.32, 124.52, 127.59, 129.30, 129.54, 132.88, 134.26, 136.45, 137.21, 137.52, 138.39, 141.51, 146.49, 157.99, 165.95.

[Co(L^{N2O})(bpy)] (18)

Pro-ligand H_2**L^{N2O}** (48.7 mg, 0.100 mmol), bpy (15.6 mg, 1.0 eq.), and $Co(ClO_4)_2 \cdot 6H_2O$ (36.6 mg, 1.0 eq.) were added to a 25 mL flask containing 5 mL of DCM and MeCN in a 1:1 ratio. After stirring for 5 minutes, NEt_3 (28 μL, 2.0 eq.) was added, causing the solution to turn from brown to reddish brown. The mixture was stirred for two hours and then filtered through Celite. Removal of solvent under vacuum produced a reddish brown powder as the crude product. Pure product and X-ray-quality crystals were obtained by laying with a concentrated DCM solution with pentane. Yield = 25 mg (35.7%). UV-vis [λ_{max}, nm (ε, $M^{-1}cm^{-1}$) in MeCN]: 340 (21,000), 410 (13,000), 503 (11,500). FTIR (cm^{-1}; solid): 2956 (m), 2901 (w), 2859 (w), 1576 (m), 1516 (m), 1495 (m), 1459 (m), 1422 (m), 1383 (s), 1241 (s). ^{1}H NMR (400 MHz, $CDCl_3$) δ -1.13 (1H), 0.88 (3H), 1.99 (9H), 3.26 (6H), 3.67 (9H), 7.83 (1H), 8.36 (1H), 8.71 (1H), 13.22 (2H), 15.03 (1H), 16.03 (1H), 16.71 (1H), 25.79 (1H), 31.75 (1H). μ_{eff} = 1.70 μ_B (Evans method).

Acid Titration Experiments. Various equivalents of acetic acid (AcOH) were added to a solution of $[Co_2($**L^{N3O2}**$)(bpy)_2]ClO_4$ in MeCN with tetrabutylammonium hexafluorophosphate ($TBAPF_6$) as the supporting electrolyte. The electrochemical cell contained Ag/AgCl as the reference electrode, platinum wire as the auxiliary electrode, and a working electrode. Two types of working electrodes were employed: glassy carbon

and gold amalgam; the latter was prepared by dipping a gold working electrode in mercury for 30 minutes, followed by removal of excess mercury.

Bulk Electrolysis Experiments (Proton Reduction): (Note: this work was carried out by our collaborator at Wayne State University). The experiment was carried out in a custom-made airtight H-type cell in the presence of mercury-pool as a working electrode, Ag/AgCl as the reference electrode placed in the same compartment, and Pt-coil as the auxiliary electrode. The Pt coil was placed in the other compartment separated by a frit. Tetrabutylammonium hexafluorophosphate ($TBAPF_6$) was used as the supporting electrolyte. The main chamber was filled with the electrolyte solution and proton source ($TBAPF_6$: 1.560 g; AcOH: 0.024 g [0.4 mmol], 20 mL CH_3CN) and the frit-fitted chamber was filled with electrolyte solution ($TBAPF_6$: 0.390 g; 5 mL CH_3CN). The cell was purged with N_2 gas for 20 minutes followed by sampling head space gas (100μl) to ensure O_2 free environment with GC. Then the solution without catalyst was electrolyzed for three hours at -1.6 V vs. Ag/AgCl.

The head space gas was again injected into the GC in triplicates to record the amount of dihydrogen H_2. The experiment was repeated for the catalyst. The main chamber was filled with electrolyte solution and proton source ($TBAPF_6$: 1.560 g; AcOH: 0.048 g [0.8 mmol], 20 mL CH_3CN) and the glass-fitted chamber was filled with electrolyte solution (TBAPF6: 0.390 g; 5 mL CH_3CN). The cell was again purged with N_2 gas for another 20 minutes followed by injection of the catalyst (0.004 mmol)

dissolved in CH_3CN. Bulk electrolysis was conducted for another three hours at -1.6 V vs. Ag/AgCl and head space gas (100 μL) was injected into the GC to record the amount of H_2 produced. The turnover number was calculated (after background subtraction) as the ratio between moles of H_2 produced divided by moles of catalyst. The amount of charge consumed was measured by analysis of the "charge versus time" plot during bulk electrolysis. Faradaic efficiency was calculated from the GC measurements.

Bulk Electrolysis Experiments (Water Oxidation). (Note: this work was carried out by our collaborator at Wayne State University). A controlled potential bulk electrolysis experiment was performed at 1.5 V vs Ag/AgCl using a fluorine-doped tin oxide (FTO) plate as the working electrode. A two compartment H-cell separated by a fine frit was used for these experiments. The working compartment of the electrochemical cell contained the FTO working electrode and the Ag/AgCl reference electrode. This compartment was filled with the catalyst (0.2 μmol) in MeCN/borate buffer (1:9 v/v, 0.1 M, pH 8.0). The second compartment of the electrochemical cell contained the platinum wire auxiliary electrode and was filled with MeCN/borate buffer (1:9 v/v, 0.1 M, pH 8.0). Nitrogen was used as an internal standard.

Crystallographic Studies. X-ray diffraction data were collected at 100 K with an Oxford Diffraction SuperNova diffractometer equipped with a 135 mm Atlas CCD detector and Cu(Kα) radiation source. The resulting data were processed with the CrysAlis Pro program package (Agilent Technologies, 2011). An absorption correction

was performed on the real crystal shape followed by an empirical multi-scan correction using SCALE3 ABSPACK routine. Structures were solved using the SHELXS program and refined with the SHELXL program[102] within the Olex2 crystallographic package.[103] All non-hydrogen atoms were refined with anisotropic displacement parameters. Hydrogen atoms were generally positioned geometrically and refined using appropriate geometric restrictions on bond lengths and bond angles within a riding/rotating model, and the torsion angles of $–CH_3$ hydrogens were optimized to better fit residual electron density. X-ray crystallographic parameters are provided in **Table 7.2**.

7.3 Result and discussion

7.3.1 Ligand design and characterization of mononuclear analogue complex

As reported in Chapter 5, the bimetallic cobalt complex $[Co_2(\mathbf{L}^{\mathbf{N3O2}})(bpy)_2]ClO_4$ (**15**) structure shows that the $\mathbf{L}^{\mathbf{N3O2}}$(3–) ligand supports a dicobalt(II) unit in which the metal centers are bridged by the N-atom of the diarylamido donor. Each five-coordinate Co(II) center is additionally coordinated by a imine N and phenolate O donor from $\mathbf{L}^{\mathbf{N3O2}}$, in addition to a bidentate 2,2'-bipyridine (bpy) ligand. (**Figure 7.1**) Based on the cyclic and square-wave voltammograms data, we found six redox couples over a potential range of 3.0 V arising from both metal- and ligand-based events.

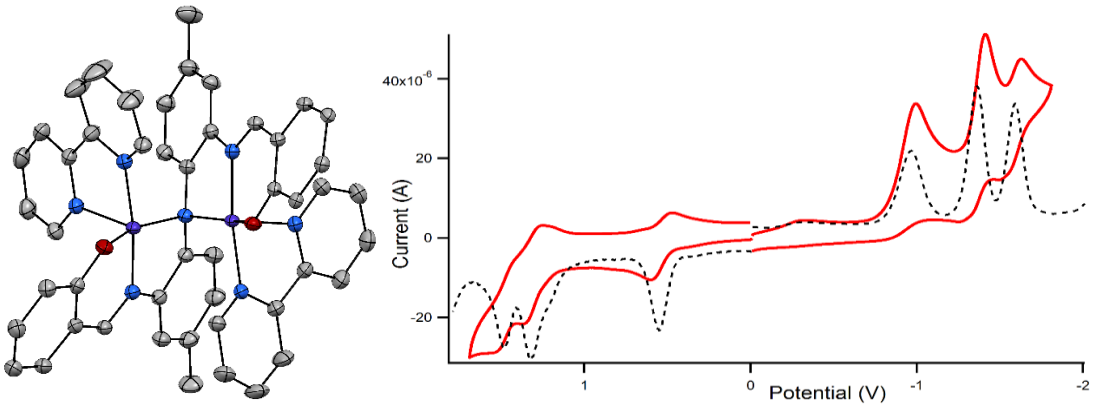

Figure 7.1 Structure and CV data (vs. Ag/AgCl reference) of $[Co_2(\mathbf{L}^{\mathbf{N3O2}})(bpy)_2]ClO_4$ (**15**).

In order to examine the catalytic mechanism and elucidate the role of the second metal ion catalytic processes, we have designed and synthesized an analogue of $\mathbf{L}^{\mathbf{N3O2}}$

capable of supporting a mononuclear cobalt complex. The structure of the pro-ligand, referred to as $H_2\mathbf{L}^{N2O}$ is shown in **Scheme 7.1**. Like $\mathbf{L}^{N3O2}$, the $\mathbf{L}^{N2O}$ framework provides imine, phenolate, and diarylamido donors in a meridional (pincer-like) arrangement, thus allowing for the binding of auxiliary ligands.

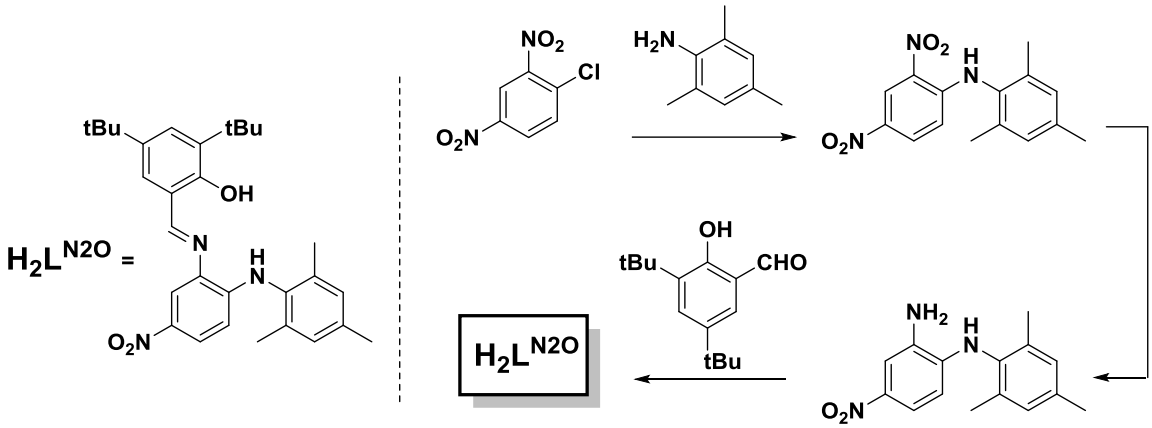

Scheme 7.1 Structure (a) and synthesis (b) of the analogue pro-ligand $H_2\mathbf{L}^{N2O}$.

Ligand and complex synthesis

The pro-ligand $H_2\mathbf{L}^{N2O}$ was prepared by the route shown in **Scheme 7.1** and its identity was confirmed by ^{1}H NMR spectroscopy. The monometallic Co(II) complex was prepared by reaction of $H_2\mathbf{L}^{N2O}$ with one equivalent of $Co(ClO_4)_2 \cdot 6H_2O$ in the presence of two equivalents of NEt_3, along with addition of one equivalent of the auxiliary ligand 2,2'-bipyridine (bpy). The resulting complex, [Co($\mathbf{L}^{N2O}$)(bpy)] (**18**), is soluble in most organic solvents but insoluble in pentane. Complex **18** possesses a dark reddish-brown color due to an absorption manifold with λ_{max} near 430 nm ($\varepsilon \sim 10^4$ $M^{-1}cm^{-1}$). As

expected, this mononuclear cobalt(II) complex gives rise to ^{1}H NMR spectra with broad, paramagnetically shifted peaks. A magnetic moment of μ_{eff} = 1.70 μ_B was measured at room temperature using the Evans method. This value nicely matches the spin-only value of 1.73 μ_B expected for a low-spin Co(II) center with S = 1/2 spin.

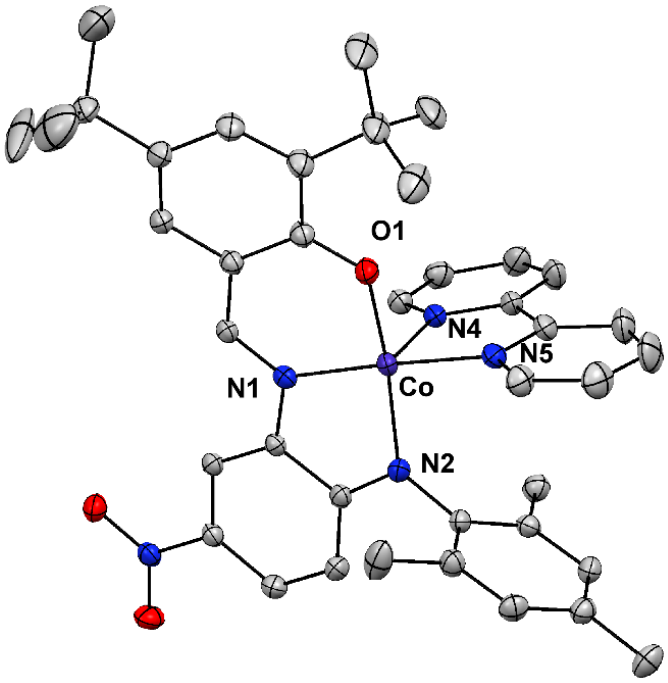

Figure 7.2 Thermal ellipsoid plot (50% probability) of the cationic unit in the X-ray structure of [Co(**L**^{N2O})(bpy)] (**18**). All hydrogen atoms have been omitted for clarity.

Dark reddish-brown crystals of the mononuclear cobalt complex suitable for X-ray diffraction analysis were grown by layering a concentrated DCM solution with pentane. As shown in **Figure 7.2**, the complex features a five-coordinate Co(II) center coordinated to 2,2-bipyridine and the dianionic pincer ligand **L**^{N2O}. The Co(II) ion adopts

a square-pyramidal coordination geometry (τ value = 0.175) with one of pyridyl groups in the axial position. Selected bond distances and angles are provided in **Table 7.1,** and values for the bimetallic complex $[Co_2(\mathbf{L^{N3O2}})(bpy)_2]ClO_4$ (**15**) are also indicated for the sake of comparison. Metric parameters for the two complexes (**15** and **18**) are quite similar, with differences in bond distances less than ±0.04 Å. Simply put, complex **18** is a suitable mononuclear analogue of the bimetallic complex **15**.

Table 7.1 Selected Bond Distances (Å) and Angles (°) Obtained from the Crystal Structures of Complexes **15** and **18**.

Bond distances	$[Co_2(\mathbf{L^{N3O2}})(bpy)_2]^+$ (**15**)		$Co(\mathbf{L^{N2O}})(bpy)$ (**18**)
	Co1	Co2	
Co1-O1	1.899(2)	1.895(2)	1.872(2)
Co1-N1	1.889(2)	1.888(2)	1.889(2)
Co1-N2	1.966(2)	1.964(2)	1.926(2)
Co1-N4	2.064(2)	2.059(2)	2.075(2)
Co1-N5	1.942(2)	1.943(2)	1.953(2)
Bond angles			
O1-Co1-N1	93.52(8)	93.92(7)	94.34(9)
O1-Co1-N2	158.41(7)	156.69(7)	166.61(10)
O1-Co1-N4	84.38(7)	86.33(7)	88.49(9)
O1-Co1-N5	106.01(7)	105.79(7)	96.68(9)
N1-Co1-N2	85.02(8)	84.76(7)	84.15(10)
N1-Co1-N4	91.98(8)	91.57(8)	93.03(10)
N1-Co1-N5	99.83(8)	98.11(7)	99.39(9)
N2-Co1-N4	171.85(8)	172.13(8)	177.15(10)
N2-Co1-N5	95.57(8)	97.51(8)	96.69(9)
N4-Co1-N5	81.08(8)	80.81(8)	80.55(10)
τ-value	0.22	0.26	0.18

Electrochemical Studies of [Co(L^{N2O})(bpy)] (18).

Voltammetric methods were used to examine the electrochemical properties of [Co(**L^{N2O}**)(bpy)] (**18**) in MeCN solutions with 0.1 M $(NBu_4)PF_6$ as the supporting electrolyte and scan rates of 100 mV/s. The reported potentials are relative to the Ag/AgCl reference couple. Assignment of these features to either metal- or ligand-based redox events is aided by comparison to data collected for complex **15**. The cyclic and square-wave voltammograms (CV and SWV) of complex **18** (**Figure 7.3**) reveal two redox features at negative potentials of -1.15, and -1.52 V. The lowest-potential event is quasi-reversible whereas the peak at -1.20 V is irreversible. The lowest-potential feature at -1.52 V corresponds to one-electron reduction of the 2,2'-bipyridine ligand, while the wave at -1.15 V is assigned to one-electron reduction of Co(II) to Co(I). Three events are observed at more positive potentials of -0.02, 0.98, and 1.53 V. The quasi-reversible redox couple near -0.02 V arises from oxidation of the μ-NAr_2 unit of the **L^{N2O}** ligand, while the features at 0.98 and 1.53 V arise from one-electron oxidation of the Co(II) center and phenolate ligand, respectively (**Scheme 7.2**).

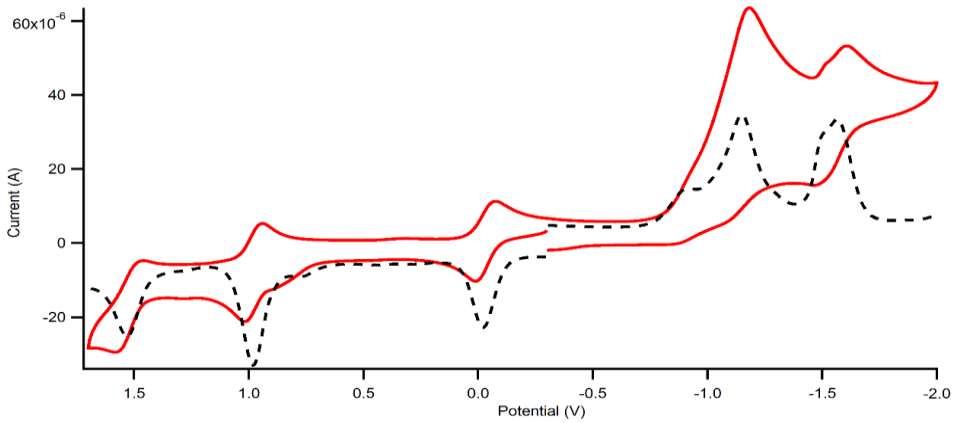

Figure 7.3 Cyclic voltammograms (solid lines) of mononuclear complex [Co(**L**^{N2O})(bpy)] (**18**) collected in MeCN with 0.1 M (NBu_4)PF_6 as the supporting electrolyte. The corresponding square-wave voltammograms are indicated by the dashed lines. All scan rates were 100 mV/s.

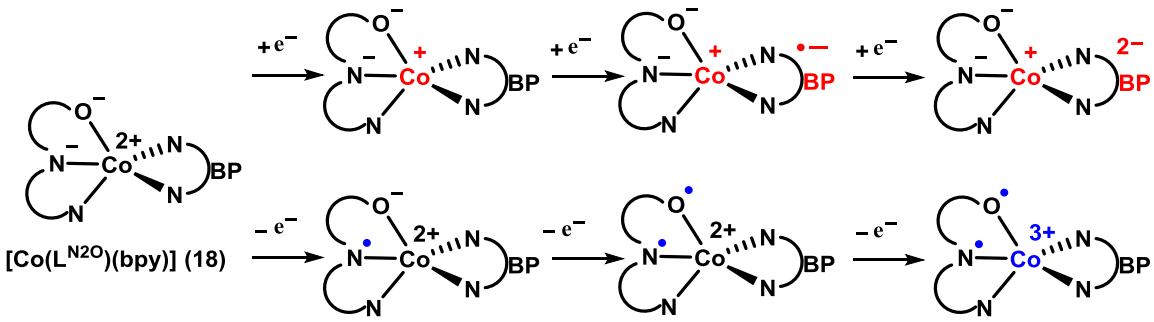

Scheme 7.2 Illustration of redox behaviors of [Co(**L**^{N2O})(bpy)] (**18**) in MeCN.

7.3.2 Proton Reduction with [Co_2(**L**^{N3O2})(bpy)$_2$]ClO_4

We tested the activity of bimetallic cobalt complex towards electrochemical proton reduction in presence of weak acids such as acetic acid (AcOH; pK_a = 22.3 in MeCN) and 4-tert-butylphenol (pK_a = 27.5 in MeCN). As shown in **Figure 7.4**, addition of acetic acid (AcOH) to solutions of [Co_2(**L**^{N3O2})(bpy)$_2$]ClO_4 (**15**) (2.0 mM) in CH_3CN

results in significant current enhancement at potentials lower than −1.2 V, suggestive of electrocatalytic proton reduction. Significantly, the enhanced catalytic wave displays two distinct events at −1.4 and −1.65; these potentials correspond to the putative reduction of the bpy ligands in the absence of acid. Plots of current versus AcOH concentration at potentials of −1.4 and −1.62 V are provided in **Figure 7.6**. At both potentials, the measured current increases linearly with [AcOH] up to 100 mM (data was not collected at higher acid concentrations). CV data were also obtained under identical conditions but in the absence of $[Co_2(\mathbf{L^{N3O2}})(bpy)_2]ClO_4$ (**15**); as indicated in **Figure 7.6**, there is very little increase in current without the presence of the dicobalt complex, even at high concentrations of AcOH. Current enhancements were also observed for complex **15** in the presence of 4-*tert*-butylphenol (**Figure 7.5**). In this case, the onset of current enhancement occurs at a lower potential (-1.5 V) due to the lower acidity of 4-*tert*-butylphenol compared to AcOH.

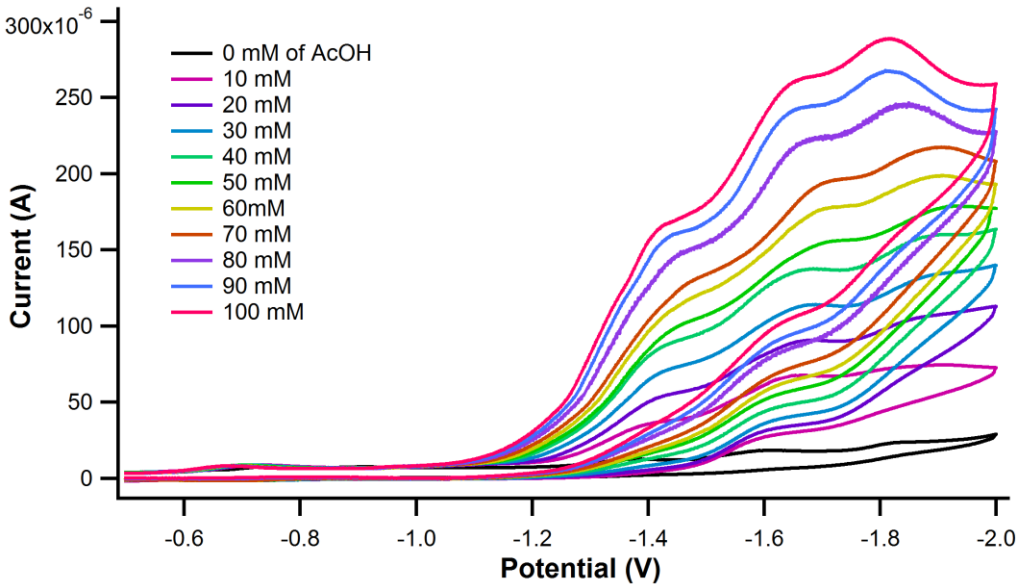

Figure 7.4 Cyclic voltammograms (CVs) of 2.0 mM catalyst **15** in MeCN with $TBAPF_6$ as the supporting electrolyte, Ag/AgCl as the reference electrode, amalgamated gold as the working electrode and platinum as the counter electrode. Acetic acid was used as acid source. Scan rate is 100 mV s^{-1}.

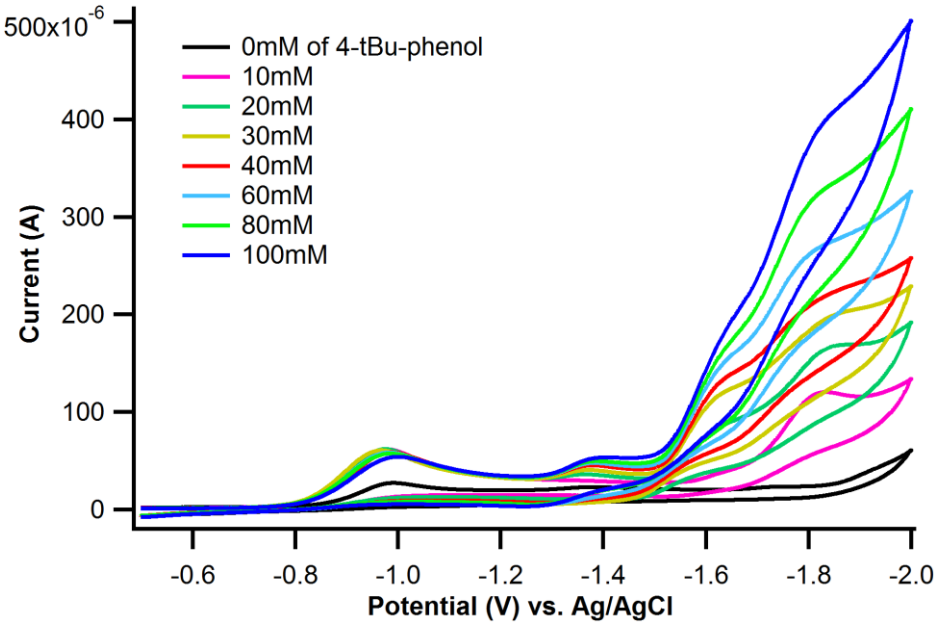

Figure 7.5 Cyclic voltammograms (CVs) of 2.0 mM catalyst **15** in MeCN with $TBAPF_6$ as the supporting electrolyte, Ag/AgCl as the reference electrode, glassy carbon as the working electrode and platinum as the counter electrode. 4-tert-butylphenol was used as acid source. Scan rate is 100 mV s^{-1}.

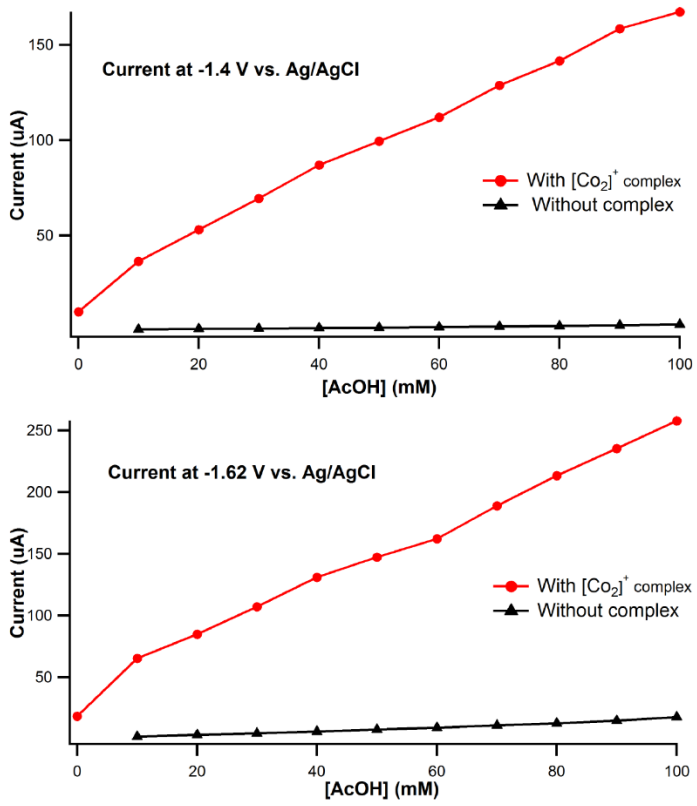

Figure 7.6 *Red dots*: CV current at -1.4 V (top) and -1.62 V (bottom) as a function of [AcOH] for solutions of $[Co_2(\mathbf{L}^{\mathbf{N3O2}})(bpy)_2]ClO_4$ (**15**) (2.0 mM) in CH_3CN. *Black triangles*: The corresponding data measured under identical conditions but in the absence of complex **15**. All results were obtained using an amalgamated gold working electrode in CH_3CN solutions with 0.1 M $(NBu_4)PF_6$ as the supporting electrolyte.

A series of two-minute bulk electrolysis experiments (**Figure**. **7.7a)** were carried out by our collaborator in Prof. Verani's lab to determine the onset potential for this proton reduction process.[298] The experiments were run with the catalyst (0.004 mmol, 4.74 mg) dissolved in a solution of acetonitrile ($TBAPF_6$: 1.560 g, 20 mL) with 200 equivalents of acetic acid (AcOH: 0.048 g [0.8 mmol]) at various applied potentials**.** The graph shows the total charge of bulk electrolysis of the catalyst in the presence of acid.

The charge remained constant until at -1.4 V (vs. Ag/AgCl) when the charge significantly increased with more negative applied potentials until -1.6 V where a maximum charge of 0.45 C was consumed during 2 minutes of electrolysis, with accompanying evolution of a gas, which was confirmed as H_2 by gas chromatography.

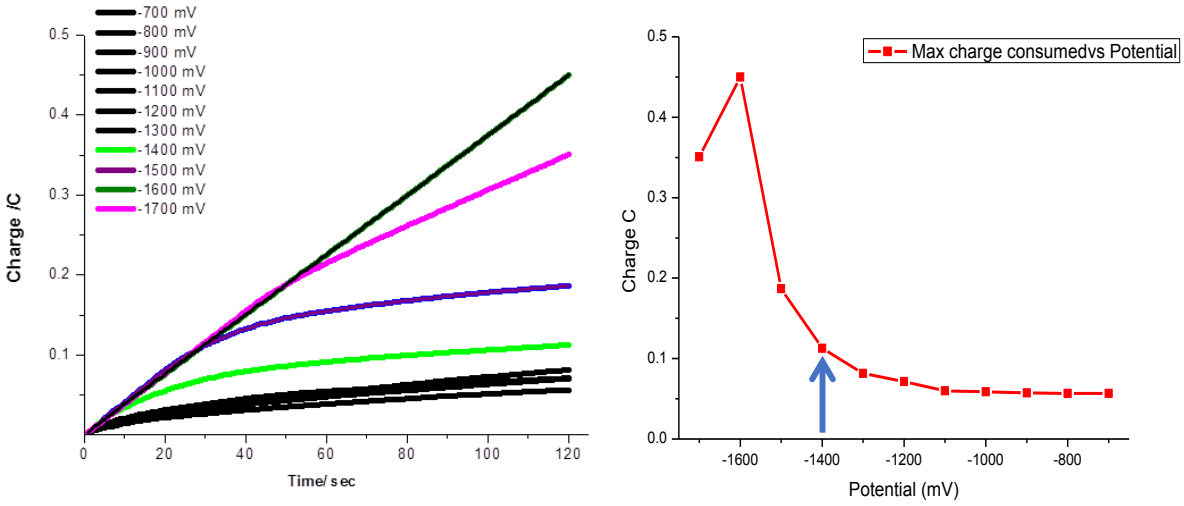

Figure 7.7 a) Charge buildup versus time from bulk electrolysis of catalyst under various applied potentials. (Hg pool as working electrode, Pt coil as counter electrode, Ag/AgCl as reference electrode). **b)** Maximum charge consumed versus applied potential.

When -1.7 V (vs. Ag/AgCl) potential was applied, the charge initially increased but plateaued after the first minute yielding a charge of only 0.35 C in 2 minutes. These results suggest that the amount of charge consumed increased at more negative potential, but the catalyst undergoes transformation at -1.7 V and lower. A plot of charge consumed versus potential applied is shown in **Figure 7.7b**. The result suggests that the onset potential for catalysis occurs at -1.4 V. In addition, 3-hour bulk electrolysis was

performed at -1.6 V to determine the efficiency of the catalyst at these potentials with 200 equivalents of acid. These results are shown in **Figures 7.8.**

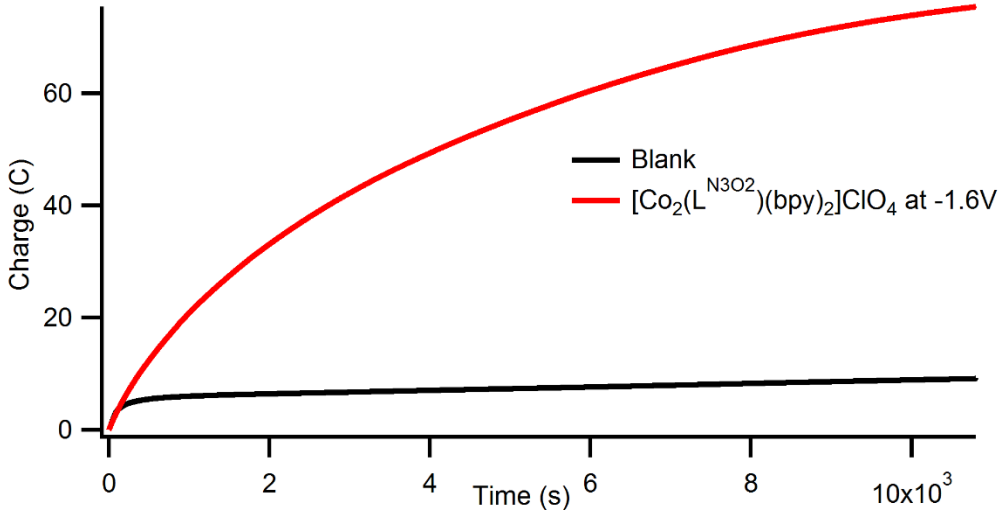

Figure 7.8 Charge buildup versus time from bulk-electrolysis at -1.6 V vs. Ag/AgCl, (Hg pool as working electrode, Pt coil as counter electrode, Ag/AgCl as reference electrode).

This bulk electrolysis experiment was carried out with 0.004 mmol (4.74 mg) of catalyst in 20 mL of MeCN, which resulted in the consumption of 76 coulombs of charge within three hours. If we assume the two cobalt centers work together, such that complex **15** only contains one catalytic site, we obtain a turnover number (TON) per molecule of 74.2 and a faradaic efficiency of 86%. The TON was calculated using the expression below:

$$TON = [H_2]/[Cat]$$

However, if each cobalt center is acting as an independent catalyst, such that complex **15** contains two catalytic sites, then the calculated TON is 37.1 for three hours. Based on the bulk electrolysis results, this bimetallic cobalt complex can be judged as good catalyst toward proton reduction by comparing with other reported catalysts.[298]

In order to prove that our catalyst is robust during the catalytic process, a UV-Visible spectrum was taken before and after bulk electrolysis at -1.6 V **(Figure 7.9).** The spectrum after electrolysis at -1.6 V showed about 10% decrease based on the band at 450 nm. This decrease can be explained by minimal diffusion of solvent from the auxiliary chamber into the catalytic chamber through the frit separating them during catalysis. Therefore, we can postulate that the identity of the catalyst is maintained during the experiment, and no obvious formation of nanoparticles was observed.

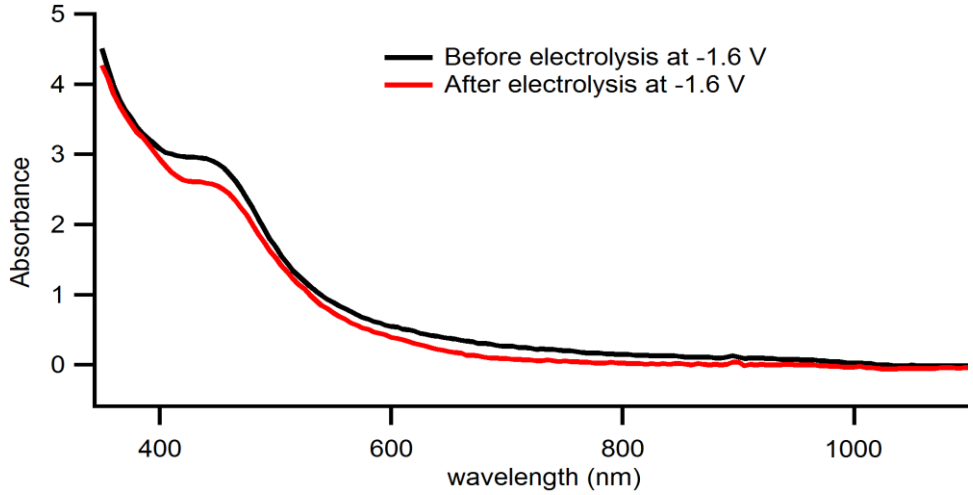

Figure 7.9 Comparison of the UV-Visible spectra before and after bulk-electrolysis at -1.6 V vs. Ag/AgCl.

7.3.3 Water Oxidation with $[Co_2(L^{N3O2})(bpy)_2]ClO_4$

The ability of $[Co_2(\mathbf{L}^{N3O2})(bpy)_2]ClO_4$ (**15**) to function as an electrocatalyst for water oxidation was investigated in the laboratory of our collaborator, Prof. Claudio Verani. The cyclic voltammograms obtained in MeCN/borate buffer[318,319] (1:9 v/v, 0.1 M, pH 8) is shown in **Figure 7.10** below.

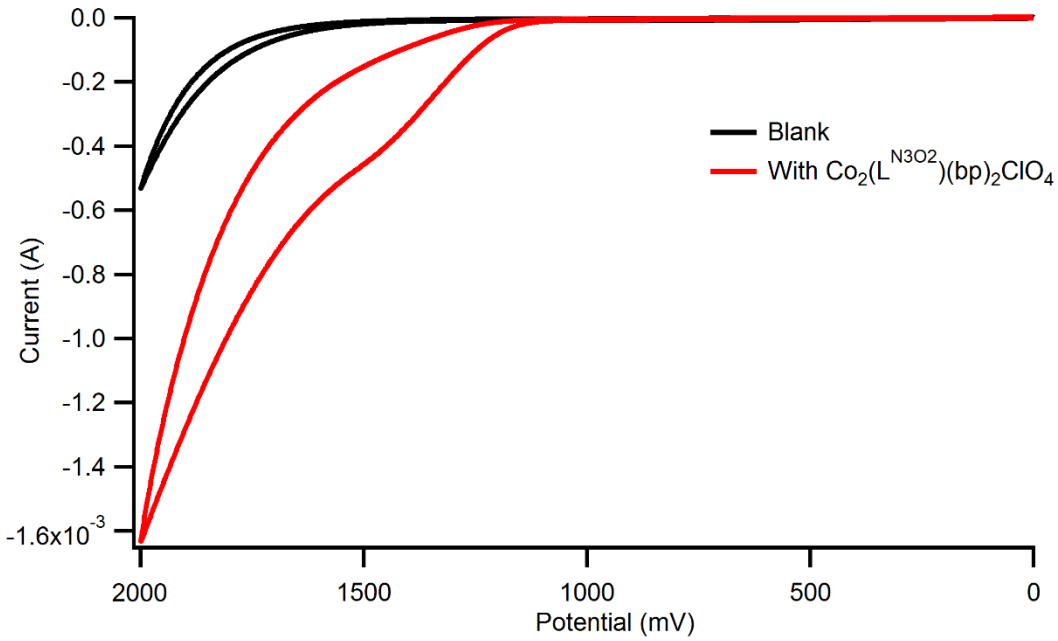

Figure 7.10 Cyclic voltammetry of catalyst **15** (red line) in a 0.1M MeCN/borate (1:9) buffer (pH=8), and the buffer alone (black line) at a scan rate of 100 mV/s under Ar atmosphere with an FTO working electrode, a Pt wire as auxiliary electrode and a Ag/AgCl as reference electrode.

The control sample (borate buffer without the catalyst) exhibits a current enhancement peak of -0.5 mA starting from 1.5 V to 2.0 V vs. Ag/AgCl. Upon the

addition of the catalyst, two peaks were observed. An oxidation peak is observed at 1.45 V and is followed by a catalytic wave for water oxidation. This indicates that complex **15** can be effective as a catalyst for water oxidation.

A controlled potential bulk electrolysis experiment **(Figure 7.11)** was performed at 1.5 V (vs. Ag/AgCl) using a fluorine-doped tin oxide (FTO) plate as working electrode. A two compartment H-cell separated by a fine frit was used for these experiments. The working compartment of the electrochemical cell contained the FTO working electrode and the Ag/AgCl reference electrode. This compartment was filled with the catalyst (0.2 μmol) in MeCN/borate buffer (volume ratio = 1:9, 0.1 M, pH 8.0). The second compartment of the electrochemical cell contained the platinum wire auxiliary electrode and was filled with MeCN/borate buffer (1:9 v/v, 0.1 M, pH 8.0). Nitrogen was used as an internal standard. A control (blank) experiment was conducted where the working compartment contained no catalyst and only MeCN/borate buffer (1:9 v/v, 0.1 M, pH 8.0). Both experiments were run for 3 hours. During the 3 hour bulk electrolysis (1.5 V vs Ag/AgCl), a charge of -11.3 C was consumed and a turnover frequency ($TON \bullet h^{-1}$) of 32 with a faradaic efficiency of 91%. Based on those data, this bimetallic cobalt complex can be defined as effective bifunctional catalyst for both proton reduction and water oxidation.

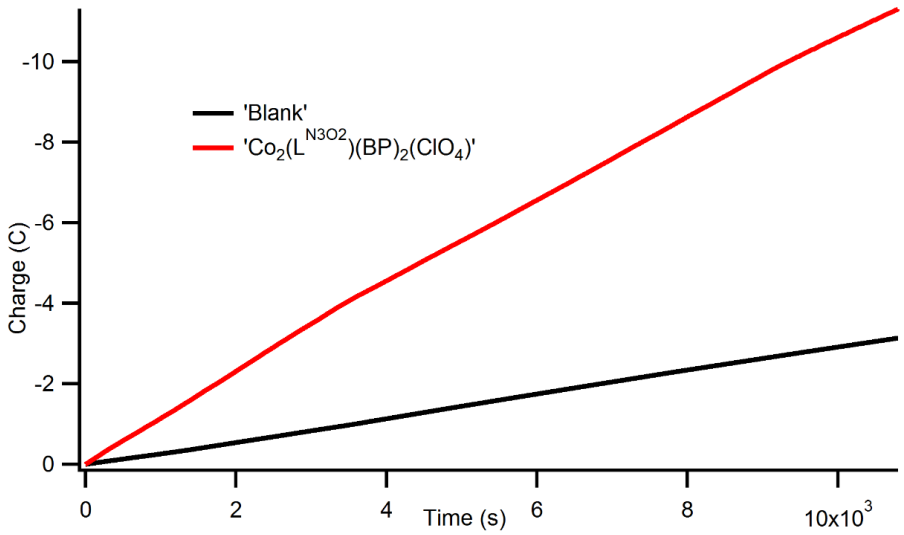

Figure 7.11 0.1M MeCN/borate buffer (pH 8), FTO as working electrode; Ag/AgCl as reference electrode; Pt wire as auxiliary electrode; Applied Potential at 1.5 V vs Ag/AgCl.

7.3.4 Proton reduction of mononuclear [Co($\mathbf{L^{N2O}}$)(bpy)]

An acid titration experiment[320] was performed for the mononuclear catalyst by the addition of various equivalents of acetic acid (AcOH) to a solution of [Co($\mathbf{L^{N2O}}$)(bpy)] (**18**) in MeCN. An observed catalytic current of 150 μA was measured after addition of 20 equiv of AcOH as shown in **Figure 7.12**. The current enhancement current is lower than the current observed for the binuclear analogue [Co_2($\mathbf{L^{N3O2}}$)$(bpy)_2$]ClO_4 (**15**) although at a lower potential of -1.5 V vs Ag/AgCl.

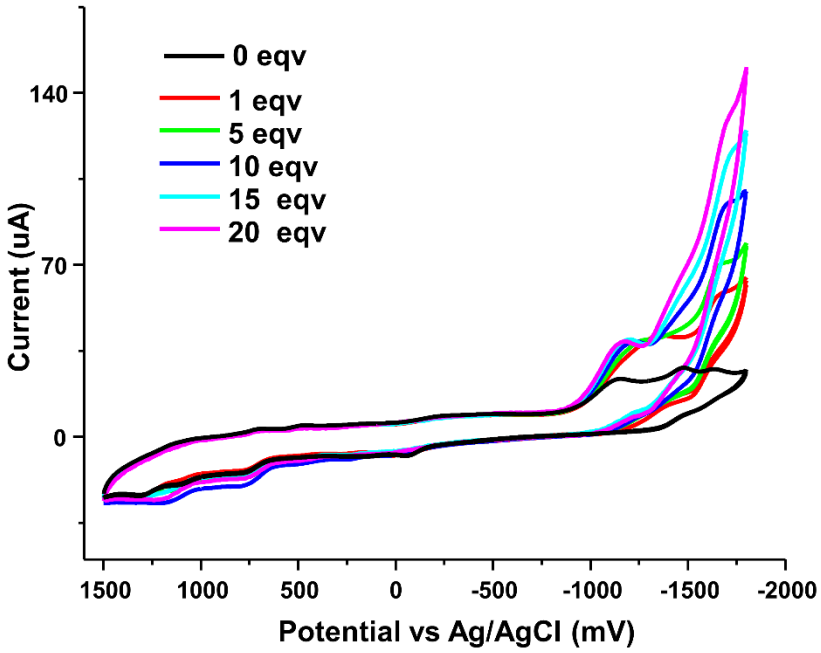

Figure 7.12 Cyclic voltammetry in MeCN with $TBAPF_6$ as supporting electrolyte, Ag/AgCl as reference electrode, glassy carbon as working electrode and Pt as the counter electrode. Acetic acid was used as acid source. Scan rate is 100mV/s

The hydrogen produced by the catalyst **18** was measured by bulk electrolysis experiments in the presence of AcOH. Bulk electrolysis was conducted for three hours at -1.5 V vs Ag/AgCl and the head space gas (100 μL) was injected in to the GC to record the amount of H_2 produced. The turnover number was calculated after background subtraction. Faradaic efficiency was calculated from the maximum charge consumed from the charge versus time plot during bulk electrolysis (shown as **Figure 7.13**). A turnover number (TON) of 35.4 after 3 h was calculated with 100 equiv of acid. Faradaic efficiency was significantly lower than the binuclear analogue at 64%. The results revealed a respectable TON but low faradaic efficiency. This could be an indication that

the [Co($\mathbf{L}^{\mathbf{N2O}}$)(bpy)] (**18**) catalyst is either being transformed into a different species which is itself catalytic, the catalyst is undergoing other molecular processes, or the compound is a procatalyst that loses a ligand before catalysis occurs.

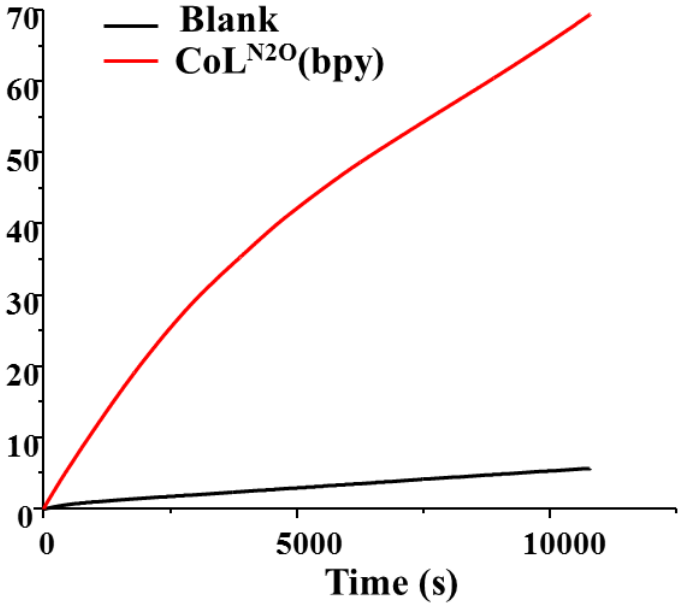

Figure 7.13 Charge buildup versus time from bulk-electrolysis (BE) at -1.5 V vs. Ag/AgCl, (Hg pool as working electrode, Pt coil as counter electrode, Ag/AgCl as reference electrode).

During the catalytic process, the color of the solution changes from dark brown to light yellow. UV-visible spectra were taken before and after bulk electrolysis at -1.5 V to determine the robustness of the catalyst during catalysis **(Figure 7.14)**. The spectrum obtained after electrolysis shows a significant disappearance of the two bands at 500 nm and 450 nm respectively. This is probably due to exchange of the bipyridine ligand with

acetate in solution, or perhaps the $\mathbf{L^{N2O}}$ ligand has dissociated from the complex. Regardless, it is clear that the identity of the catalyst changes during bulk electrolysis.

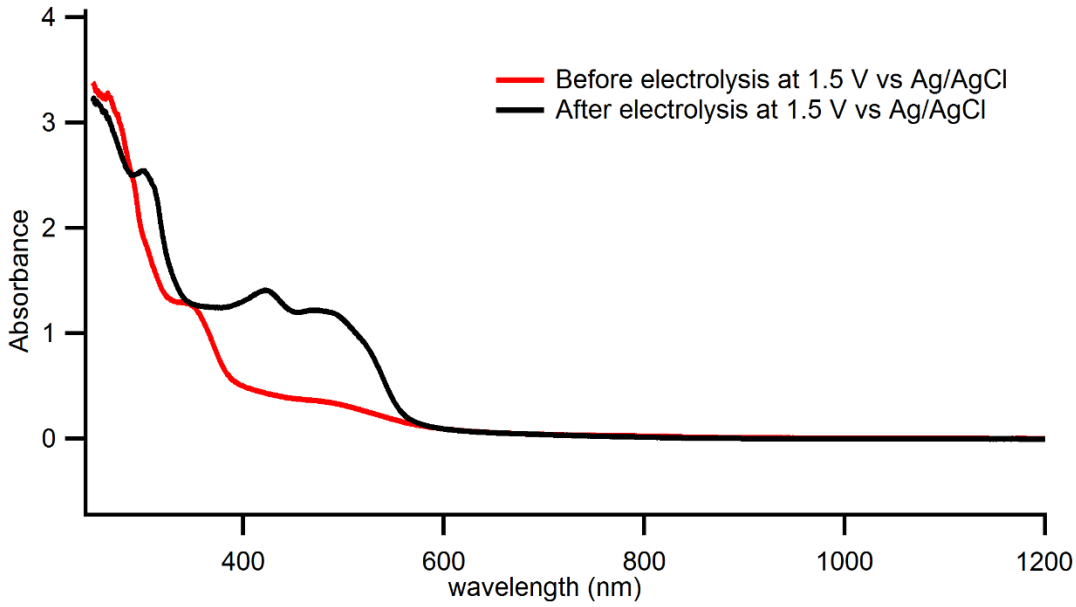

Figure 7.14 Comparison of the UV-Visible spectra before and after bulk-electrolysis (BE) at 1.5 V vs. Ag/AgCl

7.3.5 Proposed mechanism

The mono- and dinuclear cobalt(II) complexes (**15** and **18**) have similar ligand coordination environments, electronic structures, and electrochemical properties. However, the dicobalt complex **15** is a more robust and efficient catalyst for H_2 generation than complex **18**. These results indicate that the second cobalt ion can stabilize the catalyst and improve catalytic efficiency.

Schemes 7.3 and **7.4** offer possible catalytic mechanisms to explain both proton reduction and water oxidation by the dicobalt complex **15**. However, these proposals should be considered preliminary until further investigation with both experimental and computational methods. Importantly, DFT calculations are now underway in the lab of Prof. Bernhard Schlegel (Wayne State University) to determine the most energetically-feasible catalytic cycles for both processes.

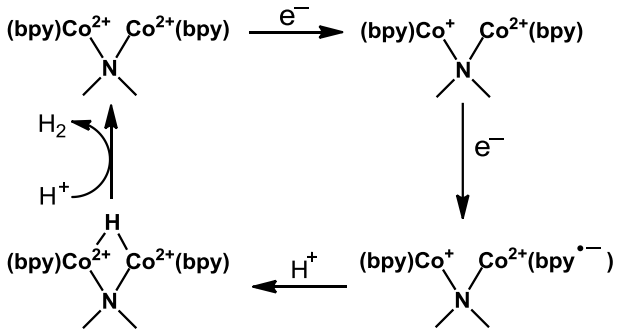

Scheme 7.3 Possible mechanism of electrocatalytic proton reduction.

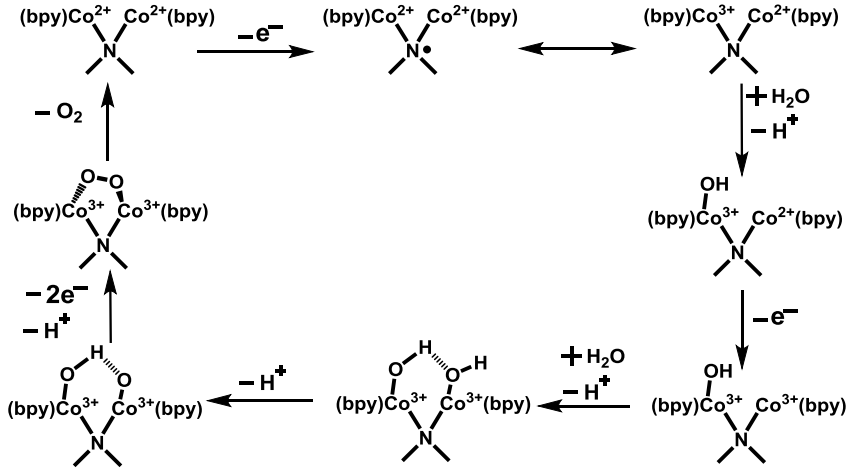

Scheme 7.4 Possible mechanism of electrocatalytic water oxidation.

Our lab successfully isolated a dicobalt(III)-peroxo complex with the 4,4'-dibromo-2,2'-bipyridine auxiliary ligand, as reported in Chapter 5. A similar peroxo complex may be an intermediate in the catalytic mechanism of electrocatalytic water oxidation (**Scheme 7.4**).

7.4 Conclusion

As demonstrated in this chapter, $Co_2(\mathbf{L^{N3O2}})(bpy)_2]ClO_4$ (**15**) and [Co($\mathbf{L^{N2O}}$)(bpy)] (**18**) are able to serve as electrocatalysts for H_2 generation under weakly acidic conditions. The dinuclear cobalt complex **15** is an efficient proton reduction catalyst, exhibiting a high turnover frequency ($TON \bullet h^{-1}$) of 24.7 and faradaic efficiency of 86%. Comparison of TONs and efficiencies for the analogous mononuclear complex **18** suggests that the second Co(II) ion is essential to both stabilize the catalyst and facilitate reactivity. In addition, we explored the catalytic activity of dinuclear cobalt complex **15** toward water oxidation and found a turnover frequency ($TON \bullet h^{-1}$) of 32 with a faradaic efficiency of 91%. Mechanistic studies involving DFT calculations are ongoing.

Table 7.2 Summary of X-ray crystallographic data collection and structure refinement

	[Co($\mathbf{L^{N2O}}$)(bpy)] (**18**)
Empirical formula	$C_{41.91}H_{46.82}Cl_{3.82}CoN_5O_3$
Formula weight	863.05
Crystal system	monoclinic
Space group	$P2_1/c$
a [Å]	18.11795(12)
b [Å]	12.89174(9)
c [Å]	18.53322(10)
[°]	90
[°]	93.5186(6)
[°]	90
Volume [Å^3]	4320.68(5)
Z	4
ρ_{calc} [g/cm^3]	1.327
(Å)	1.5418
[mm^{-1}]	5.631
range [^{o}]	8.36 to 148.18
Reflections collected	41446
Independent reflections (R_{int})	8684 [R_{int} = 0.0439, R_{sigma} = 0.0295]
Data/restraints/parameters	8684/6/519
Goodness-of-fit on F^2	1.044
*R*1/*wR*2 indexes [I >2σ(I)]	R_1 = 0.0624, wR_2 = 0.1801
*R*1/*wR*2 indexes [all data]	R_1 = 0.0665, wR_2 = 0.1863

BIBLIOGRAPHY

(1) Cao, X.; Antonyuk, S. V.; Seetharaman, S. V.; Whitson, L. J.; Taylor, A. B.; Holloway, S. P.; Strange, R. W.; Doucette, P. A.; Valentine, J. S.; Tiwari, A.; Hayward, L. J.; Padua, S.; Cohlberg, J. A.; Hasnain, S. S.; Hart, P. J. *Journal of Biological Chemistry* **2008**, *283*, 16169.

(2) Kraatz, H.-B., Metzler-Nolte, Nils *Concepts and Models in Bioinorganic Chemistry*; Wiley-VCH: Weinheim, **2006**.

(3) Ivano Bertini, H. B. G., Edward I. Stiefel and Joan S. Valentine *Biological Inorganic Chemistry-Structure and Reactivity*; University Science Books, **2007**.

(4) Berg, S. J. L. J. M. *Principles of Bioinorganic Chemistry*; University Science Books, **1994**.

(5) Pettifor, D. G. *Bonding and Structure of Molecules and Solids*; Oxford University Press, **1995**.

(6) Crabtree, R. H. *The Organometallic Chemistry of the Transition Metals, Fourth Edition*; New Jersey: Wiley-Interscience, **2005**.

(7) Jamieson, E. R.; Lippard, S. J. *Chemical Reviews* **1999**, *99*, 2467.

(8) Jones, J. H. *Platium Metals Review* **2000**, *44*, 94.

(9) Kendrew JC, B. G., Dintzis HM, Parrish RG, Wyckoff H, Phillips DC *Nature* **1958**, *181*, 662.

(10) Dawson, J. *Science* **1988**, *240*, 433.

(11) Holm, R. H.; Kennepohl, P.; Solomon, E. I. *Chemical Reviews* **1996**, *96*, 2239.

(12) Ortiz de Montellano, P. R. *Accounts of Chemical Research* **1987**, *20*, 289.

(13) Borovik, A. S. *Accounts of Chemical Research* **2005**, *38*, 54.

(14) Colquhoun, H. M.; Stoddart, J. F.; Williams, D. J. *Angewandte Chemie International Edition* **1986**, *25*, 487.

(15) Santos, M. A.; Marques, S.; Vullo, D.; Innocenti, A.; Scozzafava, A.; Supuran, C. T. *Bioorganic & Medicinal Chemistry Letters* **2007**, *17*, 1538.

(16) Springer, B. A.; Sligar, S. G.; Olson, J. S.; Phillips, G. N., Jr. *Chemical Reviews* **1994**, *94*, 699.

(17) Zambelli, B.; Musiani, F.; Benini, S.; Ciurli, S. *Accounts of Chemical Research* **2011**, *44*, 520.

(18) Li, H.; Poulos, T. L. *Acta Crystallographica Section D* **1995**, *51*, 21.

(19) Christianson, D. W.; Lipscomb, W. N. *Accounts of Chemical Research* **1989**, *22*, 62.

(20) Stoddard, B. L.; Howell, P. L.; Ringe, D.; Petsko, G. A. *Biochemistry* **1990**, *29*, 8885.

(21) Vance, C. K.; Miller, A. F. *Journal of the American Chemical Society* **1998**, *120*, 461.

(22) Miller, A.-F. *Accounts of Chemical Research* **2008**, *41*, 501.

(23) Collman, J. P. *Accounts of Chemical Research* **1977**, *10*, 265.

(24) Collman, J. P.; Zhang, X.; Wong, K.; Brauman, J. I. *Journal of the American Chemical Society* **1994**, *116*, 6245.

(25) Wuenschell, G. E.; Tetreau, C.; Lavalette, D.; Reed, C. A. *Journal of the American Chemical Society* **1992**, *114*, 3346.

(26) Chang, C. K.; Liang, Y.; Aviles, G.; Peng, S.-M. *Journal of the American Chemical Society* **1995**, *117*, 4191.

(27) Yeh, C.-Y.; Chang, C. J.; Nocera, D. G. *Journal of the American Chemical Society* **2001**, *123*, 1513.

(28) Kitajima, N.; Komatsuzaki, H.; Hikichi, S.; Osawa, M.; Moro-oka, Y. *Journal of the American Chemical Society* **1994**, *116*, 11596.

(29) Harata, M.; Jitsukawa, K.; Masuda, H.; Einaga, H. *Chemistry Letters* **1995**, *24*, 61.

(30) Ogo, S.; Wada, S.; Watanabe, Y.; Iwase, M.; Wada, A.; Harata, M.; Jitsukawa, K.; Masuda, H.; Einaga, H. *Angewandte Chemie-International Edition* **1998**, *37*, 2102.

(31) Ogo, S.; Yamahara, R.; Roach, M.; Suenobu, T.; Aki, M.; Ogura, T.; Kitagawa, T.; Masuda, H.; Fukuzumi, S.; Watanabe, Y. *Inorganic Chemistry* **2002**, *41*, 5513.

(32) Wada, A.; Harata, M.; Hasegawa, K.; Jitsukawa, K.; Masuda, H.; Mukai, M.; Kitagawa, T.; Einaga, H. *Angewandte Chemie-International Edition* **1998**, *37*, 798.

(33) Wada, A.; Ogo, S.; Nagatomo, S.; Kitagawa, T.; Watanabe, Y.; Jitsukawa, K.; Masuda, H. *Inorganic Chemistry* **2002**, *41*, 616.

(34) Yamaguchi, S.; Wada, A.; Funahashi, Y.; Nagatomo, S.; Kitagawa, T.; Jitsukawa, K.; Masuda, H. *European Journal of Inorganic Chemistry* **2003**, *2003*, 4378.

(35) Garner, D. K.; Fitch, S. B.; McAlexander, L. H.; Bezold, L. M.; Arif, A. M.; Berreau, L. M. *Journal of the American Chemical Society* **2002**, *124*, 9970.

(36) Mareque Rivas, J. C.; Torres Martin de Rosales, R.; Parsons, S. *Dalton Transactions* **2003**, 2156.

(37) Mareque-Rivas, J. C.; Prabaharan, R.; Parsons, S. *Dalton Transactions* **2004**, 1648.

(38) Mareque-Rivas, J. C.; Prabaharan, R.; Martin de Rosales, R. T. *Chemical Communications* **2004**, 76.

(39) Metteau, L.; Parsons, S.; Mareque-Rivas, J. C. *Inorganic Chemistry* **2006**, *45*, 6601.

(40) MacBeth, C. E.; Golombek, A. P.; Young, V. G.; Yang, C.; Kuczera, K.; Hendrich, M. P.; Borovik, A. S. *Science* **2000**, *289*, 938.

(41) Larsen, P. L.; Gupta, R.; Powell, D. R.; Borovik, A. S. *Journal of the American Chemical Society* **2004**, *126*, 6522.

(42) Shook, R. L.; Gunderson, W. A.; Greaves, J.; Ziller, J. W.; Hendrich, M. P.; Borovik, A. S. *Journal of the American Chemical Society* **2008**, *130*, 8888.

(43) Shook, R. L.; Borovik, A. S. *Inorganic Chemistry* **2010**, *49*, 3646.

(44) Lucas, R. L.; Zart, M. K.; Murkerjee, J.; Sorrell, T. N.; Powell, D. R.; Borovik, A. S. *Journal of the American Chemical Society* **2006**, *128*, 15476.

(45) Richard Cammack, M. F., Robert Robson *Hydrogen as a Fuel: Learning from Nature*; Taylor & Francis, **2001**.

(46) Pandelia, M.-E.; Ogata, H.; Currell, L.; Flores, M.; Lubitz, W. *Journal of Biological Inorganic Chemistry* **2009**, *14*, 1227.

(47) Berggren, G.; Adamska, A.; Lambertz, C.; Simmons, T. R.; Esselborn, J.; Atta, M.; Gambarelli, S.; Mouesca, J. M.; Reijerse, E.; Lubitz, W.; Happe, T.; Artero, V.; Fontecave, M. *Nature* **2013**, *499*, 66.

(48) Umena, Y.; Kawakami, K.; Shen, J.-R.; Kamiya, N. *Nature* **2011**, *473*, 55.

(49) Justice, A. K.; De Gioia, L.; Nilges, M. J.; Rauchfuss, T. B.; Wilson, S. R.; Zampella, G. *Inorganic Chemistry* **2008**, *47*, 7405.

(50) Zhao, X.; Georgakaki, I. P.; Miller, M. L.; Yarbrough, J. C.; Darensbourg, M. Y. *Journal of the American Chemical Society* **2001**, *123*, 9710.

(51) Zhao, X.; Chiang, C.-Y.; Miller, M. L.; Rampersad, M. V.; Darensbourg, M. Y. *Journal of the American Chemical Society* **2003**, *125*, 518.

(52) Cheah, M. H.; Tard, C.; Borg, S. J.; Liu, X.; Ibrahim, S. K.; Pickett, C. J.; Best, S. P. *Journal of the American Chemical Society* **2007**, *129*, 11085.

(53) Tard, C.; Pickett, C. J. *Chemical Reviews* **2009**, *109*, 2245.

(54) Frederix, P. W. J. M.; Kania, R.; Wright, J. A.; Lamprou, D. A.; Ulijn, R. V.; Pickett, C. J.; Hunt, N. T. *Dalton Transactions* **2012**, *41*, 13112.

(55) Jablonskyte, A.; Wright, J. A.; Fairhurst, S. A.; Webster, L. R.; Pickett, C. J. *Angewandte Chemie International Edition* **2014**, *53*, 10143.

(56) Ringenberg, M. R.; Kokatam, S. L.; Heiden, Z. M.; Rauchfuss, T. B. *Journal of the American Chemical Society* **2008**, *130*, 788.

(57) Barton, B. E.; Zampella, G.; Justice, A. K.; De Gioia, L.; Rauchfuss, T. B.; Wilson, S. R. *Dalton Transactions* **2010**, *39*, 3011.

(58) Camara, J. M.; Rauchfuss, T. B. *Nature Chemistry* **2012**, *4*, 26.

(59) Rauchfuss, T. B. *Accounts of Chemical Research* **2015**, *48*, 2107.

(60) Kanady, J. S.; Tsui, E. Y.; Day, M. W.; Agapie, T. *Science* **2011**, *333*, 733.

(61) Tsui, E. Y.; Agapie, T. *Proceedings of the National Academy of Sciences of the United States of America* **2013**, *110*, 10084.

(62) Tsui, E. Y.; Day, M. W.; Agapie, T. *Angewandte Chemie International Edition* **2011**, *50*, 1668.

(63) Tsui, E. Y.; Kanady, J. S.; Agapie, T. *Inorganic Chemistry* **2013**, *52*, 13833.

(64) Tsui, E. Y.; Kanady, J. S.; Day, M. W.; Agapie, T. *Chemical Communications* **2011**, *47*, 4189.

(65) Park, Y. J.; Cook, S. A.; Sickerman, N. S.; Sano, Y.; Ziller, J. W.; Borovik, A. S. *Chemical Science* **2013**, *4*, 717.

(66) Park, Y. J.; Ziller, J. W.; Borovik, A. S. *Journal of the American Chemical Society* **2011**, *133*, 9258.

(67) Rajput, A.; Mukherjee, R. *Coordination Chemistry Reviews* **2013**, *257*, 350.

(68) Kwong, H. L.; Yeung, H. L.; Yeung, C. T.; Lee, W. S.; Lee, C. S.; Wong, W. L. *Coordination Chemistry Reviews* **2007**, *251*, 2188.

(69) Belda, O.; Moberg, C. *Coordination Chemistry Reviews* **2005**, *249*, 727.

(70) Patra, A. K.; Mukherjee, R. *Inorganic Chemistry* **1999**, *38*, 1388.

(71) Marlin, D. S.; Olmstead, M. M.; Mascharak, P. K. *Inorganic Chemistry* **2001**, *40*, 7003.

(72) Marlin, D. S.; Olmstead, M. M.; Mascharak, P. K. *Angewandte Chemie-International Edition* **2001**, *40*, 4752.

(73) Noveron, J. C.; Olmstead, M. M.; Mascharak, P. K. *Journal of the American Chemical Society* **2001**, *123*, 3247.

(74) Marlin, D. S.; Mascharak, P. K. *Chemical Society Reviews* **2000**, *29*, 69.

(75) Chavez, F. A.; Olmstead, M. M.; Mascharak, P. K. *Inorganica Chimica Acta* **1998**, *269*, 269.

(76) Donoghue, P. J.; Gupta, A. K.; Boyce, D. W.; Cramer, C. J.; Tolman, W. B. *Journal of the American Chemical Society* **2010**, *132*, 15869.

(77) Donoghue, P. J.; Tehranchi, J.; Cramer, C. J.; Sarangi, R.; Solomon, E. I.; Tolman, W. B. *Journal of the American Chemical Society* **2011**, *133*, 17602.

(78) Huang, D.; Makhlynets, O. V.; Tan, L. L.; Lee, S. C.; Rybak-Akimova, E. V.; Holm, R. H. *Inorganic Chemistry* **2011**, *50*, 10070.

(79) Huang, D. G.; Holm, R. H. *Journal of the American Chemical Society* **2010**, *132*, 4693.

(80) Jain, S. L.; Bhattacharyya, P.; Milton, H. L.; Slawin, A. M. Z.; Crayston, J. A.; Woollins, J. D. *Dalton Transactions* **2004**, 862.

(81) Trost, B. M.; Hachiya, I. *Journal of the American Chemical Society* **1998**, *120*, 1104.

(82) Belda, O.; Moberg, C. *Accounts of Chemical Research* **2004**, *37*, 159.

(83) Adolfsson, H.; Moberg, C. *Tetrahedron-Asymmetry* **1995**, *6*, 2023.

(84) Che, C. M.; Cheng, W. K. *Journal of the Chemical Society-Chemical Communications* **1986**, 1443.

(85) Yang, L.; Wu, Z. Q.; Liang, L.; Zhou, X. G. *Journal of Organometallic Chemistry* **2009**, *694*, 2421.

(86) Yang, L.; Wei, R. N.; Li, R.; Zhou, X. G.; Zuo, J. L. *Journal of Molecular Catalysis a-Chemical* **2007**, *266*, 284.

(87) Lee, S. H.; Han, J. H.; Kwak, H.; Lee, S. J.; Lee, E. Y.; Kim, H. J.; Lee, J. H.; Bae, C.; Lee, S. N.; Kim, Y.; Kimal, C. *Chemistry-a European Journal* **2007**, *13*, 9393.

(88) Vance, C. K.; Miller, A.-F. *Biochemistry* **2001**, *40*, 13079.

(89) Hadt, R. G.; Sun, N.; Marshall, N. M.; Hodgson, K. O.; Hedman, B.; Lu, Y.; Solomon, E. I. *Journal of the American Chemical Society* **2012**, *134*, 16701.

(90) Marshall, N. M.; Garner, D. K.; Wilson, T. D.; Gao, Y. G.; Robinson, H.; Nilges, M. J.; Lu, Y. *Nature* **2009**, *462*, 113.

(91) Schlichting, I.; Berendzen, J.; Chu, K.; Stock, A. M.; Maves, S. A.; Benson, D. E.; Sweet, R. M.; Ringe, D.; Petsko, G. A.; Sligar, S. G. *Science* **2000**, *287*, 1615.

(92) Nagano, S.; Poulos, T. L. *Journal of Biological Chemistry* **2005**, *280*, 31659.

(93) Christianson, D. W.; Lipscomb, W. N. *Accounts of Chemical Research* **1989**, *22*, 62.

(94) Hernick, M.; Fierke, C. A. *Archives of Biochemistry and Biophysics* **2005**, *433*, 71.

(95) Lipscomb, J. D. *Current Opinion in Structural Biology* **2008**, *18*, 644.

(96) Borovik, A. S. *Accounts of Chemical Research* **2005**, *38*, 54.

(97) Redmore, S. M.; Rickard, C. E. F.; Webb, S. J.; Wright, L. J. *Inorganic Chemistry* **1997**, *36*, 4743.

(98) Gudasi, K.; Vadavi, R.; Shenoy, R.; Patil, M.; Patil, S. A.; Nethaji, M. *Inorganica Chimica Acta* **2005**, *358*, 3799.

(99) Fan, R. Q.; Wang, P.; Yang, Y. L.; Zhang, Y. J.; Yin, Y. B.; Hasi, W. *Polyhedron* **2010**, *29*, 2862.

(100) Connelly, N. G.; Geiger, W. E. *Chemical Reviews* **1996**, *96*, 877.

(101) Yu, Q.; Baroni, T. E.; Liable-Sands, L.; Yap, G. P. A.; Rheingold, A. L.; Borovik, A. S. *Chemical Communications* **1999**, 1467.

(102) Sheldrick, G. M. *Acta Crystallographica Section A* **2008**, *64*, 112.

(103) Dolomanov, O. V.; Bourhis, L. J.; Gildea, R. J.; Howard, J. A. K.; Puschmann, H. *Journal of Applied Crystallography* **2009**, *42*, 339.

(104) Neese, F.; version 2.7 ed.; University of Bonn: Bonn, Germany, 2008.

(105) Becke, A. D. *Journal of Chemical Physics* **1986**, *84*, 4524.

(106) Perdew, J. P. *Physical Review B* **1986**, *33*, 8822.

(107) Schafer, A.; Huber, C.; Ahlrichs, R. *Journal of Chemical Physics* **1994**, *100*, 5829.

(108) Schafer, A.; Horn, H.; Ahlrichs, R. *Journal of Chemical Physics* **1992**, *97*, 2571.

(109) Kawamoto, T.; Prakash, O.; Ostrander, R.; Rheingold, A. L.; Borovik, A. S. *Inorganic Chemistry* **1995**, *34*, 4294.

(110) Kawamoto, T.; Hammes, B. S.; Ostrander, R.; Rheingold, A. L.; Borovik, A. S. *Inorganic Chemistry* **1998**, *37*, 3424.

(111) Shirin, Z.; Thompson, J.; Liable-Sands, L.; Yap, G. P. A.; Rheingold, A. L.; Borovik, A. S. *Journal of the Chemical Society-Dalton Transactions* **2002**, 1714.

(112) Shaban, S. Y.; Heinemann, F. W.; van Eldik, R. *European Journal of Inorganic Chemistry* **2009**, 3111.

(113) Balamurugan, R.; Palaniandavar, M.; Halcrow, M. A. *Polyhedron* **2006**, *25*, 1077.

(114) Geiser, U.; Gaura, R. M.; Willett, R. D.; West, D. X. *Inorganic Chemistry* **1986**, *25*, 4203.

(115) Battaglia, L. P.; Corradi, A. B.; Geiser, U.; Willett, R. D.; Motori, A.; Sandrolini, F.; Antolini, L.; Manfredini, T.; Menabue, L.; Pellacani, G. C. *Journal of the Chemical Society-Dalton Transactions* **1988**, 265.

(116) Fronczek, F. R.; Mamo, A.; Pappalardo, S. *Inorganic Chemistry* **1989**, *28*, 1419.

(117) An analysis of five-coordinate CuCl2N3 structures in the Cambridge Structural Database revealed a median Cu-Cl distance of 2.31 A

(118) Addison, A. W.; Rao, T. N.; Reedijk, J.; Vanrijn, J.; Verschoor, G. C. *Journal of the Chemical Society-Dalton Transactions* **1984**, 1349.

(119) Rowland, J. M.; Olmstead, M. M.; Mascharak, P. K. *Inorganic Chemistry* **2000**, *39*, 5326.

(120) Sinnecker, S.; Neese, F.; Noodleman, L.; Lubitz, W. *Journal of the American Chemical Society* **2004**, *126*, 2613.

(121) Lever, A. B. P. *Inorganic Electronic Spectroscopy*; Elsevier: Amsterdam, **1968**.

(122) Tomlinson, A. A. G.; Hathaway, B. J. *Journal of the Chemical Society A: Inorganic, Physical, Theoretical* **1968**, 2578.

(123) Tomlinson, A. A. G.; Hathaway, B. J. *Journal of the Chemical Society A: Inorganic, Physical, Theoretical* **1968**, 1905.

(124) Procter, I. M.; Hathaway, B. J.; Nicholls, P. *Journal of the Chemical Society A: Inorganic, Physical, Theoretical* **1968**, 1678.

(125) Tamboura, F. B.; Gaye, M.; Sall, A. S.; Barry, A. H.; Jouini, T. *Inorganic Chemistry Communications* **2002**, *5*, 235.

(126) Flanagan, S.; Dong, J.; Haller, K.; Wang, S. K.; Scheidt, W. R.; Scott, R. A.; Webb, T. R.; Stanbury, D. M.; Wilson, L. J. *Journal of the American Chemical Society* **1997**, *119*, 8857.

(127) Ray, M.; Ghosh, D.; Shirin, Z.; Mukherjee, R. *Inorganic Chemistry* **1997**, *36*, 3568.

(128) Marlin, D. S.; Olmstead, M. M.; Mascharak, P. K. *Inorganic Chemistry* **1999**, *38*, 3258.

(129) Ghosh, S.; Roehm, B.; Begum, R. A.; Kut, J.; Hossain, M. A.; Day, V. W.; Bowman-James, K. *Inorganic Chemistry* **2007**, *46*, 9519.

(130) Singh, A. P.; Gupta, R. *European Journal of Inorganic Chemistry* **2010**, 4546.

(131) Patil, V.; Tilekar, K.; Mehendale-Munj, S.; Mohan, R.; Ramaa, C. S. *European Journal of Medicinal Chemistry* **2010**, *45*, 4539.

(132) Chomitz, W. A.; Minasian, S. G.; Sutton, A. D.; Arnold, J. *Inorganic Chemistry* **2007**, *46*, 7199.

(133) Lee, H. G.; Lee, J. H.; Jang, S. P.; Park, H. M.; Kim, S.-J.; Kim, Y.; Kim, C.; Harrison, R. G. *Tetrahedron* **2011**, *67*, 8073.

(134) Maresca, K. P.; Hillier, S. M.; Femia, F. J.; Zimmerman, C. N.; Levadala, M. K.; Banerjee, S. R.; Hicks, J.; Sundararajan, C.; Valliant, J.; Zubieta, J.; Eckelman, W. C.; Joyal, J. L.; Babich, J. W. *Bioconjugate Chemistry* **2009**, *20*, 1625.

(135) Lu, H.-J.; Fan, Y.-T.; Yin, M.-C.; Wu, Y.-J. *Synthesis and Reactivity in Inorganic and Metal-Organic Chemistry* **2002**, *32*, 1537.

(136) Boer, J. L.; Mulrooney, S. B.; Hausinger, R. P. *Archives of Biochemistry and Biophysics* **2014**, *544*, 142.

(137) Ragsdale, S. W.; Pierce, E. *Biochimica et Biophysica Acta - Proteins and Proteomics* **2008**, *1784*, 1873.

(138) Volbeda, A.; Charon, M. H.; Piras, C.; Hatchikian, E. C.; Frey, M.; Fontecilla-Camps, J. C. *Nature* **1995**, *373*, 580.

(139) Volbeda, A.; Fontecilla-Camps, J. C. *Coordination Chemistry Reviews* **2005**, *249*, 1609.

(140) Bruschi, M.; Zampella, G.; Fantucci, P.; De Gioia, L. *Coordination Chemistry Reviews* **2005**, *249*, 1620.

(141) Ogata, H.; Lubitz, W.; Higuchi, Y. *Dalton Transactions* **2009**, 7577.

(142) Drennan, C. L.; Doukov, T. I.; Ragsdale, S. W. *Journal of Biological Inorganic Chemistry* **2004**, *9*, 511.

(143) Kung, Y.; Drennan, C. L. *Current Opinion in Chemical Biology* **2011**, *15*, 276.

(144) Volbeda, A.; Fontecilla-Camps, J. C. *Dalton Transactions* **2005**, 3443.

(145) Amara, P.; Mouesca, J.-M.; Volbeda, A.; Fontecilla-Camps, J. C. *Inorganic Chemistry* **2011**, *50*, 1868.

(146) Jeoung, J.-H.; Dobbek, H. *Science* **2007**, *318*, 1461.

(147) Jeoung, J.-H.; Dobbek, H. *Journal of Biological Inorganic Chemistry* **2012**, *17*, 167.

(148) Huang, D.; Holm, R. H. *Journal of the American Chemical Society* **2010**, *132*, 4693.

(149) Zhang, X.; Huang, D.; Chen, Y.-S.; Holm, R. H. *Inorganic Chemistry* **2012**, *51*, 11017.

(150) Uyeda, C.; Peters, J. C. *Chemical Science* **2013**, *4*, 157.

(151) Hazra, S.; Bhattacharya, S.; Singh, M. K.; Carrella, L.; Rentschler, E.; Weyhermueller, T.; Rajaraman, G.; Mohanta, S. *Inorganic Chemistry* **2013**, *52*, 12881.

(152) Kon, H.; Nagata, T. *Dalton Transactions* **2013**, *42*, 5697.

(153) Jarenmark, M.; Haukka, M.; Demeshko, S.; Tuczek, F.; Zuppiroli, L.; Meyer, F.; Nordlander, E. *Inorganic Chemistry* **2011**, *50*, 3866.

(154) Yao, S.; Herwig, C.; Xiong, Y.; Company, A.; Bill, E.; Limberg, C.; Driess, M. *Angewandte Chemie International Edition* **2010**, *49*, 7054.

(155) Roth, A.; Buchholz, A.; Rudolph, M.; Schuetze, E.; Kothe, E.; Plass, W. *Chemistry - A European Journal* **2008**, *14*, 1571.

(156) Danjobara, K.; Mitsuka, Y.; Miyasato, Y.; Ohba, M.; Okawa, H. *Bulletin of the Chemical Society of Japan* **2003**, *76*, 1769.

(157) Dutta, S. K.; Werner, R.; Floerke, U.; Mohanta, S.; Nanda, K. K.; Haase, W.; Nag, K. *Inorganic Chemistry* **1996**, *35*, 2292.

(158) Holman, T. R.; Juarez-Garcia, C.; Hendrich, M. P.; Que, L., Jr.; Munck, E. *Journal of the American Chemical Society* **1990**, *112*, 7611.

(159) Jarenmark, M.; Carlsson, H.; Nordlander, E. *Comptes Rendus Chimie* **2007**, *10*, 433.

(160) Belle, C.; Pierre, J.-l. *European Journal of Inorganic Chemistry* **2003**, 4137.

(161) Daumann, L. J.; Schenk, G.; Ollis, D. L.; Gahan, L. R. *Dalton Transactions* **2014**, *43*, 910.

(162) Connelly, N. G.; Geiger, W. E. *Chemical Reviews* **1996**, *96*, 877.

(163) Wang, Q.; Wilson, C.; Blake, A. J.; Collinson, S. R.; Tasker, P. A.; Schroeder, M. *Tetrahedron Letters* **2006**, *47*, 8983.

(164) Belostotskaya, I. S.; Komissarova, N. L.; Prokof'eva, T. I.; Kurkovskaya, L. N.; Vol'eva, V. B. *Russian Journal of Organic Chemistry* **2005**, *41*, 703.

(165) Koval, I. A.; Pursche, D.; Stassen, A. F.; Gamez, P.; Krebs, B.; Reedijk, J. *European Journal of Inorganic Chemistry* **2003**, 1669.

(166) Sheldrick, G. M. *Acta Crystallographica Section A Foundations of Crystallography* **2008**, *64*, 112.

(167) Dolomanov, O. V.; Bourhis, L. J.; Gildea, R. J.; Howard, J. A. K.; Puschmann, H. *Journal of Applied Crystallography* **2009**, *42*, 339.

(168) Addison, A. W.; Rao, T. N.; Reedijk, J.; Van Rijn, J.; Verschoor, G. C. *Dalton Transactions* **1984**, 1349.

(169) Evans, D. F. *Journal of the Chemical Society (Resumed)* **1959**, 2003.

(170) Hematian, S.; Garcia-Bosch, I.; Karlin, K. D. *Accounts of Chemical Research* **2015**, *48*, 2462.

(171) The background feature was modeled as a simple Gaussian curve in order to avoid introducing spurious features into the experimental spectrum.

(172) Ciampolini, M.; Nardi, N.; Speroni, G. P. *Coordination Chemistry Reviews* **1966**, *1*, 222.

(173) Allard, M. M.; Sonk, J. A.; Heeg, M. J.; McGarvey, B. R.; Schlegel, H. B.; Verani, C. N. *Angewandte Chemie International Edition* **2012**, *51*, 3178.

(174) Lanznaster, M.; Hratchian, H. P.; Heeg, M. J.; Hryhorczuk, L. M.; McGarvey, B. R.; Schlegel, H. B.; Verani, C. N. *Inorganic Chemistry* **2006**, *45*, 955.

(175) Adam, B.; Bill, E.; Bothe, E.; Goerdt, B.; Haselhorst, G.; Hildenbrand, K.; Sokolowski, A.; Steenken, S.; Weyhermueller, T.; Wieghardt, K. *Chemistry - A European Journal* **1997**, *3*, 308.

(176) Appel, A. M.; Bercaw, J. E.; Bocarsly, A. B.; Dobbek, H.; DuBois, D. L.; Dupuis, M.; Ferry, J. G.; Fujita, E.; Hille, R.; Kenis, P. J. A.; Kerfeld, C. A.; Morris, R. H.; Peden, C. H. F.; Portis, A. R.; Ragsdale, S. W.; Rauchfuss, T. B.; Reek, J. N. H.; Seefeldt, L. C.; Thauer, R. K.; Waldrop, G. L. *Chemical Reviews* **2013**, *113*, 6621.

(177) *The Chemistry of Pincer Compounds*; Morales-Morales, D.; Jensen, C. M., Eds.; Elsevier: Amsterdam, 2007.

(178) *The Pincer Ligand: Its Chemistry and Applications (Catalytic Science)*; Chase, P. A.; Koten, G. v., Eds.; Imperial College Press: London, 2010.

(179) O'Reilly, M. E.; Veige, A. S. *Chemical Society Reviews* **2014**, *43*, 6325.

(180) van Koten, G. *Journal of Organometallic Chemistry* **2013**, *730*, 156.

(181) Szabo, K. J. *Topics in Organometallic Chemistry* **2013**, *40*, 203.

(182) Albrecht, M.; Lindner, M. M. *Dalton Transactions* **2011**, *40*, 8733.

(183) van der Boom, M. E.; Milstein, D. *Chemical Reviews* **2003**, *103*, 1759.

(184) Wieczorek, B.; Dijkstra, H. P.; Egmond, M. R.; Gebbink, R. J. M. K.; van Koten, G. *Journal of Organometallic Chemistry* **2009**, *694*, 812.

(185) Albrecht, M.; van Koten, G. *Angewandte Chemie International Edition* **2001**, *40*, 3750.

(186) Hawk, J. L.; Craig, S. L. *Topics in Organometallic Chemistry* **2013**, *40*, 319.

(187) South, C. R.; Weck, M. *Langmuir* **2008**, *24*, 7506.

(188) Fan, L.; Foxman, B. M.; Ozerov, O. V. *Organometallics* **2004**, *23*, 326.

(189) Liang, L.-C. *Coordination Chemistry Reviews* **2006**, *250*, 1152.

(190) Mindiola, D. J. *Accounts of Chemical Research* **2006**, *39*, 813.

(191) Kieltsch, I.; Dubinina, G. G.; Hamacher, C.; Kaiser, A.; Torres-Nieto, J.; Hutchison, J. M.; Klein, A.; Budnikova, Y.; Vicic, D. A. *Organometallics* **2010**, *29*, 1451.

(192) Inagaki, T.; Phong, L. T.; Furuta, A.; Ito, J.-i.; Nishiyama, H. *Chemistry - A European Journal* **2010**, *16*, 3090.

(193) Peters, J. C.; Harkins, S. B.; Brown, S. D.; Day, M. W. *Inorganic Chemistry* **2001**, *40*, 5083.

(194) Breitenfeld, J.; Vechorkin, O.; Corminboeuf, C.; Scopelliti, R.; Hu, X. *Organometallics* **2010**, *29*, 3686.

(195) Wanniarachchi, S.; Liddle, B. J.; Toussaint, J.; Lindeman, S. V.; Bennett, B.; Gardinier, J. R. *Dalton Transactions* **2010**, *39*, 3167.

(196) Hollas, A. M.; Gu, W.; Bhuvanesh, N.; Ozerov, O. V. *Inorganic Chemistry* **2011**, *50*, 3673.

(197) Mudadu, M. S.; Singh, A. N.; Thummel, R. P. *Journal of Organic Chemistry* **2008**, *73*, 6513.

(198) Gaunt, J. A.; Gibson, V. C.; Haynes, A.; Spitzmesser, S. K.; White, A. J. P.; Williams, D. J. *Organometallics* **2004**, *23*, 1015.

(199) Barbe, J.-M.; Habermeyer, B.; Khoury, T.; Gros, C. P.; Richard, P.; Chen, P.; Kadish, K. M. *Inorganic Chemistry* **2010**, *49*, 8929.

(200) Fafard, C. M.; Adhikari, D.; Foxman, B. M.; Mindiola, D. J.; Ozerov, O. V. *Journal of the American Chemical Society* **2007**, *129*, 10318.

(201) Golisz, S. R.; Labinger, J. A.; Bercaw, J. E. *Organometallics* **2010**, *29*, 5026.

(202) Zarkesh, R. A.; Heyduk, A. F. *Organometallics* **2011**, *30*, 4890.

(203) Broere, D. L. J.; Demeshko, S.; de Bruin, B.; Pidko, E. A.; Reek, J. N. H.; Siegler, M. A.; Lutz, M.; van der Vlugt, J. I. *Chemistry - A European Journal* **2015**, *21*, 5879.

(204) Chan, C.-W.; Mingos, M. P.; White, A. J. P.; Williams, D. J. *Chemical Communications* **1996**, 81.

(205) Steenwinkel, P.; Kooijman, H.; Smeets, W. J. J.; Spek, A. L.; Grove, D. M.; Van Koten, G. *Organometallics* **1998**, *17*, 5411.

(206) Zhao, C.-Q.; Jennings, M. C.; Puddephatt, R. J. *Dalton Transactions* **2008**, 1243.

(207) Kocher, S.; van Klink, G. P. M.; van Koten, G.; Lang, H. *Journal of Organometallic Chemistry* **2003**, *684*, 230.

(208) Tsubomura, T.; Tanihata, T.; Yamakawa, T.; Ohmi, R.; Tamane, T.; Higuchi, A.; Katoh, A.; Sakai, K. *Organometallics* **2001**, *20*, 3833.

(209) Herbert, D. E.; Ozerov, O. V. *Organometallics* **2011**, *30*, 6641.

(210) Samanta, S.; Demesko, S.; Dechert, S.; Meyer, F. *Angewandte Chemie International Edition* **2015**, *54*, 583.

(211) van der Vlugt, J. I.; Demeshko, S.; Dechert, S.; Meyer, F. *Inorganic Chemistry* **2008**, *47*, 1576.

(212) Harkins, S. B.; Peters, J. C. *Journal of the American Chemical Society* **2005**, *127*, 2030.

(213) Adhikari, D.; Mossin, S.; Basuli, F.; Dible, B. R.; Chipara, M.; Fan, H.; Huffman, J. C.; Meyer, K.; Mindiola, D. J. *Inorganic Chemistry* **2008**, *47*, 10479.

(214) Fout, A. R.; Basuli, F.; Fan, H.; Tomaszewski, J.; Huffman, J. C.; Baik, M.-H.; Mindiola, D. J. *Angewandte Chemie International Edition* **2006**, *45*, 3291.

(215) Harkins, S. B.; Mankad, N. P.; Miller, A. J. M.; Szilagyi, R. K.; Peters, J. C. *Journal of the American Chemical Society* **2008**, *130*, 3478.

(216) Mankad, N. P.; Harkins, S. B.; Antholine, W. E.; Peters, J. C. *Inorganic Chemistry* **2009**, *48*, 7026.

(217) Adhikari, D.; Mossin, S.; Basuli, F.; Huffman, J. C.; Szilagyi, R. K.; Meyer, K.; Mindiola, D. J. *Journal of the American Chemical Society* **2008**, *130*, 3676.

(218) Radosevich, A. T.; Melnick, J. G.; Stoian, S. A.; Bacciu, D.; Chen, C.-H.; Foxman, B. M.; Ozerov, O. V.; Nocera, D. G. *Inorganic Chemistry* **2009**, *48*, 9214.

(219) Suarez, A. I. O.; Lyaskovskyy, V.; Reek, J. N. H.; van der Vlugt, J. I.; de Bruin, B. *Angewandte Chemie International Edition* **2013**, *52*, 12510.

(220) Lyaskovskyy, V.; de Bruin, B. *ACS Catalysis* **2012**, *2*, 270.

(221) Ma, L.; Woloszynek, R. A.; Chen, W.; Ren, T.; Protasiewicz, J. D. *Organometallics* **2006**, *25*, 3301.

(222) Wong, J. L.; Sanchez, R. H.; Logan, J. G.; Zarkesh, R. A.; Ziller, J. W.; Heyduk, A. F. *Chemical Science* **2013**, *4*, 1906.

(223) Sharma, S. K.; May, P. S.; Jones, M. B.; Lense, S.; Hardcastle, K. I.; MacBeth, C. E. *Chemical Communications* **2011**, *47*, 1827.

(224) Min, K. S.; Weyhermueller, T.; Wieghardt, K. *Dalton Transactions* **2004**, 178.

(225) Olmstead, M. M.; Power, P. P.; Shoner, S. C. *Inorganic Chemistry* **1991**, *30*, 2547.

(226) Vigato, P. A.; Peruzzo, V.; Tamburini, S. *Coordination Chemistry Reviews* **2012**, *256*, 953.

(227) Clarke, R. M.; Storr, T. *Dalton Transactions* **2014**, *43*, 9380.

(228) Radlauer, M. R.; Buckley, A. K.; Henling, L. M.; Agapie, T. *Journal of the American Chemical Society* **2013**, *135*, 3784.

(229) Radlauer, M. R.; Day, M. W.; Agapie, T. *Journal of the American Chemical Society* **2012**, *134*, 1478.

(230) Stoll, S.; Schweiger, A. *Journal of Magnetic Resonance* **2006**, *178*, 42.

(231) Munha, R. F.; Zarkesh, R. A.; Heyduk, A. F. *Inorganic Chemistry* **2013**, *52*, 11244.

(232) Murdock, K. C.; Lin, Y.-I.; Thomas, J. P.; Lang, S. A., Jr. *Journal of Medicinal Chemistry* **1978**, *21*, 403.

(233) Becke, A. D. *Journal of Chemical Physics* **1993**, *98*, 5648.

(234) Lee, C. T.; Yang, W. T.; Parr, R. G. *Physical Review B* **1988**, *37*, 785.

(235) Weigend, F.; Ahlrichs, R. *Physical Chemistry Chemical Physics* **2005**, *7*, 3297.

(236) Klamt, A.; Schueuermann, G. *Journal of the Chemical Society, Perkin Transactions 2* **1993**, 799.

(237) Noodleman, L. *Journal of Chemical Physics* **1981**, *74*, 5737.

(238) Laaksonen, L. *Journal of Molecular Graphics* **1992**, *10*, 33.

(239) Marshak, M. P.; Chambers, M. B.; Nocera, D. G. *Inorganic Chemistry* **2012**, *51*, 11190.

(240) Kolchinski, A. G.; Korybut-Daszkiewicz, B.; Rybak-Akimova, E. V.; Busch, D. H.; Alcock, N. W.; Clase, H. J. *Journal of the American Chemical Society* **1997**, *119*, 4160.

(241) Szalda, D. J.; Schwarz, C. L.; Endicott, J. F.; Fujita, E.; Creutz, C. *Inorganic Chemistry* **1989**, *28*, 3214.

(242) Eerdun, C.; Hisanaga, S.; Setsune, J.-i. *Chemistry - A European Journal* **2015**, *21*, 239.

(243) Magdesieva, T. V.; Levitskiy, O. A.; Grishin, Y. K.; Ambartsumyan, A. A.; Paseshnichenko, K. A.; Kolotyrkina, N. G.; Kochetkov, K. A. *Organometallics* **2014**, *33*, 4639.

(244) Eerdun, C.; Hisanaga, S.; Setsune, J.-i. *Angewandte Chemie International Edition* **2013**, *52*, 929.

(245) Soloshonok, V. A.; Ono, T.; Ueki, H.; Vanthuyne, N.; Balaban, T. S.; Burck, J.; Fliegl, H.; Klopper, W.; Naubron, J.-V.; Bui, T. T. T.; Drake, A. F.; Roussel, C. *Journal of the American Chemical Society* **2010**, *132*, 10477.

(246) Constable, E. C. *Chemical Society Reviews* **2013**, *42*, 1637.

(247) Baum, G.; Constable, E. C.; Fenske, D.; Housecroft, C. E.; Kulke, T.; Neuburger, M.; Zehnder, M. *Dalton Transactions* **2000**, 945.

(248) Mamula, O.; von Zelewsky, A. *Coordination Chemistry Reviews* **2003**, *242*, 87.

(249) Murner, H.; von Zelewsky, A.; Hopfgartner, G. *Inorganica Chimica Acta* **1998**, *271*, 36.

(250) Kaim, W. *Coordination Chemistry Reviews* **1987**, *76*, 187.

(251) Coombe, V. T.; Heath, G. A.; MacKenzie, A. J.; Yellowlees, L. J. *Inorganic Chemistry* **1984**, *23*, 3423.

(252) Braterman, P. S.; Song, J. I.; Peacock, R. D. *Inorganic Chemistry* **1992**, *31*, 555.

(253) England, J.; Scarborough, C. C.; Weyhermueller, T.; Sproules, S.; Wieghardt, K. *European Journal of Inorganic Chemistry* **2012**, *2012*, 4605.

(254) Wang, M.; Weyhermueller, T.; Wieghardt, K. *Chemistry - A European Journal* **2014**, *20*, 9037.

(255) Wang, M.; England, J.; Weyhermueller, T.; Wieghardt, K. *Inorganic Chemistry* **2014**, *53*, 2276.

(256) Wang, M.; England, J.; Weyhermueller, T.; Kokatam, S.-L.; Pollock, C. J.; DeBeer, S.; Shen, J.; Yap, G. P. A.; Theopold, K. H.; Wieghardt, K. *Inorganic Chemistry* **2013**, *52*, 4472.

(257) Bowman, A. C.; England, J.; Sproules, S.; Weyhermuller, T.; Wieghardt, K. *Inorganic Chemistry* **2013**, *52*, 2242.

(258) Scarborough, C. C.; Wieghardt, K. *Inorganic Chemistry* **2011**, *50*, 9773.

(259) Scarborough, C. C.; Sproules, S.; Weyhermueller, T.; DeBeer, S.; Wieghardt, K. *Inorganic Chemistry* **2011**, *50*, 12446.

(260) Davidson, J. J.; DeMott, J. C.; Douvris, C.; Fafard, C. M.; Bhuvanesh, N.; Chen, C.-H.; Herbert, D. E.; Lee, C.-I.; McCulloch, B. J.; Foxman, B. M.; Ozerov, O. V. *Inorganic Chemistry* **2015**, *54*, 2916.

(261) Vreeken, V.; Siegler, M. A.; de Bruin, B.; Reek, J. N. H.; Lutz, M.; van der Vlugt, J. I. *Angewandte Chemie International Edition* **2015**, *54*, 7055.

(262) Wanniarachchi, S.; Liddle, B. J.; Toussaint, J.; Lindeman, S. V.; Bennett, B.; Gardinier, J. R. *Dalton Transactions* **2011**, *40*, 8776.

(263) Allard, M. M.; Sonk, J. A.; Heeg, M. J.; McGarvey, B. R.; Schlegel, H. B.; Verani, C. N. *Angewandte Chemie-International Edition* **2012**, *51*, 3178.

(264) Allard, M. M.; Xavier, F. R.; Heeg, M. J.; Schlegel, H. B.; Verani, C. N. *European Journal of Inorganic Chemistry* **2012**, *2012*, 4622.

(265) Lanznaster, M.; Hratchian, H. P.; Heeg, M. J.; Hryhorczuk, L. M.; McGarvey, B. R.; Schlegel, H. B.; Verani, C. N. *Inorganic Chemistry* **2006**, *45*, 955.

(266) Imbert, C.; Hratchian, H. P.; Lanznaster, M.; Heeg, M. J.; Hryhorczuk, L. M.; McGarvey, B. R.; Schlegel, H. B.; Verani, C. N. *Inorganic Chemistry* **2005**, *44*, 7414.

(267) Pantazis, D. A.; Krewald, V.; Orio, M.; Neese, F. *Dalton Transactions* **2010**, *39*, 4959.

(268) Sandala, G. M.; Noodleman, L. *Methods in Molecular Biology* **2011**, *766*, 293.

(269) Yamaguchi, K.; Takahara, Y.; Fueno, T. In *Applied Quantum Chemistry*; Smith, V. H., Ed.; Reidel: Dordrecht, 1986, p 155.

(270) Soda, T.; Kitagawa, Y.; Onishi, T.; Takano, Y.; Shigeta, Y.; Nagao, H.; Yoshioka, Y.; Yamaguchi, K. *Chemical Physics Letters* **2000**, *319*, 223.

(271) Jones, R. D.; Summerville, D. A.; Basolo, F. *Chemical Reviews* **1979**, *79*, 139.

(272) Smith, D. A.; Ozerov, O. V. *Chemical Communications* **2011**, *47*, 10779.

(273) Crabtree, R. H. *The Organometallic Chemistry of the Transition Metals, 6th Edition*; Wiley, **2014**.

(274) Blackmore, K. J.; Ziller, J. W.; Heyduk, A. F. *Inorganic Chemistry* **2005**, *44*, 5559.

(275) Nguyen, A. I.; Blackmore, K. J.; Carter, S. M.; Zarkesh, R. A.; Heyduk, A. F. *Journal of the American Chemical Society* **2009**, *131*, 3307.

(276) Szigethy, G.; Heyduk, A. F. *Inorganic Chemistry* **2011**, *50*, 125.

(277) Shaffer, D. W.; Szigethy, G.; Ziller, J. W.; Heyduk, A. F. *Inorganic Chemistry* **2013**, *52*, 2110.

(278) Smith, A. L.; Hardcastle, K. I.; Soper, J. D. *Journal of the American Chemical Society* **2010**, *132*, 14358.

(279) Lippert, C. A.; Arnstein, S. A.; Sherrill, C. D.; Soper, J. D. *Journal of the American Chemical Society* **2010**, *132*, 3879.

(280) Rolle, C. J.; Hardcastle, K. I.; Soper, J. D. *Inorganic Chemistry* **2008**, *47*, 1892.

(281) Milsmann, C.; Semproni, S. P.; Chirik, P. J. *Journal of the American Chemical Society* **2014**, *136*, 12099.

(282) Trovitch, R. J.; Lobkovsky, E.; Bill, E.; Chirik, P. J. *Organometallics* **2008**, *27*, 1470.

(283) Wang, D.; Lindeman, S. V.; Fiedler, A. T. *Inorganic Chemistry* **2015**.

(284) Creutz, S. E.; Peters, J. C. *Journal of the American Chemical Society* **2015**, *137*, 7310.

(285) Jarvis, A. G.; Sehnal, P. E.; Bajwa, S. E.; Whitwood, A. C.; Zhang, X.; Cheung, M. S.; Lin, Z.; Fairlamb, I. J. S. *Chemistry - A European Journal* **2013**, *19*, 6034.

(286) Jarvis, A. G.; Whitwood, A. C.; Fairlamb, I. J. S. *Dalton Transactions* **2011**, *40*, 3695.

(287) Eisenberg, R. *Science* **2009**, *324*, 44.

(288) Esswein, A. J.; Nocera, D. G. *Chemical Reviews* **2007**, *107*, 4022.

(289) Cook, T. R.; Dogutan, D. K.; Reece, S. Y.; Surendranath, Y.; Teets, T. S.; Nocera, D. G. *Chemical Reviews* **2010**, *110*, 6474.

(290) Turner, J. A. *Science* **2004**, *305*, 972.

(291) Teets, T. S.; Nocera, D. G. *Chemical Communications* **2011**, *47*, 9268.

(292) Wang, F.; Wang, W.-G.; Wang, H.-Y.; Si, G.; Tung, C.-H.; Wu, L.-Z. *Acs Catalysis* **2012**, *2*, 407.

(293) Walter, M. G.; Warren, E. L.; McKone, J. R.; Boettcher, S. W.; Mi, Q.; Santori, E. A.; Lewis, N. S. *Chemical Reviews* **2010**, *110*, 6446.

(294) McEvoy, J. P.; Brudvig, G. W. *Chemical Reviews* **2006**, *106*, 4455.

(295) Eckenhoff, W. T.; Brennessel, W. W.; Eisenberg, R. *Inorganic Chemistry* **2014**, *53*, 9860.

(296) McNamara, W. R.; Han, Z. J.; Yin, C. J.; Brennessel, W. W.; Holland, P. L.; Eisenberg, R. *Proceedings of the National Academy of Sciences of the United States of America* **2012**, *109*, 15594.

(297) Du, P. W.; Schneider, J.; Luo, G. G.; Brennessel, W. W.; Eisenberg, R. *Inorganic Chemistry* **2009**, *48*, 4952.

(298) Basu, D.; Mazumder, S.; Shi, X. T.; Baydoun, H.; Niklas, J.; Poluektov, O.; Schlegel, H. B.; Verani, C. N. *Angewandte Chemie-International Edition* **2015**, *54*, 2105.

(299) Basu, D.; Allard, M. M.; Xavier, F. R.; Heeg, M. J.; Schlegel, H. B.; Verani, C. N. *Dalton Transactions* **2015**, *44*, 3454.

(300) Han, Z. J.; Eisenberg, R. *Accounts of Chemical Research* **2014**, *47*, 2537.

(301) Han, Z. J.; McNamara, W. R.; Eum, M. S.; Holland, P. L.; Eisenberg, R. *Angewandte Chemie-International Edition* **2012**, *51*, 1667.

(302) Han, Z. J.; Shen, L. X.; Brennessel, W. W.; Holland, P. L.; Eisenberg, R. *Journal of the American Chemical Society* **2013**, *135*, 14659.

(303) Eisenberg, R.; Gray, H. B. *Inorganic Chemistry* **2008**, *47*, 1697.

(304) Zhang, T.; Wang, C.; Liu, S.; Wang, J.-L.; Lin, W. *Journal of the American Chemical Society* **2014**, *136*, 273.

(305) Duan, L.; Bozoglian, F.; Mandal, S.; Stewart, B.; Privalov, T.; Llobet, A.; Sun, L. *Nature Chemistry* **2012**, *4*, 418.

(306) Fillol, J. L.; Codolà, Z.; Garcia-Bosch, I.; Gómez, L.; Pla, J. J.; Costas, M. *Nature Chemistry* **2011**, *3*, 807.

(307) Barnett, S. M.; Goldberg, K. I.; Mayer, J. M. *Nature Chemistry* **2012**, *4*, 498.

(308) Yin, Q.; Tan, J. M.; Besson, C.; Geletii, Y. V.; Musaev, D. G.; Kuznetsov, A. E.; Luo, Z.; Hardcastle, K. I.; Hill, C. L. *Science* **2010**, *328*, 342.

(309) Kanan, M. W.; Nocera, D. G. *Science* **2008**, *321*, 1072.

(310) Du, S.; Ren, Z.; Zhang, J.; Wu, J.; Xi, W.; Zhu, J.; Fu, H. *Chemical Communications* **2015**, *51*, 8066.

(311) Tong, L.; Kopecky, A.; Zong, R.; Gagnon, K. J.; Ahlquist, M. S. G.; Thummel, R. P. *Inorganic Chemistry* **2015**, *54*, 7873.

(312) Wakerley, D. W.; Gross, M. A.; Reisner, E. *Chemical Communications* **2014**, *50*, 15995.

(313) Kal, S.; Filatov, A. S.; Dinolfo, P. H. *Inorganic Chemistry* **2014**, *53*, 7137.

(314) Hsieh, C.-H.; Ding, S.; Erdem, O. F.; Crouthers, D. J.; Liu, T.; McCrory, C. C. L.; Lubitz, W.; Popescu, C. V.; Reibenspies, J. H.; Hall, M. B.; Darensbourg, M. Y. *Nature Communications* **2014**, *5*, 3684.

(315) Nippe, M.; Khnayzer, R. S.; Panetier, J. A.; Zee, D. Z.; Olaiya, B. S.; Head-Gordon, M.; Chang, C. J.; Castellano, F. N.; Long, J. R. *Chemical Science* **2013**, *4*, 3934.

(316) Zhu, H.; Huang, W.-z.; Pu, J.-q. *Shanghai Daxue Xuebao* **2007**, *13*, 77.

(317) Aldahash Ehsan, A.; Sebe, I. *Scientific Bulletin-University Politehnica of Bucharest, Ser. B* **2012**, *74*, 77.

(318) Wang, H.-Y.; Mijangos, E.; Ott, S.; Thapper, A. *Angewandte Chemie International Edition* **2014**, *53*, 14499.

(319) Lee, W.-T.; Muñoz, S. B.; Dickie, D. A.; Smith, J. M. *Angewandte Chemie International Edition* **2014**, *53*, 9856.

(320) Basu, D.; Mazumder, S.; Shi, X.; Baydoun, H.; Niklas, J.; Poluektov, O.; Schlegel, H. B.; Verani, C. N. *Angewandte Chemie International Edition* **2015**, *54*, 2105.